



HAL
open science

Study and design of a thermodynamic system generating mechanical work from a hot source at 120°C

Samer Maalouf

► **To cite this version:**

Samer Maalouf. Study and design of a thermodynamic system generating mechanical work from a hot source at 120°C. Other. Ecole Nationale Supérieure des Mines de Paris, 2013. English. NNT : 2013ENMP0074 . tel-01924552

HAL Id: tel-01924552

<https://pastel.hal.science/tel-01924552>

Submitted on 16 Nov 2018

HAL is a multi-disciplinary open access archive for the deposit and dissemination of scientific research documents, whether they are published or not. The documents may come from teaching and research institutions in France or abroad, or from public or private research centers.

L'archive ouverte pluridisciplinaire **HAL**, est destinée au dépôt et à la diffusion de documents scientifiques de niveau recherche, publiés ou non, émanant des établissements d'enseignement et de recherche français ou étrangers, des laboratoires publics ou privés.

École doctorale n° 432 : Sciences des Métiers de l'Ingénieur

Doctorat ParisTech

T H È S E

pour obtenir le grade de docteur délivré par

l'École nationale supérieure des mines de Paris
Spécialité " Énergétique "

présentée et soutenue publiquement par

Samer MAALOUF

le 27 septembre 2013

**Etude et conception d'un système thermodynamique producteur
du travail mécanique à partir d'une source chaude à 120°C**

**Study and design of a thermodynamic system generating
mechanical work from a hot source at 120°C**

Thèse confidentielle
(date de fin le 27/09/2018)

Directeur de thèse : **Denis CLODIC**
Co-encadrement de la thèse : **Elias BOULAWZ KSAYER**

Jury

M. Jocelyn BONJOUR, Professeur, INSA de Lyon
M. Michel FEIDT, Professeur des Universités, LEMTA
M. Predrag HRNJAK, Professeur, University of Illinois
M. Denis CLODIC, Directeur de recherche émérite, CES, MINES ParisTech
M. Elias BOULAWZ KSAYER, Docteur, CES, MINES ParisTech

Rapporteur
Rapporteur
Rapporteur
Examineur
Examineur

**T
H
È
S
E**

«The greatest challenge to any thinker is stating the problem in a way that will allow a solution»

«Le plus grand défi pour tout penseur est de poser le problème d'une manière qui permettra une solution»

Bill Watterson (1958 -)

Acknowledgement

It would not have been possible to write this doctoral thesis without the help and support of the kind people around me, to only some of whom it is possible to give particular mention here.

The first person I would like to thank is my principal supervisor *Denis Clodic*, President and Director of “EReIE Company”. His wisdom, knowledge, and commitment to the highest standards inspired and motivated me.

I would like to express my deepest gratitude to my supervisor *Elias BouLawz Ksayer* for his excellent guidance, caring, patience, and helping me to develop my background in research, not to mention his advice and unsurpassed knowledge. His support has been invaluable on both an academic and a personal level, for which I am extremely grateful.

I would like to thank *Maroun Nemer*, Director of “CES”, who provided me valuable comments, continuous advice and offered me an excellent environment for research.

Special thanks to *Jocelyn Bonjour*, *Michel Feidt* and *Predrag Hrnjak*, for accepting to be members of the Examination Board and evaluating my work.

I would like to express my sincere appreciation and gratitude to *Anne-Marie Bonnet* for her professional and linguistic involvement.

I gratefully acknowledge *Olivier Calmels* and *Ludovic De Oliveira*, whom partly contributed to my work. Their involvement, scientific intuition, and technical competences were of great assistance.

I would like to thank also the working team of the **Center for Energy and Systems Efficiencies “CES”**, who created a suitable environment for me to work.

Finally, I wish to express my gratitude to my **Parents**, whom always supporting me and encouraging me with their best wishes.

Nomenclature

Symbol

A, S	section area		m^2
a	specific surface area		$m^2.m^{-3}$
b	corrugation base length	m	
B	surface ratio		-
BV	burning velocity		$cm.s^{-1}$
C	coil characteristic		-
c	heat transfer exponent	-	
c_p	specific heat capacity		$J.kg^{-1}.K^{-1}$
D, d	diameter		m
D	diffusion coefficient		$m^2.s^{-1}$
DT	temperature difference / pinch	K	
DP	pressure drop		Pa
Dh	enthalpy difference		$kJ.kg^{-1}$
DTLM	log mean temperature difference		K
E, Ex	exergy		$kJ.kg^{-1}$
e	thickness		m
f	fanning friction factor		-
F	load factor		$m.s^{-1}.(kg.m^{-3})^{0.5}$
G	mass velocity		$kg.m^{-2}.s^{-1}$
h	mass enthalpy	$kJ.kg^{-1}$	
h	heat transfer coefficient	$W.m^{-2}.K^{-1}$	
h	corrugation height		m
h_L	liquid hold-up		%
h_{fg}	latent heat of vaporization		$kJ.kg^{-1}$
H	height		m
I	irreversibility		$kJ.kg^{-1}$
I	flammability		-
j	colburn j-factor	-	
J	superficial velocity		$m.s^{-1}$
k	mass transfer coefficient		$m.s^{-1}$
k	thermal conductivity		$W.(m.K)^{-1}$
L	length		m
LNF	number of fins per linear meter	m^{-1}	
L_v	latent heat of vaporization		$kJ.kg^{-1}$
M	molar mass		$g.mol^{-1}$
m	mass flow rate	$kg.s^{-1}$	
m	fin parameter		-
MIE	minimum ignition energy		mJ
n	moles number		mol
P	pressure		Pa
q	heat flux		$W.m^{-2}$
Q	heat capacity		$kJ.kg^{-1}$
R	thermal resistance		$K.W^{-1}$
r	radius		mm
s	mass entropy		$kJ.(kg.K)^{-1}$
s	corrugation side length	m	
SC	sub-cooling		K
SH	superheat		K
T	temperature		$^{\circ}C$
V	volume	m^3	
V, u	velocity	$m.s^{-1}$	
U	global heat transfer coefficient	$W.m^{-2}.K^{-1}$	

w	absolute humidity	kg.kg ⁻¹ _{dg}
W	power	kJ.kg ⁻¹
x	vapor quality	-
y	dry mass fraction / molar fraction	adim

Greek letters

η	efficiency	%
μ	chemical potential	kJ.kg ⁻¹
Δ	relative variation	%
Υ	turbine expansion ratio	-
α	slope of the saturation vapor line	-
α	corrugation angle	°
ρ	density	kg.m ⁻³
ξ	friction factor	-
ζ	overall coefficient losses	-
ψ	fraction of gas flow channels ending at column walls	-
σ, γ	surface tension	N.m ⁻¹
φ	heat flux	W.m ⁻²
ξ	mass fraction of lithium-bromide	-
δ	thickness	mm
θ	angle	°
λ	thermal conductivity	W.(m.K) ⁻¹
ε	void fraction	-
Ω	loading point constant	-

Subscripts

a	air / dry flue gases
c	condensate / convective / circuit
cond	condenser
cr	critical point
D	division
d	dry
DC	direction change
dp	dew point
dg	dry gases
evap	evaporator/ evaporation
e	effective
f	fin
fr	frontal
G, g	gas
H	high / horizontal
i	inside
in	inlet
is	isentropic
L	low / liquid / longitudinal / lithium bromide
m	mean / metal
max	maximal
nb	normal boiling
o	reference conditions / outside / overall
out	outlet
p	pitch / pump / packing
pb	packing bed
pe	packing element

pnb	pool normal boiling
r	refrigerant
s	spacing / superficial / surface / solid / saturated
sw	saturated water
T	transversal
t	turbine/ total / tube
tp	two-phase / triple point
v	volume / vertical / vapor
w	wet / wall/ water
wb	wet bulb
wf	working fluid
wv	water vapor

Abbreviations

CT	Cooling tower
CU	Condensing unit
GWP	Global Warming Potential ($\text{kg}_{\text{CO}_2\text{eq}} \cdot \text{kg}^{-1}_{\text{wf}}$)
HEX	Heat exchanger
HFC	Hydro - Fluoro – Carbon
NBP	Normal Boiling Point
NBP	Number of Transfer Unit
ODP	Ozone Depletion Potential
EU	Evaporating Unit

Non-dimensional numbers

$Nu = \frac{h.D}{k}$	Nusselt number
$Pr = \frac{\mu.c_p}{k}$	Prandtl number
$Re = \frac{\rho.V.D}{\mu}$	Reynolds number
$Fr_l = \frac{G^2}{\rho_l^2 \cdot g \cdot D}$	Froude number
$D_n = Re \sqrt{\frac{r}{R}}$	Dean number
$Sc = \frac{\mu}{\rho.D}$	Schmidt number
$Sh = \frac{k.L}{D}$	Sherwood number

CONTENTS

GENERAL INTRODUCTION	1
CHAPTER 1: STUDY AND DESIGN OF THERMODYNAMIC CYCLES FOR LOW TEMPERATURE HEAT SOURCES	3
1.1 LOW-TEMPERATURE WASTE HEAT RECOVERY: POTENTIAL AND CHALLENGE	3
1.1.1 <i>Prioritization of industrial gas-waste heat sources</i>	3
1.1.2 <i>Low-temperature waste heat: large and unexploited heat sources</i>	4
1.1.3 <i>Challenges to recovering low-temperature waste heat</i>	7
1.1.3.1 Non-conventional heat sources.....	7
1.1.3.2 Heat extraction	7
1.1.3.3 Conversion	9
1.2 ENERGY AND EXERGY RECOVERY FROM LOW-TEMPERATURE HEAT SOURCES	9
1.2.1 <i>Heat load and exergy availabilities</i>	10
1.2.2 <i>Ideal overall and exergy efficiencies</i>	13
1.3 POWER GENERATION CYCLES	14
1.3.1 <i>Organic Rankine Cycle</i>	15
1.3.2 <i>Kalina Cycle</i>	15
1.4 LOW-TEMPERATURE HEAT EXCHANGE.....	16
1.4.1 <i>Indirect Contact Water-Vapor Condensation Recovery</i>	16
1.4.2 <i>Direct Contact Water-Vapor Condensation Recovery</i>	17
1.4.3 <i>Transport Membrane Condenser</i>	17
1.5 SIMPLE ORC WITH INDIRECT-CONTACT HEAT RECOVERY	18
1.5.1 <i>Simple ORC with direct evaporator</i>	18
1.5.1.1 Parameters of the simple ORC	18
1.5.1.2 Results and interpretations.....	21
1.5.2 <i>Simple ORC with indirect evaporator</i>	26
1.6 ORC WITH DIRECT-CONTACT HEAT RECOVERY	28
1.7 TWO-STAGE ORC.....	33
1.7.1 <i>Typical two-stage ORC</i>	33
1.7.2 <i>Improved two-stage ORC</i>	36
1.7.3 <i>Two-stage ORC using direct-contact condensation at the low-pressure stage</i>	37
1.8 NET POWER COMPARISON BETWEEN THE HEAT RECOVERY MODES.....	38
1.9 EFFECT OF AUXILIARY CONSUMPTIONS ON ORC PERFORMANCES	39
1.9.1 <i>Effect of auxiliary consumptions on condensation pressure</i>	40
1.9.2 <i>Effect of auxiliary consumptions on evaporator superheat</i>	41
1.9.3 <i>Effect of auxiliary consumptions on evaporation temperature</i>	41
1.9.4 <i>Effect of auxiliary consumptions on working fluid selection</i>	42
1.9.5 <i>Pure working fluid</i>	43
1.9.6 <i>Binary blends as working fluid</i>	47
1.9.6.1 Binary blends for simple ORC with indirect-contact condensation.....	47
1.9.6.2 Binary blends for simple ORC with direct-contact condensation.....	50
1.9.6.3 Enhanced two-stage ORC with binary blends	53
1.9.7 <i>Effects of auxiliary consumptions on heat recovery modes</i>	54
1.10 TRANS-CRITICAL ORGANIC RANKINE CYCLE.....	55
1.10.1 <i>Trans-critical ORC with R-134a, R-1234yf, R-1234ze, and R-32 as working fluids</i>	56
1.10.2 <i>Trans-critical ORC with carbon dioxide as working fluid</i>	56
1.11 CONCLUSIONS	57
REFERENCES.....	60
CHAPTER 2: INDIRECT CONTACT-CONDENSATION HEAT RECOVERY	63
2.1 INTRODUCTION.....	63

2.2	CHEMISTRY OF THE CONDENSING FLUE GASES	63
2.2.1	<i>Acid dew point calculations</i>	64
2.2.2	<i>Heat-exchanger corrosion zones</i>	65
2.2.3	<i>Potential solutions for acid corrosion</i>	67
2.3	GENERAL DESIGN METHOD FOR FIN-AND-TUBE HEX AT LOW TEMPERATURE	67
2.3.1	<i>Design criteria</i>	68
2.3.2	<i>Heat and mass transfer model</i>	71
2.3.2.1	Heat-transfer model	71
2.3.2.2	Mass transfer model	75
2.3.3	<i>Optimization procedure</i>	77
2.3.3.1	Operating parameters.....	77
2.3.3.2	Tube length.....	79
2.3.3.3	Fin types and fin pitches.....	80
2.3.3.4	Tube diameters and tube pitches.....	81
2.3.3.5	Fin-and-tube heat exchanger circuitry	82
2.3.4	<i>Effect of evaporation pressure on fin-and-tube heat-exchanger parameters</i>	82
2.3.5	<i>Effect of material selection on fin-and-tube heat-exchanger parameters</i>	83
2.4	CONDENSATION MODES.....	84
2.5	EXPERIMENTAL METHODS	85
2.5.1	<i>Description of the heat-exchanger specimens</i>	85
2.5.2	<i>Experimental apparatus and procedure</i>	87
2.6	DATA REDUCTION AND INTERPRETATION	89
2.7	TESTS RESULTS AND DISCUSSION	90
2.7.1	<i>Dry-condition test data</i>	91
2.7.2	<i>Partially wet-condition test data</i>	96
2.8	CONCLUSIONS	99
	REFERENCES.....	101

CHAPTER 3: DIRECT CONTACT-CONDENSATION HEAT RECOVERY 103

3.1	INTRODUCTION.....	103
3.2	DESIGN OF A CONDENSING UNIT	103
3.2.1	<i>Description of a Condensing unit</i>	103
3.2.2	<i>Packing types and corrugation geometry</i>	104
3.2.3	<i>Hydraulics of the condensing unit</i>	107
3.2.4	<i>Heat and mass transfer model inside the packing</i>	109
3.2.5	<i>Hydraulics and mass transfer predicting model for structured packing</i>	113
3.2.5.1	Liquid hold-up.....	114
3.2.5.2	Pressure drop	115
3.2.5.3	Effective surface area	118
3.2.5.4	Mass transfer coefficients.....	118
3.2.5.5	Heat-transfer coefficients	119
3.3	MODEL SIMULATION AND RESULTS	120
3.4	EXPERIMENTAL METHODS	123
3.4.1	<i>Description of the lab-scale condensing unit</i>	123
3.4.2	<i>Experimental apparatus and procedure</i>	125
3.4.3	<i>Data reduction and interpretation</i>	128
3.5	TESTS RESULTS AND DISCUSSION	128
3.5.1	<i>Experimental pressure drop at the airside</i>	129
3.5.2	<i>Comparison of the overall heat-transfer coefficient</i>	130
3.5.3	<i>Comparison between the predicted and correlated heat-exchange capacity</i>	131
3.6	CONCLUSIONS	132
	REFERENCES.....	134

CHAPTER 4:	INNOVATIVE THERMODYNAMIC CYCLES FOR LOW-TEMPERATURE WET HEAT SOURCES	136
4.1	INTRODUCTION.....	136
4.2	REVIEW OF THE EXISTING HEAT RECOVERY TECHNOLOGIES	137
4.3	DESICCANT: OPERATION AND SELECTION	139
4.3.1	<i>Desiccant operation</i>	139
4.3.2	<i>Liquid sorption</i>	139
4.3.3	<i>Desiccant selection</i>	140
4.4	PROPERTIES OF AQUEOUS LITHIUM-BROMIDE SOLUTION	141
4.4.1	<i>Composition</i>	141
4.4.2	<i>Vapor pressure</i>	141
4.4.3	<i>Heat capacity and enthalpy of water – lithium bromide solutions</i>	142
4.4.4	<i>Equilibrium chart (“Dühring” Plot)</i>	144
4.5	DIRECT-CONTACT CONDENSATION USING AQUEOUS LITHIUM-BROMIDE SOLUTION.....	144
4.6	REGENERATION PROCESS USING SOLAR ENERGY	149
4.7	CONVENTIONAL REGENERATION CYCLE (CRC) USING AN EVAPORATING UNIT.....	154
4.8	IMPROVED REGENERATION CYCLE (IRC)	156
4.8.1	<i>Operating point</i>	157
4.8.2	<i>Effect of water dew point temperature</i>	159
4.8.3	<i>Effect of condensation temperature</i>	160
4.9	MODEL VALIDATION USING “ASPEN” SOFTWARE	161
4.10	CONCLUSIONS	162
	REFERENCES.....	164
GENERAL CONCLUSIONS.....	165	
ANNEX A: EVALUATION OF THE CHEMICAL EXERGY.....	169	
ANNEX B: COOLING TOWER PARAMETERS	170	
ANNEX C: OPTIMIZATION PROCEDURES.....	171	
ANNEX D: HEAT-TRANSFER AND PRESSURE DROP CORRELATIONS USED IN FIN-AND-TUBE HEAT EXCHANGER	176	
ANNEX E: TEST-BENCH DESCRIPTION	180	
ACKNOWLEDGEMENTS: APPLICATION OF THE RESULTS AND FRAMEWORK TO THE CEMENT PRODUCTION INDUSTRY	190	

General introduction

The valorization of waste heat within processes in industry undoubtedly plays a crucial role in improving overall energy efficiency of those processes. When there is no potential use of process waste heat, or when high-temperature waste heat has already been used inside the process itself or possibly with the surrounding community, the conversion of the remaining heat (< 120 to 150°C) in electricity should be considered. Investigation of current waste-heat recovery practices shows that waste heat is generally recovered from clean, high-temperature waste heat sources in large capacity systems. Most unrecovered waste heat (more than 50%) is at low temperatures (< 120 - 150°C). Due to lack of efficient recovery methods, low-grade waste heat has generally been discarded in industry. While low-temperature waste heat has less thermal and economic value than high-temperature heat, it is ubiquitous and available in large quantities. The field of low-temperature waste heat is addressed through novel science and ambitious technological solutions.

Low-temperature heat valorization faces technical barriers that impede their wider application. The maximum thermodynamic efficiency represented by the Carnot factor is only around 25%. Heat extraction challenges arise from the fact that large heat-transfer areas for heat exchangers are required due to the low-temperature level. In addition, industrial flue gases may contain high-moisture content and there would be significant benefits to cooling flue gases to temperatures below the water-vapor dew point. However, the presence of pollutant substances (SO_x , NO_x ...) is of particular concern because of potential corrosion of heat exchangers.

The thesis focuses on particularly energy-hungry industrial sectors characterized by presently unsolved challenges in terms of environmentally hostile low-temperature heat sources. It will open very important technological perspectives of increased energy efficiency through low-temperature waste heat valorization by way of electricity production. The results from this thesis are identified in two broad areas: 1) extending the range of existing technologies to low-temperature level in order to enhance their feasibility and recovery efficiency, and 2) exploring new methods for waste heat recovery.

Chapter 1 details the heat recovery options from low-temperature waste heat for generating electrical power using the well-proven Organic Rankine Cycle (ORC). Current recovery technologies include indirect and direct-contact water-vapor condensation recovery depending on which the heat is transferred between the hot stream (flue gases) and the cold stream (working fluid) using or not an intervening wall respectively. The effects of water-vapor condensation on cycle performance using the two condensing heat recovery processes (direct and indirect heat exchange) are pointed out. Thermodynamic optimization is conducted in order to maximize the net power produced. The impacts of auxiliary consumptions on the ORC behavior are studied. The benefits of using a blend as working fluid instead of pure working fluid when computing auxiliary consumptions are highlighted.

Chapter 2 presents the heat recovery from low-temperature heat sources using an indirect-contact heat-recovery process (fin-and-tube heat exchanger). A theoretical prediction for acid dew-point calculations is presented and the typical corrosion zones in the heat exchanger are identified. A general method to design the fin-and-tube heat exchanger adapted to low-temperature level has been elaborated. Advanced coating materials that can minimize chemical attack by cooling exhaust gases below the acid and water dew points are proposed and laboratory tested. The impacts of surface wettabilities on thermal hydraulic performances of the fin-and-tube heat exchanger are underlined.

Chapter 3 deals with the process of direct-contact heat transfer between flue gases and water flowing counter-currently in a condensing unit filled with packing materials. General design method for the condensing unit based on hydraulics parameters (pressure drop and liquid hold-up) and on heat and mass transfer between flue gases and water inside the packing is elaborated. Experimental studies are performed in order to validate the developed model and to examine performances of various packing types with distinct surface geometry and wet-ability on the condensing unit behavior.

In chapter 4, innovative opportunities are proposed by developing new heat-recovery technologies for replacing existing ones enabling heat recovery from heat sources with high-moisture contents and therefore increasing effective options for heat recovery. Novel thermodynamic cycles based on the liquid desiccant technology are presented. The water sorption characteristics of desiccant materials are discussed and the implications of those characteristics in low-temperature heat recovery systems are explained.

Chapter 1: Study and design of thermodynamic cycles for low temperature heat sources

1.1 Low-temperature waste heat recovery: Potential and Challenge

In December 2008, under the “20-20-20” designation, the European Parliament adopted the EU climate change package (SET-Plan 1) with the aim of reaching three main energy-climate targets by 2020: (a) 20% greenhouse gases (GHG) emissions reduction, (b) 20% energy efficiency increase, and (c) 20% renewable energies share in the EU energy mix [DUP 09]. In the EU 27, the industry sector represents 28% of the final energy consumption, 21% of the GHG emissions and it must therefore be considered in the 20-20-20 context [FP7 07]. Efforts to improve industrial energy efficiency focus on reducing the energy consumed by the equipment used in manufacturing (e.g. boilers, furnaces, dryers, reactors...). Using Best Available Technologies (BATs), energy savings of 20% are reachable in the European industrial sector. A valuable approach to improve overall energy efficiency is to recover and reuse the waste heat that is intrinsic to all industrial manufacturing. Waste heat recovery implies capturing and reusing the waste heat in industrial processes for heating or for generating mechanical or electrical power. The exact quantity of industrial waste heat is poorly quantified, but various studies have estimated that as much as 20 to 50% of industrial energy consumption is ultimately discharged as waste heat [BCS 08]. While some waste heat losses from industrial processes are inevitable, facilities can reduce these losses by improving equipment efficiency or installing waste heat recovery technologies.

1.1.1 Prioritization of industrial gas-waste heat sources

Typical waste-gas heat sources include combustion exhausts such as glass melting furnace, cement kiln, incinerator, aluminum furnace, and boiler. Waste heat losses arise both from equipment inefficiencies and from thermodynamic limitations on equipment and processes [WEN 13]. For example, consider furnaces frequently used in aluminum melting operations: exhaust gases leaving the furnace can have temperatures as high as 1200-1300°C. Consequently, these gases have high heat content, carrying away as much as 60% of furnace energy inputs. Efforts can be made to design more energy efficient furnaces with better heat transfer and lower exhaust temperatures; however, the laws of thermodynamics place a lower limit on the temperature of exhaust gases. Since heat exchange involves energy transfer from a high temperature source to a lower temperature sink, the combustion gas temperature must always exceed the molten aluminum temperature in order to facilitate aluminum melting. The gas temperature in the furnace will never decrease below the temperature of the molten aluminum. Therefore, the minimum possible temperature of combustion gases immediately exiting an aluminum furnace corresponds to the aluminum pouring point temperature from 650 to 750°C. In this scenario, at least 40% of the energy input to the furnace is still lost as waste heat.

To better calculate a realistic potential of waste heat, several guidelines suggest a prioritization of waste heat recovery [WEN 13]. First, avoiding waste heat should be prioritized over recovering waste heat. Before implementing waste heat recovering actions, one should first think of possibilities to avoid the creation of waste heat through more efficient equipment or control systems. If waste heat is unavoidable, one should prioritize the reuse of waste heat to substitute heat demand for secondary processes within the production system on site (heat exchanger, heat pumps, heat storage...). For example, the use of the combustion exhaust gases to preheat combustion air or feed-water in industrial boilers. By preheating the feed-water before it enters the boiler, the amount of energy required to heat the water to its final temperature is reduced. Alternately, the heat can be transferred to another process;

for example, a heat exchanger could be used to transfer heat from combustion exhaust gases to hot air needed for a drying oven. In this manner, the recovered heat can replace fossil energy that would have otherwise been used in the oven.

Once on-site heat reutilization is exploited, the possibility to reuse heat for neighboring sites and district heating grids should be used. Only if heat reutilization is fully exploited on- and off-site, one can use the remaining waste heat for electricity generation. These prioritization rules are incorporated in an energy flow diagram, which illustrates the method for evaluating waste heat recovery potential (Fig. 1.1). In Stage 1, the total waste heat potential is quantified and characterized in a chosen sector. During Stage 2, the potential of avoidable waste heat will be estimated. Stage 3 is evaluating the on-site reusable waste heat potential. Finally, in Stage 4, the off-site reusable waste heat potential is assessed.

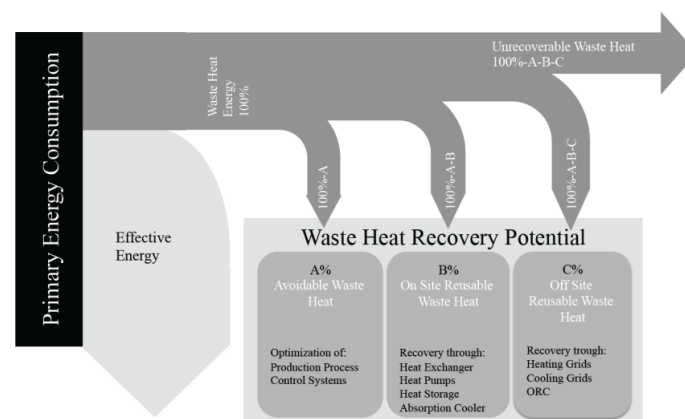


Fig. 1.1: Prioritization and recovery options for industrial gas waste heat sources [WEN 13]

Such methods for recovering waste heat can help facilities significantly reduce their fossil fuel consumption, as well as reduce associated operating costs and pollutant emissions. Another advantage of waste heat recovery is that it can reduce capacity requirements for facilities thermal conversion devices, leading to reductions in capital costs. In addition to the economic benefits of waste heat recovery for the facility, waste heat recovery is a green-house-gas-free source of energy. Reducing the fossil fuel demand will result in accompanying reductions in greenhouse-gas emissions.

1.1.2 Low-temperature waste heat: large and unexploited heat sources

Investigation of current waste-heat recovery practices shows that waste heat is generally recovered from clean, high-temperature waste-heat sources in large capacity systems. Most unrecovered waste heat, more than 50%, is at low temperatures ($< 150^{\circ}\text{C}$) [BCS 08]. Due to lack of efficient recovery methods, low-grade waste heat has generally been discarded in industry. While low-temperature waste heat has less thermal and economic value than high-temperature heat, it is ubiquitous and available in large quantities. Literature reveals that the total work potential of low-temperature waste heat is sufficiently large that it should not be neglected in pursuing researches and development opportunities for waste heat recovery [FP7 07].

As shown in Fig. 1.2, when there is no potential use of process waste heat or when high-temperature waste heat has already been used inside the process itself or possibly with the surrounding community, the conversion of the remaining heat (low-temperature heat $< 120^{\circ}\text{C}$) in electricity should be considered. The field of low-temperature waste heat is addressed through novel science and ambitious technological solutions.

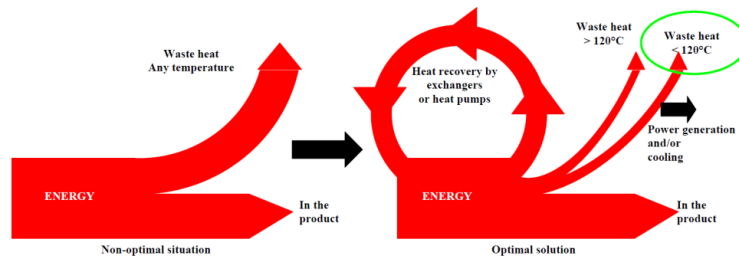


Fig. 1.2: Process industry waste heat recovery principle [FP7 07]

In order to illustrate the potential of low-temperature heat sources (100-150°C), Fig. 1.3 shows the repartition of waste heat by temperature in the French industry.

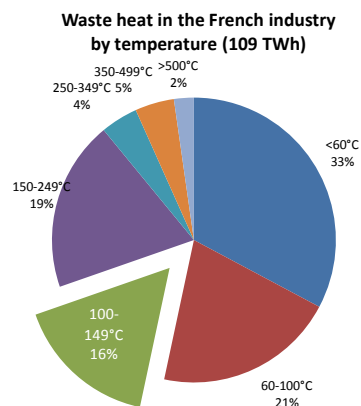


Fig. 1.3: Repartition of waste heat in the French industry by temperature [CER 99]

Fig. 1.3 shows that the waste heat sources within the interval 100 to 150°C represents around 16% of the total waste heat, resulting in a 17.5 TWh/yr of energy recovered. In quantitative terms, assuming an overall efficiency of the order of 4%, 700 GWh/yr of electrical energy could be potentially produced through waste heat recovery in the temperature range (100 to 150°C) in the French industry.

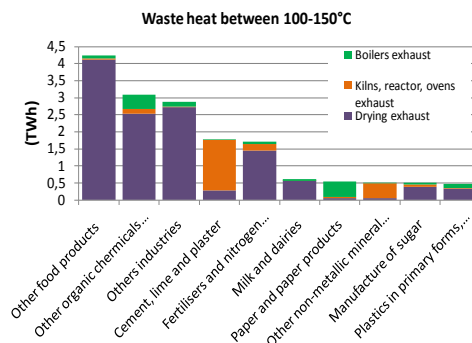


Fig. 1.4: Repartition of waste heat (100 to 150°C) in the French industry by industrial sectors [CER 99]

Fig. 1.4 shows the repartition of waste heat (100 to 150°C) in the French industry by industrial sectors. Waste heat is mainly released in the food, chemical, cement, and fertilizers industries. The drying exhaust represents the major part of the waste heat in the food, chemical, fertilizers, and milk industries, while the kiln exhaust accounts for the major portion in the cement industry.

The cement industry represents one of the most energy-intensive industrial sectors, since it accounts for 8% of the energy use in industry and 25% of the energy and process CO₂ emissions worldwide. It represents one of the main applications about low-temperature waste-heat recovery.

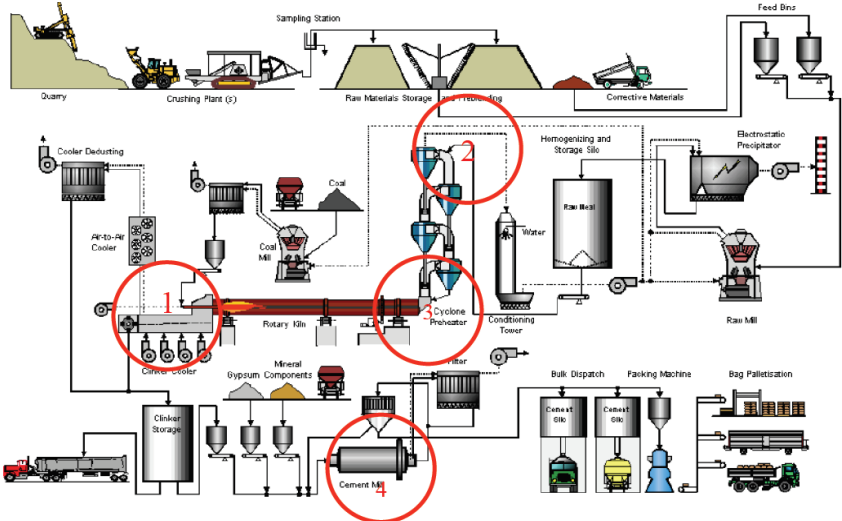


Fig. 1.5: Dry cement process flow diagram [CEM 99]

In order to better understand and identify the waste heat released in the cement industry, Fig. 1.5 depicts a process diagram for a dry cement production process [CEM 99]. The cement production process consists of five main steps: mining and extraction of limestone and clay, mixing of the raw materials, grinding and drying of the raw meal, clinker production in a pre-heater and kiln system, mixing with additional materials and grinding of the resulting cement powder. The raw materials are crushed and grinded in the raw mill. Then it goes through the cyclone pre-heater to the rotary kiln where pyro-chemical reactions take place at around 2000°C. Directly afterwards, the hot clinker is quickly cooled down to 100 to 200°C and stored for further processing. After the clinker and additives are grinded in the cement mill, the resulting raw powder is the finished cement [BOR 13].

Based on this process diagram, four main waste heat sources can be identified. Those are (1): clinker cooler gases, (2): kiln combustion gases, (3): bypass gases, and (4): cement mill gases. Flue gases are released into the atmosphere at the raw mill exit and after cleaning, at 120°C or below. Low-temperature gases are also released at the cement mill exit (< 120°C). The bypass gases appear in low quantities (2% of energy consumption) and do not exist in every cement factory. Clinker cooler gases exit at relatively high temperature (~ 400°C).

Table 1.1 shows the potential of low-temperature waste heat in the cement sector (France, Germany, and Poland). The total available low-temperature waste heat is around “3.84 TWh/yr” leading to a total available exergy around “0.56 TWh/yr”.

Table 1.1: Potential of low-temperature waste heat in the cement sector (France, Germany & Poland) [BOR 13]

Country	Waste heat source	Temperature (°C)	Waste heat (TWh/yr)	Exergy (TWh/yr)
France	Rawmill gases	100°C - 120°C	1.0	0.1
	Cement mill gases	100°C - 120°C	0.2	0.05
Germany	Raw mill gases	100°C - 120°C	1.4	0.2
	Cement mill gases	100°C - 120°C	0.29	0.07
Poland	Raw mill gases	100°C - 120°C	0.8	0.1
	Cement mill gases	100°C - 120°C	0.15	0.04
Total	-	-	3.84	0.56

Another example on low-temperature waste heat application is the iron and steel industry. Low-temperature gases are released into the atmosphere at the blast furnaces exit and after, at 150°C or below. Table 1.2 shows the potential of low-temperature waste heat in the iron and steel industry at the blast furnace exit (France and Germany). The total available low-temperature waste heat is around “4.41 TWh/yr” resulting to a total available exergy around “0.90” TWh/yr”.

Table 1.2: Potential of low-temperature waste heat in the iron and steel industry (France and Germany) [BOR 13]

Country	Waste heat source	Temperature (°C)	Waste heat (TWh/yr)	Exergy (TWh/yr)
France	Blast furnace gases	< 150°C	1.15	0.2
Germany			3.26	0.7
Total	-	-	4.41	0.90

In quantitative terms, assuming an overall efficiency in the range of 4%, 153 GWh and 176 GWh of electrical energy can be potentially produced, through waste heat recovery on gas exit of, respectively, raw/cement mills and iron-steel industries (France, Germany, and Poland).

1.1.3 Challenges to recovering low-temperature waste heat

From thermodynamic and thermal points of views, generating power from waste heat recovery below 120°C is a challenging task. Three main scientific and technical challenges identified are as follows.

1.1.3.1 Non-conventional heat sources

State-of-the-art heat recovery technologies require a minimum temperature of 150°C to work efficiently. In thermally optimized industrial processes, only a limited amount of high-temperature heat is available. The number of potential heat sources in low-temperature streams (< 120°C) is limited, although their energy content is significant. Presently, low-temperature waste heat sources are mainly valorized to provide heat to other applications and only rarely, to produce electricity, often considered as less attractive. However, generating electricity represents a rational alternative, since it circumvents drawbacks linked to heat demand seasonality and location.

1.1.3.2 Heat extraction

The heat extraction from low-temperature waste streams is often closely connected with material corrosion problems. Depending on the fuel used, combustion-related flue gases contain varying concentrations of carbon dioxide, water vapor, nitric oxides, and sulfuric oxides. In addition, most of the low-temperature gas streams have high moisture contents associated to many processes such as flashing, washing, cleaning, and drying. The water dew point of these heat sources could range from 30°C (~ 4% moisture, dry heat sources) up to 70°C (~ 30% moisture, wet heat sources) [FP7 07]. Example on drying process is the raw mill exit gas in cement industry. During the raw mill preparation, the raw mill gas will be charged with moisture when drying of the raw material in the mill. The charged moisture varies during the year, depending on the moisture content of the material that is driven by seasons and weather conditions.

Cooling the flue gas below the water vapor dew point could significantly increase heat recovery by allowing the latent heat of vaporization to be recovered. However, in this case, the water vapor in the gas will condense and react with sulfuric and nitric oxides, resulting in a corrosive substance deposition on the heat-exchanger surface that will reduce heat-transfer rates, lifetimes, and lead to increased pressure drops and reduced efficiency. In this case, heat exchangers designed from low-cost materials will quickly fail due to chemical attack. Material constraints and costs associated with high

chemical activity streams require more advanced recovery equipment materials to withstand corrosive environments.

Another challenge for heat exchangers when working with low-temperature fluids is the large heat transfer area required. Fig. 1.6 shows the influence of temperature difference on required heat-exchanger area. It shows the surface area required for recovering “1 MW_{th}” from a gaseous exhaust stream. “ΔT” denotes the difference in temperatures between heat source and heat sink. The expression for heat transfer can be generalized by the following equation:

$$Q = U.A.\Delta T \tag{Eq.1.1}$$

Where: “Q” is the heat-transfer rate; “U” is the heat-transfer coefficient; “A” is the surface area for heat exchange; and “ΔT” is the temperature difference between two streams. Since heat transfer is a function of “U”, “A”, and “ΔT”, a small “ΔT” will require a larger heat transfer.

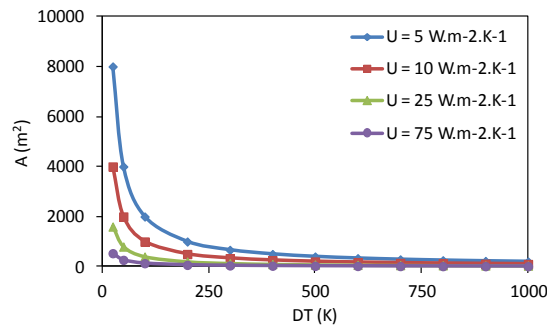


Fig. 1.6: The Influence of source and sink temperature (ΔT) on required heat-exchanger area (Q = 1 MW_{th})

For temperatures < 150°C - and thus < 120°C - conventional heat exchangers present high-exergy losses that inhibit their economical deployment for such low-temperature energy streams. One of the main challenges, even for heat extraction from clean gases, is the combination of a very low driving temperature difference for heat extraction with a very low-pressure drop for the gas stream. Fig. 1.7 shows that, for low-temperature heat sources, it is not acceptable to reduce significantly the temperature during heat transfer from the gas to the power cycle fluid, because the related losses in cycle efficiency would be dramatic. The same statement is valid for the pressure drop of the gas stream. Only a few mbar of pressure drop can lead to an increase in blower power demand in the same range of the generated capacity. These specifications lead to the basic conclusion that a very low heat-transfer resistance is required.

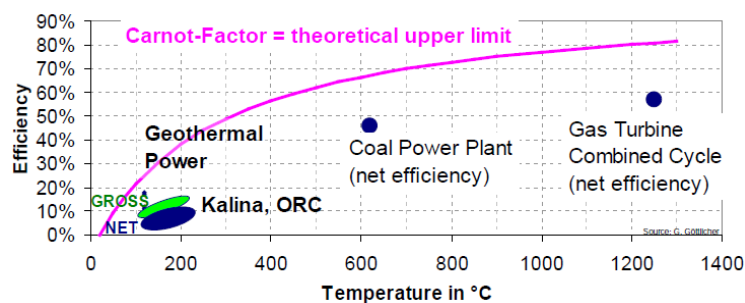


Fig. 1.7: State-of-the-art efficiencies and Carnot factors of power generation cycles/processes vs. process temperatures [FP7 07]

1.1.3.3 Conversion

To date, only very few cycles have been proposed and optimized below 120°C. In all fields and for physical reasons, generating power from heat sources below 120°C is a challenging task as the thermodynamic maximum represented by the Carnot factor efficiencies is only around 25% (Fig. 1.8). Maximum efficiency at a given temperature is based on the Carnot efficiency, which is defined as:

$$\eta_{carnot} = 1 - \frac{T_L}{T_H} \quad \text{Eq. 1.2}$$

Where: “ T_H ” is the waste heat temperature; and “ T_L ” is the temperature of the heat sink.

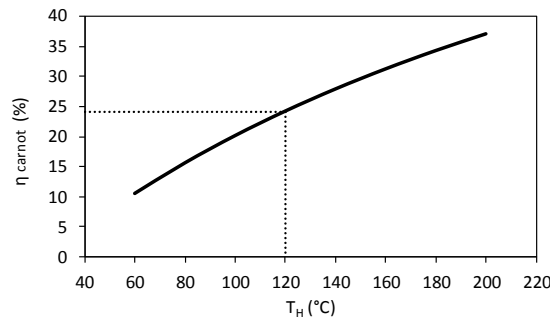


Fig. 1.8: Carnot efficiency as a function of the waste heat temperature ($T_L = 25^\circ\text{C}$)

State-of-the-art actual applications presently have overall electrical efficiencies from 3 to 5%. This reduced efficiency is caused by several losses e.g. heat transfer losses, friction losses, leakage in the turbine, heat losses, and other losses. The power surplus even shrinks further taking into account the auxiliary power consumption. There is thus a clear and compelling need to increase the cycle efficiency, i.e. to optimize exergy recovery of the entire system.

In conclusion, while challenges limit the feasibility of the low-temperature waste heat recovery, the potential of these heat sources is sufficiently large to be valorized into electricity production. The objective of this chapter is to recover the low-temperature heat sources depending on their moisture content via electricity production by using suitable optimized thermodynamic cycles.

Next section will show the energy and exergy that could be extracted from low-temperature heat sources and the effect of cooling flue gases below the water dew point temperature that can achieve significant increases in energy efficiency via recovering the latent heat of water vapor condensation.

1.2 Energy and exergy recovery from low-temperature heat sources

The aim of this section is to quantify the energy and exergy availability for low-temperature heat sources. Analyzing the exergy potential is a good measurement to identify the overall potential for electricity production of a given heat source.

In flue gases with high moisture content (wet flue gases), heat is available in both sensible and latent forms. The sensible heat is determined by the flue-gas temperature and the combined heat capacities of

its components. The latent heat portion is determined by the amount of water present in flue gases in vapor phase [BCS 08].

The flue-gas characteristics used in this study are tabulated in Table 1.3. Flue gases to be cooled consist in a mixture of water vapor (H₂O), nitrogen (N₂), oxygen (O₂), and carbon dioxide (CO₂). Values of CO₂ and O₂ compositions in Table 1.3 correspond generally to those at the “Raw Mill” exhaust in the cement plants. The ambient pressure and temperature at the specified dead reference state (P_o and T_o) are considered to be atmospheric pressure and 20°C. As stated previously, depending on the moisture content, the water vapor dew point could vary between 30 and 70°C. When not mentioned, the inlet flue-gas temperature is set to 120°C.

Table 1.3:Flue-gas characteristics

Compositions	molar basis	CO ₂ - 15.5% v , O ₂ - 6.8% v
Inlet temperature	T _{inlet}	90°C - 150°C
Water dew point temperatures	T _{dp}	30 - 70°C
Corresponding wet bulb temperatures	T _{wb}	45 - 72°C
Water vapor fraction	molar basis	4.19 % v - 30.79% v

The enthalpy (resp. entropy) of a gas mixture is equal to the sum of the individual partial enthalpies (resp. entropies) of the components [BUT 07]. Therefore, the mass enthalpy and entropy of flue gases can be written as follows:

$$h_g(T) = h_{dg}(T) + w.h_{wv}(T) = (y_{O_2}h_{O_2}(T) + y_{CO_2}h_{CO_2}(T) + y_{N_2}h_{N_2}(T)) + w.h_{wv}(T) \quad \text{Eq. 1.3}$$

$$s_g(T) = s_{dg}(T) + w.s_{wv}(T) = (y_{O_2}s_{O_2}(T) + y_{CO_2}s_{CO_2}(T) + y_{N_2}s_{N_2}(T)) + w.s_{wv}(T) \quad \text{Eq. 1.4}$$

$$y_{O_2} + y_{CO_2} + y_{N_2} = 1 \quad \text{Eq. 1.5}$$

Where: subscript “g” denotes gas, “dg” denotes dry gases, “wv” denotes water vapor, “T” is the temperature of the mixture, “w” is the humidity ratio, “y” is the dry mass fraction, and “h” and “s” represent the mass enthalpy and entropy respectively. The mass enthalpies and entropies of the different components (O₂, CO₂, N₂ and H₂O) are calculated at the corresponding partial pressures.

The humidity ratio is calculated by:

$$w = \frac{M_{wv}}{M_{dg}} \cdot \frac{P_w}{P_t - P_w} \quad \text{Eq. 1.6}$$

Where: “M_{wv}” and “M_{dg}” are the molar masses of the water vapor and dry gases respectively, “P_w” is the partial pressure of water vapor, and “P_t” is the total pressure.

The thermodynamic data of gases adopted in the present work are calculated using REFPROP 9.0 [LEM 10].

1.2.1 Heat load and exergy availabilities

The characterization of the temperature and the available heat load referred to the ambient temperature are presented in Fig. 1.9. The enthalpy difference is calculated for a 1-K gas cooling. The water vapor condensation is considered starting at the water vapor dew point, and for each temperature step, flue gases are considered saturated with water vapor. The sudden breaks in slope indicate initial water dew

points. Water vapor in the flue gases is in superheated state above the initial water dew points. Cooling reaches the initial water dew points of the flue gases and water vapor condensation begins. The partial pressure of water vapor decreases continuously and so the water dew point. Sensible heat recovery occurs down to initial water dew points. Cooling below this level increases the energy recovery rate by recovery of the water latent heat. Fig. 1.9 shows that a large amount of heat within the streams is in the form of latent heat and can only be recovered by condensing water vapor. The fraction of latent heat depends on the water dew point temperature.

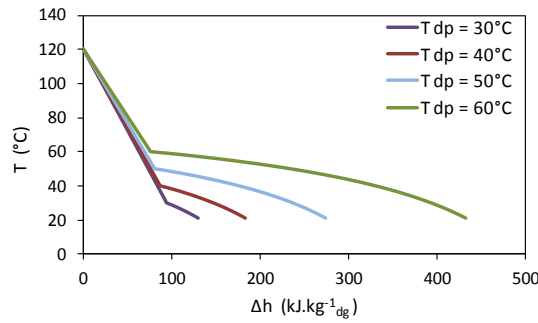


Fig. 1.9: Flue-gas heat load availability for various water dew point temperatures

Calculation of the exergy availability allows the identification of the overall potential for electricity production of a given heat source. In order to identify the amount of energy available for conversion into work, the temperature is replaced by the Carnot-Factor (Fig. 1.10).

$$\text{Carnot - Factor} = 1 - T_0/T_m \quad \text{Eq. 1.7}$$

$$T_m = \Delta h/\Delta s \quad \text{Eq. 1.8}$$

The Carnot-Factor (Eq. 1.7) is calculated between the temperature at a given state and the ambient temperature (T_0). Fig. 1.10 shows the evolution of the Carnot-Factor over the heat load. In Eq. 1.8, “ Δh ” and “ Δs ” are respectively the enthalpy and entropy difference and are calculated for a 1-K gas cooling. The surface under the graphs represents the exergy of heat sources. As the exergy is the work that could be extracted by a perfect cycle, it gives the maximum potential of electricity production from a heat source.

The exergy of a system (relative to the assumed reference environment) depends on system temperature, pressure, and composition; the first two contribute to thermo-mechanical exergy, and the effect of composition to chemical exergy. The mass exergy can be expressed as [LOZ 03]:

$$Ex = (h - T_o \cdot s)_i + \sum y_i \cdot (\mu_i - \mu_{i_o})_{T_o, P_o} \quad (i = \text{CO}_2, \text{O}_2, \text{N}_2, \text{H}_2\text{O}) \quad \text{Eq. 1.9}$$

Where: subscript “o” refers to the specified reference state, “ μ ” is the chemical potential, and “y” is the mass fraction. The calculations show that the chemical exergy is less than 2% of the thermo-mechanical exergy and can be neglected. For more detail about the chemical exergy calculation, refer to “Annex A”.

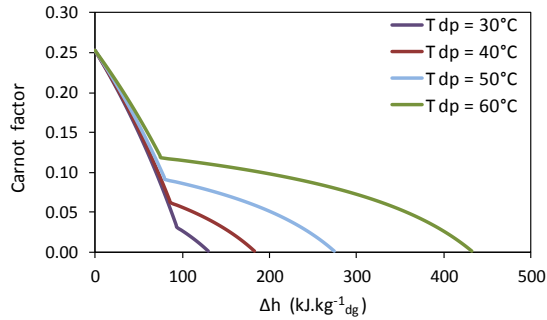


Fig. 1.10: Carnot factor as a function of heat load for various water dew point temperatures

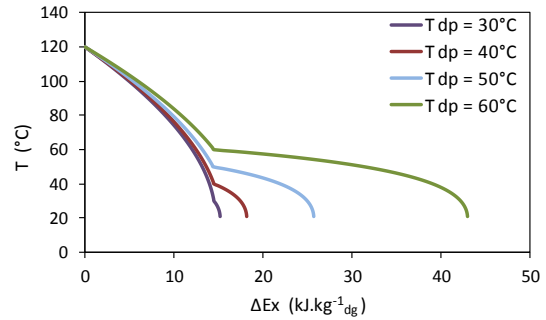


Fig. 1.11: Flue-gas exergy availability for various water dew point temperatures

Fig. 1.11 illustrates the exergy availability for various water dew point temperatures. The exergy difference is calculated for a 1-K gas cooling. The same analysis as for Fig. 1.9 can be applied. As the exergy is the work that could be extracted by an ideal cycle [LAL 05], it is a good measurement to identify the overall potentials for electricity production of a heat source. The electricity that can be produced in a real process is of course lower than the available exergy.

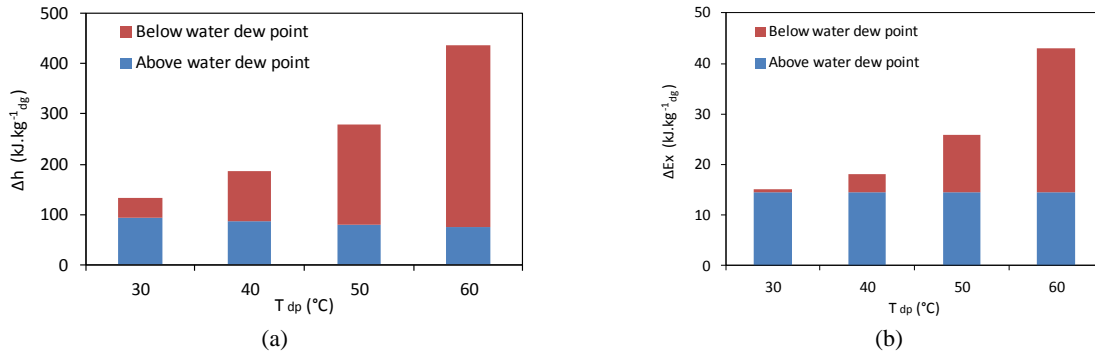


Fig. 1.12: Flue-gas histograms: a) heat load availability, b) exergy availability with and without water vapor condensation for various water dew point temperatures

The heat load and exergy availabilities are drawn Fig. 1.12.a and Fig. 1.12.b respectively. The blue parts represent the portion that could be extracted without water vapor condensation; the red parts account for the sensible and latent portion below water dew point.

Table 1.4 shows the values of the flue-gas heat load and exergy availabilities for various water dew point temperatures. Available heat loads with and without condensation are in the same range for a water dew point temperature of 40°C. The effect of water vapor condensation appears clearly at high water dew point temperatures. For a water dew point temperature of 60°C, the available heat load below it is around 4.7 times that above it and the available exergy below it is around 2 times that above it.

Table 1.4: Values of the flue-gas heat load and exergy availabilities for various water dew point temperatures

T_{dp} (°C)	Heat load availability (kJ.kg^{-1}_{dg})			Exergy availability (kJ.kg^{-1}_{dg})		
	Below water dew point	Above water dew point	Ratio *	Below water dew point	Above water dew point	Ratio *
30	39.1	94.3	0.41	0.7	14.5	0.05
40	99.8	86.9	1.15	3.7	14.5	0.26
50	197.4	80.7	2.45	11.3	14.4	0.78
60	360.7	76.1	4.74	28.5	14.5	1.97

*Ratio: heat load (resp. exergy) with- over- without water vapor condensation

The effects of inlet heat-source temperature on both heat load and exergy availabilities are shown in Fig. 1.13.a and Fig. 1.13.b respectively, for a water dew point temperature of 60°C. The water dew point (60°C) is visible. As the inlet heat-source temperature increases, both energy and exergy recovered by sensible heat extraction increase while the latent heat remaining the same, which is obvious.

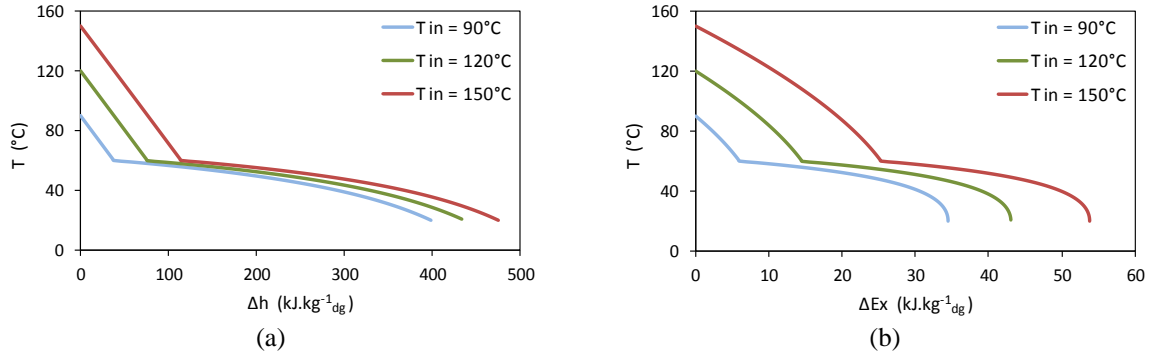


Fig. 1.13: Effect of inlet heat-source temperature on flue gases:
a) heat load availability, b) exergy availability ($T_{dp} = 60^\circ\text{C}$)

1.2.2 Ideal overall and exergy efficiencies

The ideal overall efficiency is the maximal overall efficiency that can be reached into a conversion cycle; it is equal to the amount of energy available for transformation into work (exergy) over the maximal heat load released by the heat source by cooling it down to the ambient temperature (Eq. 1.10).

$$\eta_{overall\ ideal} = \frac{Ex_{available}}{Q_{max}} = \frac{(h_{in} - T_o \cdot s_{in}) - (h_{out} - T_o \cdot s_{out})}{h_{in} - h_o} \quad \text{Eq. 1.10}$$

The ideal exergy efficiency is equal to the amount of energy available for transformation into work (exergy) over the maximal available exergy obtained by cooling down the heat source to the ambient temperature (Eq. 1.11).

$$\eta_{exergy\ ideal} = \frac{Ex_{available}}{Ex_{available\ max}} = \frac{(h_{in} - T_o \cdot s_{in}) - (h_{out} - T_o \cdot s_{out})}{(h_{in} - T_o \cdot s_{in}) - (h_o - T_o \cdot s_o)} \quad \text{Eq. 1.11}$$

Where in Eq. 1.10 and Eq. 1.11:

h_{in}, h_{out} : enthalpies of flue gases at inlet and outlet flue-gas temperatures respectively.

s_{in}, s_{out} : entropies of flue gases at inlet and outlet flue-gas temperatures respectively.

h_o, s_o : enthalpy and entropy of flue gases at the dead reference state.

The ideal overall and exergy efficiencies over the heat source temperature are presented Fig. 1.14 and Fig. 1.15 respectively. These efficiencies are calculated for a 1-K gas cooling. The sudden breaks in slope indicate initial water dew points. As shown in Fig. 1.14, a maximal overall efficiency around 10% can be reached for a water dew point temperature above 40°C. As the water dew point increases, the overall and exergy efficiencies decrease in the sensible heat zone since an important heat load and exergy are released below the water dew point temperature.

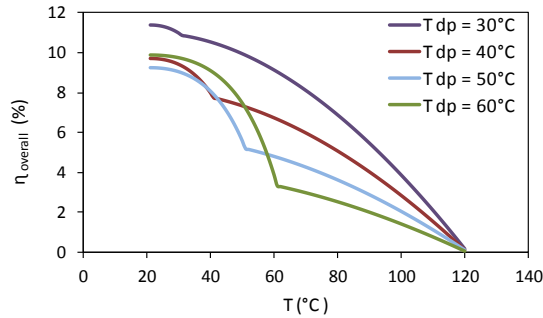


Fig. 1.14: Ideal overall efficiency

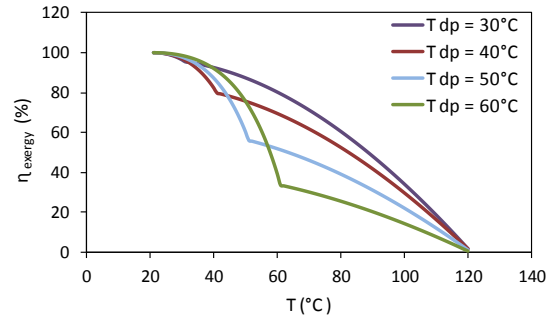


Fig. 1.15: Ideal exergy efficiency

The analysis carried in this section shows that the sensible energy could be recovered at relatively high temperatures compared to the latent energy. However, for the same change in flue-gas stream temperature, much higher quantities of energy are available below the water vapor dew point rather than above it.

After estimating the heat load and exergy availabilities of the low-temperature heat sources depending on their moisture content, the next step consists in reviewing the existing thermodynamic cycles adapted at low-temperature level ($\sim 120^{\circ}\text{C}$) in order to recover the heat-source energy via electricity production.

1.3 Power generation cycles

Generating power from waste heat typically involves using the waste heat to generate mechanical energy that then drives an electric generator. When considering power generation options for waste heat recovery, an important factor to keep in mind is the thermodynamic limitations on power generation at different temperatures. As discussed in §1.1.3.2, the efficiency of power generation is heavily dependent on the temperature of the waste heat source. In general, power generation from waste heat has been limited to only medium-to-high-temperature waste heat sources. However, advances in alternate power cycles may increase the feasibility of generation at low temperatures. While maximum efficiency at these temperatures is lower, these systems could still be economical in recovering large quantities of energy from waste heat.

The most frequently used system for power generation from waste heat involves using the heat to generate steam, which then drives a steam turbine. A schematic of waste heat recovery with a Rankine cycle is shown in Fig. 1.16. The pump supplies water to the evaporator, where water is heated and vaporized by the flue-gas heat stream. The generated high-pressure steam is expanded by the turbine, which is directly coupled to an electrical generator producing power, and then, the low-pressure vapor is condensed in a condenser. The traditional steam Rankine cycle is the most efficient option for waste-heat recovery with temperatures above 350°C . At lower waste heat temperatures, steam cycles become less cost effective, since low-pressure steam will require bulkier equipment. Moreover, low-temperature waste heat may not provide sufficient energy to superheat the steam, which is a requirement for preventing steam condensation and erosion of the turbine blades. Therefore, low temperature heat recovery applications are better suited for the “Organic Rankine Cycle (ORC)” or “Kalina Cycle” that use fluids with lower boiling point temperatures compared to steam [BCS 08].

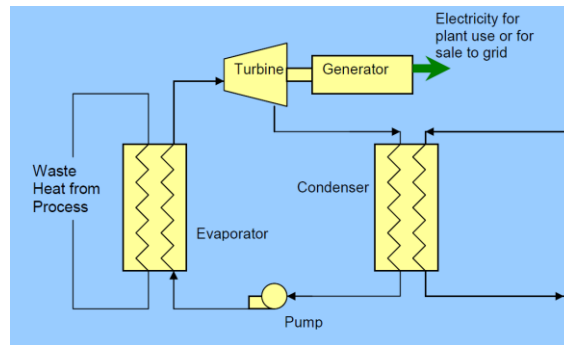


Fig. 1.16: Waste heat recovery with Rankine Cycle [BCS 08]

1.3.1 Organic Rankine Cycle

The Organic Rankine Cycle (ORC) operates similarly to the steam Rankine cycle, but uses an organic working fluid instead of steam. Options include HFC (R-245fa, R-152a, R-1234yf...), and hydrocarbons (butane, isobutane, pentane...) that have a lower boiling point and higher vapor pressure than water. This allows the Rankine cycle to operate with significantly lower waste heat temperatures, sometimes as low as 60°C. The most appropriate temperature range for ORCs will depend on the fluid used, as the thermodynamic properties of the fluids will influence the cycle efficiency at various temperatures.

In comparison with water, the organic working fluids used in ORCs have a higher molecular mass, enabling compact designs, higher mass flow, and higher turbine efficiencies (as high as 80 to 85%). However, since the cycle operates at lower temperatures, the overall efficiency is only around 3 to 5%, depending on the temperature of the condenser and evaporator. While this efficiency is much lower than at high-temperature steam power plant (> 30%), it is important to remind that low-temperature cycles are inherently less efficient than high-temperature cycles [BCS 08]. Limits on efficiency can be expressed according to Carnot efficiency as shown previously (refer to Fig. 1.8).

1.3.2 Kalina Cycle

The Kalina cycle is a variation of the Rankine cycle, using a mixture of ammonia and water as the working fluid. A key difference between single fluid cycles and cycles that use binary fluids is the temperature profile during boiling and condensation. For pure fluid cycles (e.g., Steam or Organic Rankine Cycle), the temperature remains constant during boiling. As heat is transferred to the working medium (e.g. isobutane), the isobutane temperature increases to boiling temperature, at which point the temperature remains constant until all the liquid has evaporated. In contrast, a binary mixture of water and ammonia (each of which has a different boiling point) will increase its temperature during evaporation. This allows better thermal matching with the waste heat source and with the cooling medium in the condenser.

Configuration shown in Fig. 1.17 is a version of the Kalina Cycle [BEC 12]. In this cycle, a basic ammonia/water mixture is partially evaporated using the heat source and internal recuperation. The stream is then separated, where the ammonia-rich vapor is sent to the turbine and the ammonia-lean liquid is used for heat recovery before being injected at the turbine exhaust. This heat recovery maximizes the efficiency by cooling the source down to low-temperatures thanks to the temperature glide during the evaporation.

1.4.2 Direct Contact Water-Vapor Condensation Recovery

Direct contact condensation recovery involves direct mixing of the process stream (flue gases) and cooling fluid (typically water) (Fig. 1.18). Since these systems do not involve a separating wall across which heat must be transferred, they avoid some of the challenges of large heat-transfer surfaces required for indirect contact units. The direct-contact heat exchanger has received attention because there are no heat-transfer surfaces exposed to corrosion, clogging, and fouling.

A challenge with direct-contact condensation is that the water can be contaminated by substances in the flue gases. A water treatment system should be provided in order to ensure that the water is cleaned before being re-used for another heat extraction cycle. The use of the direct-contact condenser makes sense when recovering energy from heat sources with high-moisture contents.

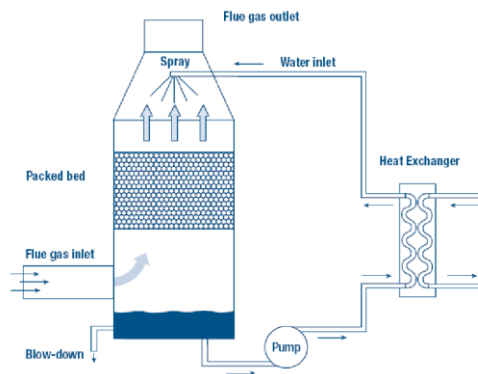


Fig. 1.18: Heat recovery using direct contact condensation (Condensing Unit) [BCS 08]

1.4.3 Transport Membrane Condenser

Transport Membrane Condensers (TMCs) are a developing technology for capturing water (along with water’s latent heat) from the water vapor in gas exhaust streams. Water is extracted from flue gases at temperatures above water dew point by employing capillary condensation. A schematic of the TMC in operation is shown Fig. 1.19. Like direct-contact heat-recovery units, TMCs extract hot water directly from the flue gases; however, since TMCs recover the water via transport through a membrane, the recovered water does not become contaminated as in a direct-contact unit. The technology has been demonstrated for clean exhaust streams in a natural gas-fired boiler; however, TMCs require more research in advanced materials before widespread implementation for dirtier waste streams is possible. Needed areas of research & development for enhancement include TMC strength and resistance to contaminants.

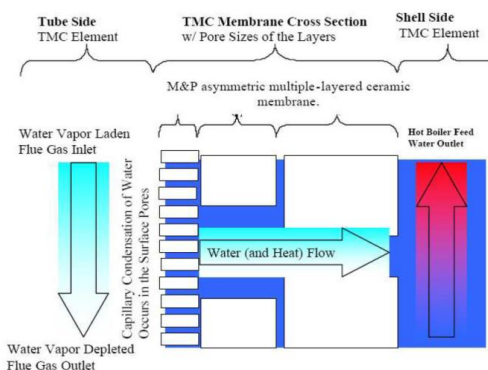


Fig. 1.19: Transport membrane condenser [BCS 08]

After reviewing the main existing thermodynamic cycles adapted at low-temperature level ($\sim 120^{\circ}\text{C}$) and the heat recovery technologies, the next step consists in the study and optimization of the thermodynamic cycles for recovering low-temperature heat sources by optimizing the net power produced. The study will be based on the well-proven Organic Rankine Cycle (ORC). The two main water-vapor condensing heat recovery modes will be investigated: direct and indirect water vapor condensation.

Many investigations were carried out about heat recovery using ORC. Comprehensive researches on appropriate working fluids for low-temperature applications have been investigated by many authors such as [DAI 09], [HUN 97], and [LIU 04]. Others researchers have focused on the parametric optimization and performance analysis of the ORC like [ROY 10], [ROY 11a], [WEI 07], [ROY 11b], and [ROY 12]. However, these studies deal with the indirect-contact condensation recovery based on sensible heat extraction from flue gases with low-moisture contents. The originality of the following work is to extend the ORC applications to low-grade gas heat sources with high-moisture contents by pointing out the effect of water vapor condensation on cycle performance using the two condensing heat recovery processes (direct and indirect heat exchange).

For this purpose, several ORC configurations will be analyzed and optimized:

- Simple ORC with indirect-contact condensation heat recovery
- Simple ORC with direct-contact condensation heat recovery
- Two-stage ORC
- Trans-critical ORC

1.5 Simple ORC with indirect-contact heat recovery

1.5.1 Simple ORC with direct evaporator

1.5.1.1 Parameters of the simple ORC

The simple ORC is called “direct evaporator cycle” when flue gases heat directly the ORC working fluid in the evaporator without using a heat-transfer medium.

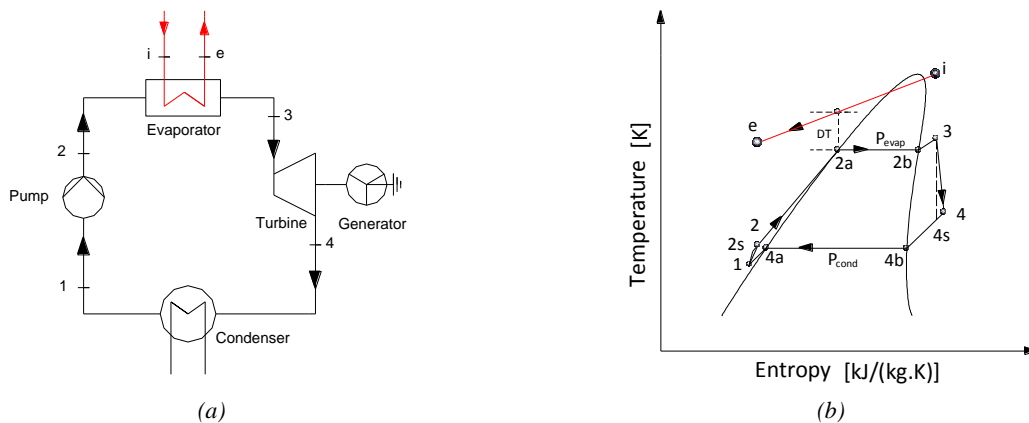


Fig. 1.20: Simple ORC: a) layout diagram, b) (T-s) diagram

The layout diagram of a simple ORC is presented Fig. 1.20. The ORC system consists of an evaporator, a turbine, a condenser, and a pump. As shown in Fig. 1.20, the pump supplies the working fluid to the evaporator, where the working fluid is heated and vaporized by the flue-gas heat stream (Point i). The generated high-pressure (Point 3) vapor is expanded by the turbine, which is directly coupled to an electrical generator producing power, and then, the low-pressure vapor is condensed in a

condenser where it is pumped back to the evaporator. The T-s diagram of the studied ORC is shown Fig. 1.20.b.

Because of the thermodynamic irreversibility occurring in each of the components, the ORC performance is evaluated using the exergy analysis [HUN 97]. The exergy balance for an open thermodynamic system can be expressed as:

$$\sum Ex_{input} - \sum Ex_{output} = I \quad \text{Eq. 1.12}$$

Each process in the ORC can be described as follows:

Process 2 to 3: This is an isobaric heating process in the evaporator. The heat transferred from the waste heat to the working fluid is:

$$Q_{evap} = m_r (h_3 - h_2) \quad \text{Eq. 1.13}$$

The evaporator superheat is given by:

$$SH_{evap} = T_3 - T_{2b} \quad \text{Eq. 1.14}$$

The exergy loss in the evaporator can be given as:

$$I_{evap} = E_i + E_2 - E_e - E_3 \quad \text{Eq. 1.15}$$

Process 3 to 4: This is a non-isentropic expansion process in the turbine. Ideally, this is an isentropic process 3-4s. However, the efficiency of the energy transformation in the turbine never reaches 100%, and the state of the working fluid at the exit of the turbine is indicated by point 4. The isentropic efficiency of the turbine can be expressed as:

$$\eta_{is,turbine} = (h_3 - h_4) / (h_3 - h_{4s}) \quad \text{Eq. 1.16}$$

The power generated by the turbine can be given as:

$$W_{turbine} = m_r (h_3 - h_4) \quad \text{Eq. 1.17}$$

The exergy loss in the turbine is given by:

$$I_{turbine} = E_3 - W_{turbine} - E_4 \quad \text{Eq. 1.18}$$

Process 4 to 1: A constant pressure heat-rejection process occurs in the condenser. The heat transferred from the working fluid is:

$$Q_{cond} = m_r (h_4 - h_1) \quad \text{Eq. 1.19}$$

The condenser sub-cooling is given by:

$$SC_{cond} = T_{Aa} - T_1 \quad \text{Eq. 1.20}$$

The exergy loss in the condenser can be given as:

$$I_{cond} = E_4 - E_1 \quad \text{Eq. 1.21}$$

Process 1 to 2: This is a non-isentropic compression process in the liquid pump. Ideally, this is an isentropic process 1-2s. However, the pump efficiency never reaches 100%, and the state of the working fluid at the pump exit is indicated by point 2. The pump isentropic efficiency can be expressed as:

$$\eta_{is,pump} = (h_{2s} - h_1)/(h_2 - h_1) \quad \text{Eq. 1.22}$$

The pump power is given by:

$$W_{pump} = m_r (h_2 - h_1) \quad \text{Eq. 1.23}$$

The exergy loss in the pump can be given as:

$$I_{pump} = W_{pump} + E_1 - E_2 \quad \text{Eq. 1.24}$$

By subtracting the power consumed by the pump from the power generated by the turbine, the net power generated by the ORC system is:

$$W_{net} = W_{turbine} - W_{pump} \quad \text{Eq. 1.25}$$

Based on the first law of thermodynamics, the ORC thermal efficiency is defined as the ratio of the net power output to the heat addition:

$$\eta_{thermal} = (W_{turbine} - W_{pump})/Q_{evap} \quad \text{Eq. 1.26}$$

The thermal efficiency cannot reflect the ability to convert energy from low-grade waste heat into usable power and might be misleading since the maximum power output is not achieved concurrently with the maximum thermal efficiency [ROY 10]. Therefore, the exergy efficiency is considered in order to evaluate the performance for waste heat recovery. The exergy efficiency of the ORC system can be expressed as [DAI 09]:

$$\eta_{exergy} = (E_i - \Sigma I - E_e)/E_i \quad \text{Eq. 1.27}$$

The recovery efficiency of the heat from flue gases is defined by:

$$\eta_{recovery} = Q_{exchanged}/Q_{exchanged\ max} = (h_{in} - h_{out})/(h_{in} - h_o) \quad \text{Eq. 1.28}$$

The overall efficiency is defined by:

$$\eta_{overall} = W_{net} / Q_{exchanged\ max} \quad \text{Eq. 1.29}$$

Where: “ $Q_{exchanged\ max}$ ” is defined as the maximum amount of heat that can be extracted from flue gases when cooling them to the ambient temperature.

The overall efficiency can also be written as:

$$\eta_{overall} = \eta_{cycle} \cdot \eta_{recovery} \quad \text{Eq. 1.30}$$

For the calculation, the ORC operating conditions are given in Table 1.5. The turbine efficiency is supposed to be the global turbine efficiency that includes the isentropic and the mechanical efficiencies; the mechanical efficiency is considered to be near 100%.

Table 1.5: Input data for the ORC analysis

Condensing temperature	T_{cond}	25°C
Condenser sub-cooling	SC_{cond}	2 K
Turbine efficiency	η_t	80%
Pump efficiency	η_p	85%

Taking into account the pinch value (ΔT) between the flue gases and the working fluid in the evaporator is essential to define the maximal heat recovery from the energy source. As pointed out by Butcher *et al.* [BUT 07] and Srinivasan *et al.* [SRI 10], the system performance is sensitive to the pinch point and should be as low as possible to improve the overall energy performance. However, this will result in a larger heat-exchanger area to transfer the same amount of heat, hence an increase in size and cost. Following calculations have been done for a 3-K pinch at the evaporator. By referring to Becquin *et al.* [BEC 12], this value is considered as aggressive boundary conditions. Nevertheless, technical and economic optimizations will be promising in developing sensitivity analysis on cost variations around the pinch while thermodynamic optimization of energy system requires only that the pinch is as small as possible.

Following results will be presented using R-245fa as working fluid. As stated by Kosmadais *et al.* [KOS 09] and Zyhowski *et al.* [ZYH 10], R-245fa is a promising candidate for ORC operating on low-temperature heat sources, and presents one of the best compromise between thermal efficiency, power output, and environmental performance. The properties of R-245fa are calculated using REFPROP 9.0 [LEM 10] developed by NIST. A computer program employing “Excel/VBA” was developed to simulate the thermodynamic performances of the ORC system.

According to the heat source, the main parameters of the simple ORC are the evaporation temperature and the evaporator outlet superheat.

1.5.1.2 Results and interpretations

A parametric optimization of the evaporation temperature and evaporator superheat is performed to obtain the maximal ORC net power.

Fig. 1.21 shows the evolution of the net power as a function of the evaporator superheat for an evaporation pressure of 0.5 MPa. It is observed from Fig. 1.21 that the evaporator superheat is detrimental for the net power. This is consistent to the conclusion reported by [WEI 07], which

pointed out that, for the working fluids with the positive slope of the saturation vapor curves ($dT/ds > 0$, dry fluid) such as R-245fa, a nil evaporator superheat should produce the greatest turbine power. Note that the working fluids can be classified into three categories: dry, isentropic, and wet depending on the slope of the T-s curve; (dT / ds) to be positive, infinite, and negative, respectively. For wet and isentropic working fluids, the evaporator superheat leading to maximal net power could be not nil and therefore should be calculated.

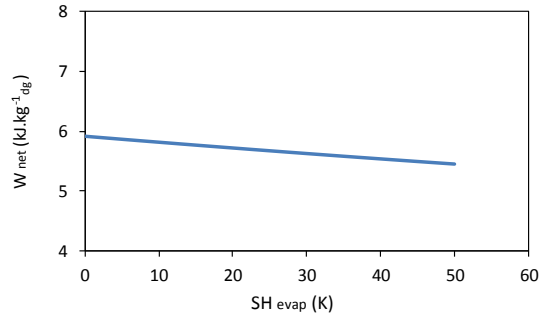


Fig. 1.21: Evolution of the net power as a function of the evaporator superheat ($P_{\text{evap}} = 0.5 \text{ MPa}$, $T_{\text{dp}} = 30^\circ\text{C}$)

Fig. 1.22 and Fig. 1.23 show, respectively, the evolutions of the net output power and the mass of water vapor condensate for various water dew point temperatures under a wide range of evaporation temperatures.

The mass of water condensate is given by:

$$m_c = m_{dg} \cdot (w_{in} - w_{out}) \quad \text{Eq. 1.31}$$

As shown in Fig. 1.22 and Fig. 1.23, starting from a water dew point of 40°C , the value “ $T_{\text{evap}} = T_{\text{dp}} - \Delta T$ ” breaks each corresponding curve into two regions classified as follows:

- Sensible heat region ($T_{\text{evap}} > T_{\text{dp}} - \Delta T$): where mostly sensible heat is recovered. A small portion of latent heat recovery takes place because a little water vapor condensation occurs near the water dew point temperature (Fig. 1.23).
- Latent heat region ($T_{\text{evap}} < T_{\text{dp}} - \Delta T$): in this region, a large quantity of water vapor condensation will condense, thereby recovering a great portion of latent heat (Fig. 1.23). The value of the net power is strongly affected by the water dew point temperature (Fig. 1.22).

It should be noted that, practically, the quantity of water vapor condensation could be larger because latent heat starts to be removed through moisture condensation when the surface temperature (between cold working fluid and hot flue gases) is lower than the water dew point temperature of the flue gas passing over it.

Further, in Fig. 1.22, an optimum for the net power output can be identified in each region: sensible and latent heat optima. The corresponding evaporation temperature at the sensible heat optimum ($\sim 73^\circ\text{C}$) is almost independent of the water dew point temperature. Also, as shown in Fig. 1.22, at low water dew point temperature ($T_{\text{dp}} = 40^\circ\text{C}$), the sensible heat optimum greatly exceeds the latent one whereas it is much lower at high-water dew point temperature ($T_{\text{dp}} = 60^\circ\text{C}$).

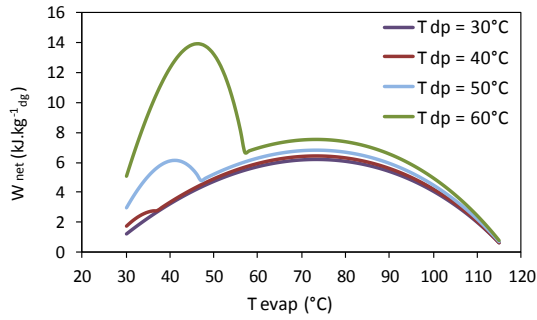


Fig. 1.22: Evolution of net power as a function of the evaporation temperature

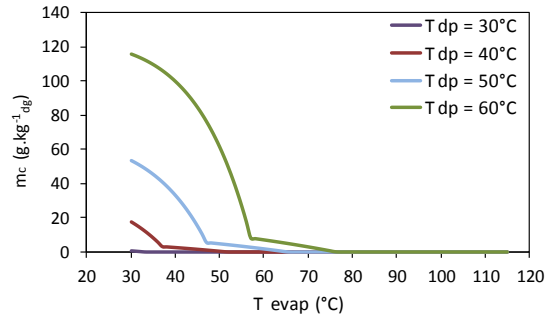


Fig. 1.23: Evolution of the mass of water vapor condensate as a function of the evaporation temperature

A comparison between the net power values at both sensible and latent heat optima is shown in Table 1.6 for various water dew point temperatures. The value of the net power at the latent heat optimum is almost twice that at the sensible one for a water dew point temperature of 60°C, and can reach almost 4 times for a water dew point temperature of 70°C.

Table 1.6: Comparison between the net power values at both sensible and latent heat optima

W_{net} (kJ.kg ⁻¹ .dg)	$T_{dp} = 30^{\circ}\text{C}$	$T_{dp} = 40^{\circ}\text{C}$	$T_{dp} = 50^{\circ}\text{C}$	$T_{dp} = 60^{\circ}\text{C}$	$T_{dp} = 70^{\circ}\text{C}$
Sensible optimum	6.23	6.45	6.83	7.52	8.75
Latent optimum	-	3.37	6.15	13.89	32.49

To illustrate the temperature profiles in the evaporator, Fig. 1.24a and Fig. 1.24b show the hot composite curves (T-h diagrams) for water dew point temperatures of 30°C and 60°C respectively at the respective evaporation temperatures leading to the maximal net powers. Fig. 1.24a and Fig. 1.24b show that, for a pure working fluid (R-245fa), the pinch point in the evaporator (“DT” as shown in Fig. 1.20.b) is located at the corresponding saturated liquid point of the working fluid even for heat sources with high-water dew point temperature (60°C).

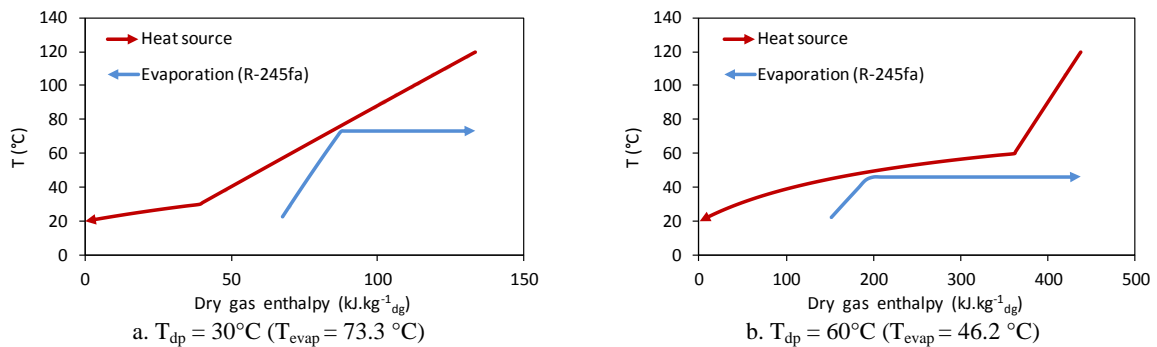


Fig. 1.24: Evaporator hot composite curves for R-245fa: (a) $T_{dp} = 30^{\circ}\text{C}$, (b) $T_{dp} = 60^{\circ}\text{C}$

The evolution of the exit flue-gas temperature as a function of the evaporation temperature is shown Fig. 1.25. The exit flue-gas temperature decreases by decreasing the evaporation temperature until reaching a plateau around the water dew point temperature where it remains constant before continuing to decrease.

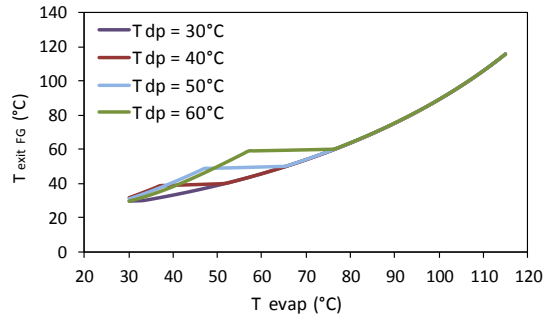


Fig. 1.25: Evolution of exit flue-gas temperature as a function of the evaporation temperature

The evolutions of the cycle, overall, recovery and exergy efficiencies are shown Fig. 1.26 for a water dew point of 50°C. Similarly to the net power, the overall and exergy efficiencies present two optima above and below the value " $T_{\text{evap}} = T_{\text{dp}} - \Delta T$ ". The cycle efficiency increases by increasing the evaporation temperature, which is obvious. The recovery efficiency presents a change of slope when crossing the value " $T_{\text{evap}} = T_{\text{dp}} - \Delta T$ ".

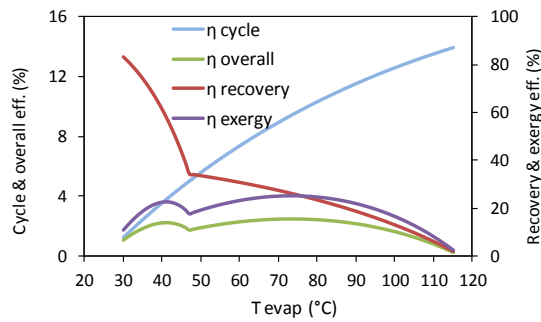


Fig. 1.26: Evolution of efficiencies as a function of the evaporation temperature ($T_{\text{dp}} = 50^\circ\text{C}$)

Fig. 1.27 illustrates the contribution of exergy and overall efficiencies in optimization procedure. It has to be underlined that by increasing the moisture rate, the exergy and overall efficiencies decrease in the sensible heat region since an important exergy content is released below the water dew point temperature. By referring to Fig. 1.22, it could be concluded that the maximal net power is achieved concurrently with the maximal exergy and overall efficiencies. Fig. 1.27.b shows that the actual application ($T_{\text{in}} = 120^\circ\text{C}$) presents an overall efficiency less than 5%.

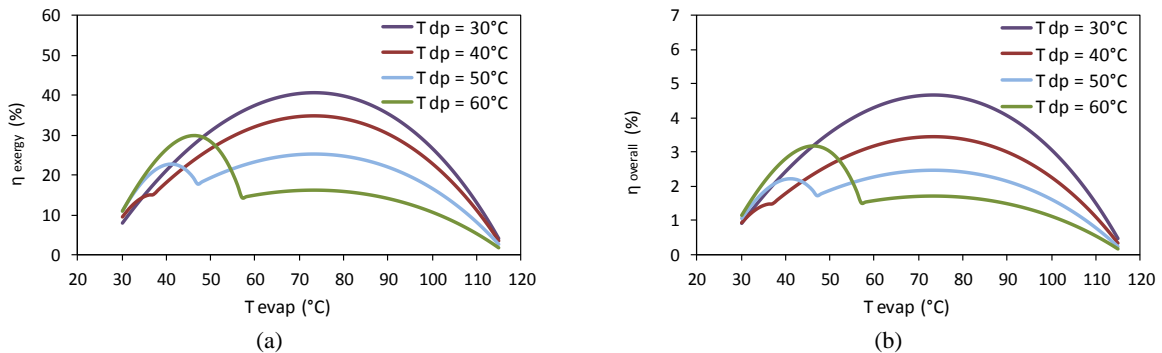


Fig. 1.27: Evolutions of the overall and exergy efficiencies as a function of the evaporation temperature for various water dew point temperatures

Fig. 1.28 and Fig. 1.29 show, respectively, the evaporation capacity and the working fluid mass flow rate as a function of the evaporation temperature for various water dew point temperatures. The same evolution is underlined in the two figures. In particular, Fig. 1.28 illustrates the amount of latent heat recovered in the evaporator.

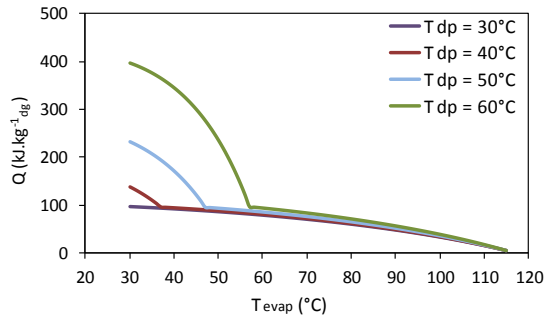


Fig. 1.28: Evolution of the evaporator capacity as a function of the evaporation temperature

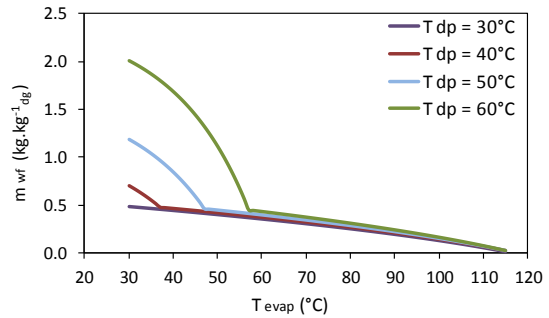


Fig. 1.29: Evolution of the working fluid mass flow rate as a function of the evaporation temperature

Fig. 1.30 shows the evolution of the net power and evaporator heat capacity ratios between sensible and latent heat optima for a wide range of water dew point temperatures. By varying the water dew point of the heat source between 30°C and 70°C, the corresponding net power and evaporator heat capacity ratios vary from 0.2 to 3.7 and from 1.3 to 5.7 respectively. The net power ratio reaches the unity at a water dew point temperature around 51.5°C, below which the sensible heat optimum appears dominant and above which the latent heat optimum becomes prevailing.

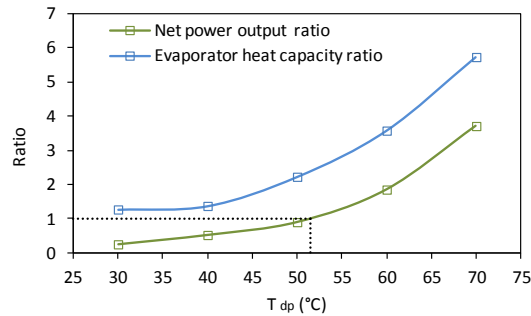


Fig. 1.30: Latent over sensible optima for a wide range of water dew point temperatures

Fig. 1.31 shows the effect of inlet heat-source temperature on the net power for a water dew point of 60°C. The sensible heat region is greatly affected by the inlet heat-source temperature. The sensible and latent heat recovery contribute in the same range at high inlet heat source temperature ($T_{in} = 150^\circ\text{C}$).

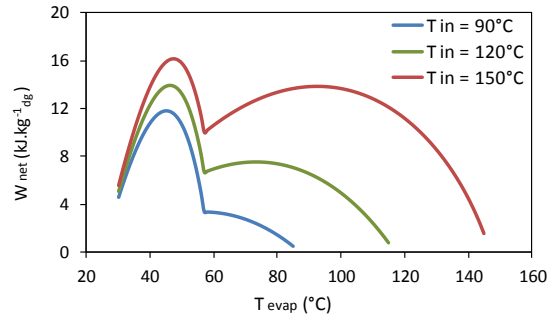


Fig. 1.31: Effect of inlet heat source temperature on the net power ($T_{dp} = 60^{\circ}\text{C}$)

In conclusion, this section shows that, for a simple ORC operating with indirect-contact condensation using a direct evaporator; two operating regions can be identified in the evaporator starting from a water dew point temperature of 40°C : “sensible heat region” and “latent heat region”. An optimum for the net power can be identified in each region. The net power ratio between these two optima varies mainly as a function of the water dew point and the inlet flue-gas temperature.

1.5.2 Simple ORC with indirect evaporator

Another option with indirect-contact water vapor condensation for heat recovery from wet flue gases is to use an indirect evaporator where the heat is transferred to the ORC evaporator with an intermediate cycle operating with pressurized heat-transfer medium. The heat can be transferred between the waste heat source and the power plant using one of two different media: thermal oil or pressurized water via generally a fin-and-tube heat exchanger. Thermal oil is generally designed for running at high temperatures, typically around $300/250^{\circ}\text{C}$ (supply/return). When the appropriate oil is chosen, the cycle can be operated at lower temperatures. Pressurized water, on the other hand, is designed to operate at lower temperatures ($< 200^{\circ}\text{C}$). The temperature of the waste heat determines the choice of intermediate medium. In addition to the design temperatures, other parameters have to be considered such as specific heat capacity, viscosity, pumping energy, physical properties, pressure, and flammability [BOR 11].

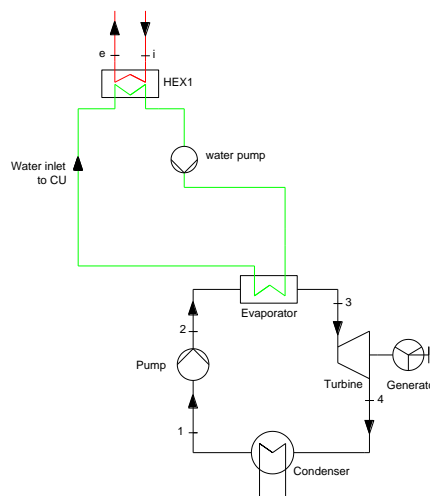


Fig. 1.32: ORC with indirect-contact condensation using heat-transfer medium (indirect evaporator)

A parametric optimization of the water temperature at the evaporator inlet was performed with respect to the net power by setting a 3-K temperature pinch in both “HEX1” and the evaporator. The ORC parameters are the same as those indicated in Table 1.5. R-245fa is used as working fluid. The maximal water temperature at the evaporator inlet is limited to 115°C and the water pressure is set to 0.2 MPa. For each water temperature at the evaporator inlet, the evaporation temperature of the working fluid (R-245fa) is calculated in order to optimize the net power. For more details about the optimization procedure, refer to Fig.C.2b in “Annex C”.

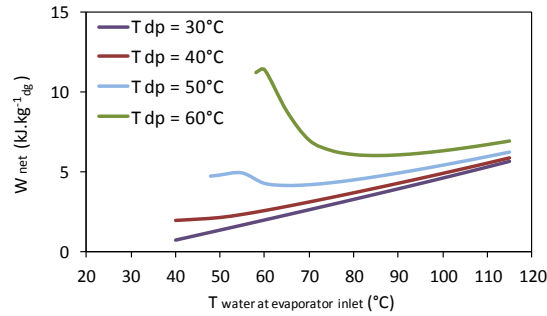


Fig. 1.33: Evolution of net power as a function of water temperature at evaporator inlet

The evolution of the net power for various water dew point temperatures under a wide range of evaporation temperatures is shown in Fig. 1.33. At high-water dew point temperature ($T_{dp} \geq 60^\circ\text{C}$), the maximal net power is reached for a water temperature at the evaporator inlet equal to the water dew point temperature, while at low-water dew point temperature ($T_{dp} \leq 50^\circ\text{C}$), as the water temperature at evaporator inlet increases, the net power increases.

The evolutions of the working fluid and the hot water mass flow rates as a function of the water temperature at the evaporator inlet are shown Fig. 1.34.a and Fig. 1.34.b respectively. Fig. 1.34.b shows that high hot water mass flow rate is expected below the water dew point temperature due to the increase in the mass of water vapor condensate.

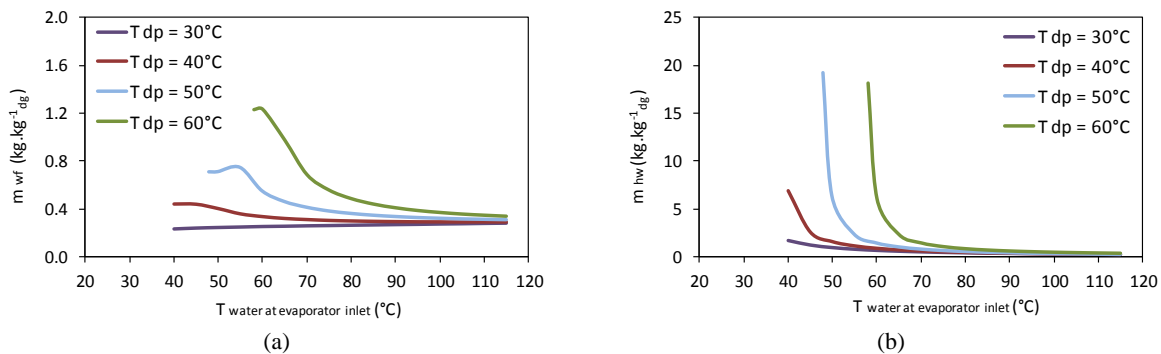


Fig. 1.34: Evolution of: a) working fluid mass flow rate, and b) hot water mass flow rate as a function of the water temperature at the evaporator inlet

A comparison for the net power between the direct and indirect evaporator is shown Fig. 1.35 for a water dew point temperature of 60°C. Compared to the direct evaporator, a loss around 18% is expected at the maximal net power value.

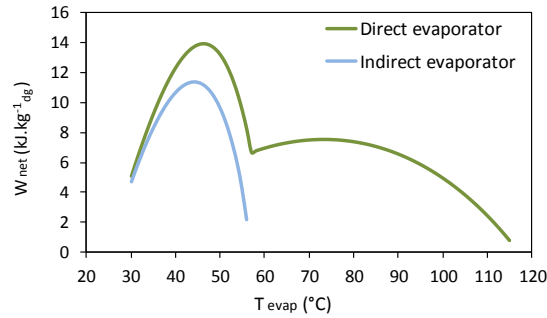


Fig. 1.35: Comparison of the net power between direct and indirect evaporators for ORC with indirect water vapor contact condensation ($T_{dp} = 60^{\circ}\text{C}$)

Other than the decrease in the conversion efficiency, the use of intermediate loop presents many disadvantages such as increase in the system cost, additional components, which increase complexity and therefore opportunity for failure, and adds thermal mass, which could reduce rate of system start-up [BOR 11]. The advantage is that the heat recovery system is isolated from the ORC system, thus putting away from the ORC system the dirt accompanying flue gases and making easy the replacement of flue-gas heat-exchanger components in case of failure due to corrosion problem accompanying the gas cooling. Another advantage is that the evaporator size of the ORC system is reduced since it will be liquid-liquid heat exchanger and not gas-liquid heat exchanger; therefore, the amount of working fluid in the system will be smaller.

1.6 ORC with direct-contact heat recovery

Direct condensation heat recovery involves direct mixing between flue gases and cooling fluid, generally water. Since these systems do not involve a separating wall across which heat must be transferred, they avoid some of the challenges of large heat transfer surfaces required for indirect-contact units [BCS 08]. An example system is shown Fig. 1.36. As the flue gases enter the condensing unit (point i), they are cooled by cold water introduced at the top of the unit. The heated water stream recovered at the bottom of the condensing unit is then sent to an evaporator to transfer heat to the organic working fluid of the power generation unit. Once heat is extracted from water, a treatment system will ensure that the water is cleaned before being re-used for another heat extraction cycle.

The absence of tubes reduces maintenance, increases system reliability, and decreases system cost. The elimination of the interfering wall increases the heat-transfer rate between the two fluids. The direct-contact heat exchanger is an ideal candidate for transferring latent heat from flue gases because a spraying of fine water droplets can provide a large heat-transfer surface area in the presence of relatively small temperature differences between the heating and cooling media. Direct contact of a water spray with the flue gases also turns out to be a rather effective low-energy scrubber, which can reduce flue-gas emissions significantly.

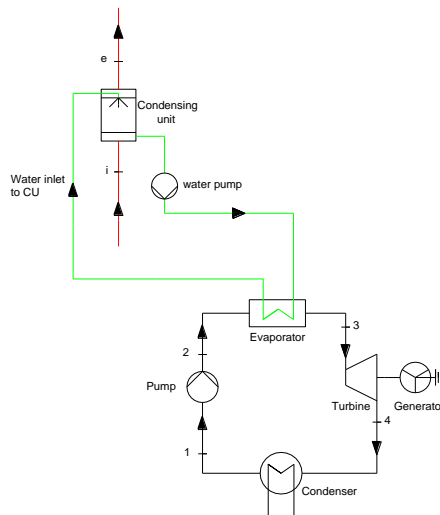


Fig. 1.36: ORC with direct-contact condensation

The low-temperature flue gases are exhausted from the direct-contact heat-recovery process with lower water gas content than the hot entering flue gases, even though a water spray is used to realize the process. The thermal performance of the condensing unit depends mainly on the entering flue-gas wet bulb temperature. The entering flue-gas dry bulb temperature and relative humidity, taken independently, have insignificant effect on thermal performance of the condensing unit [ASH 08].

Fig. 1.37 illustrates the process of adiabatic cooling and water vapor condensation of flue gases using the psychrometric chart. Flue gases enter at Point A, release heat and mass (moisture) to water and exit at Point B in saturated conditions (at very light loads, the discharge flue gases may not be saturated). The amount of heat transferred from flue gases to water is proportional to the enthalpy difference of flue gases between the inlet and outlet ($h_A - h_B$). It is worth noting that the constant enthalpy lines correspond almost exactly to constant wet bulb temperature lines; the change in enthalpy of flue gases may be determined by the change in wet bulb temperature of flue gases. The humidification and cooling of flue gases follow a line of constant enthalpy (roughly the wet bulb temperature line) from the entering point, left to the saturation line (Point A to Point C). The temperature at the intersection with the saturation line is the adiabatic saturation temperature. By definition, no heat is added to, or extracted from, an adiabatic process. Up to this point in the process, no energy has been removed from the system, since all energy given by the flue gases has gone into vaporizing the water and carried in latent form by the water gas/humidity of the now saturated gases [ASH 08], and [THO 69]. Continued cooling results in the condensation of moisture from the flue gases (dehumidification) yielding the latent heat of the water vapor (Point C to Point B). The end of the process will be determined by the temperature and flow rate of water coming to the recovery system for heating and, thereby, its ability to remove heat.

The cooling of flue gases, represented by vector AB in Fig. 1.37, may be separated into component DB, which represents the sensible portion of the heat released by flue gases as the water is heated, and component AD, which represents the latent portion. The ratio of latent to sensible heat is important to analyze the water vapor condensation of the condensing unit. Mass transfer occurs only in the latent portion of the heat-transfer process and is proportional to the change of absolute humidity. The entering flue-gas dry bulb temperature or relative humidity affects the latent to sensible heat transfer ratio.

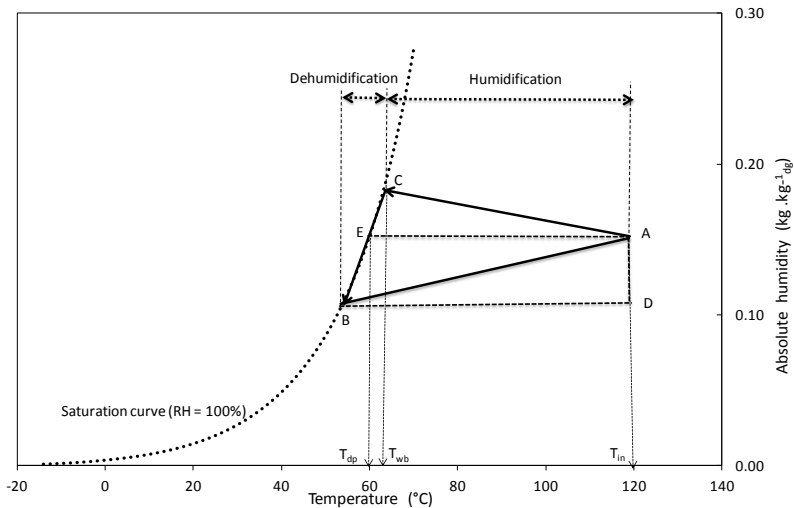


Fig. 1.37: Direct-contact heat-exchanger performance using the psychrometric chart

Therefore, the circulating water can only reach a temperature equivalent to adiabatic saturation temperature of flue gases, and the heat can only be transferred to the ORC working fluid at temperature lower than the entering wet bulb temperature. In order to reach a higher circulating water temperature, an indirect-contact heat exchanger (HEX 1) could be added resulting into a “hybrid heat recovery process” (Fig. 1.38). In this case, “HEX 1” will recover almost all sensible heat above the water dew point temperature so no condensation will occur on the heat-exchanger surface, and the condensing unit will recover most of the latent heat below water dew point temperature.

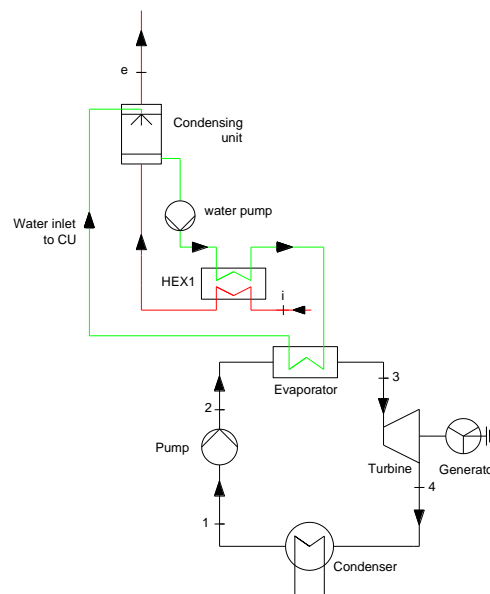


Fig. 1.38: Hybrid heat recovery process

The use of the direct-contact heat exchanger makes sense when recovering energy from heat sources with high-moisture contents. The cycle will be analyzed for heat sources with high-water dew point temperature ($T_{dp} > 50^\circ\text{C}$).

For the calculation, the ORC operating conditions are given Table 1.7. The condenser, turbine, and pump parameters are the same as those indicated in Table 1.5. Calculations are done using R-245fa as working fluid.

Table 1.7: ORC input data for direct-contact and hybrid heat recovery processes

Parameters		Values
Pinch in HEX 1	$\Delta T_{\text{HEX 1}}$	3 K
Minimum pinch in CU	$\Delta T_{\text{min CU}}$	0.5 K
$T_{\text{out flue gases from CU}} - T_{\text{in water to CU}}$	-	2 K
Water pressure after water pump	P_{water}	0.2 MPa

In Fig. 1.39.a and Fig. 1.39.b, a parametric optimization of the water temperature at the evaporator inlet was performed with respect to the net power and exergy efficiency. For each water temperature at the evaporator inlet, the evaporation temperature of the working fluid (R-245fa) is calculated to optimize the net power. In the hybrid heat-recovery process, the exit water temperature from “HEX1” is calculated in order to reach the corresponding pinch in the condensing unit. For more details about the optimization procedure, refer to Fig.C.2b and Fig.C.3 in “Annex C”.

In Fig. 1.39.a and Fig. 1.39.b, vertical lines represent the boundary limit between the direct-contact process (zone I) and the hybrid heat-recovery process (zone II). The small green circles denote the temperatures at which the water temperatures at the evaporator inlet are equal to the corresponding wet bulb temperatures for the different water dew point temperatures. The vertical lines cross the horizontal axis at evaporator inlet-water temperatures equal to the wet bulb temperatures minus 0.5 K (minimum pinch in the condensing unit). In zone I, the net power increases slightly by increasing the inlet water temperature at the evaporator and reaches the maximal value at the boundary limit between the two zones. In zone II, the net power decreases by increasing the inlet water temperature at the evaporator inlet until reaching roughly 100°C where it begins to present a slight increase. The maximal value of the net power in zone II occurs for a water temperature at the evaporator inlet equal to the entering wet bulb temperature.

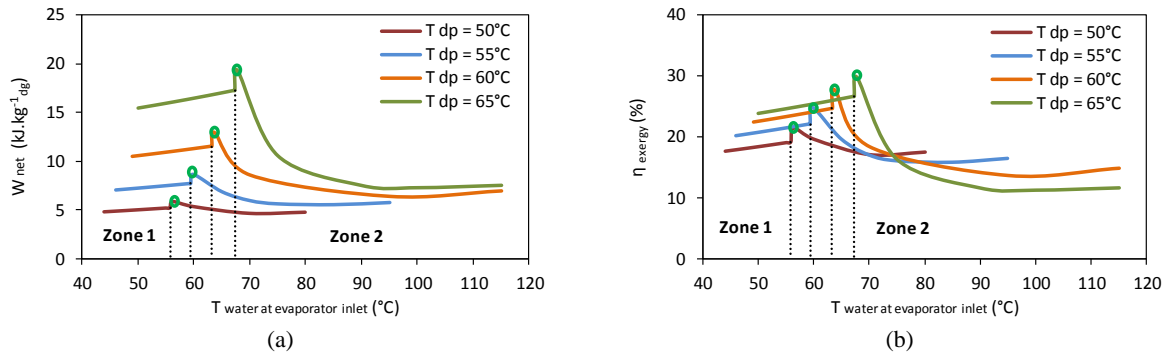


Fig. 1.39: Evolutions of: (a) net power, (b) exergy efficiency as a function of the water temperature at the evaporator inlet

The evolution of the evaporator capacity as a function of the water temperature at the evaporator inlet is shown Fig. 1.40.a. The evaporator capacity is almost constant in zone I, and reaches a maximal value in zone II for a water temperature at the evaporator inlet equal to the entering wet bulb temperature, before it starts to decrease by increasing the inlet water temperature at the evaporator inlet. The repartition of the heat load between the condensing unit and “HEX1” are shown Fig. 1.40.b. The capacity of “HEX1” is constant in the hybrid heat-recovery zone and nil in the direct heat-recovery zone.

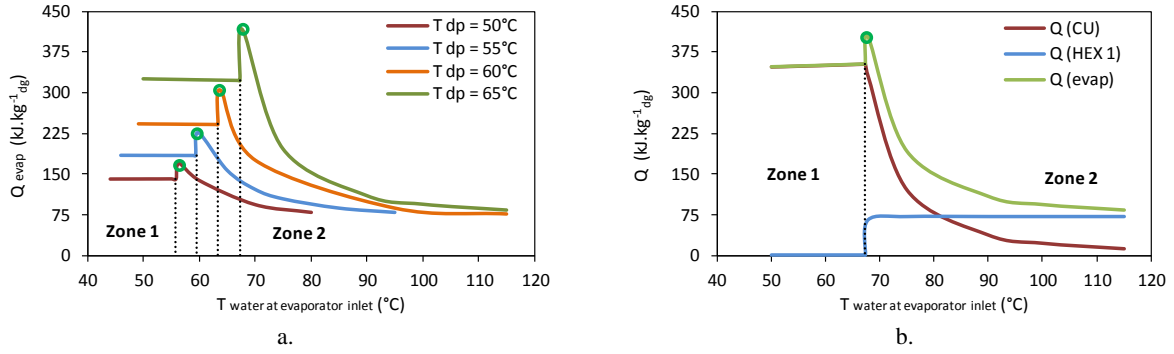


Fig. 1.40: Evolutions of: a) evaporator capacity, b) “CU” and “HEX 1” capacities ($T_{dp} = 65^{\circ}\text{C}$) as a function of water temperature at the evaporator inlet

Evolutions of the working fluid and hot water mass flow rates are shown Fig. 1.41.a and Fig. 1.41.b respectively. The working fluid mass flow rate (Fig. 1.41.a) presents the same evolution as for the evaporator capacity. Fig. 1.41.b shows that a high hot water mass flow rate is expected below the entering wet bulb temperature.

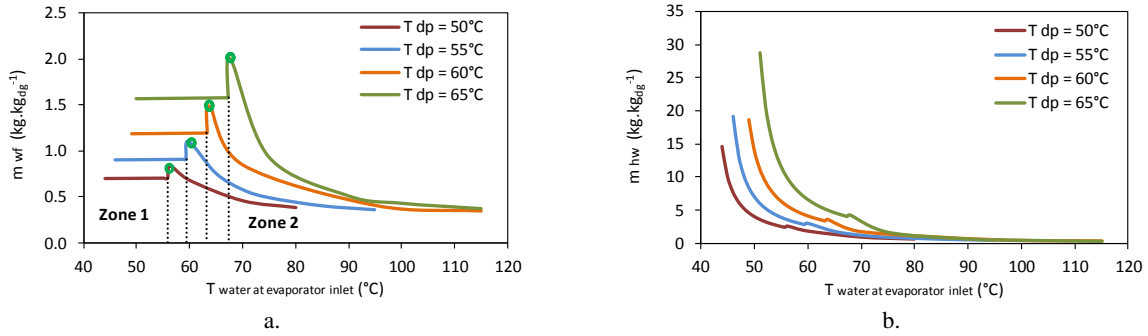


Fig. 1.41: Evolutions of: a) working fluid and b) hot water mass flow rates as a function of the water temperature at evaporator inlet

The evolution of the mass of water vapor condensate as a function of the water temperature at the evaporator inlet is shown Fig. 1.42. The maximal water vapor condensation occurs for a water temperature at the evaporator inlet equal to the entering wet bulb temperature.

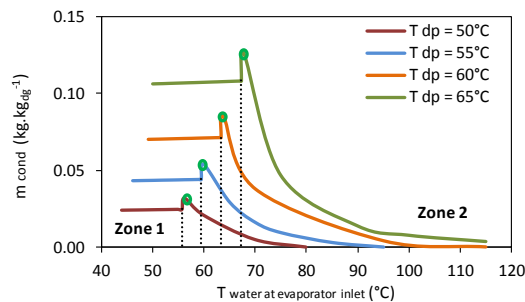


Fig. 1.42: Evolution of the mass of water vapor condensate as a function of water temperature at the evaporator inlet

This section shows that, in the direct-contact heat-recovery system, the maximal net power is reached for a final water temperature nearby the entering wet bulb temperature of flue gases with a minimum of 0.5 K (minimum pinch in condensing unit) below it. In the hybrid heat-recovery zone, the maximal net power is reached for a final water temperature equal to the entering wet bulb temperature.

1.7 Two-stage ORC

1.7.1 Typical two-stage ORC

A simple ORC is limited when the heat recovery from sensible heat and latent heat are in the same range ($45^{\circ}\text{C} < T_{dp} < 55^{\circ}\text{C}$). Consequently, a two-stage ORC could be necessary in order to enhance the heat-work conversion ability of the system by taking advantage of both optima. Two-stage ORC introduces an additional pressure level, leading to an evaporation occurring at two different pressures. The ORC system is split into a high-pressure and a low-pressure loop. The high-pressure evaporation stage will recover mostly sensible heat taking advantage of the sensible heat optimum, while the low-pressure evaporation stage will recover mostly latent heat taking advantage of the latent heat optimum (Fig. 1.43).

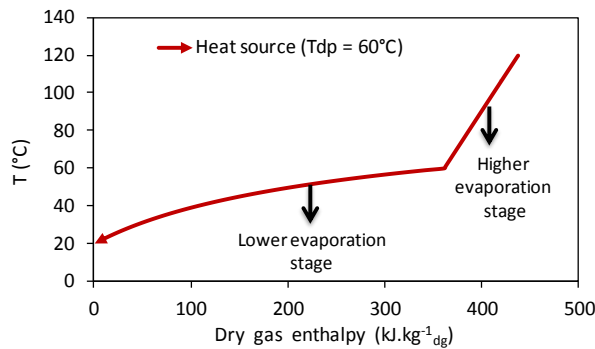
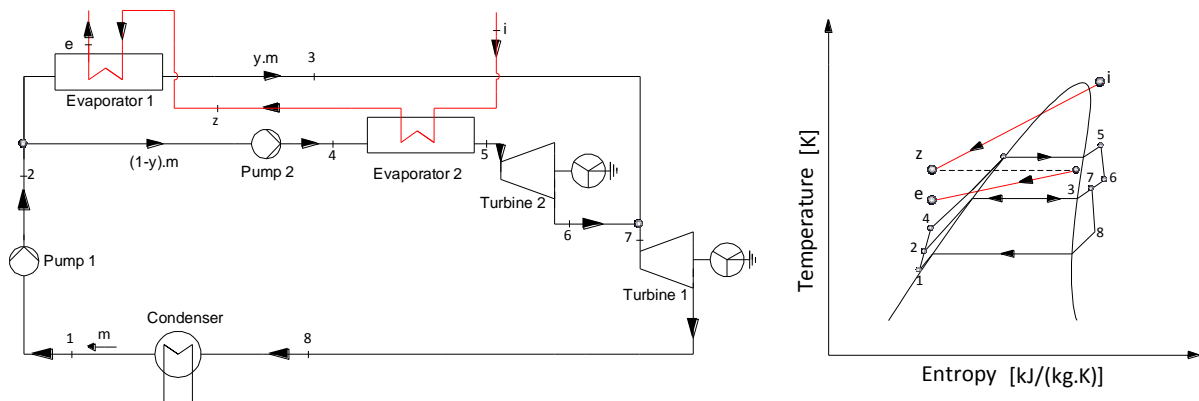


Fig. 1.43: Enthalpy diagram for a heat source ($T_{dp} = 60^{\circ}\text{C}$) showing the integration of a two-stage ORC

The two-stage ORC layout presented Fig. 1.44, which describes the cycle used in this study, is just one solution among others for the implementation of a two-stage ORC. The operating principle of the two-stage ORC system is as follows (Fig. 1.44): the working fluid, sub-cooled liquid at the condenser outlet (Point 1) is compressed to intermediate pressure (Point 2) and then split into two mass fractions. Mass fraction (y) enters Evaporator 1 where it is heated by the flue gases at the intermediate pressure, and mass fraction ($1-y$) is compressed to a high pressure (Point 4) before entering into Evaporator 2 where it is heated and evaporated by flue gases. The vapor stream leaving Evaporator 2 expands in Turbine 2. At Turbine 2 discharge, the two mass fractions are grouped together, expanded to low pressure in Turbine 1 and enter the condenser to complete the cycle.



a- Lay-out diagram

b- T-s diagram

Fig. 1.44: Typical two-stage ORC

Becquin *et al.* [BEC 12] have reported that the two-stage ORC offers a great performance increase for heat source temperatures between 80°C and 150°C using R-245fa with a gain of roughly 10% to 20% in the net power in that range. They also reported that the power increase offered by the two-stage ORC increases as the heat-source temperature decreases, but reaches a plateau of 20% net power increase for heat-source temperatures of 120°C and below. However, their study deals with heat extraction from dry heat sources. In this section, attempts are made to show the effect of latent heat recovery on the two-stage ORC behavior. It should be noted that on top of the overall increase in system complexity, working with two pressure levels might require to use two turbines, potentially leading to a further increase in the system cost. The T-s diagram for the investigated two-stage ORC system is as shown Fig. 1.44.b.

In order to analyze the typical two-stage ORC, the same operating parameters as for the simple ORC are considered (refer to Table 1.5). R-245fa is selected as working fluid. The heat exchange in the two evaporators is defined by a 3-K pinch.

The evolution of the net power as a function of the evaporation temperature in Evaporator 1 is shown in Fig. 1.45, the evaporation pressure in evaporator 2 is set to 1.5 MPa. Similarly to the simple ORC, two regions can be identified: sensible and latent heat regions depending on whether the evaporation temperature in Evaporator 1 is, respectively, above or below the value ($T_{dp} - \Delta T$).

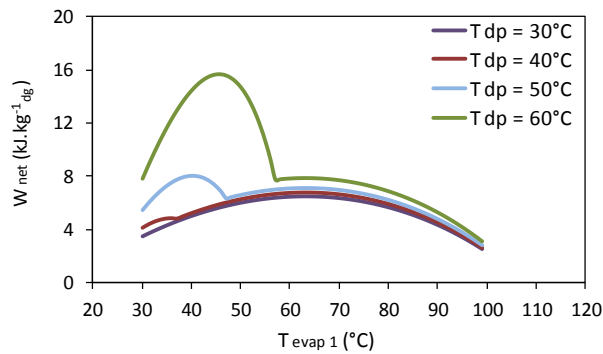


Fig. 1.45: Evolutions of net power as a function of the evaporation temperature in Evaporator 1 ($P_{evap 2} = 1.5$ MPa)

The evaporation temperature in Evaporator 1 is calculated in order to maximize the net power of the two-stage ORC. Within the same aim, a parametric optimization of the evaporation temperature in Evaporator 2 will be performed. Fig. 1.46 shows the evolutions of net power as a function of the evaporation temperature in Evaporator 2. A comparison with Fig. 1.22 shows that the two-stage ORC has a tendency to establish an equivalency between the net powers at the two optima at high-water dew point temperatures ($T_{dp} \geq 50^\circ\text{C}$), because a great portion of latent heat is recovered in Evaporator 1 (refer to Fig. 1.45).

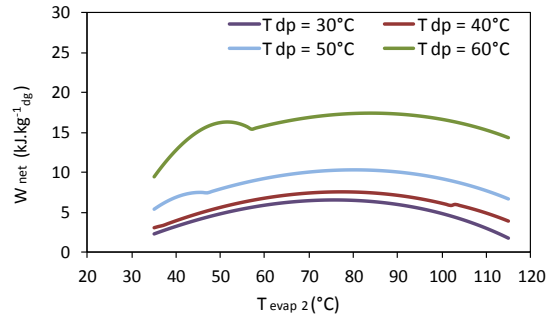


Fig. 1.46: Evolution of the net power as a function of the evaporation temperature in Evaporator 2

Fig. 1.47 shows the repartition of net power, evaporator capacity, mass of water vapor condensate, and working fluid mass fraction as a function of the evaporation temperature in Evaporator 2 for a water dew point temperature of 60°C. As shown in Fig. 1.47, operating at the sensible heat optimum in Evaporator 2 leads to higher heat capacity for Evaporator 1 compared to Evaporator 2 (Fig. 1.47.b), and the preponderant turbine power will be generated by Turbine 1 (Fig. 1.47.a) since a high quantity of latent heat will be recovered in Evaporator 1 (Fig. 1.47.c). By contrast, operating at the latent optimum in Evaporator 2 leads to higher heat capacity for Evaporator 2 compared to Evaporator 1 (Fig. 1.47.b) and the powers generated by the two turbines are in the same range (Fig. 1.47.a).

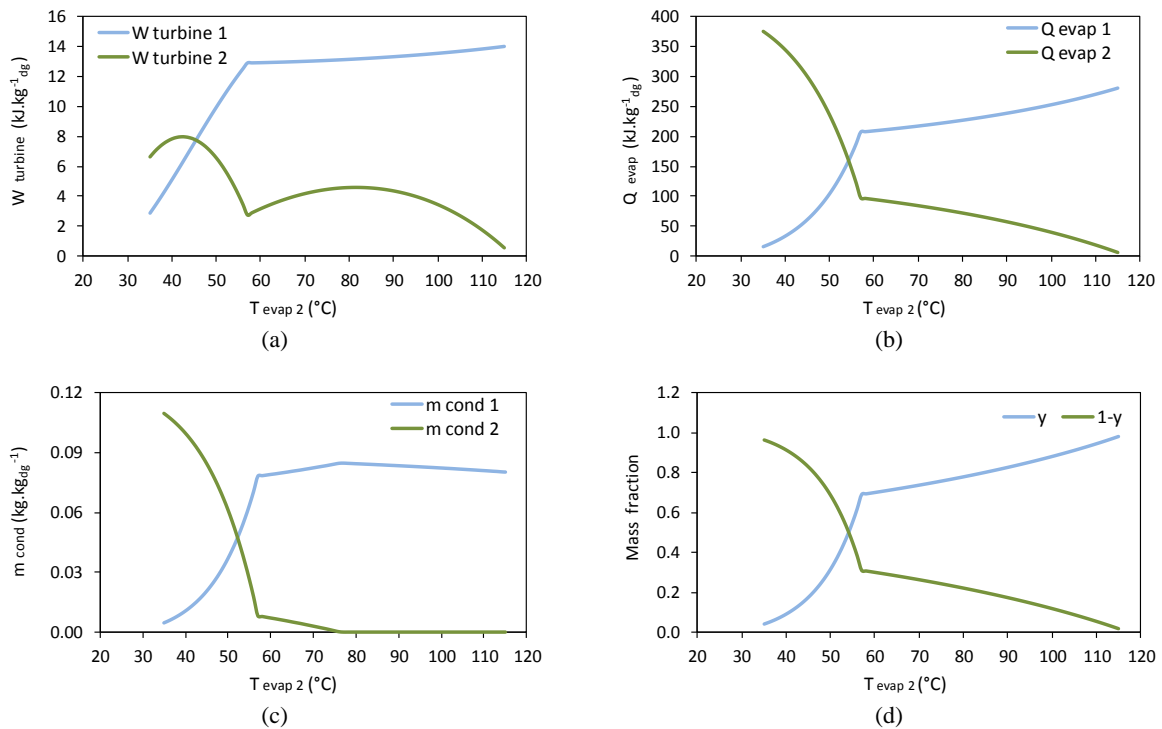


Fig. 1.47: Repartition of: (a) net power, (b) evaporation capacity, (c) mass of water vapor condensate and (d) mass fraction as a function of the evaporation temperature in Evaporator 2 ($T_{\text{dp}} = 60^{\circ}\text{C}$)

It should be noted that, operating at dry optimum in Evaporator 2 instead of wet optimum presents an advantage in case of a pollutant heat source (SO_2 and NO_x contents). In this case, an indirect-contact evaporator could be used to recover the sensible heat above the water dew point temperature and a direct-contact condenser could be used to recover the sensible and latent heat below the water dew point temperature.

Fig. 1.48 shows the net power improvement provided by the two-stage ORC compared to simple ORC with direct evaporator. The parameters of both simple and two-stage ORCs are optimized with respect to the net power. For more details about the optimization procedures, refer to Fig.C.2a and Fig.C.4a in “Annex C”. It could be observed from Fig. 1.48 that the two-stage ORC offers a significant performance increase at a water dew point around 51.5°C, with a reached maximal net power improvement around 60%. By referring to Fig. 1.22, which is plotted for simple stage ORC, the net power is almost equal at the two optima at this water dew point value. The net power improvement offered by the two-stage ORC decreases gradually by moving away from this value in which one of the two optima becomes dominant (refer to Fig. 1.22).

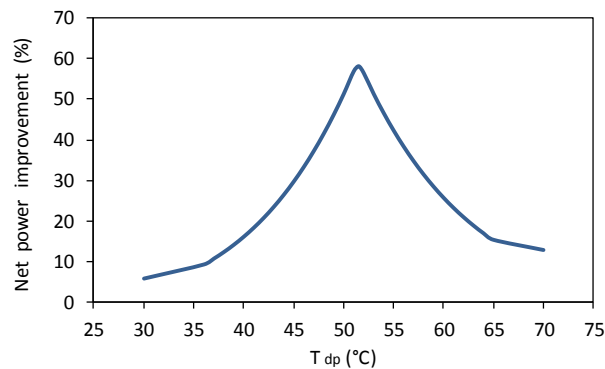


Fig. 1.48: Net power improvement provided by the two-stage ORC compared to simple ORC with direct evaporator

1.7.2 Improved two-stage ORC

With the aim to increase the net power, an improvement of the basic two-stage ORC is suggested as shown in Fig. 1.49. A flash separator is introduced at the exit of the low-pressure evaporator in order to separate the stream (3) into a vapor (8) and a liquid (4) streams. Thus, stream (3) can exit Evaporator 1 in a two-phase state. In order to analyze the improved two-stage ORC, the same operating parameters as for the typical two-stage ORC are adopted (refer to section 1.7.1) using R-245fa as working fluid. The working fluid at the inlet of Pump 2 is considered at saturated liquid state.

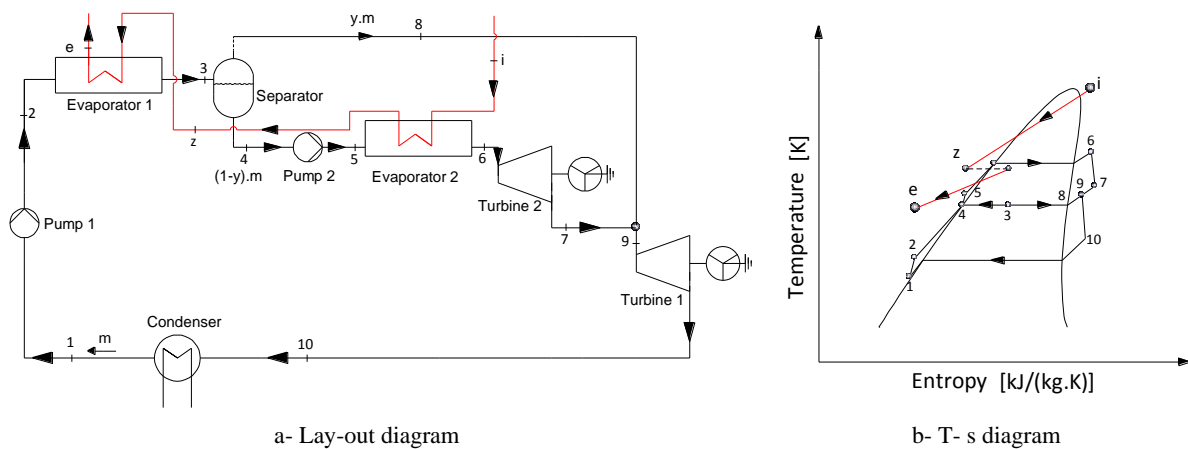


Fig. 1.49: Enhanced two-stage ORC

Fig. 1.49.a and Fig. 1.49.b show the effect of adding a flash separator on the net power improvement compared to simple ORC with direct evaporator and typical two-stage ORC respectively. The

parameters of the simple ORC, typical and enhanced two-stage ORCs are optimized with respect to the net power. For more details about the optimization processes, refer to Fig.C.2 and Fig.C.4 in “Annex C”. As shown, the addition of a flash separator is more promising at both high ($> 60^{\circ}\text{C}$) and low ($< 40^{\circ}\text{C}$) water dew point temperatures. Depending on the latter, the actual cycle improves the net power between 2 and 16% compared to the typical two-stage ORC (Fig. 1.49.b) and between 22 and 64% compared to the simple-stage ORC (Fig. 1.49.a).

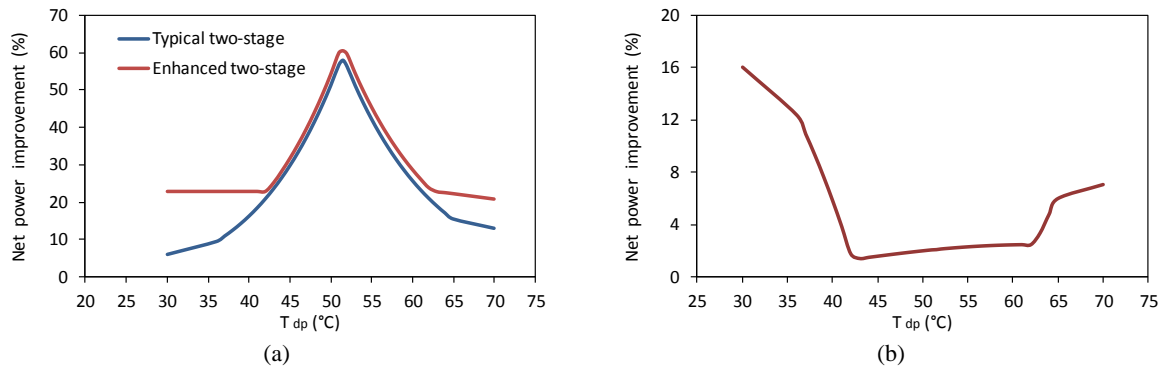


Fig. 1.50: Effect of adding a flash separator on the net power improvement compared to: a) simple ORC with direct evaporator, b) typical two-stage ORC

1.7.3 Two-stage ORC using direct-contact condensation at the low-pressure stage

As stated previously, in a two-stage ORC, operating at dry optimum in Evaporator 2 instead of wet optimum presents an advantage in case of a pollutant wet heat sources (SO_2 and NO_x contents). In this case, an indirect contact evaporator could be used to recover the sensible heat above the water dew point temperature and a direct-contact condenser could be used to recover the sensible and latent heat below the water dew point temperature. Therefore, the high-pressure evaporation stage will recover mostly sensible heat taking advantage of the sensible heat optimum, while the low-pressure evaporation stage will recover mostly latent heat using a condensing unit taking advantage of the latent heat optimum (Fig. 1.51). In order to analyze the present cycle, the same operating parameters as for the typical two-stage ORC are adopted (refer to section 1.7.1). The parameters of the condensing unit are the same as those indicated in Table 1.7. R-245fa is used as working fluid.

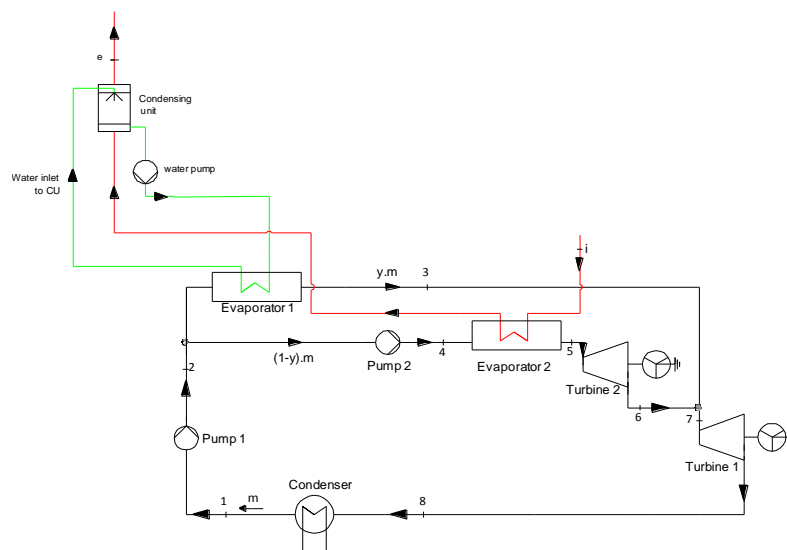


Fig. 1.51: Typical two-stage ORC using direct-contact condensation at the low-evaporation pressure stage

The evolution of the net power as a function of the evaporation temperature in Evaporator 2 is shown in Fig. 1.52 for various water dew point temperatures; optimal evaporation temperature leading to maximal net power is considered in Evaporator 1. In addition, a comparison between the typical two-stage ORC using a direct and an indirect-contact condensation at the low-pressure stage is shown Fig. 1.53 for a water dew point temperature of 60°C. Net power losses around 10% are expected at the maximal net power value when operating in the sensible heat region for Evaporator 2 (Fig. 1.53).

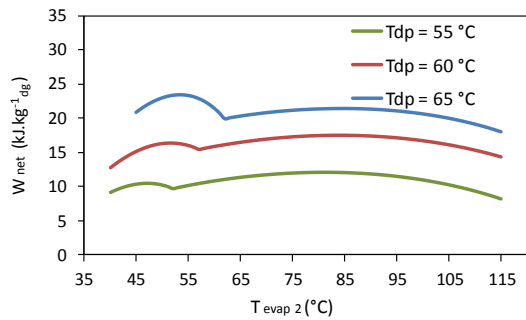


Fig. 1.52: Evolution of the net power as a function of the evaporation temperature in Evaporator 2

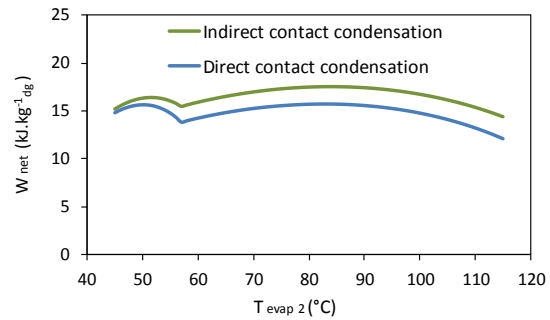


Fig. 1.53: Comparison between typical two-stage ORC using direct and indirect-contact condensation at the lower pressure evaporation stage ($T_{dp} = 60^{\circ}\text{C}$)

1.8 Net power comparison between the heat recovery modes

Table 1.8 shows a comparison for the maximal net power between the heat recovery modes for various water dew point temperatures. The comparison is done using the operating parameters listed in Table 1.5 and Table 1.7 and using R-245fa as working fluid. Parameters of ORCs are optimized with respect to the net power. For more details about the optimization processes, refer to “Annex C” (Fig.C.1 to Fig.C.4).

In addition, Table 1.8 shows the percentage ratio of the net power for a given heat recovery mode calculated with respect to the net power obtained for simple ORC using indirect-contact condensation with direct evaporator. Table 1.8 shows that the indirect-contact condensation process using direct evaporator is the most favorable heat recovery scheme concerning the net power. Further, no significant difference observed between the net power produced in the indirect-contact condensation using indirect evaporator and the direct-contact condensation for water dew point temperatures higher than 60°C. Moreover, the hybrid heat-recovery process could lead to an increase in the net power, around 10%, compared to the direct-contact condenser.

Table 1.8: Comparisons between the heat recovery modes for various water dew point temperatures (R-245fa)

$W_{net\ max}$ (kJ.kg ⁻¹ .dg)		30°C	40°C	50°C	60°C	70°C
ICC	DE	6.23 (100%)	6.45 (100%)	6.83 (100%)	13.9 (100%)	32.49 (100%)
	IE	5.65 (90.7%)	5.88 (91.1%)	6.26 (91.6%)	11.37 (82.7%)	26.97 (83.1%)
DCC	-	-	-	5.16 (75.5%)	11.5 (82.7%)	26.09 (80.3%)
HHR	-	-	-	5.8 (84.9%)	12.86 (92.5%)	28.92 (89.1%)
TTS	ICC	7.08 (113.6%)	7.33 (113.6%)	10.33 (151.2%)	17.47 (125.7%)	36.68 (112.4%)
	DCC*	-	-	9.67 (141.6%)	15.7 (112.9%)	30.35 (93.4%)
ETS	ICC	7.66 (122.9%)	7.93 (122.9%)	10.54 (154.3%)	17.9 (128.8%)	39.27 (120.8%)
	DCC*	-	-	10.12 (148.2%)	16.35 (117.6%)	31.42 (96.7%)

ICC : Indirect Contact Condensation; DE: Direct Evaporator; IE: Indirect Evaporator; DCC: Direct Contact Condensation; HHR: Hybrid Heat recovery Process; TTS: Typical Two-Stage, ETS: Enhanced Two-Stage, DCC*: Direct Contact Condensation occurring at low pressure evaporation stage.

Despite the increase in system complexity, working with two-stage evaporation could be promising especially when the heat recovery from sensible heat and latent heat are in the same range ($T_{dp} \sim 50^{\circ}\text{C}$). Using a direct-contact condenser at the low-pressure evaporation stage instead of a direct-contact condenser could lead to significant reduction in the net power especially at high water dew point temperatures ($T_{dp} \geq 60^{\circ}\text{C}$).

After studying and optimizing the parameters of the simple and the two-stage ORCs with respect to the net power output and analyzing the effects of latent heat recovery on cycle performances using both direct and indirect water vapor condensation processes, the next step consists in the study of the effect of auxiliary consumptions on the behavior of ORCs. As stated previously, ORC actual applications presently have overall electrical efficiencies less than 5%. In addition, these efficiencies could even shrink further taking into account the auxiliary power consumptions. There is thus a clear and compelling need to study the effects of these latter's on the ORC behavior in order to reduce their effect on the net power losses.

1.9 Effect of auxiliary consumptions on ORC performances

The auxiliary consumptions generated by the cold-water source in the condenser and by the hot source in the evaporator play a crucial role for the present applications ($T_{in} \sim 120^{\circ}\text{C}$) because the overall efficiency is as low as 5%. In addition, the auxiliary consumptions are important criteria in the comparison and optimization of the thermodynamic cycles; they might affect the operating parameters of the cycle (condensation and evaporation pressures, evaporator superheat).

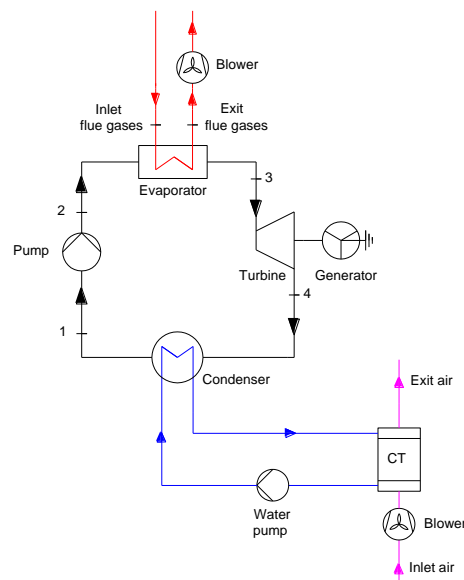


Fig. 1.54: Simple ORC lay-out with direct evaporator taking into account the auxiliary consumptions

A simple ORC layout with direct evaporator taking into account the auxiliary consumptions is shown Fig. 1.54. A cooling tower is used as a cooling water source for the condenser. The auxiliary consumptions of the conversion cycle include the blower consumptions to overcome the gas pressure drop of flue gases in the evaporator and the ambient air in the cooling tower, and the pump consumptions to overcome the water pressure drop in the cooling tower circuit. The pressure drop at the gas side has the predominant effect. The pressure drop at the waterside for the cooling tower

circuit is set to 50 KPa. Details on cooling tower operation and parameters are presented in “Annex B”.

Three configurations will be distinguished (Table 1.9):

- ORC with Configuration 1: no auxiliary consumptions
- ORC with Configuration 2: mean auxiliary consumptions
- ORC with Configuration 3: high auxiliary consumptions

In ORC with Configuration 2 (resp. ORC with Configuration 3), the pressure drop at the flue-gas side in the evaporator and the blower efficiency are considered to be 150 Pa and 80% respectively (resp. 300 Pa and 60%). Same values are set for the pressure drop and blower efficiency for the air in the cooling tower.

Table 1.9: ORC configurations

Parameters	η_{blower} (%)	DP _{flue gas in evaporator} (Pa)	DP _{air in cooling tower} (Pa)
ORC with Configuration 2	80	150	150
ORC with Configuration 3	60	300	300

The ORC process parameters are listed in Table 1.10. These parameters are used to evaluate the net power of the ORC system with the three ORC configurations listed above. As shown in Table 1.10, a real case approach is adopted taking into account the pressure drop at the working fluid side in both evaporator and condenser. The efficiency of the cold-water pump is set to 85%. The efficiencies of the turbine and the ORC pump are the same as those indicated in Table 1.5.

Table 1.10: ORC process parameters

Parameters	Values
$T_{\text{in water to condenser}}$	18°C
SC_{cond}	2 K
Pinch condenser	2 K
Pinch evaporator	3 K
$CT_{\text{approach}} = T_{\text{out cold water from CT}} - T_{\text{in air wet bulb to CT}}$	5 K
$DT_{\text{CT}} = T_{\text{in water to CT}} - T_{\text{out air from CT}}$	3 K
$T_{\text{air dry/wet bulb inlet to CT}}$	18 °C/13 °C
Pressure drop in evaporator (working fluid side)	
DP _{liquid heater} / DP _{boiler}	5 kPa / 15 kPa
Pressure drop in condenser (working fluid side)	
DP _{sub-cooler} / DP _{two-phases} / DP _{desuperheater}	2 kPa / 7 kPa / 1 kPa

1.9.1 Effect of auxiliary consumptions on condensation pressure

The auxiliary consumptions of the cold-water source in the condenser affect the condensation pressure.

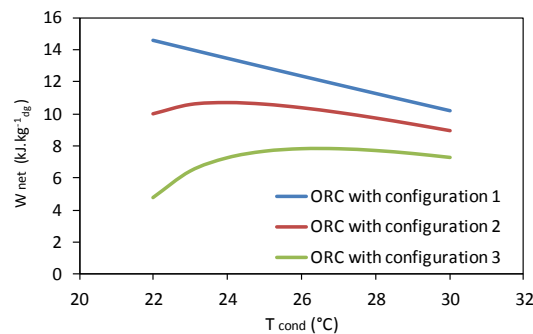


Fig. 1.55: Effect of auxiliary consumptions on condensation pressure (R-245fa, $P_{\text{evap}} = 0.35$ MPa, $SH_{\text{evap}} = 0$, $T_{\text{dp}} = 60^\circ\text{C}$)

Fig. 1.55 shows that the optimal condensation pressure is slightly moved away from the minimal condensation pressure for ORC with Configuration 2, while it is more displaced for ORC with Configuration 3. Therefore, depending on the auxiliary consumptions (ORC with Configuration 1, 2 or 3), an optimal condensation pressure exists at which the net power is maximal.

1.9.2 Effect of auxiliary consumptions on evaporator superheat

Fig. 1.56 shows the evolution of the evaporator superheat leading to a maximal net power as a function of the evaporation temperature for the three ORC configurations. The condensation pressure is optimized with respect to the net power.

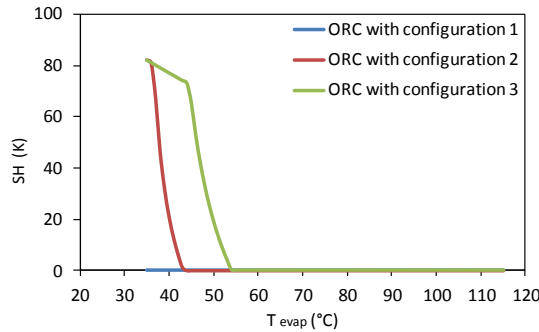


Fig. 1.56: Effect of auxiliary consumptions on evaporator superheat (R-245fa, $T_{dp}=60^{\circ}\text{C}$)

As stated previously, superheating is detrimental to ORC efficiency for the working fluids with positive slope of the saturation vapor curves ($dT/ds > 0$, dry fluid) such as R-245fa (refer to Fig. 1.21). However, it is not the case for high auxiliary consumptions at low evaporation temperatures (Fig. 1.56). Indeed, the increase in the evaporator superheat leads to a decrease in working fluid and cold water mass flow rates (Fig. 1.57), and then to a decrease in the auxiliary consumptions. Thus, for ORC with Configurations 2 and 3 and at low evaporation temperature, where the working fluid and cold water mass flow rates in the cycle are relatively high (Fig. 1.58), the evaporator superheat leading to the maximal net power will be not nil. In other term, the decrease in auxiliary consumptions induced by increasing the evaporator superheat will overcome the decrease in the net power.

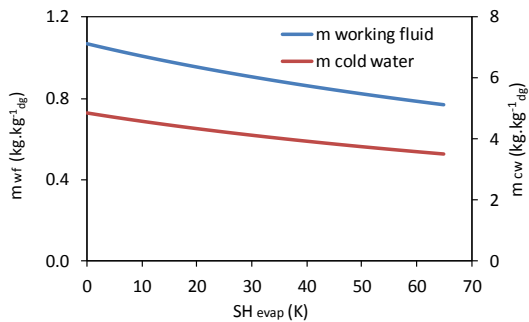


Fig. 1.57: Evolution of the mass fractions as a function of the evaporator superheat (R-245fa, $P_{evap} = 0.35 \text{ MPa}$, $T_{dp} = 60^{\circ}\text{C}$, ORC with Configuration 1)

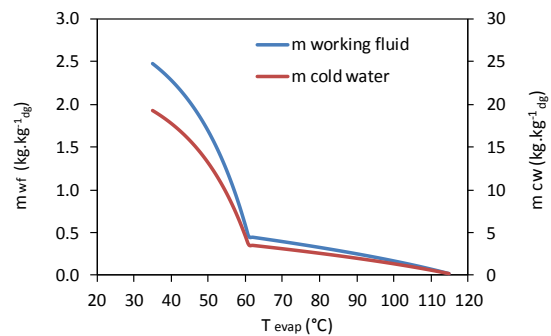


Fig. 1.58: Evolution of the mass fractions as a function of the evaporation temperature (R-245fa, $T_{dp} = 60^{\circ}\text{C}$, $SH_{evap} = 0$, ORC with Configuration 1)

1.9.3 Effect of auxiliary consumptions on evaporation temperature

The effects of auxiliary consumptions on the net power are shown Fig. 1.59.a and Fig. 1.59.b for water dew point temperatures of 30°C and 60°C respectively. The condensation pressure and evaporator

superheat are optimized with respect to the net power. The major effect of auxiliary consumptions appears on the latent heat region for a water dew point temperature of 60°C where the working fluid mass flow rate in the cycle and thus the auxiliary consumptions are relatively high (refer to Fig. 1.58). The evaporation temperature at which the net power is maximal is slightly moved away for ORC with Configuration 2 while it is more displaced for ORC with Configuration 3.

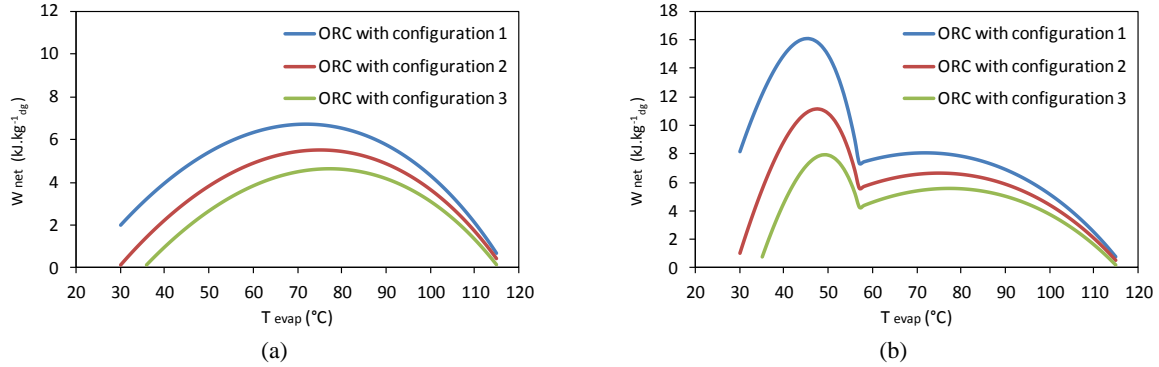


Fig. 1.59: Effect of ORC Configurations on the net power (R-245fa): a) $T_{dp}=30^{\circ}\text{C}$, b) $T_{dp}=60^{\circ}\text{C}$

Table 1.11 shows the effect of the ORC configurations on the maximal net power. ORC parameters are optimized with respect to the net power. For more details about the optimization process, refer to Fig.C.5a in “Annex C”.

Compared to ORC with Configuration 1, the net power is reduced by 18% (resp. 31%) for ORC with Configuration 2 (resp. ORC with Configuration 3) for a water dew point temperature of 30°C and by 31% (resp. 51%) for ORC with Configuration 2 (resp. ORC with Configuration 3) for a water dew point temperature of 60°C.

Table 1.11: Effect of ORC configurations on the net power (R-245fa)

$W_{net\ max}$ ($\text{kJ.kg}^{-1}.\text{dg}$)	$T_{dp} = 30^{\circ}\text{C}$	$T_{dp} = 60^{\circ}\text{C}$
ORC with Configuration 1	6.7 (100%)	16.1 (100%)
ORC with Configuration 2	5.5 (82%)	11.2 (69%)
ORC with Configuration 3	4.6 (69%)	7.9 (49%)

Table 1.12 shows the effect of ORC configurations on net power ratio between sensible and latent heat optima. This ratio is reduced from “2” for ORC with Configuration 1 to “1.42” for ORC with Configuration 3.

Table 1.12 : Effect of ORC configurations on net power ratio between latent and sensible heat optima (R-245fa)

ORC Configuration	Net power ratio (latent over sensible)
1	2.00
2	1.67
3	1.42

1.9.4 Effect of auxiliary consumptions on working fluid selection

To select the most suitable working fluid, it is not easy to evaluate the cycle performance with different working fluids under different operating parameters because different operating parameters could result in better or worse performances. Therefore, it is necessary to evaluate the ORC performance with different working fluids under their optimal conditions [DAI 09]. The choice of the working fluid has a significant influence on conversion efficiency. Numerous authors investigated the selection of pure working fluids such as [DAI 09], [HUN 97], [LIU 04], [LIU 04], [MAD 07], and [HUN 10].

An interesting approach to optimize the net power is the use of blends as working fluids [ANG 98], [HEB 12], [BLI 87] and [UEM 84]. For those blends, a temperature glide at phase change occurs, which provides a good match of temperature profiles in the condenser and evaporator. It was shown that the use of blends as working fluids leads to an efficiency increase compared to pure fluids, due to a glide match of temperature profiles in the condenser and evaporator. Angelino *et al.* [ANG 98] pointed out that the temperature glide of blends at condensation leads up to 40% reduction of the air-cooler blower powers in comparison to pure fluids. In this section, the effect of auxiliary consumptions on working fluid selection will be analyzed for pure working fluids. In addition, the effect of using blends as working fluids on the net power will be studied in order to reduce the auxiliary consumptions by providing a good match of temperature profiles in the evaporator and condenser.

1.9.5 Pure working fluid

A method for selecting the working fluid is developed to identify the most suitable fluid for this application. The working fluid for ORC systems with low-temperature heat sources must satisfy several safety, environmental, performance, and economic criteria. Among the safety aspects, flammability and toxicity are particularly important. Environmental criteria include the ozone depletion potential (ODP) and the global warming potential (GWP).

The criteria for selecting the working fluid are as follows [AOU 08], [PAP 10]:

- Thermo physical criteria
 - It should cause high efficiency and power output for ORC
 - It should cause high volumetric capacity at the turbine outlet
 - The selected working fluid must present good heat-transfer characteristics (high-thermal conductivity), which would result in a high effectiveness and low-cost heat exchangers.
- Safety Criteria
 - Non or moderately flammable
 - Non toxic
- Low environmental impact
 - $GWP < 1000 \text{ kg}_{\text{CO}_2 \text{ eq.}} \cdot \text{kg}^{-1}_{\text{wf}}$
 - Zero ODP
- Availability and cost
- Material compatibility: the working fluid should be non-corrosive to common engineering materials, so that it does not dictate the use of more expensive materials.

Note that the condenser pressure must be greater than 100 kPa to prevent air infiltration and to have acceptable condenser size. Low-temperature organic fluids such as R-245fa or R-134a meet this requirement since they condense at pressure higher than the atmospheric pressure. However, fluids with higher critical temperature such as pentane or hexane are sub-atmospheric at ambient temperature.

The pressure in the evaporator will be limited to 2.5 MPa for cost reasons and feasibility (availability of system components). For wet fluids, the two-phase state at the turbine outlet for wet fluids is prevented by increasing the outlet superheat in order to avoid turbine erosion and corrosion.

Table 1.13: Physical and safety characteristics, types, and categories of the compared working fluids [LEM 10]

Fluid	M (g.mol ⁻¹)	T _{nb} (°C)	T _{cr} (°C)	P _{cr} (MPa)	h _{fp} (kJ.kg ⁻¹)	K (mw.(m.K) ⁻¹)	α	GWP (2010)	I	Category
-------	-----------------------------	----------------------	----------------------	--------------------------	---	--------------------------------	---	---------------	---	----------

	1)		1)		1)		1)		1)		
	at T_{nb}										
R-134a	102.03	-26.1	101.1	4.0593	216.97	103.91	Wet	1370	1	HFC	
R-1234yf	114.04	-29.2	94.8	3.2660	178.21	81.87	Isent.	<4.4	2	HFC	
R-1234ze	114.04	-18.9	109.4	3.6363	201.06	90.35	Isent.	6	1	HFC	
R-152a	66.05	-24.0	113.3	4.5168	329.91	120.18	Wet	133	2	HFC	
R-227ea	170.03	-16.3	101.8	2.9250	131.77	71.70	Isent.	3580	1	HFC	
R-245fa	134.05	15.1	154.0	3.6510	196.05	91.19	Dry	1030	1	HFC	
R-32	52.02	-51.7	78.1	5.7820	381.86	187.39	Wet	716	2	HFC	
R-365mfc	148.07	40.2	186.8	3.2660	188.19	75.15	Dry	890	1	HFC	
propane	44.09	-42.1	96.7	4.2512	425.59	129.18	Wet	~20	3	Hydrocarbon	
propylene	42.08	-47.6	91.1	4.5550	438.96	149.34	Wet	~20	3	Hydrocarbon	
butane	58.12	-0.5	152.0	3.7960	385.71	115.53	Dry	~20	3	Hydrocarbon	
isobutane	58.12	-11.8	134.7	3.6290	365.10	103.29	Dry	~20	3	Hydrocarbon	
pentane	72.16	36.1	196.6	3.3700	357.58	107.27	Dry	~20	3	Hydrocarbon	
isopentane	72.15	27.8	187.2	3.3780	343.29	106.33	Dry	~20	3	Hydrocarbon	
neopentane	72.15	9.5	160.6	3.1960	315.69	98.69	Dry	~20	3	Hydrocarbon	
hexane	86.18	68.7	234.7	3.0340	334.93	112.09	Dry	~20	3	Hydrocarbon	
isohexane	86.18	60.2	224.6	3.0400	323.06	94.05	Dry	~20	3	Hydrocarbon	
ammonia	17.03	-33.3	132.3	11.333	1369.50	665.68	Wet	<1	2	Inorganic	

α : Slope of the saturation vapor line; M: molecular weight; T_{cr} : critical point temperature; P_{cr} : critical point pressure; T_{tp} : triple point temperature; T_{nb} : normal boiling point temperature; h_{fg} : latent heat of vaporization at T_{nb} ; K: saturated liquid thermal conductivity at 1 atm; I: inflammability

Table 1.14 : Comparison between the compared working fluids ($T_{dp} = 30^\circ\text{C}$, ORC with Configuration 1)

Fluids	P_{evap}	SH_{evap}	P_{cond}	$V_{turbine}$	\bar{T}	x_{out}	η_{system}	$\eta_{recovery}$	$\eta_{overall}$	η_{exergy}	W_{net}
	MPa	K	MPa	$\text{kJ}\cdot\text{m}^{-3}$	-	-	%	%	%	%	$\text{kJ}\cdot\text{kg}^{-1}_{dg}$
R-134a	2.5	2.1	0.6	645.30	4.1	1.00	9.9	55.2	5.5	48.0	7.3
R-1234yf	2.5	0.0	0.6	620.35	4.0	1.01	9.7	62.6	6.1	53.5	8.1
R-1234ze	1.9	0.0	0.5	486.82	4.1	1.04	9.9	54.8	5.4	47.6	7.2
R-152a	2.0	6.5	0.5	559.34	3.7	1.00	9.9	50.8	5.0	44.2	6.7
R-227ea	2.5	0.0	0.4	520.10	6.0	1.12	10.6	57.8	6.1	53.9	8.2
R-245fa	0.6	0.0	0.1	165.90	4.8	1.07	9.7	51.5	5.0	44.1	6.7
R-32	2.5	34.8	1.6	584.82	1.6	1.12	4.6	68.5	3.2	27.9	4.2
R-365mfc	0.3	0.0	0.1	80.08	5.4	1.11	9.6	51.6	4.9	43.5	6.6
propane	2.5	1.4	0.9	698.27	2.8	1.00	8.7	61.1	5.3	46.6	7.1
propylene	2.5	4.6	1.1	701.45	2.3	1.00	7.5	64.2	4.8	42.3	6.4
butane	0.8	0.0	0.2	233.78	3.8	1.07	9.8	51.2	5.0	43.8	6.7
isobutane	1.2	0.0	0.3	320.87	3.6	1.07	9.7	52.6	5.1	44.9	6.8
pentane	0.3	0.0	0.1	98.51	3.4	1.09	8.2	41.9	3.4	30.2	4.6
isopentane	0.4	0.0	0.1	108.62	3.9	1.10	9.1	47.4	4.3	37.8	5.7
neopentane	0.6	0.0	0.2	168.24	3.9	1.12	9.5	52.9	5.0	44.3	6.7
hexane	0.2	0.0	0.1	57.01	2.0	1.07	4.8	23.1	1.1	9.8	1.5
isohexane	0.2	0.0	0.1	67.01	2.3	1.09	5.6	28.0	1.6	13.9	2.1
ammonia	2.5	58.9	0.9	756.70	2.7	1.06	8.8	53.6	4.7	41.2	6.3

$V_{turbine}$: outlet turbine volumetric capacity; \bar{T} : turbine expansion ratio; x_{out} : vapor quality at turbine outlet

Table 1.13 summarizes the physical properties, safety, and environmental features, types, and categories of the analyzed working fluids for comparison. These fluids are pure fluids containing no chlorine atom and therefore present a zero ODP, having a relatively low GWP (<1000), except R-134a and R-227ea. Note that the slope of the saturation vapor line in Table 1.13 is indicated in the corresponding operating range ($T_{heat\ source} \sim 120^\circ\text{C}$, $T_{cold\ water} > 18^\circ\text{C}$).

A comparison between the compared working fluids using the simple ORC with direct evaporation is shown in Table 1.14. The comparison is done by applying for each working fluid the optimization algorithm shown in Fig.C.5a in ‘‘Annex C’’.

The volumetric capacity at the turbine outlet is given by:

$$V_{\text{turbine}} = \Delta h_{\text{turbine}} * \rho_{\text{outlet turbine}} \quad \text{Eq. 1.32}$$

Where: $\rho_{\text{outlet turbine}}$ is the density of the working fluid at the turbine outlet.

As shown in Table 1.14, R-227ea and R-1234yf are identified as interesting working fluids due to their high net power compared to the other working fluids. For these two fluids, the sensible preheating zone exceeds the vaporization latent heat zone (Fig. 1.60.a) since they present low latent heat of vaporization compared to other fluids (Table 1.13) leading to better temperature matching between the working fluid and the heat source. Note that an increase in the ratio of the vaporization latent heat over the sensible heat leads to an acute pinch at the end of the preheating zone, which may increase exergy losses in the evaporator. As well, compared to other fluids, R-1234yf is characterized by high volumetric capacity at the turbine outlet, which might lead to compact and small turbine.

Hydrocarbons present generally a low GWP, a low triple point temperature (except neopentane), and are not toxic, but they are flammable and present a high latent heat of vaporization (Table 1.13). From the considered hydrocarbons, hexane, isohexane, pentane, and isopentane present a relatively high normal boiling point (NBP); which is reflected in low-condensation pressures and therefore will be disregarded. The only hydrocarbons that will be promising for this application are propane, propylene, butane, isobutane, and neopentane. R-32 is characterized by low-critical temperature (78.1°C), which leads to low-system efficiency and therefore will be excluded.

Table 1.15: Comparison of the net power between the three ORC configurations (Possible candidate working fluids)

Net power output (kJ.kg ⁻¹ .dg)	T _{dp} = 30°C			T _{dp} = 60°C		
	1	2	3	1	2	3
ORC configuration						
Working fluid						
R-134a	7.3	6.0	4.9	16.2	11.5	8.6
R-1234yf	8.1	6.7	5.5	16.4	11.3	8.3
R-1234ze	7.2	6.0	5.0	16.3	11.3	8.3
R-152a	6.7	5.5	4.6	16.2	11.8	8.9
R-227ea	8.2	6.9	5.9	16.6	11.5	8.1
R-245fa	6.7	5.5	4.6	16.1	11.2	8.1
propane	7.1	5.6	4.5	16.1	11.4	8.5
propylene	6.4	5.0	3.9	16.2	11.7	8.6
butane	6.7	5.5	4.6	16.0	11.1	8.1
isobutane	6.8	5.6	4.7	16.1	11.2	8.1
neopentane	6.7	5.6	4.6	16.1	11.2	8.0
ammonia	6.3	5.0	3.9	16.0	12.7	9.5

Table 1.15 shows a comparison of the net power between the possible working-fluid candidates for the three ORC configurations. The comparison is done by applying for each working fluid the optimization algorithm shown in Fig.C.5a in “Annex C”. By observing Table 1.15, it could be concluded that the auxiliary consumptions do not affect the working fluid selection at low-water dew point temperature (T_{dp} = 30°C). For the three ORC configurations, R-1234yf and R-227ea present the highest overall efficiency compared to other fluids.

At high water dew point temperature (T_{dp} = 60°C), the evaporation temperature in the evaporator becomes lower than the water dew point temperature when operating at the latent heat optimum. In this case, the vaporization latent zone dominates the sensible preheating zone (Fig. 1.60.b). As the

auxiliary consumptions increase, the evaporator superheat will be an asset for wet fluids such as ammonia, R-152a, and R-134a (refer to Fig. 1.56) where they present the highest net power.

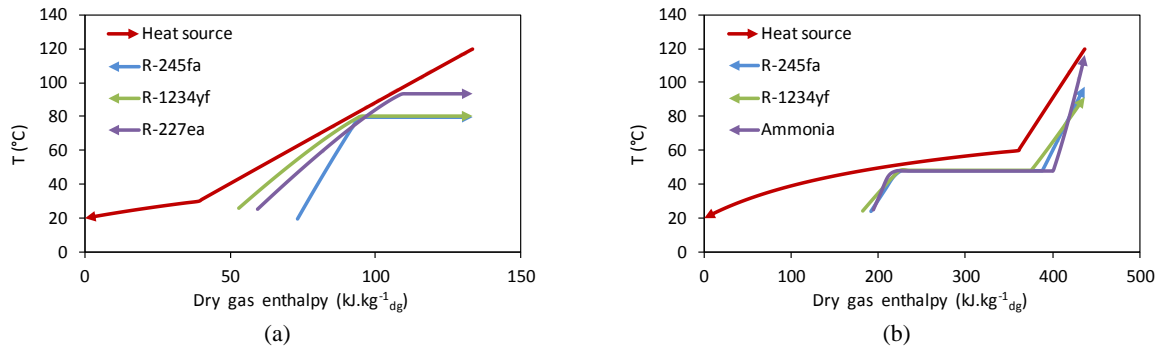


Fig. 1.60: Hot composite curves plotted following the optimization algorithm shown in Fig.C.5a in “Annex C” (ORC with Configuration 3): a) $T_{dp} = 30^{\circ}\text{C}$, b) $T_{dp} = 60^{\circ}\text{C}$

The ORC using R-227ea, even proved as the better solution for low water dew point temperature, cannot be used in practice due to its high GWP value ($3580 \text{ kg}_{\text{CO}_2\text{eq}}/\text{kg}_{\text{wf}}$). Another drawback of the R-227ea is that it presents a high-turbine expansion ratio (Table 1.14) and may require the use of a multi-stage turbine. However, R-1234yf, an environmentally friendly working fluid, is a good compromise between environmental impact and performance for heat source with low water dew point temperature.

For heat source with high water dew point temperature, R-1234yf, R-152a, R-134a, and ammonia show the highest overall efficiencies. The drawback for using R-134a is the non-friendly environmental aspect ($\text{GWP} > 1000$). Compared to other fluids, ammonia presents high-thermal conductivity (Table 1.13), which leads to high effectiveness and low-cost heat exchanger. However, the ammonia is classified as a toxic fluid with a threshold in terms of acceptable level that is very restrictive (0.35 g.m^{-3}) [CLO 10].

By comparing the flammability level between R-1234yf, R-152a, and ammonia, these fluids belong to Class 2 (Table 1.13). However, the new classification of flammability divides the low-flammable fluids in Class 2 into two sub-classes. The sub-class 2L is for fluids whose burning velocity (BV) is less than 10 cm.s^{-1} , which making R-1234yf ($\text{BV}=1.5 \text{ cm.s}^{-1}$) and ammonia ($\text{BV}=7.2 \text{ cm.s}^{-1}$) in this new class 2L while R-152a ($\text{BV}=23 \text{ cm.s}^{-1}$) is not included in class 2L and its flammability is intermediate between hydrocarbons and substances with ($\text{BV} < 10 \text{ cm.s}^{-1}$). Also the ignition energy (MIE) of R-1234yf (MIE = 5000 mJ) is very high compared to R-152a (MIE = 0.38 mJ) and ammonia (MIE = 100 mJ), which means that R-1234yf presents a great difficulty in ignition [CLO 10].

In conclusion, respecting all the listed criteria for the working fluid selection, R-1234yf could be a candidate working fluid for the entire range of water dew point temperature. The use of R-1234yf requires taking into account safety issues because it is a moderately flammable fluid. Despite its relatively higher flammability compared to R-1234yf, R-152a could be a candidate working fluid at high water dew point temperature and for high auxiliary consumptions (e.g. ORC with Configuration 3). Finally, R-245fa could be selected as a non-flammable fluid since it presents a compromise between net power and availability with a restrictive implementation due to its relatively high GWP ($1030 \text{ kg}_{\text{CO}_2\text{eq}}.\text{kg}^{-1}_{\text{wf}}$).

1.9.6 Binary blends as working fluid

As stated previously, the use of blends as working fluids in ORC has been proposed by many authors ([ANG 98], [HEB 12]) just for the aim to reduce the thermal irreversibility in the heat introduction and rejection processes. For the present application ($T \sim 120^\circ\text{C}$), the use of blends will be interesting since the temperature difference between heat source/sink is around 100 K.

1.9.6.1 Binary blends for simple ORC with indirect-contact condensation

In order to determine a promising blend, a series of binary blends has been tested. Results show that binary blends whose R-1234yf is one of the components are the most promising for the present application ($T_{\text{in}} \sim 120^\circ\text{C}$) and will be presented. The second component of the binary blend has been selected with the aim to increase the critical temperature of R-1234yf by approaching the latter to the inlet heat-source temperature on one side and to generate the necessary glide to minimize the auxiliary consumptions and the exergy losses in the evaporator and the condenser on the other side. Note that by increasing the blend critical temperature with R-1234yf, the cycle efficiency will increase leading to an increase in the overall efficiency.

In case of using a binary blend, the position of the pinch points must be calculated carefully in the evaporator and the condenser due to the temperature glide between hot and cold-stream sides. The pinch point is determined by dividing the composite curve into many intervals (100 intervals in our calculations) and by proceeding by trial and error procedure.

The net power using an R-1234yf/R-245fa blend depending on mole fraction is shown in Fig. 1.61 by optimizing the ORC parameters (condensation pressure, evaporator superheat and evaporation temperature) with respect to the net power. Fig. 1.61 shows that a local maximal exists for a molar fraction of R-1234yf around 50%.

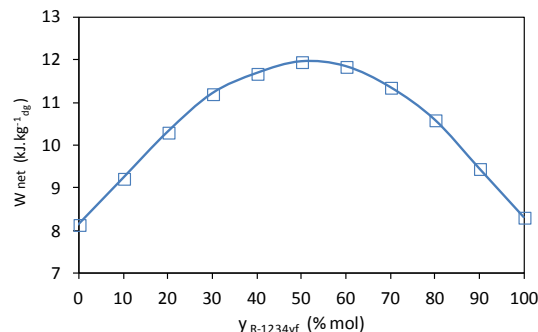


Fig. 1.61: Evolution of the net power as a function of the R-1234yf molar fraction using an R-1234yf/R-245fa blend (ORC with Configuration 3, $T_{\text{dp}} = 60^\circ\text{C}$)

Table 1.16 and Table 1.17 list the most promising binary blends at their optimized molar fractions, which lead to maximal net power for water dew point temperatures of 30°C and 60°C respectively. Values listed in Table 1.16 and Table 1.17 are calculated following the optimization algorithm given in Fig.C.5b in “Annex C”. Using a R-1234yf/R-245fa blend with a mole fraction of 80.4% R-1234yf (resp. 51.1% R-1234yf) leads to an increase in the net power by 5.4% (resp. 45.6%) for a water dew point temperature of 30°C (resp. 60°C).

Among the hydrocarbons blends with R-1234yf, pentane, isopentane, and neopentane show a good agreement compared to others hydrocarbons (butane, isobutane, hexane, and isohexane) at $T_{\text{dp}} = 60^\circ\text{C}$, although the flammability remains the main drawback of using such blends.

Further, Table 1.16 shows that at low-water dew-point temperature ($T_{dp} = 30^{\circ}\text{C}$), small temperature glides in the evaporator and the condenser are required whereas at high-water dew-point temperature ($T_{dp} = 60^{\circ}\text{C}$), large temperature glides in the evaporator and the condenser are required (Table 1.17). In fact, the auxiliary consumptions are mainly due to the cold-water source in the condenser (cooling tower). Temperature glides in the condenser will increase the cold-water temperature at the condenser outlet, and thus decreasing the cold-water mass flow rate and therefore reducing the auxiliary consumptions. Thus, as the cold-water mass flow rate increases, more temperature glide is needed in the condenser and vice versa. At high-water dew-point temperature ($T_{dp} = 60^{\circ}\text{C}$), the mass of working fluid and cold water in the system will be relatively high when water vapor condensation occurs (refer to Fig. 1.58), therefore, a large temperature glide in the condenser is needed.

Table 1.16: Binary blends for ORC with Configuration 3 ($T_{dp} = 30^{\circ}\text{C}$)

Component 1 (C1)	Component 2 (C2)	Optimal composition (% mol)	Glide evap. (K)	Glide cond. (K)	W_{net} (kJ.kg^{-1}_{dg})	$(\Delta W/W)^*$ (%)
R-1234yf	R-365mfc	96.5/3.5	2.6	6.1	5.89	6.20
R-1234yf	R-245fa	80.4/19.6	2.1	6.1	5.85	5.39
R-1234yf	Butane	89.9/10.1	1.4	3.2	5.68	2.42
R-1234yf	Isobutane	88.2/11.8	0.7	1.8	5.61	1.08
R-1234yf	Pentane	97.3/2.7	1.9	4.9	5.88	5.93
R-1234yf	Isopentane	96.3/3.7	1.6	3.9	5.86	5.66
R-1234yf	Neopentane	79.2/20.8	3.8	6.6	5.85	5.39
R-1234yf	Hexane	97.8/2.2	2.1	6.4	5.86	5.66
R-1234yf	Isohexane	97.4/2.6	3.1	8.0	5.89	6.20

* $(\Delta W/W)$: Relative variation of the net power compared to R-1234yf

Table 1.17: Binary blends for ORC with Configuration 3 ($T_{dp} = 60^{\circ}\text{C}$)

Component 1 (C1)	Component 2 (C2)	Optimal composition (% mol)	Glide evap. (K)	Glide cond. (K)	W_{net} (kJ.kg^{-1}_{dg})	$(\Delta W/W)^*$ (%)
R-1234yf	R-365mfc	85.4/14.6	15.7	19.6	11.89	43.04
R-1234yf	R-245fa	51.1/48.9	13.2	16.8	12.10	45.57
R-1234yf	Butane	52.1/47.9	6.5	7.9	11.26	35.44
R-1234yf	Isobutane	52.4/47.6	4.6	6.6	10.19	22.66
R-1234yf	Pentane	84.4/16.6	17.6	20.5	12.20	46.84
R-1234yf	Isopentane	79.2/20.8	16.4	18.8	12.31	48.10
R-1234yf	Neopentane	54.0/46.0	12.6	14.4	12.36	48.73
R-1234yf	Hexane	97.2/2.8	9.3	12.9	10.36	24.68
R-1234yf	Isohexane	91.0/9.0	19.4	23.5	11.52	38.61

* $(\Delta W/W)$: Relative variation of the net power compared to R-1234yf

For ORC with Configuration 2, the auxiliary consumptions are less significant compared to ORC with Configuration 3; therefore, a little glide in the evaporator and the condenser will be sufficient (Table 1.18).

Table 1.18: Binary blends for ORC with Configuration 2

T_{dp}	C1	C2	Optimal composition (% mol)	Glide evap. (K)	Glide cond. (K)	W_{net} (kJ.kg^{-1}_{dg})	$(\Delta W/W)^*$ (%)
$T_{dp} = 30^{\circ}\text{C}$	R-1234yf	R245fa	89.6/10.4	1.2	2.7	6.8	1.7
$T_{dp} = 60^{\circ}\text{C}$	R-1234yf	R-245fa	68.4/31.6	8.6	10.9	13.5	19.5

* $(\Delta W/W)$: Relative variation of the net power compared to R-1234yf

Further, results show that, for ORC with Configuration 1, the use of blends does not improve the net power. Thus, without taken into account the auxiliary consumptions (i.e. ORC with Configuration 1), the exergy benefits in the evaporator and in the condenser is overcompensated by the decrease in the turbine power because higher temperature glide occurs generally in the condenser compared to the evaporator.

Fig. 1.62, Fig. 1.63, and Fig. 1.64 show, the hot and cold composite curves using R-1234yf with ORC with Configuration 3, an optimized blend fraction between R-1234yf and R-245fa with ORC with Configurations 2 and 3 respectively. These figures are plotted following the optimization algorithms given in Fig.C.5a and Fig.C.5b in “Annex C”. For a water dew point temperature of 60°C, Fig. 1.64.b shows that the cold composite curves are almost parallel, and similar case for the hot composite curve below water dew point temperature is shown. A comparison between Fig. 1.63.b and Fig. 1.64.b shows that as the glide in the condenser increases, the cold-water temperature at the condenser outlet increases.

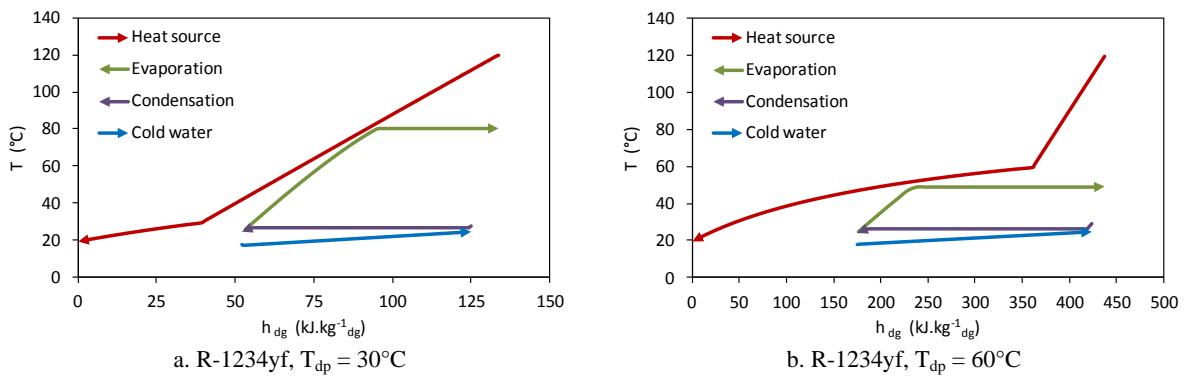


Fig. 1.62: Composites curves for R-1234yf (ORC with Configuration 3)

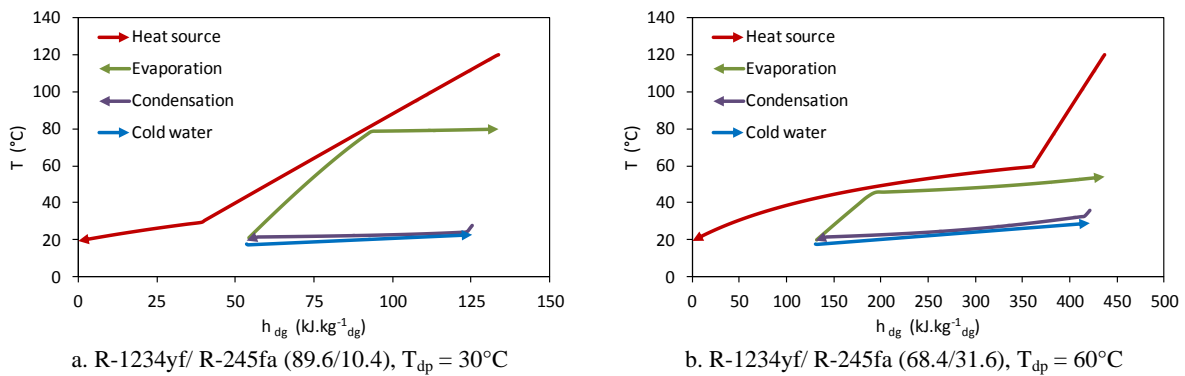


Fig. 1.63: Composites curves for R-1234yf/ R-245fa (ORC with Configuration 2)

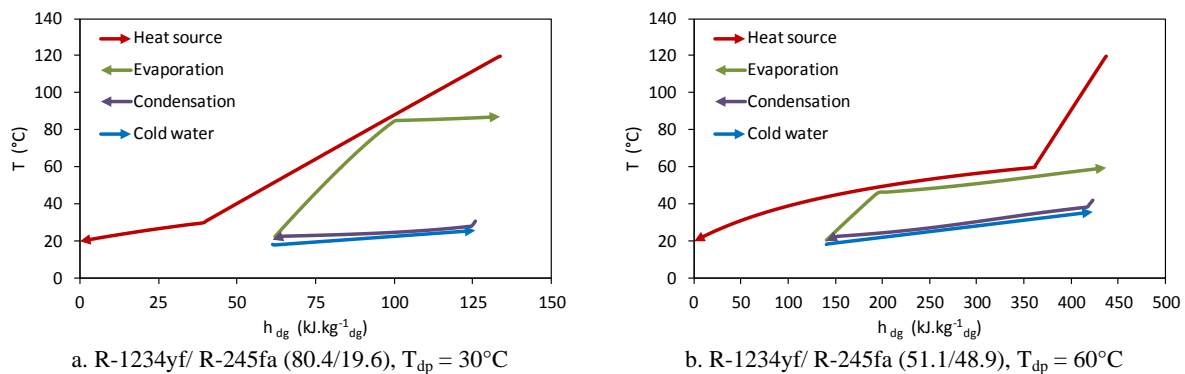


Fig. 1.64: Composites curves for R-1234yf/ R-245fa (ORC with Configuration 3)

Fig. 1.65 shows the net power evolution for a wide range of the evaporation pressures for R-245fa, R-1234yf, and a blend between R-1234yf and R-245fa at its optimized molar fraction. The condensation pressure and evaporator superheat are optimized with respect to the net power. Compared to R-1234yf, the corresponding binary blend between R-1234yf and R-245fa at its optimized molar fraction reduces the auxiliary consumptions by 5.4% (resp. 45.6%) for a water dew point temperature of 30°C (resp. 60°C) at the corresponding evaporation pressure leading to the maximal net power (ORC with Configuration 3).

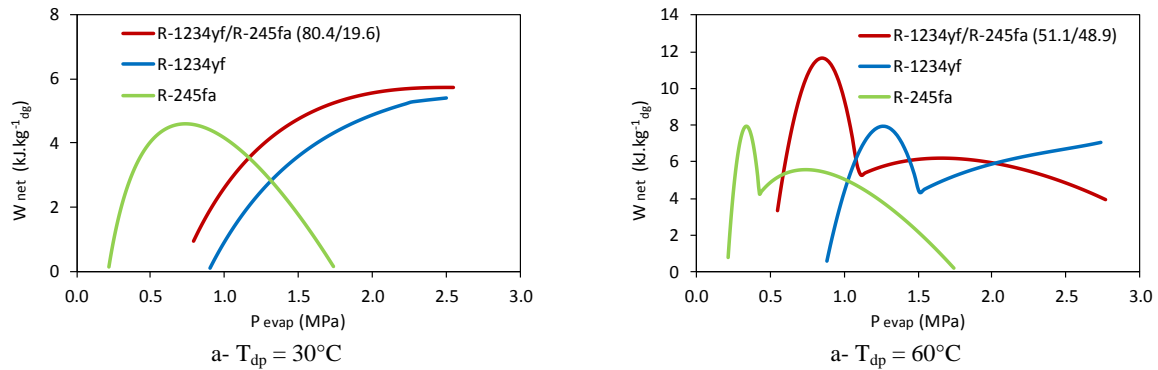


Fig. 1.65: Evolution of the net power for a wide range of evaporation pressure for ORC with Configuration 3 (R-1234yf, R-245fa and a R-1234yf/R-245fa blend at its optimized molar fraction)

1.9.6.2 Binary blends for simple ORC with direct-contact condensation

In the direct-contact condensation process, the auxiliary consumptions play also a significant role especially for water temperature at the evaporator inlet around to the wet bulb temperature where the working mass flow rate is relatively high in the cycle (refer to Fig. 1.41.a).

A simple ORC layout with direct-contact condensation taking into account the auxiliary consumptions is shown in Fig. 1.66. Parameters of the condensing unit are the same as those indicated in Table 1.7. The pressure drop in the hot-water circuit is set to 50 KPa. Additional pressure drop values at the flue-gas side for the different ORC configurations are shown in Table 1.19.

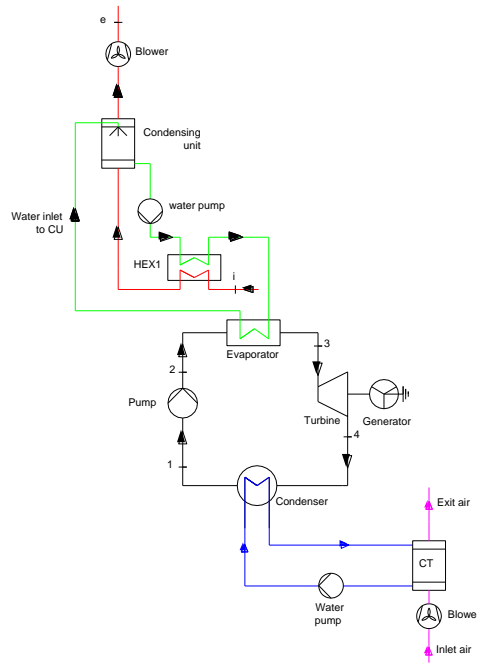


Fig. 1.66: Simple ORC lay-out with direct-contact condensation taking into account the auxiliary consumptions

Table 1.19: Pressure drop values at the flue-gas side in “CU” and “HEX1” for ORC with Configurations 2 and 3

Parameters	η_{blower} (%)	DP _{flue gas in CU} (Pa)	DP _{flue gas in HEX1} (Pa)
ORC with Configuration 2	80	150	150
ORC with Configuration 3	60	300	300

The effects of auxiliary consumptions on the net power are shown in Fig. 1.67 for a wide range of water temperatures at the evaporator inlet and in Table 1.20 at the maximal net power values. Fig. 1.67 is plotted following the optimization algorithms given in Fig.C.6a and Fig.C.7a in “Annex C”. Net power losses around 24% (resp. 55%) is expected for ORC with Configuration 2 (resp. ORC with Configuration 3) for a water temperature at the evaporator inlet around the entering wet bulb temperature.

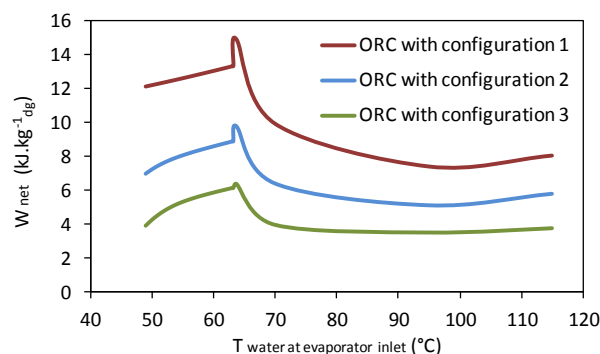


Fig. 1.67: Effect of auxiliary consumptions on direct-contact and hybrid heat-recovery processes (R-245fa, $T_{\text{dp}} = 60^\circ\text{C}$)

Table 1.20: Effect of auxiliary consumptions on direct-contact and hybrid heat-recovery processes
(R-245fa, $T_{dp} = 60^{\circ}\text{C}$)

$w_{net\ max}$ ($\text{kJ.kg}^{-1}\text{.dg}$)	Direct-contact process	Hybrid-heat-recovery process
ORC with Configuration 1	13.3 (100%)	14.9 (100%)
ORC with Configuration 2	8.9 (76%)	9.8 (65%)
ORC with Configuration 3	6.1 (45%)	6.3 (42%)

Similar to ORC with indirect evaporation process, it is interesting to use a binary blend in order to reduce the auxiliary consumptions for ORC with Configurations 2 and 3. Results show that the most promising binary blends for the hot-water temperature range (50°C to 115°C) are R-1234yf/R-245fa, R-1234yf/R-365mfc, and R-1234yf/R-32.

Fig. 1.68 shows the evolution of the net power as a function of the water temperature at the evaporator inlet for R-245fa, R-1234yf, and the selected binary blends. The binary-blend fractions are optimized for a 5-K step of water temperature at the evaporator inlet and are shown in Fig. 1.69. Note that the curves in Fig. 1.68 and Fig. 1.69 are plotted following the optimization algorithms given in Fig.C.6 and C.7 in “Annex C”. As shown in Fig. 1.68, the net power improvement by using a binary blend increases as the water temperature at the evaporator inlet decreases (starting from 115°C), and reaches a maximal value around the entering wet bulb temperature.

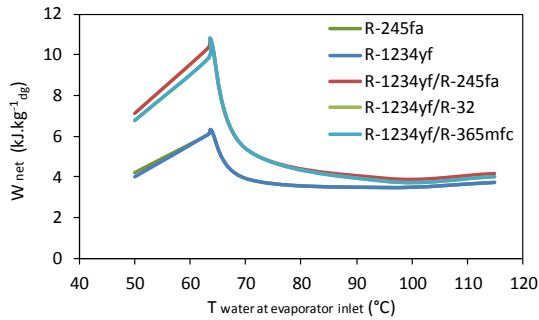


Fig. 1.68: Effects of the selected binary blends on the net power (ORC with Configuration 3)

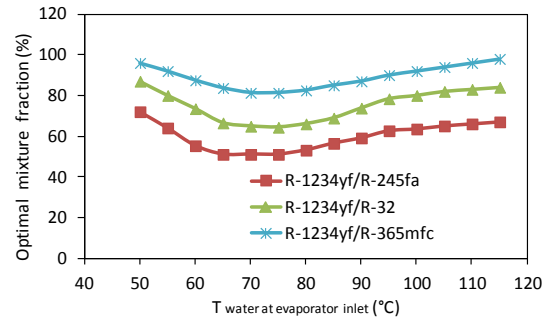


Fig. 1.69: Evolution of the optimal blend fractions (%R-1234yf, %v) (ORC with Configuration 3)

Table 1.21 shows the improvement of the maximal value of net power induced by using the corresponding binary blends for ORC with Configuration 3. Compared to R-1234yf (pure working fluid), the net power improvement could reach 60% in the direct-contact process and 70% in the hybrid heat-recovery process. R-1234yf/R-245fa blend is promising compared to other blends since it is characterized by low-flammability level and it gives the highest net power.

Table 1.21: Effect of binary blends on the improvement of the maximal net power for direct-contact and hybrid heat-recovery processes (ORC with Configuration 3, $T_{dp} = 60^{\circ}\text{C}$)

	Direct-contact process		Hybrid heat-recovery process	
	$w_{net\ max}$ ($\text{kJ.kg}^{-1}\text{.dg}$)	$(\Delta W/W)^*$ (%)	$w_{net\ max}$ ($\text{kJ.kg}^{-1}\text{.dg}$)	$(\Delta W/W)^*$ (%)
R-1234yf	6.1	-	6.3	-
R-1234yf/R-245fa	9.8	60.7	10.7	69.8
R-1234yf/R-32	9.5	55.7	10.6	68.3
R-1234yf/R-365mfc	9.3	52.5	10.7	69.1

* $(\Delta W/W)$: Relative variation of net power compared to R-1234yf

1.9.6.3 Enhanced two-stage ORC with binary blends

Similarly to simple ORC, the use of a blend working fluid will be of importance in case of two-stage ORC. A blend between R-1234yf and R-245fa is used to analyze the cycle operation. Note that when using a blend in the two-stage ORC containing a flash separator, the blend-component separation (distillation process) should be taken into account. Additional pressure drop values at the flue-gas side for the different ORC configurations are shown in Table 1.22.

Table 1.22: Pressure drop values at the flue-gas side in Evaporators 1 and 2 for ORC with Configurations 2 and 3

Parameters	η_{blower} (%)	DP _{flue gas in evap.1} (Pa)	DP _{flue gas in evap. 2} (Pa)
ORC with Configuration 2	80	150	150
ORC with Configuration 3	60	300	300

To illustrate the temperature profiles and thermodynamic irreversibility in the ORC system, Fig. 1.70 and Fig. 1.71 show the “T-h” diagrams for the enhanced two-stage ORC with R-1234yf and R-1234yf/R-245fa as working fluids for a water dew point temperatures of 30°C and 60°C respectively. These figures are plotted following the optimization algorithms given in Fig.C.8a and Fig.C.8b in “Annex C”. In consequence of glide matching in the condenser, the blend leads to lower exergy destruction rate.

The composite curves of the two-stage ORC are sketched in Fig. 1.70 and Fig. 1.71 for R-1234yf and R-1234yf/R-245fa blend at its optimized mole fraction for a water dew point temperature of 30°C and 60°C respectively (ORC with Configuration 3).

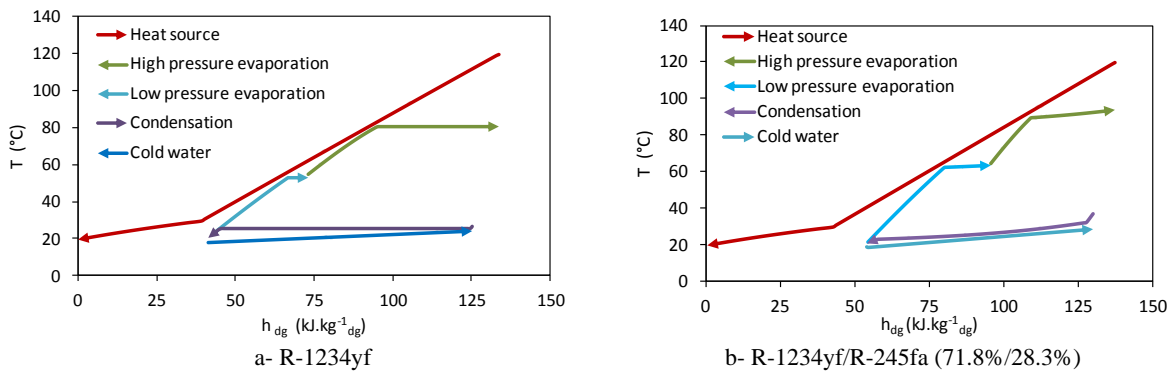


Fig. 1.70: Hot and cold composite curves for the two-stage ORC ($T_{\text{dp}} = 30^\circ\text{C}$, ORC with Configuration 3)

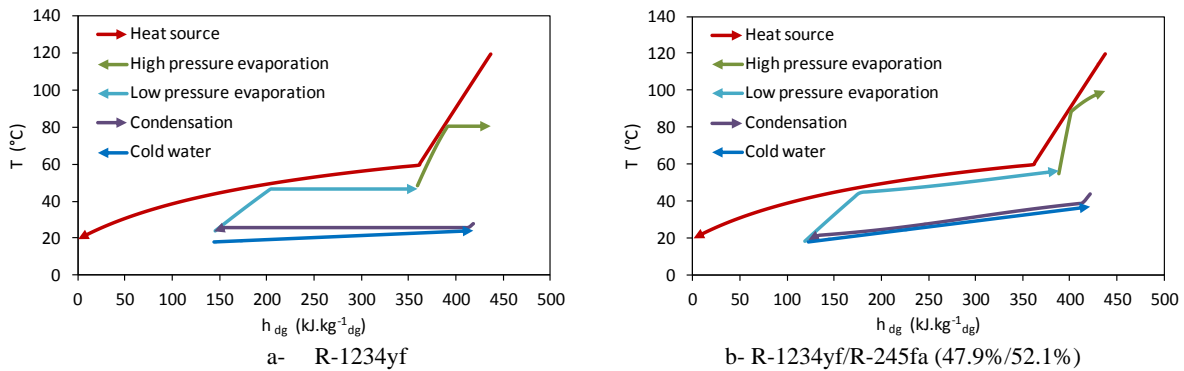


Fig. 1.71: Hot and cold composite curves for the two-stage ORC ($T_{\text{dp}} = 60^\circ\text{C}$, ORC with Configuration 3)

Fig. 1.72 shows the effect of the selected binary blend on the net power (ORC with Configuration 3) compared to R-245fa and R-1234yf over a wide range of evaporation pressures. The improvements provided by the selected binary blend on the net power are clearly visible.

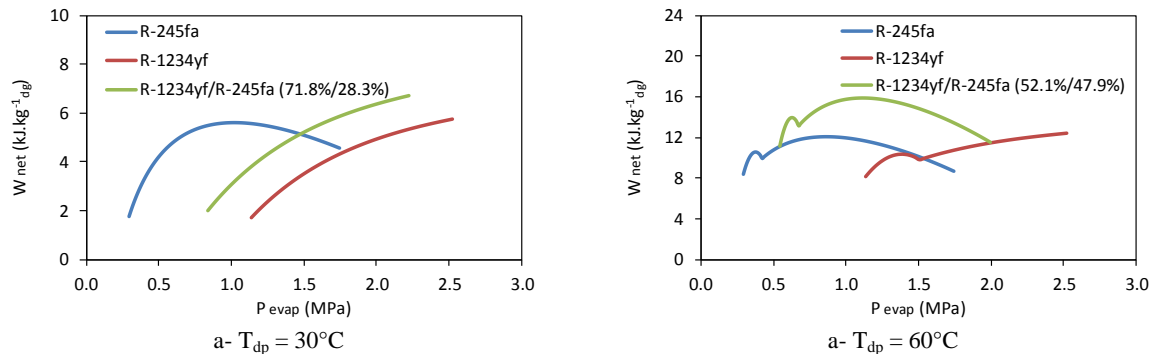


Fig. 1.72: Evolution of the net power for a wide range of evaporation pressure for ORC with Configuration 3 (R-1234yf, R-245fa and a blend between R-1234yf and R-245fa at its optimized mole fraction)

Table 1.23 the effect of the selected binary blend on the maximal net powers values (ORC with Configuration 3). The used binary blend could improve the net power by 17.2 % for a water dew point temperature of 30°C and by 32.4% for a water dew point temperature of 60°C.

Table 1.23: Binary blend for enhanced two-stage ORC with Configuration 3

T_{dp}	C1	C2	Optimal composition (% mol)	Glide evaporator 1 (K)	Glide evaporator 2 (K)	Glide cond. (K)	W_{net} ($\text{kJ.kg}^{-1}.\text{dg}$)	$(\Delta W/W)^*$ (%)
30°C	R-1234yf	R245fa	71.8/28.3	1.2	4.2	9.3	4.51	17.2
60°C	R-1234yf	R-245fa	47.9/52.1	12.0	11.5	17.2	14.76	32.4

* $(\Delta W/W)$: Relative variation of net power compared to R-1234yf

1.9.7 Effects of auxiliary consumptions on heat recovery modes

This section summarizes the effect of auxiliary consumptions on the different heat recovery modes.

Table 1.24: Effect of auxiliary consumptions on the net power for the different heat-recovery modes

$W_{net\ max}$ ($\text{kJ.kg}^{-1}.\text{dg}$)	ORC configurations	$T_{dp} = 30^\circ\text{C}$			$T_{dp} = 60^\circ\text{C}$		
		R-245fa	R-1234yf	R-1234yf/R-245fa	R-245fa	R-1234yf	R-1234yf/R-245fa
Indirect contact condensation	1	6.7	8.1	-	16.1	16.4	-
	2	5.5	6.7	6.8	11.2	11.3	13.5
	3	4.6	5.5	5.9	8.1	8.3	12.1
Direct contact condensation	1	-	-	-	13.3	13.4	-
	2	-	-	-	8.9	8.9	10.2
	3	-	-	-	6.1	6.1	9.8
Hybrid heat recovery	1	-	-	-	14.9	15.1	-
	2	-	-	-	9.8	9.9	11.8
	3	-	-	-	6.3	6.3	11.0

Table 1.24 shows a comparison of the net power between the heat recovery modes for the three ORC configurations using pure working fluids (R-1234yf, R-245fa) and a blend between R-1234yf/R-245fa at its optimized molar fraction. Values of the net power listed in Table 1.24 are calculated following the optimization algorithms given in Fig.C.6, Fig.C.7, and Fig.C.8 in “Annex C”. In particular, Table 1.24 shows the advantage for using the R-1234yf/R-245fa blend as working fluid for ORC with

Configuration 3, especially at high-water dew-point temperature (60°C). In this case, the net power rises from 8.1 to 12.1 kJ.kg⁻¹_{dg} (resp. 6.1 to 9.8 kJ.kg⁻¹_{dg}) for simple ORC with indirect-contact condensation (resp. direct-contact condensation).

Table 1.25 shows the percentage ratio of the net power for a given heat recovery mode calculated with respect to the net power obtained for ORC with Configuration 1 using R-1234yf as working fluid. Table 1.25 shows that, at high water dew point temperature (60°C), the net power is reduced by more than its half for the ORC with Configuration 3 for the different heat recovery modes, while it is reduced by about 27% when using a blend between R-1234yf and R-245fa at its optimized mole fraction.

Table 1.25: Percentage ratio of net power for ORC with Configurations 2 and 3 with respect to that obtained for ORC with Configuration 1 using R-1234yf

W _{net max} (kJ.kg ⁻¹ _{dg})	ORC configurations	T _{dp} = 30°C		T _{dp} = 60°C	
		R-1234yf	R-1234yf/ R-245fa	R-1234yf	R-1234yf/ R-245fa
Indirect contact condensation	1	100 %	-	100 %	-
	2	82.7 %	84.0 %	68.9 %	82.3 %
	3	67.9 %	72.8 %	50.6 %	73.8 %
Direct contact condensation	1	-	-	100 %	-
	2	-	-	66.4 %	76.1 %
	3	-	-	45.5 %	73.1 %
Hybrid heat recovery	1	-	-	100 %	-
	2	-	-	65.6 %	78.1 %
	3	-	-	41.7 %	71.9 %

1.10 Trans-critical Organic Rankine Cycle

The ORC presented in Fig. 1.20 is a "classical" Rankine cycle in the sense that the working fluid remains in liquid or vapor state. However, another type of ORC cycle can be considered based on the same scheme. When the heat transfer between flue gases and the working fluid in the evaporator is at a pressure higher than the working fluid critical pressure, the cycle is called "trans-critical cycle". This means subcritical on the low-pressure side and supercritical on the high-pressure side. Fig. 1.73 shows the supercritical state (or hypercritical) in the state diagram "P-T" (pressure-temperature), under certain conditions of temperature and pressure. Fig. 1.74 shows the T-s diagram of the trans-critical cycle where there is no phase change from liquid to vapor at constant temperature in the evaporator.

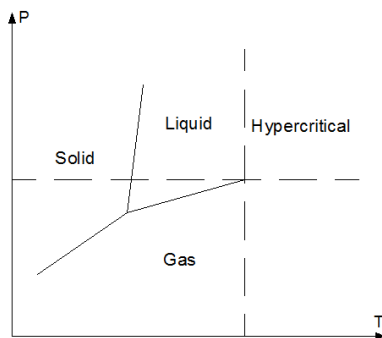


Fig. 1.73: State diagram (P - T).

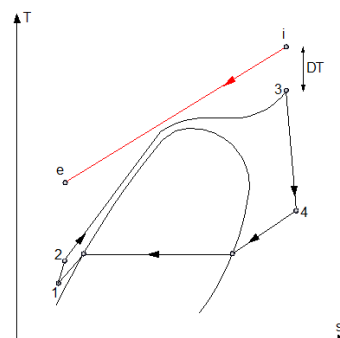


Fig. 1.74: T-s diagram for trans-critical ORC.

An ORC cycle operating with a working fluid can operate in trans-critical mode if the corresponding working fluid presents a critical temperature lower than the inlet heat-source temperature. Among the listed working fluids in Table 1.13, ORC using R-134a, R-1234yf,

R-227ea, and R-32 could operate in trans-critical mode, and thus these working fluids will be studied and analyzed (except R-227ea due to its high GWP). For the calculation, the ORC parameters are the same as those indicated in Table 1.10. Efficiencies of the turbine and the ORC pump are the same as those indicated in Table 1.5.

1.10.1 Trans-critical ORC with R-134a, R-1234yf, R-1234ze, and R-32 as working fluids

Fig. 1.75 shows the evolution of the net power as a function of the evaporation pressure in the subcritical and the trans-critical ORC operation modes using R-1234yf as working fluid. The supercritical pressure is varied between the critical pressure and a maximum value, which is to be limited by a vapor quality slightly higher than one at the turbine exit. The temperature difference between the inlet flue gas and the exit working fluid from evaporator (“DT” as shown in Fig. 1.74) can be varied and optimized with respect to the net power. Fig. 1.75 shows that for R-1234yf, the trans-critical ORC reduces the net power compared to subcritical ORC.

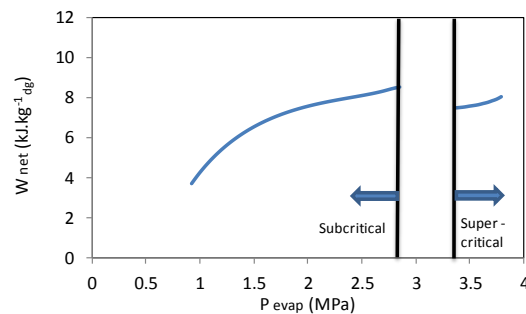


Fig. 1.75: Comparison between the subcritical and the trans-critical ORC (ORC with Configuration 1, DT = 15 K, R-1234yf, $T_{dp} = 30^{\circ}\text{C}$)

Table 1.26 shows a comparison for the net power between the subcritical and the trans-critical ORC. To make sense for the comparison, the “2.5 MPa” set as limit for the evaporator pressure in the subcritical case will be disregarded. Values of the net power listed in Table 1.26 are calculated following the optimization algorithms given in Fig.C.5a and Fig.C.9 in “Annex C” for the subcritical and trans-critical states respectively. Table 1.26 shows that, compared to subcritical ORC, the net power undergoes a decrease for the four considered fluids in the trans-critical zone.

Table 1.26: Comparison of the maximal net power between the subcritical and the trans-critical ORC (ORC with Configuration 1, $T_{dp} = 30^{\circ}\text{C}$)

W_{net} (kJ.kg^{-1}_{dg})	Subcritical ORC	Trans-critical ORC	$(\Delta W/W)^*$ (%)
R-1234yf	8.1	7.5	7.93
R-1234ze	7.2	6.6	8.97
R-134a	7.3	6.2	15.48
R-32	4.2	4.1	2.48

* $(\Delta W/W)$: Relative variation of net power between the subcritical and the trans-critical ORC

1.10.2 Trans-critical ORC with carbon dioxide as working fluid

Carbon dioxide (R-744) is a non-flammable and non-toxic refrigerant with no-ozone depletion potential and a global warming potential of one (which is the GWP reference for all other greenhouse gases). The critical pressure and temperature are “7.38 MPa” and “31°C”. The temperature and pressure for the triple point of CO_2 are “-56.6°C” and “520 kPa”, respectively, and the saturation pressure at “0°C” is “3.5 MPa”. Due to its lower critical temperature, the heat transfer between CO_2 and flue gases will occur at a pressure higher than the critical pressure.

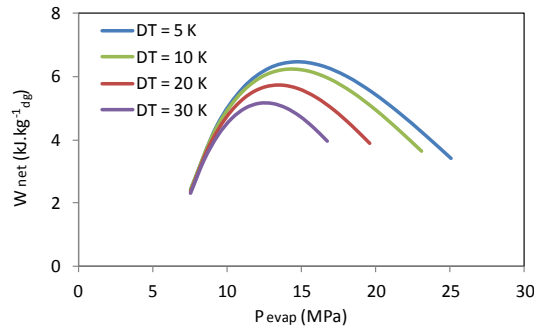


Fig. 1.76: Evolution of the net power as a function of the evaporation pressure for various DTs (CO_2 , ORC with Configuration 1, $T_{dp} = 30^\circ\text{C}$)

Fig. 1.76 shows evolution of the net power as a function of the evaporation pressure for the trans-critical CO_2 cycle. In particular, it reveals the presence of an optimum value of the net power for each DT. As DT decreases, the net power increases. However, the net power is lower than that obtained in subcritical cycle using R-1234yf as working fluid (refer to Fig. 1.75).

As conclusion, the trans-critical ORC operating with CO_2 as working fluid is not recommended for the present application, especially when operating at high-supercritical pressure (15 MPa).

Finally, it should be noted that, compared to other fluids, the ORC working with carbon dioxide as working fluid presents the lower exergy losses in the evaporator. This can be shown clearly in Fig. 1.77 where the hot composite curves are sketched for carbon dioxide in trans-critical mode ($\text{DT} = 5 \text{ K}$) and for R-1234yf in both subcritical and trans-critical modes. Curves plotted in Fig. 1.77 are calculated according to the optimization algorithms given, respectively, in Fig.C.5a and Fig.C.9 in “Annex C” for subcritical state and trans-critical state.

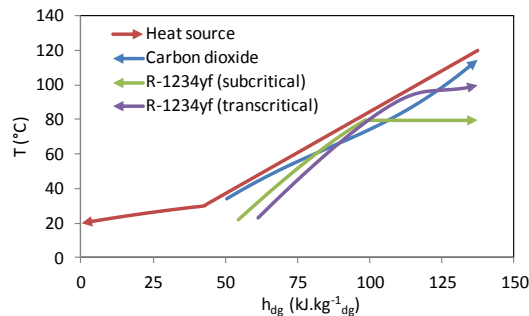


Fig. 1.77: Hot composite curves for carbon dioxide and R-1234yf (ORC with Configuration 1, $T_{dp} = 30^\circ\text{C}$)

1.11 Conclusions

Recovery and reuse of waste heat is an emission-free substitute for costly purchased fuels or electricity. Most unrecovered waste heat (more than 50%) is at low temperatures ($\sim 120^\circ\text{C}$). Due to lack of efficient recovery methods, low-grade waste heat has generally been discarded in industry. While low-temperature waste heat has less thermal and economic value than high-temperature heat, it is ubiquitous and available in large quantities and it should not be neglected in pursuing researches and development opportunities for waste heat recovery.

This chapter details heat recovery from low-temperature waste heat in industrial processes for generating electrical power. The well-proven ORC is studied and optimized at this temperature level ($\sim 120^\circ\text{C}$). Depending on the industrial process (flashing, washing, drying ...), the moisture contents in the flue-gas streams may vary resulting in a water vapor dew point temperature ranging between 30 and 70°C .

Based on the analysis presented in this investigation, the following conclusions are drawn:

- While the amount of latent heat in flue gases may look attractive, its recovery is hindered by the low-temperature level at which the recovered latent heat is available.
- In the indirect-contact condensation with direct evaporator, depending on the evaporation temperature, two operating regions can be identified in the evaporator: “sensible heat region” where mostly sensible heat is recovered and “latent heat region” where a great portion of latent heat is recovered. An optimum for the net power can be identified in each region. Water dew point affects very much the net power ratio between the two optima. The indirect-contact condensation is the most favorable heat recovery scheme concerning the net power, provided the acid corrosion problems can be overcome in a cost-effective way.
- Using the indirect-contact condensation with an indirect evaporator could be a solution to remove from the ORC system the dirtiness accompanying flue gases and make easy the replacement of flue-gas heat-exchanger components in case of failure due to corrosion problem accompanying the gas cooling. However, a decrease in the conversion efficiency compared to direct evaporator is expected.
- The direct-contact heat exchanger has received attention because there are no heat-transfer surfaces exposed to corrosion. It may be considered to implement a two-stage system: one humidification stage and one dehumidification stage. The use of the direct-contact heat exchanger makes sense when recovering energy from heat sources with high-moisture contents. The entering wet-bulb temperature determines the operating temperature level throughout the system and limits the circulating water temperature. The maximal net power in the direct-contact system is reached for a final water temperature nearby the entering wet bulb temperature of flue gases.
- The hybrid heat-recovery process leads to a potential increase in the net power compared to the direct-contact condenser, while avoiding surface corrosion problems faced in the indirect-contact process. However, additional heat exchanger could increase system complexity.
- The integration of a two-stage ORC in an attempt to recover heat from both optima (sensible and latent optima) is promising when heat recovery from sensible heat and latent heat is in the same range ($45^\circ\text{C} < T_{\text{dp}} < 55^\circ\text{C}$). The two-stage ORC could lead to potential increase in the net power ranging between 16 and 60% depending on the water dew point temperature.
- Incorporating a flash separator at the exit of low-pressure evaporator in a two-stage ORC is promising at both high ($T_{\text{dp}} > 60^\circ\text{C}$) and low ($T_{\text{dp}} < 40^\circ\text{C}$) water dew point temperatures. Depending on the latter, the current cycle could improve the net power up to 16% compared to the typical two-stage ORC.
- Using a direct-contact water vapor condenser at the low-pressure evaporation stage in a two-stage ORC could be an effective solution to take advantage of both optima (sensible and latent heat optima) by avoiding corrosion problems faced at the low-pressure evaporation stage due to water vapor condensation, thereby recovering the latent heat using a direct-contact condenser. However, significant decrease in the net power is expected especially at high-water dew-point temperatures by using a direct-contact condenser at low-pressure stage instead of an indirect-contact condenser.

- Since the overall efficiency is less than 5%, the auxiliary consumptions must be carefully taken into consideration. They could affect the operating parameters of the cycle (evaporation pressure, condensation pressure, and evaporator superheat).
- The selection of a suitable working fluid depends on the auxiliary consumptions. A method based on thermo-physical, safety, and environmental criteria is developed to identify the most suitable working fluid. Results shows that, at low water dew point temperatures, the working fluids having a relatively low enthalpy of vaporization (e.g. R-1234yf), i.e. the sensible preheating zone exceeds the latent vaporization zone, will be promising. This may reduce the temperature difference with the heat source, thus more heat is recovered, and the heat source can be cooled to a lower temperature. At high water dew point temperature, for relatively high auxiliary consumptions, the evaporator superheat will be an asset for wet fluids (ammonia, R-152a, and R-134a) and the latter may present higher net power compared to R-1234yf.
- The use of binary blends makes sense when taken into account the auxiliary consumptions. As the auxiliary consumptions increase, more glides are needed in the evaporator and the condenser and vice versa. Results show that the binary blends whose R-1234yf represents one of the components are the most promising for the present application ($T \sim 120^{\circ}\text{C}$). A particular importance for the R-1234yf/R-245fa blend is to be set. Concerning the economic aspects, it is interesting to evaluate whether the efficiency increase overcompensates the additional heat-transfer area.
- The trans-critical ORC operating with carbon dioxide as working fluid is not recommended for the present application ($T \sim 120^{\circ}\text{C}$), especially when needed to operate at high-supercritical pressure (15 MPa).

References

- [DUP 09] Dupont, M., Sapora, E., The heat recovery potential in the French industry: opportunities for heat pump systems. ECLEER 2009 Summer study, Act, Innovate, Deliver, Reducing energy demand sustainably.
- [FP7 07] Valorization of low temperature heat, European Community's Seventh Framework Program (FP7/2007-2013) under grant agreement n° 256790 ('LOVE').
- [BCS 08] BCS, Incorporated. Waste heat recovery: Technology and Opportunities in U.S. industry. U.S. department of Energy, March 2008.
- [WEN 13] Weng, R., Bory, D., Berthou, M., A Method to Evaluate the Waste Heat Recovery Potential Across the Industrial Sectors. ECOS 2013: Proceedings of the 26th International Conference on Efficiency, Cost, Optimization, Simulation, and Environmental Impact of Energy Systems; 2013 June 16-19; Guilin, China.
- [BOR 13] Bory, D., Merger, H., Stahl, R., Frank, D., Identification of the waste heat potential in industry, in terms of heat carrier and identification of the optimal usage. European Community's Seventh Framework Program (FP7/2007-2013) under grant agreement n° 256790 ('LOVE').
- [CER 99] CEREN, "Potentiel de récupération de chaleur à partir des effluents industriels", 2011.
- [CEM 99] CEMBUREAU, "Best Available Techniques for the Cement Industry" 1999.
- [BUT 07] Butcher, C., Reddy, B., Second law analysis of a waste heat recovery based power generation system. International Journal of Heat Mass Transfer 2007;50:2355-63.
- [LEM 10] Lemmon E.W., Huber M.L., McLinden M.O., Reference Fluid Thermodynamic and Transport Properties. NIST Standard Reference Database 23, Version 9.0, 2010.
- [LOZ 03] Lozano, M.A., Valero, A., Methodology for calculating exergy in chemical process. The American Society of Mechanical Engineers. Thermodynamic analysis of chemically reactive systems – AES, Vol. 4.
- [LAL 05] Lallemant A., Bilans entropiques et exergétiques. Techniques de l'ingénieur, Be8008, 10 avril 2005.
- [BEC 12] Becquin, G., Freund, F., Comparative Performance of Advanced Power Cycles for Low-Temperature Heat Sources. ECOS 2012: Proceedings of the 25th International Conference on Efficiency, Cost, Optimization, Simulation, and Environmental Impact of Energy Systems; 2012 June 26-29; Perugia, Italy.
- [BOM 10] Bombarda, P., Invernizzi, C., Pietra, C., Heat recovery from diesel engines: A thermodynamic comparison between Kalina and ORC cycles. Applied thermal engineering 2010; 30: 212-219.
- [DAI 09] Dai, Y., Wang, J., Gao, L., Parametric optimization and comparative study of Organic Rankine Cycle (ORC) for low grade waste heat recovery. Energy Conversion and Management 2009;50:576-582.
- [HUN 97] Hung, T.C., Shai, T.Y., Wang, S.K., A review of Organic Rankine Cycles (OECs) for the recovery of low-grade waste heat. Energy, 1997;22(7):661-667.
- [LIU 04] Liu, B.T., Chien, K.H., Wang, C.C., Effect of working fluids on Organic Rankine Cycle for waste heat recovery. Energy 2004;29:1207-17.
- [ROY 10] Roy, JP., Mishra, MK., Misra, A., Parametric optimization and performance analysis of a waste heat recovery system using Organic Rankine Cycle. Energy 2010; 35:5049-5062.
- [ROY 11a] Roy, JP., Mishra, MK., Misra, A., Performance analysis of an Organic Rankine Cycle with superheating under different heat source temperature conditions. Applied Energy 2011a;88:2995-3004.

- [WEI 07] Wei D, Lu X, Lu Z, Gu J., Performance analysis and optimization of organic Rankine cycle (ORC) for waste heat recovery. *Energy conversion and management* 2007;48:1113-1119.
- [ROY 11b] Roy, JP., Mishra, MK., Misra, A., Parametric optimization and performance analysis of a regenerative Organic Rankine Cycle using low-grade waste heat for power generation. *International Journal of Green Energy* 2011b;8:173-96.
- [ROY 12] Roy, JP., Mishra, MK., Misra, A., Parametric optimization and performance analysis of a regenerative Organic Rankine Cycle using R-123 for waste heat recovery. *Energy* 2012;39:227-235.
- [SRI 10] Srinivasan, K., Mago, P., Krishnan, S., Analysis of exhaust waste heat recovery from a dual fuel low temperature combustion engine using an Organic Rankine Cycle. *Energy* 2010;35(6):2387-99.
- [KOS 09] Kosmadakis, G., Manolakos, D., Kyritsis, S., Papadakis, G., Comparative thermodynamic study of refrigerants to select the best for use in high-temperature stage of a two-stage Organic Rankine Cycle for RO desalination. *Desalination* 2009;243:74-94.
- [ZYH 10] Zyhowski, G.J., Brown, A.P., Achaichia, A., HFC-245fa Working Fluid in Organic Rankine Cycle – A Safe and Economic Way to Generate Electricity from Waste Heat. *ECOS 2010: Proceedings of the 23th International Conference on Efficiency, Cost, Optimization, Simulation, and Environmental Impact of Energy Systems*; 2010 June 14-17; Lausanne, Switzerland.
- [BOR 11] Borrnert, T., ABB Paper “Holcim Untervaz plant improves energy-efficiency by 20% by using ABB low-temperature ORC technology,” *Global Cement Magazine*, June 2011.
- [ASH 08] Ashrae Systems and Equipment, *Evaporative Cooling Applications*. American Society of Heating, Refrigeration and Air-Conditioning Engineers. 2008, Chapter 50.
- [THO 69] Thorn W.F. *Waste heat recovery from stacks using direct contact condensing heat exchange*. Rocket Research Company. Redmond, Washington; 1969.
- [LIU 04] Liu B.T., Chien K.H., Wang C.C., Effect of working fluids on organic Rankine cycle for waste heat recovery. *Energy* 2004;29:1207-1217.
- [MAD 07] Madhawa H., Golubovic M., Worek W.M., Ikegami Y., Optimum design criteria for an Organic Rankine Cycle using low-temperature geothermal heat sources. *Energy* 2007; 32:1698–706.
- [HUN 10] Hung T.C., Wang S.K., Kuo C.H., Pei B.S., Tsai K.F., A study of organic working fluids on system efficiency of an ORC using low-grade energy sources. *Energy* 2010;35:1403-1411.
- [ANG 98] Angelino G., Colonna di Paliano P., Multicomponent working fluids for Organic Rankine Cycles (ORCs). *Energy* 1998;23:449-463.
- [HEB 12] Heberle F., Preibinger M., Bruggemann D., Zeotropic mixtures as working fluids in Organic Rankine Cycles for low-enthalpy geothermal resources. *Renewable Energy*, 2012;37:364-370.
- [BLI 87] Bliem C., Zeotropic mixtures of halocarbons as working fluids in binary geothermal power generation cycles. *Intersociety energy conversion engineering conference*; 1987; Portland (USA).
- [UEM 84] Uematsu, M., Watanabe, K., Kagawa, N., Role of thermophysical properties study of the binary refrigerant mixtures for the ORC technology. *Proceedings of the International CDI-Seminar held in Zurich*, pp. 99-111, 1984.

- [AOU 08] Aoun, B., Micro combined heat and power operating on renewable energy for residential building. Thesis, Centre of Energy and Processes (CEP), Ecole des Mines de Paris, 2008.
- [PAP 10] Papadopoulos, A.I., Stijepovic, M., Linke, P., On the systematic design and selection of optimal working fluids for Organic Rankine Cycles. Applied thermal Engineering, 2010;30:760-769.
- [CLO 10] Clodic, D., Low GWP refrigerants and flammability classification. 2010 International Symposium on Next-generation Air Conditioning and Refrigeration Technology, 17-19 February 2010, Tokyo, Japan.

Chapter 2: Indirect contact-condensation heat recovery

2.1 Introduction

Methods (Components) for low-temperature waste heat recovery to generate mechanical power include transferring heat from flue gases (hot gases or fluids) to the working fluid of the energy conversion system via a heat exchanger. One of the basic concepts for heat extraction is the indirect contact water-vapor condensation, which is a fin-and-tube heat exchanger featuring a heat exchange between flue gases and the working fluid of the energy conversion system.

The heat exchanger is the critical component in conversion cycles. At low temperature ($\sim 120^\circ\text{C}$), the heat exchanger presents high-exergy losses, which limit their economical deployment. One of the main challenges is the combination of a very low driving temperature difference for heat extraction with a very low-pressure drop for the gas stream. Thus, it is not acceptable to increase the pressure drop at the gas side because only a few mbar of pressure drop could lead to an increase in blower power demand in the same range of the cycle generation power and the related losses in cycle efficiency would be dramatic.

Furthermore, low-temperature gas steams may have high-moisture content. There would be significant benefits to cooling flue gases to temperatures below the water vapor dew point. However, the presence of acids is of particular concern for heat exchangers recovering low-temperature flue gases, because of the corrosion potential of heat-exchanger tubes. Flue gases may contain sulfur dioxide (SO_2), sulfur trioxide (SO_3), and possibly hydrochloric (HCl) and nitric acids (NO_x) due to fossil-fuel combustion processes. These oxides combine with the moisture in the flue gases to form sulfuric (H_2SO_4), sulfurous (H_2SO_3), nitric (H_2NO_3), and perhaps hydrochloric (HCl) acid vapors. When in contact with a surface below the acid dew point, condensation takes place. The exact dew point depends on the concentration of these gaseous species. Thus, surface cooler than saturation temperature is likely locations for dew-point corrosion.

This chapter details the heat recovery from low-temperature heat sources using a fin-and-tube heat exchanger. It consists mainly of three parts. Firstly, the chemistry of the condensing flue gases is discussed. A theoretical prediction for acid dew-point calculations is presented and the typical corrosion zones in the heat exchanger are identified. Secondly, a general method to design the fin-and-tube heat exchanger adapted to low-temperature heat sources is presented. The design criteria are based on the thermal performance improvement of the fin-and-tube heat exchanger by choosing appropriate geometrical configurations. Finally, advanced coating materials that can minimize chemical attack by cooling exhaust gases below the dew point are presented. A laboratory test bench is built in order to characterize the effects of coatings on the thermal hydraulic performances of the heat exchanger. An experimental study was undertaken to evaluate the airside surface wet-ability impact on the performance of the fin-and-tube heat exchanger.

2.2 Chemistry of the condensing flue gases

As a broad generality, flue gases from the combustion products are primarily composed of gaseous carbon dioxide (CO_2) and water vapor (H_2O) as well as gaseous nitrogen (N_2) and excess oxygen (O_2) remaining from the intake combustion air. Typically, the big portion of the flue gases is nitrogen. The combustion flue gases may also contain small amounts of particulate matters, carbon monoxide,

nitrogen oxides (NO_x), and sulfur oxides in the form of gaseous sulfur dioxide (SO₂) and gaseous sulfur trioxide (SO₃).

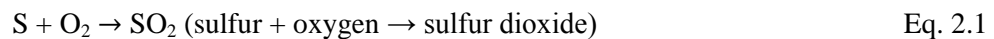
The acid dew point of flue gases is the temperature, at a given pressure, at which any gaseous acid in flue gases will start to condense into liquid acid [HUI 04]. It is referred to as the point at which flue gases are "saturated" with gaseous acid, meaning that flue gases cannot hold any more gaseous acid. When cooling flue gases below its acid dew point, the resulting liquid acid condensed from flue gases can cause serious corrosion problems to the equipment used in transporting, cooling, and emitting flue gases.

2.2.1 Acid dew point calculations

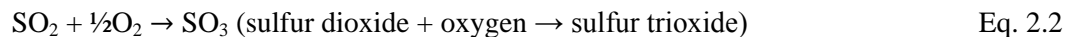
Several acid gases could be present in flue gases according to the type of burned substance and the combustion state [CHE 13].

- **Sulfuric acid**

The SO₃ is present because a portion of the SO₂ formed in the combustion of the sulfur (S) compounds in the combustion is further oxidized to SO₃. The most common cause of corrosion problems is the condensation of sulfuric acid. Sulfur in the fuel is oxidized to sulfur dioxide:



A fraction of the sulfur dioxide is oxidized to sulfur trioxide. Sulfur trioxide combines with water to form sulfuric acid at temperatures, which are at or below the dew point of flue gases. In a combustion process, most of the sulfur trioxide is formed according to the following equation:

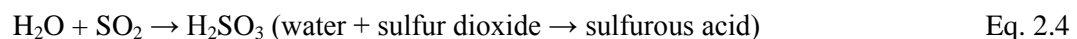


The amount of sulfur trioxide produced in any given situation is influenced by many variables, including excess air level, concentration of sulfur dioxide, temperature, gas residence time, and the presence of catalysts. The gas phase SO₃ then combines the vapor phase H₂O to form gas phase sulfuric acid (H₂SO₄):



- **Sulfurous acid**

Some of the sulfur dioxide in flue gases will also combine with water vapor in flue gases and form gas phase sulfurous acid (H₂SO₃):



- **Nitric acid**

The nitrogen in flue gases is derived from the combustion air as well as from nitrogen compounds contained in the combustion fuel. A small amount of the nitrogen is oxidized into gaseous nitrogen dioxide (NO₂) and some of that gas-phase nitrogen oxide then combines with water vapor to form gas-phase nitric acid (H₂NO₃):



- **Hydrochloric acid**

Some flue gases may also contain gaseous hydrochloric acid (HCl) derived from chloride compounds in the combustion fuel, which will condense into liquid hydrochloric acid if those flue gases are cooled to a temperature below the acid dew point of hydrochloric acid.

The following equations can be used to predict the acid dew points of the four acids that most commonly occur in typical combustion products ([HUI 04], [CHEN 10], [VER 74], [PIE 77]):

- **Sulfuric acid (H₂SO₄) dew point**

$$1000/T = 1.7842 - 0.0269 \log_{10}(P_{H_2O}) - 0.1029 \log_{10}(P_{SO_3}) + 0.0329 \log_{10}(P_{H_2O}) \log_{10}(P_{SO_3}) \quad \text{Eq. 2.6}$$

Or this equivalent form:

$$1000/T = 2.276 - 0.02943 \ln(P_{H_2O}) - 0.0858 \ln(P_{SO_3}) + 0.0062 \ln(P_{H_2O}) \ln(P_{SO_3}) \quad \text{Eq. 2.7}$$

- **Sulfurous acid (H₂SO₃) dew point**

$$1000/T = 3.9526 - 0.1863 \ln(P_{H_2O}) + 0.000867 \ln(P_{SO_2}) + 0.000913 \ln(P_{H_2O}) \ln(P_{SO_2}) \quad \text{Eq. 2.8}$$

- **Hydrochloric acid (HCl) dew point**

$$1000/T = 3.7368 - 0.1591 \ln(P_{H_2O}) - 0.0326 \ln(P_{HCl}) + 0.00269 \ln(P_{H_2O}) \ln(P_{HCl}) \quad \text{Eq. 2.9}$$

- **Nitric acid (HNO₃) dew point**

$$1000/T = 3.6614 - 0.1446 \ln(P_{H_2O}) - 0.0827 \ln(P_{NO_2}) + 0.00756 \ln(P_{H_2O}) \ln(P_{NO_2}) \quad \text{Eq. 2.10}$$

Where: “T” is the acid dew point temperature for the indicated acid (K), and “P” is the partial pressure (atm for Eq. 2.6 and mmHg for Eq. 2.7 to Eq. 2.10). State-of-the-art shows that the acid dew points predicted from Eq. 2.8 to Eq. 2.10 are within “6 K” and within “9 K for Eq. 2.6 and Eq. 2.7 [CHE 13]. As it can be seen in the above equation for the sulfuric acid dew point of flue gases, the partial pressure of sulfur trioxide in flue gases is required. That partial pressure can be readily determined given the total pressure of flue gases and the volume percent of sulfur trioxide in flue gases, since the partial pressure of any component of a gaseous mixture may be obtained by simply multiplying the total gas pressure by the component volume fraction of the gaseous mixture. It is commonly assumed that about “1” to “5” percent of the sulfur dioxide will be further oxidized into sulfur trioxide [CHE 13]. In other words, if the sulfur dioxide in the flue gases is determined to be “0.3” volume percent and it is assumed that “2” percent of that will be further oxidized to sulfur trioxide, the volume fraction of sulfur trioxide in the flue gases will be $(0.003)(.2) = 0.0006$ volume percent.

2.2.2 Heat-exchanger corrosion zones

To avoid corrosion due to condensing gases, it is of vital importance to understand the composition and amount of condensed liquid that could be formed when cooling flue gases. In clean air, the dew point can be directly obtained from the water vapor pressure, as shown in Fig. 2.1.

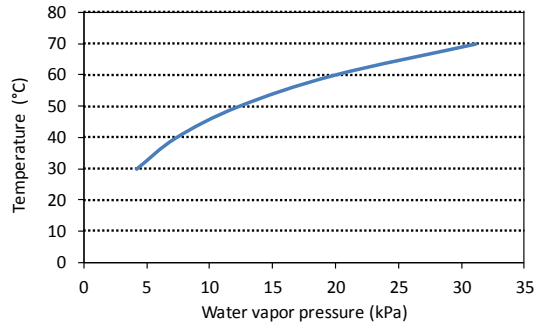


Fig. 2.1: Dew point of clean air as a function of the water vapor pressure

When other gaseous species are present, such as SO_3 , SO_2 , HCl or NO_2 in particular, the dew point will deviate from the ideal dew point line. Under the atmospheric pressure, dew points of flue gases in the presence of these species can be calculated by equations listed in §2.2.1.

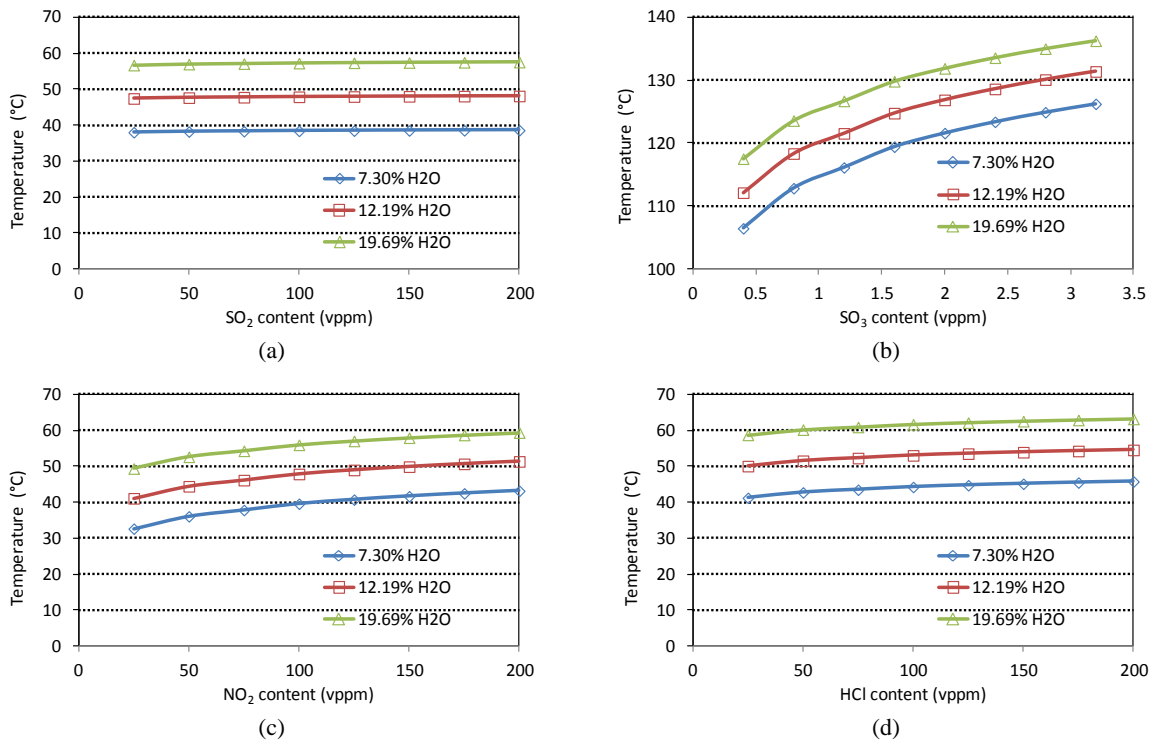


Fig. 2.2: Dew points of: a) SO_2 , b) SO_3 (2%v), c) NO_2 , and d) HCl at various water contents in flue gases

Fig. 2.2 shows the examples of calculated dew points for gases with SO_2 , SO_3 , HCl , and NO_2 respectively for different water vapor fractions. The corresponding water vapor dew points for the different water vapor concentrations shown in Fig. 2.2 are: 40°C (7.19% H_2O), 50°C (12.19% H_2O), and 60°C (19.69% H_2O).

Fig. 2.2 shows that, in the cases of very low HCl and NO_2 levels, the calculated dew points are lower than the water vapor dew point. This practically does not occur, and the water dew point should be preferred. Fig. 2.2.b depicts how the amounts of water vapor and gaseous SO_3 present in flue gases affect the sulfuric acid dew point of flue gases.

As an approximation, the sulfuric acid dew point of flue gases from the combustion of fuels is higher than 100 °C. Hence, it is apparent that the limiting dew point is due to sulfuric acid and any heat-transfer surface should be above this temperature if condensation is to be avoided.

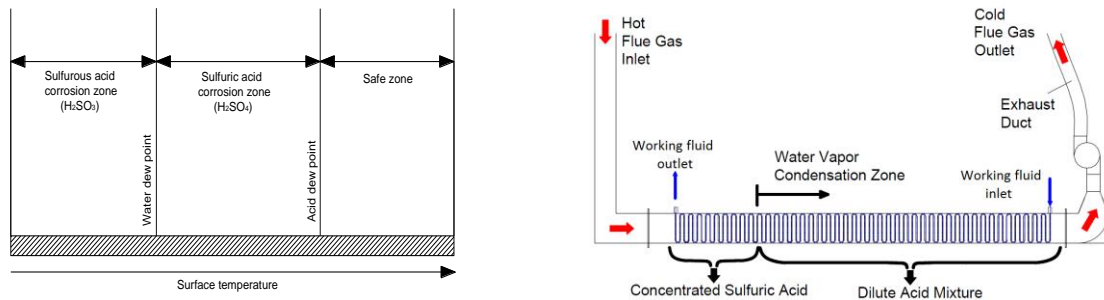


Fig. 2.3: Typical flue-gas corrosion zones ([LEV 11], [LU 87])

Fig. 2.3 shows the typical flue-gas corrosion zones. When the flue-gas temperature is lower than the sulfuric acid dew point, the acid first condenses as a highly concentrated solution of sulfuric acid and water. Based on thermodynamic liquid-vapor phase equilibrium calculations for sulfuric acid-water mixtures, concentrations of sulfuric acid in the condensate will depend on vapor phase H_2SO_4 and H_2O concentrations and will range from 75 to 85 weight percent [LEV 11]. For flue gases with moisture content in which the flue-gas temperature is lower than the water vapor dew point, the liquid mixture of water and sulfuric acid is more dilute in sulfuric acid than the highly concentrated acid solutions generated at temperatures above the water vapor dew point temperature. Both HCl and HNO_3 condense at temperatures lower than the water dew point and a high rate of corrosion is expected [HUI 04].

The analysis carried out in this section shows that the safe zone almost does not exist when recovering heat at low-temperature level ($T \sim 120^\circ\text{C}$).

2.2.3 Potential solutions for acid corrosion

There are two approaches used by engineers to handle acid corrosion:

- Avoid it by using protective measures such as maintaining a high cold end temperature so that condensation of any vapor does not occur. However, this solution is not practical at this temperature level ($T \sim 120^\circ\text{C}$) since the acid dew point temperature is in the same range as the inlet flue-gas temperature.
- Accept condensation of acid vapor or both acid and water vapor, thereby increasing the duty of the heat transfer surface, and use a stainless steel or corrosion resistant materials such as “Heresite”, “Epoxy”, “Teflon”, etc. Note that condensing heat exchangers require maintenance and their installed costs could be up to three times higher than for conventional heat exchangers.

2.3 General design method for fin-and-tube HEX at low temperature

This section shows a method to design a fin-and-tube heat exchanger at low temperature by choosing appropriate operating parameters and geometrical configurations in order to minimize the exergy losses in the fin-and-tube heat exchanger. Several studies are related to fin-and-tube heat exchangers. Shah [SHA 78] and Van den Bulck [VAN 91] employed optimal distribution of the UA value across the volume of cross-flow heat exchangers and optimized different design variables like fin thickness, fin height, and fin pitch. Bejan [BEJ 78] and Bejan [BEJ 79] used the concept of irreversibility for

estimating and minimizing the usable energy wasted in heat-exchanger design and presented an optimum design method for balanced and imbalanced counter-flow heat exchangers. Bejan [BEJ 79] proposed the use of a “Number of Entropy Production Units” as a basic parameter in describing heat-exchanger performance. Later on, Khan *et al.* [KHA 06] optimized the design of tube banks in cross flow using Entropy Generation Minimization (EGM) Method.

A considerable improvement in the thermal performance of the fin-and-tube heat exchanger is possible by choosing an appropriate geometrical configuration for the corresponding application. In this section, the geometry of fin-and-tube heat exchanger has been derived, and optimized geometrical parameters have been found out. Results show that operating parameters (flue-gas velocity, internal mass velocity), geometrical parameters (fin types, fin pitches, tube lengths, tube diameters, tube pitches) and heat-exchanger circuitry could be optimized to ensure a compromise between net power produced in the conversion cycle and the fin-and-tube heat exchanger compactness.

The thermal conductivity is an important factor in selecting material of the studied fin-and-tube heat exchangers. As stated previously, material like steel exhibits excellent resistance to a wide range of corrosion exposures but it is characterized by a very low thermal conductivity and a high density (Table 2.1) implying a large volume, a low compactness and significant weight for the heat exchanger. Copper and aluminum present high-thermal conductivities (Table 2.1) but are sensitive to acidic environment, and then, corrosion and buildups will reduce lifetime and lead to increased pressure drops and reduced efficiency; thus, an inevitable decrease in the heat-exchanger effectiveness is expected. In this case, the design must include best available corrosion protections. Following study will be done using a copper tube and aluminum fins. Fins will be made in aluminum in order to avoid heavy heat-exchanger weight since the aluminum is characterized by a lower density compared to copper ($\rho_{\text{copper}}/\rho_{\text{aluminum}} \sim 3.3$) and the fin surface area is much larger than the tube surface area. Finally, the effect of material selection on the fin-and-tube heat exchanger compactness is shown.

Table 2.1: Thermal conductivity and density of copper, aluminum and stainless steel

Material	$\lambda_{@25^\circ\text{C}}$ ($\text{W}\cdot\text{m}^{-1}\cdot\text{K}^{-1}$)	ρ ($\text{kg}\cdot\text{m}^{-3}$)
Copper	401	8940
Aluminum	250	2700
Stainless steel	16	7900

2.3.1 Design criteria

In fin-and-tube heat exchangers (Fig. 2.4 to Fig. 2.6), the external surface of tubes is primary, and the fin surface is secondary. The primary surface generally consists of rows of round tubes that might be staggered or placed in-line with respect to the flue-gas flow (Fig. 2.5). The recirculation zone behind the tubes is smaller for a staggered-tube layout than for the in-line tube layout for which the separated shear-layer bounding the wake only reattaches at the front of the downstream tube, resulting in a large recirculation zone. Therefore, the staggered tube arrangement achieves higher heat-transfer performance. The inside surface of tubes is usually smooth or plain, but some coil designs have various forms of internal fins or turbulence promoters (either fabricated or extruded) to enhance performance. However, their effects are limited since the dominant thermal resistance is usually at the flue-gas side and will be disregarded in the present study. The individual tube passes are interconnected by return bends (elbows). Fins should be spaced according to the duty to be performed, with special attention given to the corresponding pressure drop at the flue-gas side. Tube wall thickness is determined mainly by the working pressure and safety factor for hydrostatic burst

(pressure). Maximum allowable working pressure (MAWP) is derived according to ASME's Boiler and pressure vessel code, Section VIII, Division I and Section II (ASTM material properties and stress tables) [ASH 08]. Fin type and header construction also play a large part in determining wall thickness of material.

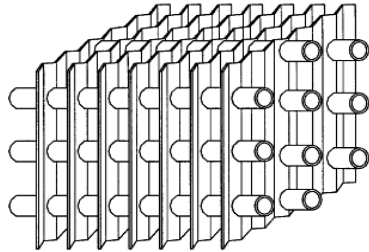


Fig. 2.4: Typical fin-and-tube heat exchanger

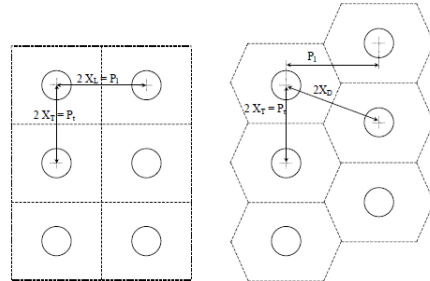


Fig. 2.5: Unit cells for inline and staggered tube layouts with continuous plate fins

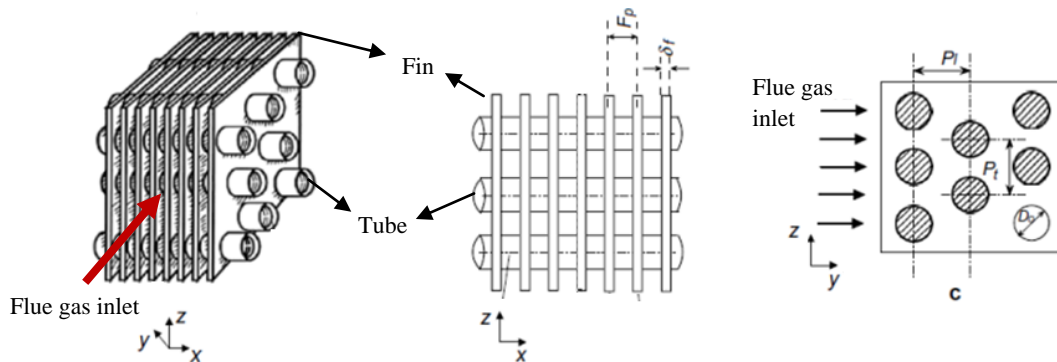


Fig. 2.6: Schematic configuration for a fin-and-tube heat exchanger

The relation of the fluid-flow arrangement greatly influences performance of the heat-transfer surface. Generally, the fin-and-tube heat exchanger is circuited for cross-counter-flow arrangement (Fig. 2.7). Inlet flue-gas is applied at right angles to the heat-exchanger tube face (heat-exchanger height), which is also at the heat-exchanger outlet-header location. Flue gases exit at the opposite face (side) of the heat exchanger where the corresponding inlet header is located. Counter-flow can produce the highest possible heat exchange in the shortest possible heat-exchanger depth because it has the closest temperature relationships between tube fluid and flue gases at each flue-gas side of the fin-and-tube heat exchanger. In this case, the temperature of entering flue gases approaches more closely the temperature of the leaving fluid than the temperature of leaving flue gases approaches the temperature of the entering fluid. The potential of realizing the highest possible mean temperature difference is thus arranged for optimum performance [ASH 08].

Flue gas exit

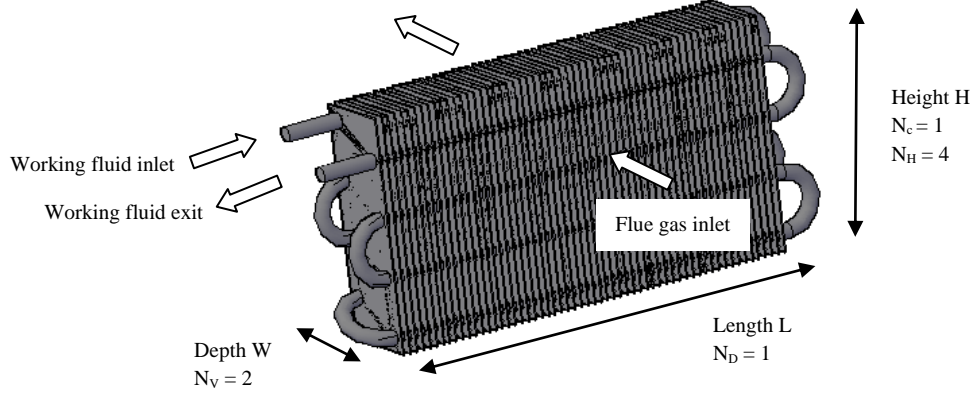


Fig. 2.7: Fin-and-tube heat exchanger lay-out showing circuitry parameters

The fin-and-tube heat exchanger will be composed of many circuits (N_C). Each circuit has a single inlet and a single outlet and includes one or many horizontal rows (N_H). The number of vertical rows (N_V) will be determined to ensure the corresponding heat-exchange capacity. Furthermore, the fin-and-tube heat exchanger can be divided into many parts along its length (N_D). Fig. 2.7 shows a typical fin-and-tube heat exchanger composed of one circuit ($N_C = 1$) with four horizontal rows per circuit ($N_H = 4$) and two vertical rows ($N_V = 2$).

The internal mass velocity is defined by:

$$G = \frac{m_r}{A_i} \quad \text{Eq. 2.11}$$

The superficial and effective flue-gas velocities are calculated respectively by:

$$V_{a,s} = \frac{m_a}{A_{fr} \cdot \rho_a}, \quad V_{a,e} = \frac{m_a}{A_{fr,e} \rho_a} \quad \text{Eq. 2.12}$$

In Eq. 2.11 and Eq. 2.12, “ m_r ” and “ m_a ” are respectively the mass of working fluid and dry flue gases, “ A_i ” is the internal tube section area, “ ρ_a ” is the flue-gas density, “ A_{fr} ” and “ $A_{fr,e}$ ” are respectively the frontal area and the effective frontal area (minimum free flow area) and are given respectively by:

$$A_{fr} = H \cdot L \quad \text{Eq. 2.13}$$

$$A_{fr,e} = (P_T - D_o) \cdot LNF \cdot (F_p - \delta_f) \cdot N_c \cdot N_H \cdot N_D \cdot L \quad \text{Eq. 2.14}$$

In order to minimize temperature differences and pressure drop at both working fluid and flue-gas sides, the “counter-current” configuration must be carefully designed. To size a fin-and-tube heat exchanger, the allowable pressure drop in the flue-gas circuit and in the working fluid circuit should be considered as well as the compactness of the heat exchanger. The pressure drop in the flue gas circuit influences the blower power while the pressure drop in the working fluid circuit influences the liquid pump power. However, a slight increase in the pressure drop in the flue-gas circuit affects significantly the blower power, which is not the case for the working fluid (liquid pump flow). Consequently, the pressure drop in the flue-gas circuit will be limited by a given blower consumption.

The use of the net power produced by the conversion cycle (ORC) to optimize the operating and geometrical parameters of the fin-and-tube heat exchanger requires the calculation of the combined effect of heat transfer and pressure drop at both flue-gas side and working fluid side. Therefore, the design criterion will be a compromise between the net power in the ORC system and the fin-and-tube heat-exchanger compactness.

The fin-and-tube heat-exchanger compactness is defined by:

$$HEX \text{ compactness} = \frac{W_{net}}{V_{HEX}} \quad \text{Eq. 2.15}$$

Where: “ W_{net} ” is the net power produced by the ORC system, “ V_{HEX} ” is the fin-and-tube heat exchanger volume (m^3).

The net power produced by the ORC system is given by:

$$W_{net} = W_{turbine} - W_{pump} - W_{blower, \text{ Fin-and-tube HEX}} \quad \text{Eq. 2.16}$$

The blower power is calculated by:

$$W_{blower, \text{ Fin-and-tube HEX}} = \frac{m_a \cdot DP_a}{\rho_a \cdot \eta_{blower}} \quad \text{Eq. 2.17}$$

The fin-and-tube heat exchanger parameters to be optimized are as follows:

- Operating parameters: internal mass velocity, flue-gas velocity
- Geometrical parameters:
 - ✓ Tube: length (L), diameter (D_o), longitudinal and transversal pitches (P_l and P_t)
 - ✓ Fin: types and pitches (F_p)
 - ✓ Fin-and-tube heat-exchanger circuitry

A fin thickness of “0.2 mm” is selected. Gray *et al.* [GRA 86] reported that the effect of fin thickness is almost negligible on both heat-transfer coefficient and pressure drop.

2.3.2 Heat and mass transfer model

2.3.2.1 Heat-transfer model

The fin-and-tube heat exchanger will remove both sensible and latent heat from entering flue gases. Flue gases to be cooled are mainly a mixture of water vapor, nitrogen, oxygen, and carbon dioxide; all loose sensible heat when in contact with a surface colder than flue gases. Latent heat is removed through moisture condensation only on heat-exchanger sections where the surface temperature is lower than the water dew point of flue gases. When the coil starts to remove moisture, the cooling surfaces carry both the sensible and latent heat loads. As flue gases approaches saturation, each degree of sensible cooling is nearly matched by a corresponding degree of dew-point decrease; the latent heat removal per degree of dew-point change is significantly greater.

Fig. 2.8 is a typical thermal diagram for a coil in which the air and a coolant are arranged in counter-flow. The top and bottom lines in the diagram indicate, respectively, changes across the coil in the

flue-gas stream enthalpy “ h_a ” and the working fluid temperature “ T_r ”. To illustrate continuity, the single middle line in Fig. 2.8 represents both surface temperature “ T_s ” and the corresponding saturated flue-gas enthalpy “ h_s ”, although the temperature and flue-gas enthalpy scales do not actually coincide as shown. The differential surface area dA_w represents any specific location within the coil thermal diagram where operating conditions are such that the flue-gas surface-interface temperature “ T_s ” is lower than the local flue-gas water dew-point temperature. Under these conditions, both sensible and latent heats are removed from the flue-gas stream, and the cooler surface actively condenses water vapor.

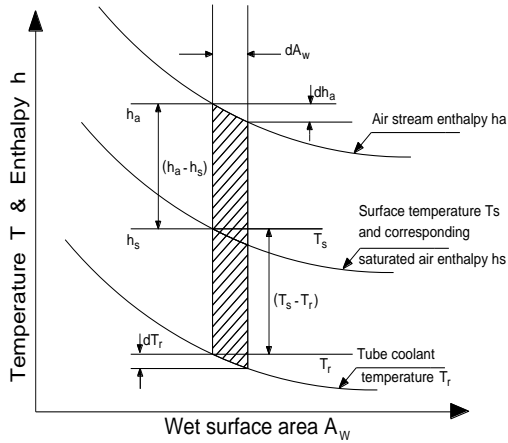


Fig. 2.8: Two component driving force between dehumidifying flue gases and coolant [ASH 08]

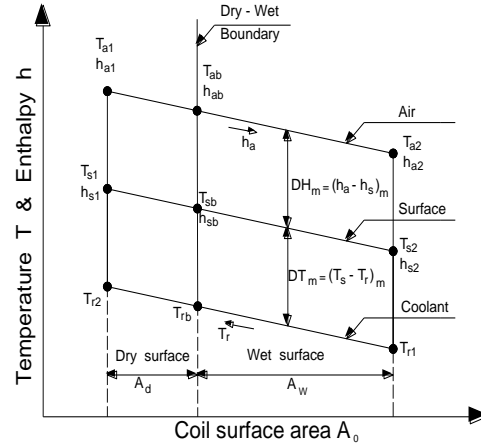


Fig. 2.9: Thermal diagram for general case when coil surface operates partially dry [ASH 08]

Fig. 2.9 shows a typical thermal diagram for the coil surface when operating partially dry (counter-flow architecture). Locations of the entering and leaving boundary conditions for both flue gases and working fluid are shown. The thermal diagram in Fig. 2.9 is similar to the one in Fig. 2.8. It shows three lines to illustrate local conditions for the flue gases, surface, and working fluid throughout a coil. The top and bottom lines in the diagram indicate, respectively, changes across the coil in the flue-gas stream enthalpy “ h_a ” and the working fluid temperature “ T_r ”. The dry-wet boundary conditions are located where the coil surface temperature “ T_{sb} ” equals the entering water dew-point temperature. Thus, the surface area A_d to the left of this boundary is dry, while the remaining “ A_w ” of the coil surface area is wet. The potential or driving force for transferring total heat (Q) from the flue-gas stream to the tube-side working fluid (coolant) is composed of two components in series heat flow: (1) an air-to-surface flue-gas enthalpy difference ($h_a - h_s$) and (2) a surface-to-coolant temperature difference ($T_s - T_r$) [ASH 08].

The total heat transferred in the fin-and-tube heat exchanger is calculated by:

$$Q_t = m_a \cdot (h_{a,in} - h_{a,out}) = m_r \cdot (h_{r,out} - h_{r,in}) \quad \text{Eq. 2.18}$$

In dry conditions, the heat transfer is based on the temperature potential and given as follows:

$$Q_d = (U_o A_o)_d \cdot \text{DTLM} \quad \text{Eq. 2.19}$$

In Eq. 2.19, the overall heat transfer coefficient in dry conditions $(U_o A_o)_d$ and DTLM are given respectively by [INC 96]:

$$\frac{1}{\underbrace{(U_o A_o)_d}_{R_{total}}} = \frac{1}{\underbrace{h_i A_i}_{R_r}} + \frac{\ln(D_o / D_i)}{\underbrace{2\pi k_i L}_{R_m}} + \frac{1}{\underbrace{\eta_o A_o h_o}_{R_{ad}}} \quad \text{Eq. 2.20}$$

$$DTLM = \frac{(T_{a,in} - T_{r,out}) - (T_{a,out} - T_{r,in})}{\ln\left[\frac{(T_{a,in} - T_{r,out})}{(T_{a,out} - T_{r,in})}\right]} \quad \text{Eq. 2.21}$$

Where: “ $T_{r,in}$ ” and “ $T_{r,out}$ ” are respectively the inlet and outlet working fluid temperatures and “ $T_{a,in}$ ” and “ $T_{a,out}$ ” are respectively the inlet and outlet flue gas temperatures.

The heat-transmission rate of flue gases, passing over a tube to a fluid flowing within it, is impeded by three thermal resistances:

- Surface flue-gas side film thermal resistance from the flue gases to the surface of the exterior fin and tube assembly (R_{ad})
- Metal thermal resistance to heat conductance through the exterior fin-and-tube assembly (R_m)
- In-tube fluid film thermal resistance, which impedes heat flow between the internal surface of the metal and the fluid flowing within the tube (R_r)

In Eq. 2.20, “ η_o ” is the overall outside surface efficiency given by ([PER 03], [PER 04]):

$$\eta_o = 1 - \frac{A_f}{A_o} (1 - \eta_{f,dry}) \quad \text{Eq. 2.22}$$

The dry fin efficiency is calculated by:

$$\eta_{f,dry} = \frac{\tanh(mr\phi)}{mr\phi} \quad \text{Eq. 2.23}$$

$$m = \sqrt{\frac{2h_o}{k_f \delta_f}} \quad \text{Eq. 2.24}$$

$$\phi = \left(\frac{r_f}{r} - 1\right) \left(1 + 0.35 \ln\left(\frac{r_f}{r}\right)\right) \quad \text{Eq. 2.25}$$

$$\frac{r_f}{r} = 1.27 \frac{(P_T / 2)}{r} \sqrt{\frac{X_D}{(P_T / 2)} - 0.3}, \quad X_D = \frac{1}{2} \sqrt{4(P_L / 2)^2 + (P_T / 2)^2} \quad \text{Eq. 2.26}$$

In dehumidifying conditions, the heat-transfer phenomenon can be treated using the method developed in [ASH 08]. Referring to Fig. 2.9, the potential or driving force for transferring the total heat from the flue-gases to the tube-side coolant is composed of two components in series heat flow: (1) a flue-gas-to-surface enthalpy difference ($h_a - h_s$) and (2) a surface-to-coolant temperature difference ($T_s - T_r$). By neglecting the enthalpy of condensed water vapor leaving the surface and any radiation and convection losses, the total heat lost from the flue-gas stream in flowing over “ dA_w ” is:

$$dQ_t = m_a \cdot dh_a \quad \text{Eq. 2.27}$$

This same total heat is transferred from the flue-gas stream to the surface interface:

$$dQ_t = (h_a - h_s) \cdot dA_w / (c_{pa} R_{aw}) \quad \text{Eq. 2.28}$$

The total heat transferred from the flue-gas-surface interface across the surface elements into the coolant is equal to:

$$dQ_t = (T_s - T_r) \cdot dA_w / (R_{mw} + R_{rw}) \quad \text{Eq. 2.29}$$

The same quantity of total heat is also gained by the coolant in passing across “ dA_w ”:

$$dQ_t = -m_r \cdot c_{pr} \cdot dT_r \quad \text{Eq. 2.30}$$

If Eq. 2.28 and Eq. 2.30 are equated and the terms rearranged, an expression for the coil characteristic “ C ” is obtained:

$$C = (R_{mw} + R_{rw}) / (c_{pa} R_{aw}) = (T_s - T_r) / (h_a - h_s) \quad \text{Eq. 2.31}$$

Eq. 2.31 shows the basic relationship of the two components of the driving force between air and coolant in terms of three principal thermal resistances. For a given coil, these three resistances of flue gases, metal, and in-tube fluid (R_{aw} , R_{mw} , and R_{rw}) are usually known or can be determined, which gives a fixed value for the constant “ C ”.

Eq. 2.31 can then be used to determine point conditions for the interrelated values of flue-gas stream enthalpy “ h_a ”, coolant temperature “ T_r ”, surface temperature “ T_s ” and enthalpy “ h_s ” of saturated air corresponding to the surface temperature. When both “ T_s ” and “ h_s ” are unknown, a trial-and-error solution is necessary.

Knowing coil characteristics “ C ” for point conditions, the interrelations between the flue-gas stream enthalpy “ h_a ”, coolant temperature “ T_r ”, and surface temperature “ T_s ” and its corresponding enthalpy of saturated flue-gas “ h_s ” can be determined by trial-and-error procedure using Eq. 2.32 (refers to Fig. 2.9):

$$C = \frac{T_{sb} - T_{rb}}{h_{ab} - h_{sb}} = \frac{T_{s2} - T_{r1}}{h_{a2} - h_{s2}} \quad \text{Eq. 2.32}$$

The overall thermal resistance R_o comprises three basic elements:

$$R_o = R_{aw} + R_{mw} + R_{rw} \quad \text{Eq. 2.33}$$

$$R_{rw} = B/h_r, R_m = e_t / (2\pi \cdot k_t), R_{aw} = 1/h_{c,o} \quad \text{Eq. 2.34}$$

$$B = \eta_{ow} \cdot A_o / A_i \quad \text{Eq. 2.35}$$

The mean effective difference air enthalpy between the flue-gas stream and the surface from Fig. 2.9 is:

$$Dh_m = \frac{(h_{ab} - h_{sb}) - (h_{a2} - h_{s2})}{\ln[(h_{ab} - h_{sb}) / (h_{a2} - h_{s2})]} \quad \text{Eq. 2.36}$$

Similarly, the mean temperature difference between surface and coolant is:

$$DT_{ms} = \frac{(T_{sb} - T_{rb}) - (T_{s2} - T_{r1})}{\ln[(T_{sb} - T_{rb}) / (T_{s2} - T_{r1})]} \quad \text{Eq. 2.37}$$

The wet heat-transfer coefficient at the flue-gas side is given by:

$$h_{o,w} = \frac{1}{\frac{c_{p,a}}{b'_w h_{c,o}} + \frac{\delta_w}{k_w}} \quad \text{Eq. 2.38}$$

Where: “ b'_w ” is the slope of the saturation enthalpy curve at the corresponding tube surface temperature. “ δ_w ” is the thickness of the condensed water film. In practice, “ δ_w/k_w ” “accounts for only 0.5 - 5% compared to “ $c_{p,a}/(b'_w h_{c,o})$ ” and has often been neglected by previous investigators.

The overall outside wet surface efficiency (η_{ow}) is given by [PER 04]:

$$\eta_{ow} = 1 - \frac{A_f}{A_o} (1 - \eta_{f,wet}) \quad \text{Eq. 2.39}$$

The wet fin efficiency “ $\eta_{f,w}$ ” is calculated with dry fin efficiency equations, using a “ m_{wet} ” parameter based on this total wet heat transfer coefficient as follows [PER 04]:

$$\eta_{f,wet} = \frac{\tanh(m^* l)}{m^* l} \quad \text{Eq. 2.40}$$

$$m^* = \sqrt{\frac{h_{o,w} P}{k_f A_{fin,base}}} = \sqrt{\frac{h_{o,w}}{k_f} \cdot \frac{2(\delta_f + F_s)}{\delta_f F_s}} = \sqrt{\frac{2h_{o,w}}{k_f \delta_f} \cdot \left(1 + \frac{\delta_f}{F_s}\right)} \quad \text{Eq. 2.41}$$

$$l = P_T / 2 - \delta_f \quad \text{Eq. 2.42}$$

The heat transfer model is done by dividing the fin-and-tube heat exchanger into many tiny segments and by applying the corresponding method for dry and wet cases. More details about the heat-transfer model under both dry and wet conditions can be found in Ashrae [ASH 08]. References of the correlations used for heat transfer and pressure drop at both flue-gas and coolant side calculations in dry and dehumidifying conditions are listed in “Annex D”.

2.3.2.2 Mass transfer model

The mass of the water condensate and the leaving air dry-bulb temperature are found by a method developed in Ashrae [ASH 08]. Fig. 2.10 represents part of a psychrometric chart showing the flue-gas saturation curve and lines of constant air enthalpy closely corresponding to constant wet-bulb temperature lines.

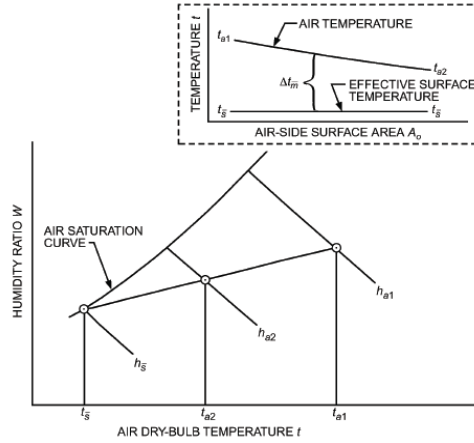


Fig. 2.10: Leaving flue-gas dry-bulb temperature determination [ASH 08]

For a given coil and flue-gas quantity, a straight line projected through the entering and the leaving flue-gas conditions intersects the flue-gas saturation curve at a point denoted as the effective coil temperature “ T_s ”. An index of the flue-gas side effectiveness is the heat-transfer exponent “ c ”, defined as:

$$c = \frac{A_o}{m_a c_{pa} R_{aw}} \quad \text{Eq. 2.43}$$

This exponent “ c ”, sometimes called the number of airside heat-transfer units “ NTU_a ”, is also defined as:

$$c = \frac{T_{a1} - T_{a2}}{\Delta T_m} \quad \text{Eq. 2.44}$$

The temperature drop ($T_{a1} - T_{a2}$) of the flue-gas stream and mean temperature difference “ ΔT_m ” between flue gases and effective surface in Eq. 2.44 are illustrated at the top of Fig. 2.10. Knowing exponent “ c ”, entering and leaving enthalpies “ h_{a1} ” and “ h_{a2} ” of the flue-gas stream, the enthalpy of saturated flue-gas “ h_s ” corresponding to the effective surface temperature “ T_s ” is calculated as follows:

$$h_s = h_{a1} - \frac{h_{a1} - h_{a2}}{1 - e^{-c}} \quad \text{Eq. 2.45}$$

After identifying the value of “ T_s ” that corresponds to “ h_s ”, by trial-and-error procedure, the leaving air dry-bulb temperature can be determined:

$$T_{a2} = T_s + e^{-c} (T_{a1} - T_s) \quad \text{Eq. 2.46}$$

Knowing “ h_{a2} ” and “ T_{a2} ”, the corresponding humidity ratio “ w_{a2} ” will be calculated. The mass of water condensate is calculated by:

$$m_c = m_a (w_{a,1} - w_{a,2}) \quad \text{Eq. 2.47}$$

2.3.3 Optimization procedure

The fin-and-tube heat exchanger realizes a direct exchange between flue gases and the working fluid and operates partially in wet mode. In this section, the operating parameters (gas velocity and internal mass velocity), geometrical parameters (fin types, fin pitches, tube lengths, tube diameters, and tube pitches), and circuitry of the fin-and-tube heat exchanger are optimized to ensure a compromise between the net power produced by the ORC system and the heat-exchanger compactness. The optimization example of the fin-and-tube geometry is based on the ORC parameters shown in Table 2.2. Using those parameters, the fin-and-tube heat exchanger capacity is around “825 kW_{th}”, and the estimated mass of water vapor condensate is “33 g.s⁻¹”.

Table 2.2: ORC parameters

Flue gas compositions	CO ₂ - 15.5% v ,O ₂ - 6.8% v	Pinch evaporator (K)	3
T _{flue gas inlet} (°C)	110.0	SH _{evap} (K)	0
T _{dp inlet} (°C)	60.0	T _{cond} (°C)	25
V _{dry flue gas} (Nm ³ .hr ⁻¹)	32,000	SC _{cond} (K)	2
m _{dry flue gas} (kg.s ⁻¹)	11.5	η _{turbine} (%)	80
P _{evap @ saturated vapor} (MPa)	0.5	η _{pump} (%)	85
Working fluid	R-245fa	η _{blower} (%)	60

For two-phase flows of R-245fa inside tubes, the respective distribution of the liquid and vapor phases in the flow channel is an important aspect of their distribution. Their respective distribution takes on some commonly observed flow structures defined as two-phase flow patterns with particular identifying characteristics. In horizontal tubes, depending on the mass velocity and vapor quality, six flow regimes could be distinguished as follows: stratified, slug, intermittent, annular, dry-out, and mist flows [THO 05]. Fig. 2.11 shows the implemented flow pattern map for R-245fa using the implemented method developed by Wojtan *et al.* [WOJ 05]. It is advised to operate in the annular flow regime because this flow regime is characterized by a high heat-transfer coefficient. In this case, the liquid forms continuous annular films around the tube perimeter. Doing so, the internal mass velocity will range within the interval “200-600” kg.m⁻².s⁻¹.

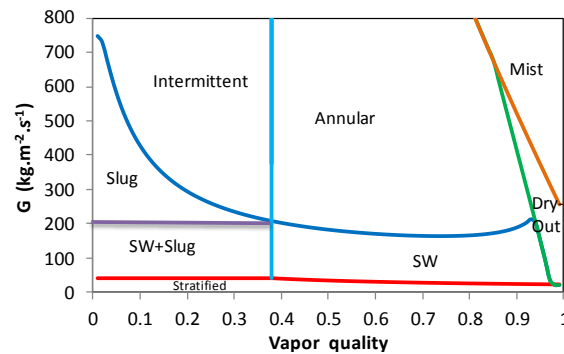


Fig. 2.11: Flow pattern map for R-245fa
(P_{evap} = 0.5 MPa, D_i = 13.84 mm, q = 5 kW/m²)

The heat-exchanger design procedure consists in the calculation of the number of circuits for a given internal mass velocity. Since the mass flow rate of flue gases is fixed, the velocity of flue gases is calculated.

2.3.3.1 Operating parameters

The operating parameters include the superficial flue-gas velocity (V_{a,s}), the effective flue-gas velocity (V_{a,e}), and the internal mass velocity (G). In the first step, the operating parameters for fixed heat-exchanger geometry will be optimized depending on the net power and heat-exchanger compactness,

and then the effect of varying the different geometrical parameters of the heat exchanger on the operating parameters will be analyzed. As stated previously, since the flue-gas mass flow rate is fixed; for each internal mass velocity, the superficial and effective flue-gas velocities, the heat-exchanger height, and the number of circuits (N_c) are calculated. By increasing the internal mass velocity, the superficial and effective flue-gas velocities increase (Fig. 2.12.a); the heat-exchanger height and the number of circuits decrease (Fig. 2.12.b).

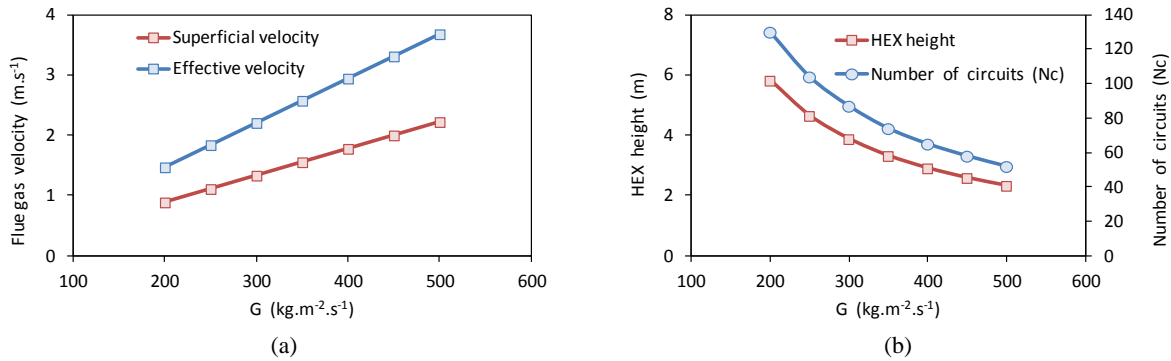
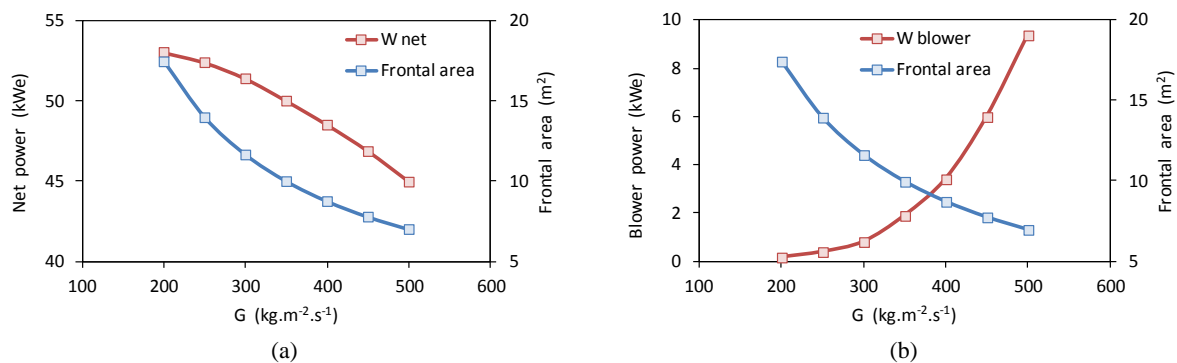


Fig. 2.12: Evolutions of: a) superficial and effective flue-gas velocities, b) heat-exchanger height and N_c as a function of G ($L = 3\text{m}$, $D_i = 13.84\text{ mm}$, $P_T = 45\text{ mm}$, $P_L = 38.97\text{ mm}$, $F_p = 3\text{ mm}$, $\delta_f = 0.2\text{ mm}$, wavy fins, $N_H = 1$, $N_D = 1$)

The evolution of the net power, frontal area, blower power, external tube surface area and fin surface area, internal and external pressure drop, heat-exchanger compactness, heat flux reported to internal tube surface area, the number of vertical rows (N_v) and the heat-exchanger depth as a function of the internal mass velocity are shown in Fig. 2.13. By increasing the internal mass velocity, the net power decreases (Fig. 2.13.a), the blower power increases (Fig. 2.13.b), the external tube-and-fin surface areas decrease (Fig. 2.13.c), the internal and external pressure drops increase (Fig. 2.13.d), the heat flux reported to internal tube surface area and the number of vertical rows (N_v) for the heat exchanger increase (Fig. 2.13.e). Fig. 2.13.e shows the presence of an optimal internal mass velocity for which the heat-exchanger compactness is maximal. In fact, as the internal mass velocity increases, the frontal area decreases (Fig. 2.13.a) and the number of vertical rows for the heat exchanger increases leading to an increase in the heat-exchanger depth (Fig. 2.13.f). Thus, an optimal internal mass velocity exists for which the heat-exchanger compactness is maximal.



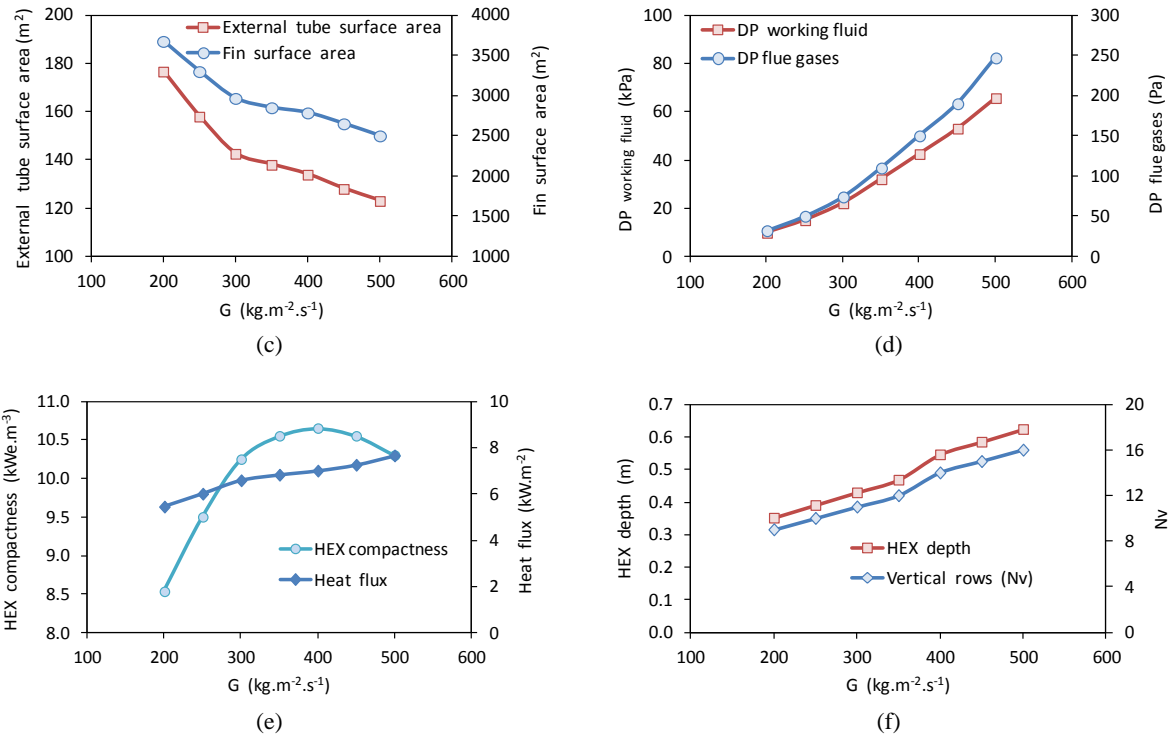
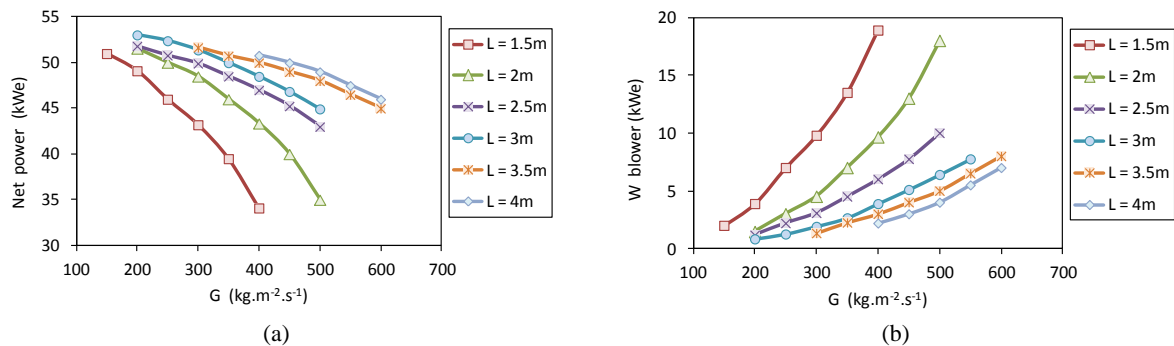


Fig. 2.13: Evolutions of: a) Net power and frontal area, b) Blower power and frontal area, c) External tube-and-fin surface areas, d) Working fluid and flue-gas pressure drops, e) Heat-exchanger compactness and heat flux, f) HEX depth and N_v , as a function of G ($L = 3\text{m}$, $D_1 = 13.84\text{ mm}$, $P_T = 45\text{ mm}$, $P_L = 38.97\text{ mm}$, $F_p = 3\text{ mm}$, $\delta_f = 0.2\text{ mm}$, wavy fins, $N_H = 1$, $N_D = 1$)

2.3.3.2 Tube length

The first geometrical parameter to be optimized is the tube length. The tube length affects the frontal area and the heat-exchanger compactness. The evolutions of the net power, blower power, and heat-exchanger compactness as a function of the internal mass velocity for different tube lengths are shown in Fig. 2.14. For a given tube length, an optimal internal mass velocity exists for which the heat-exchanger compactness is maximal. For a given internal mass velocity, as the tube length increases, the net power increases (Fig. 2.14.a), the blower power decreases (Fig. 2.14.b). As shown in Fig. 2.14.e, the optimal internal mass velocity for which the heat-exchanger compactness is maximal increases as the tube length increases. The maximal heat-exchanger compactness is reached for a tube length around 3 m. The corresponding internal mass velocity is around “ $400\text{ kg}\cdot\text{m}^{-2}\cdot\text{s}^{-1}$ ”.



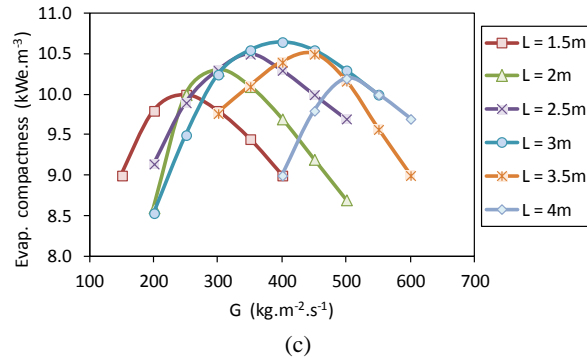


Fig. 2.14: Evolutions of: a) Net power, b) Blower power, c) Heat-exchanger compactness for different tube lengths as a function of G ($D_i = 13.84$ mm, $P_T = 45$ mm, $P_L = 38.97$ mm, $F_p = 3$ mm, $\delta_f = 0.2$ mm, wavy fins, $N_H = 1$, $N_D = 1$)

2.3.3.3 Fin types and fin pitches

The dominant resistance in the fin-and-tube heat exchanger usually is at the flue-gas side. Hence, fin surfaces (plain, wavy, louver, and slit fins) are usually adopted for improving the overall heat-transfer performance (Fig. 2.15).

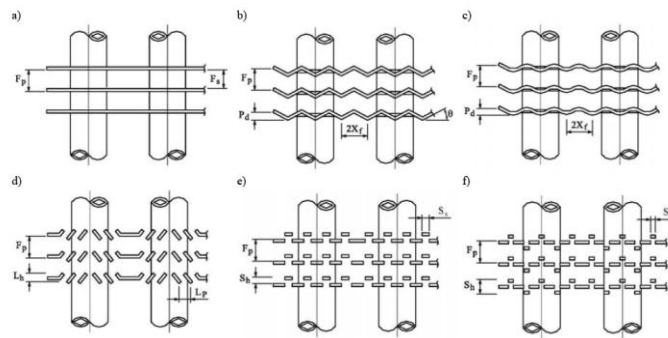


Fig. 2.15: Various fin types with round tubes [17]
a) Plate fins ; b) Herringbone wavy fins ; c) Smooth wavy fins
d) Louver fins with redirection louvers ; e) Slit fins ; f) Double-side slit fins

In this section, the performance of wavy fins will be compared to plain fins. The slit and louver fins will be disregarded due to possible slugging problems. The corrugation angle for wavy fins is estimated to be 10° . As shown in Fig. 2.16, the use of wavy fins instead of plain fins leads to more produced net power in the ORC system (Fig. 2.16.a), and to more compact heat exchanger (Fig. 2.16.b).

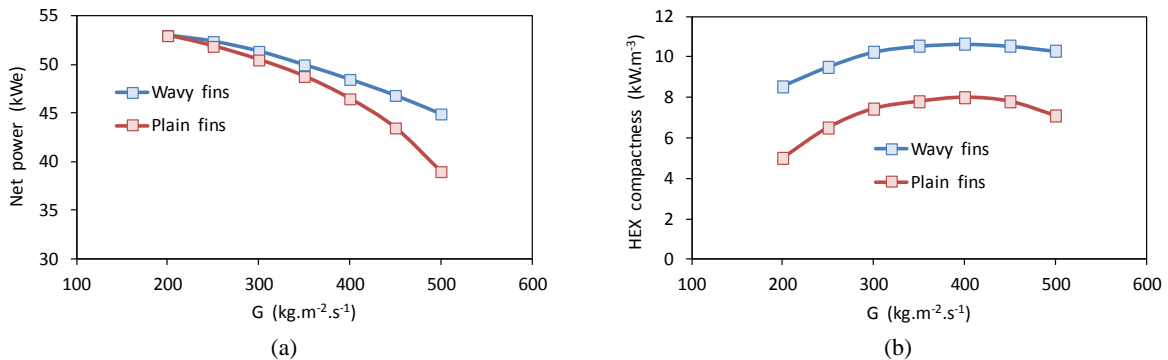


Fig. 2.16: Evolutions of: a) Net power, b) Heat-exchanger compactness, as a function of G for plain and wavy fins ($L = 3$ m, $D_i = 13.84$ mm, $P_T = 45$ mm, $P_L = 38.97$ mm, $F_p = 3$ mm, $\delta_f = 0.2$ mm, $N_H = 1$, $N_D = 1$)

For the selection of the fin pitch, Fig. 2.17 shows an increase in the net power with the increase of the fin pitches until reaching a 3-mm fin pitch where the net power almost remains constant. On the other side, the heat-exchanger compactness presents almost a linear decrease with the fin-pitch increase and then high heat-exchanger compactness can be reached for small fin pitch. A 3-mm fin pitch could be selected as a compromise choice. It will remain to validate experimentally if the fins are spaced enough to avoid condensate bridging.

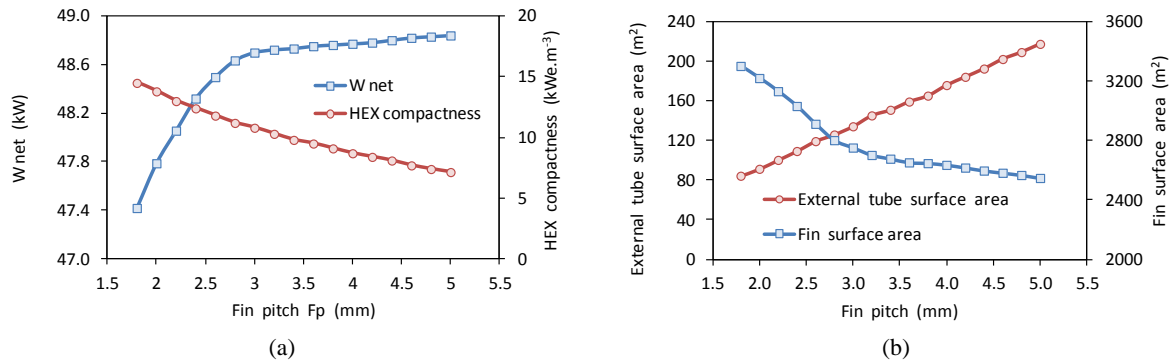


Fig. 2.17: Evolution of: a) net power and heat exchanger compactness, b) External tube and fin surface area as a function of fin pitch ($L = 3$ m, $D_i = 13.84$ mm, $P_T = 45$ mm, $P_L = 38.97$ mm, $\delta_f = 0.2$ mm, wavy fins, $N_H = 1$, $N_D = 1$)

2.3.3.4 Tube diameters and tube pitches

As stated previously, the fin-and-tube heat exchanger will be composed of continuous fin-and-tube crossing the flue-gas path. The main available configurations (tube diameters and tube pitches) for the continuous fin-and-tube heat exchangers for industry are shown in Table 2.3.

Table 2.3: Parameters of the main available configurations for continuous fin-and-tube heat exchangers

	D_i	Tube thickness (e)	P_T	P_L
Configuration 1	8 mm (3/8'')	0.76 mm	25 mm	21.65 mm
Configuration 2	10.92 mm (1/2'')	0.89 mm	37.5 mm	32.476 mm
Configuration 3	13.84 mm (5/8'')	1.01 mm	45 mm	38.97 mm

The heat-exchanger compactness and the net power in ORC system as a function of the internal mass velocity are shown in Fig. 2.18. For each configuration, the tube length is calculated at the optimal heat-exchanger compactness. By comparing configurations listed in Table 2.3, Fig. 2.18.a shows that Configuration 3 leads to more compact heat exchanger compared to Configurations 1 and 2. At the optimal internal mass velocity for which the heat-exchanger compactness is maximal (Fig. 2.18.a), Fig. 2.18.b shows that Configuration 3 leads to the highest net power produced in the ORC system. Thus, Configuration 3 seems the most appropriate for the present application.

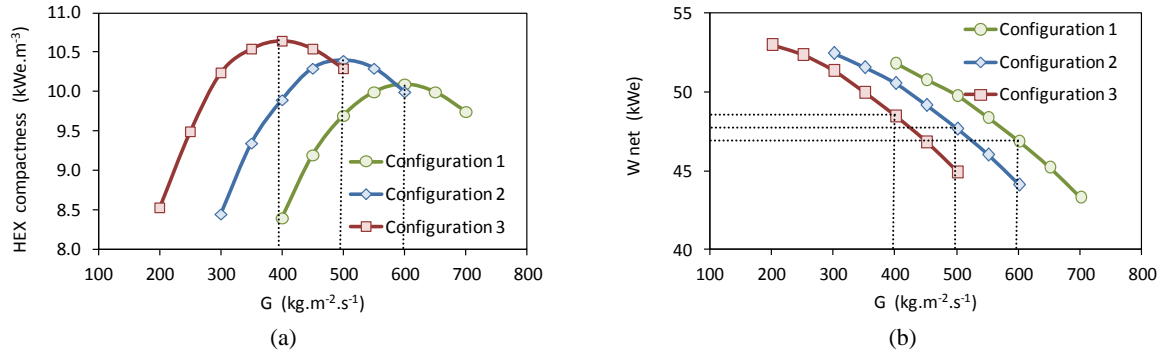


Fig. 2.18: Evolutions of: a) heat-exchanger compactness and b) Net power, vs. internal mass velocity for the different configurations listed in Table 2.3 ($F_p = 3$ mm, $\delta_f = 0.2$ mm, wavy fins, $N_H = 1$, $N_D = 1$)

2.3.3.5 Fin-and-tube heat exchanger circuitry

The main parameters for determining the fin-and-tube heat-exchanger circuitry are the number of horizontal rows per circuit (N_H) and the number of divisions along the tube length (N_D) (refers to Fig. 2.7). Table 2.4 shows the effects of “ N_H ” and “ N_D ” on the net power in ORC system. For “ $N_D = 1$ ”, the internal mass velocity at optimal heat-exchanger compactness for “ $N_H = 2$ ” is twice that for “ $N_H = 1$ ”, which leads to a decrease in the net power due to the increase of the in-tubes pressure drop because the heat exchanger will operate with higher internal mass velocity. For “ $N_D = 2$ ”, two horizontal rows per circuit ($N_H = 2$) give slightly higher net power compared to “ $N_H = 1$ ” and “ $N_H = 4$ ”. However, the net power value for “ $N_D = N_H = 2$ ” is slightly lower compared to that obtained for “ $N_D = N_H = 1$ ”. In conclusion, operating with “ $N_D = 1$ ” and “ $N_H = 1$ ” seems the most promising choice. By dividing the heat exchanger along tube length into n parts ($N_D = n$), the optimal corresponding number of horizontal rows will be equal to n ($N_H = n$).

Table 2.4: Effects of N_H and N_D on the net power produced by the ORC system ($L = 3$ m, $D_i = 13.84$ mm, $P_T = 45$ mm, $P_L = 38.97$ mm, $F_p = 3$ mm, $\delta_f = 0.2$ mm, wavy fins)

N_D	N_H	G @ optimal HEX compactness (kg.m ⁻² .s ⁻¹)	W_{net} (kWe)
1	1	~ 400	49.1
	2	~ 800	48.2
2	1	~ 200	48.5
	2	~ 400	48.7
	4	~ 800	47.9
4	1	~ 100	47.6
	2	~ 200	48.1
	4	~ 400	48.5
	8	~ 800	47.2

2.3.4 Effect of evaporation pressure on fin-and-tube heat-exchanger parameters

In this section, the effect of the evaporation pressure on the fin-and-tube heat-exchanger parameters is shown. Fig. 2.19 shows the evolution of the turbine power as a function of the evaporation pressure. The fin-and-tube heat-exchanger parameters will be compared for three evaporation pressures: “0.3”, “0.5” and “0.7” MPa. The first one corresponds to the latent heat optimum while the last one corresponds to the sensible heat optimum.

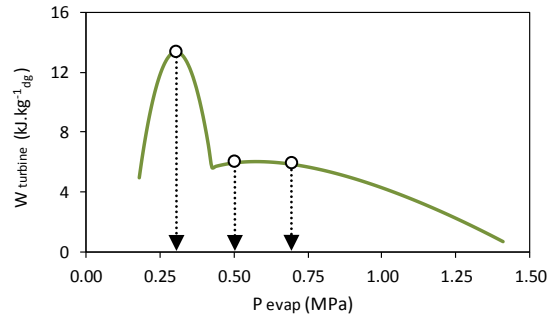


Fig. 2.19: Evolution of the turbine power as a function of the evaporation pressure (refers to Chapter 1)

The effect of evaporation pressures on heat-exchanger width is shown in Table 2.5. The comparison is done based on the same flue-gas frontal velocity and the same internal mass velocity and using the operating parameters shown in Table 2.4. Table 2.5 shows that the required number of vertical rows increases from twelve at “ $P_{\text{evap}} = 0.7$ ” MPa to twenty at “ $P_{\text{evap}} = 0.3$ ” MPa.

Table 2.5: Effect of evaporation pressure on fin-and-tube heat-exchanger parameters

$P_{\text{evap @ sat vap.}}$ (MPa)	0.3	0.5	0.7
m_{wf} (kg.s^{-1})	15.8	3.8	2.85
Q_{evap} (kW_{th})	3291	838	651
$m_{\text{c estimated}}$ (g.s^{-1})	914	33	0
$m_{\text{c calculated}}$ (g.s^{-1})	952	42	3.4
$DP_{\text{working fluid}}$ (kPa)	23	48	43
$DP_{\text{flue gases}}$ (Pa)	580	175	120
W_{turbine} (kWe)	158.30	66.83	64.5
W_{pump} (kWe)	2.45	1.31	1.50
W_{blower} (kWe)	15.10	4.40	3.10
W_{net} (kWe)	140.75	61.12	59.90
L_{tube} (m)	0.7	3.0	3.9
N_{c}	256	64	49
N_{v}	20	15	12

2.3.5 Effect of material selection on fin-and-tube heat-exchanger parameters

A comparison between stainless steel tubes and fins, and copper tubes and aluminum fins is shown in Table 2.6. The comparison is done based on the same flue-gas velocity and internal mass velocity and using the operating parameters shown in Table 2.6. Nine more vertical rows are required by replacing the copper tubes and aluminum fins with stainless steel tubes and fins.

Table 2.6: Comparison between stainless steel and copper tubes and aluminum fins

	Copper tubes - Aluminum fins	Stainless Steel tubes and fins
$P_{\text{evap @ sat vap.}}$ (MPa)	0.5	0.5
Q_{evap} (kW_{th})	838	838
$m_{\text{c estimated}}$ (g.s^{-1})	33	33
$m_{\text{c calculated}}$ (g.s^{-1})	42	44
DP_{internal} (kPa)	48	76
DP_{external} (Pa)	175	253
W_{turbine} (kWe)	66.83	66.83
W_{pump} (kWe)	1.31	1.39
W_{blower} (kWe)	4.40	6.55

W_{net} (kWe)	61.12	58.89
N_V	15	24

In conclusion, this section showed that optimized geometrical configurations could be found to ensure a compromise between net power produced in the ORC and the fin-and-tube heat-exchanger compactness. The next section will show the condensation modes that could occur in the fin-and-tube heat exchanger when the surface temperature drops below the water dew point temperature.

2.4 Condensation modes

The wet-ability of the surface with liquid depends on the contact angle between the liquid film and the flue-gas side surface. The contact angle is determined by the resultant between adhesive and cohesive forces. As shown in Fig. 2.20, a droplet is placed on the solid sample. The contact angle is defined as the angle between the solid sample surface and the tangent of ovate shape at the edge of the droplet.

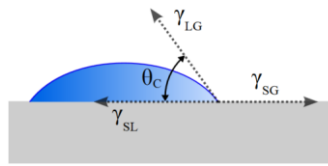


Fig. 2.20: Three-degree wetting and the corresponding contact angle

The relationship between the interfacial tensions and contact angles are expressed at a point on a three-phase contact line as follows:

$$\gamma_s = \gamma_{SL} + \gamma_L \cos \theta \quad \text{Eq.2.48}$$

Where:

γ_s : Surface tension of the solid sample

γ_L : Surface tension of the liquid

γ_{SL} : Interfacial tension between two phases

$\cos \theta$: Contact angle between liquid and solid

A contact angle less than 90° (low-contact angle) usually indicates that surface wetting is very favorable, and the fluid will spread over a large surface area. Contact angles greater than 90° (high-contact angle) generally means that surface wetting is unfavorable, so the fluid will minimize contact with the surface and form a compact liquid droplet. For water, a wet-able surface may also be termed “hydrophilic” and a non-wet-able surface “hydrophobic”. Table 2.7 describes varying contact angles and their corresponding solid/liquid interactions.

Table 2.7: Varying contact angle and their corresponding wet-ability

Contact angle	Degree of wetting	Strength of solid-liquid interaction	Surface types
$\theta_c = 0$	perfect wetting	Strong	Hydrophilic
$0 < \theta_c < 90^\circ$	high wet-ability	Strong	
$90^\circ \leq \theta_c < 180^\circ$	low wet-ability	Weak	Hydrophobic
$\theta_c = 180^\circ$	perfectly non wetting	Weak	

Depending on the wet-ability of the flue-gas side surface, water condensation on a heat exchanger can take the form of a drop-wise mode or a film-wise mode ([CHE 13], [THO 05]). The different condensing modes, together with the heat-exchanger geometry play a key role in the overall retention behavior and largely affect the thermal-hydraulic performance of the heat exchanger. Film-wise condensation occurs when heat-transfer surfaces on a heat exchanger are made of “wet-able”

materials. During condensation, a film of condensate spreads over these surfaces. As more vapor condenses on the outside of the film, its thickness increases and the film will start flowing downwards due to its weight. Heat transfer occurs through this film of condensate to the surface material beneath, then to the cooling medium. The liquid film is generally a poor heat conductor, contributing much to the thermal resistance for this mode of condensation.

If the heat-transfer surfaces are treated to become ‘non-wet-able’, the condensate that forms on the surface will be shaped like spherical beads and a drop wise condensation mode occurs. These beads adhere together to become larger as condensation proceeds. The bigger beads will then start to flow downwards due to their weight, thus collecting all other static beads along the way. As the beads increase in size, the velocity increases, finally leaving a trail of bare surface free from liquid film. This bare surface offers very little resistance to the heat transfer.

Advantages of drop-wise over film-wise condensation are apparent, resulting in a smaller heat-transfer area, smaller temperature difference, or larger heat-transfer rate for a fixed set of conditions. However, drop-wise condensation is not considered to be easily designed and controlled in process equipment. Generally, special materials must be employed (low-thermal conductivity, low-surface energy, low-wetting or highly polished materials) to reach drop-wise condensation. Hence, the process is susceptible to any surface fouling or oxidation that may bring the process back into the film-wise mode, with a corresponding reduction in thermal performance [THO 05].

On the other hand, in cases where the corrosive effect of acid liquid is a more important factor, the need arises for a surface on which the water can be removed without staying on the fin for long, resulting in a film-wise condensation mode, which is classified under the general term of hydrophilic. Hydrophilic coatings are particularly effective in environments of excessive condensation, to protect the heat-exchanger from the corrosive effect of water. In fact, water collects on the uncoated surface of the metal in large droplets. This leads to corrosion of the metals by the droplets, with the aid of the air flowing over the fins. Furthermore, the accumulated water droplets create a resistance to the airflow and have a detrimental effect on the heat-exchanger capacity. In order to prevent accumulation of water droplets on the surface, the friction coefficient between the droplets and the surface should be decreased. Hydrophilic coating, by virtue of low surface tension, enables water droplets to flow off the surface without facing a lot of resistance (film-wise mode). On coated surfaces, due to the low angle by which the droplets wet the fin surface, water does not conglomerate in large droplets and disperses easily. Thus, undesired accumulation is prevented and long operating of the heat exchanger at high performance is ensured. The controlled removal of the condensed acid liquid from the system is highly beneficial in protecting the heat exchanger [LIU 11].

2.5 Experimental methods

The objective of the experimental study is to examine the performance of heat exchangers with distinct airside surface wet-abilities, in order to develop a better understanding of the impact of surface properties on the moisture condensation and to adapt heat transfer and pressure drop correlations.

2.5.1 Description of the heat-exchanger specimens

Two types of surface coatings will be studied and tested: ‘Heresite’ treating and ‘Epoxy’ treating. The first one has a hydrophilic aspect and a film-wise condensation mode is expected when condensation occurs, while the last one has a more hydrophobic aspect.

‘Heresite’ is a unique baked phenolic coating thermal transfer uses to protect heat exchangers from acid corrosion. The ‘Heresite’ coating has effectively demonstrated its value in protecting heat transfer coils from corrosive attack, hereby appreciably increasing equipment service life. It is characterized by an excellent chemical and temperature resistance coupled with the good heat-transfer properties [THE 13].

‘Epoxy’ is also a commonly used coating material for protecting metal surfaces from salty or acidic environments. The resistance of ‘Epoxy’-coated Aluminum to corrosion delivers satisfying results in many industrial applications commonly encountered in practical applications. The ‘Epoxy’ coating method is used as the most economical and effective method, particularly in protecting metal surfaces exposed to the corrosive influence of humid and salty flue gases [FRI 04].

The heat-exchanger configurations to be tested are shown in Fig. 2.21, with their distinguished wettability. One heat exchanger is untreated (Fig. 2.21.a), the second one is treated to be hydrophilic through a ‘Heresite’ coating process (Fig. 2.21.b) and the third one is treated to be more hydrophobic through an ‘Epoxy’ coating process (Fig. 2.21.c).

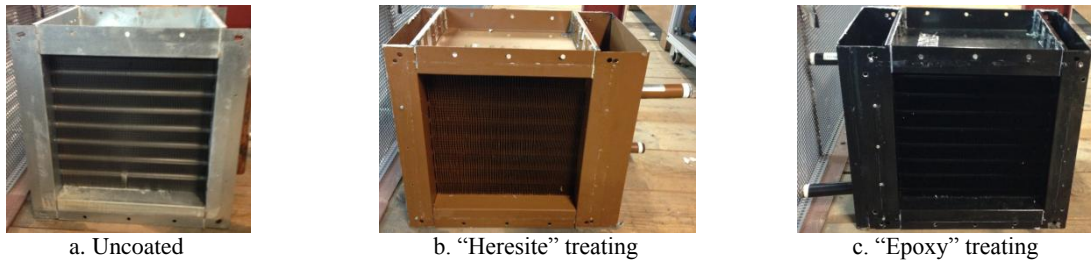


Fig. 2.21: Tested heat-exchanger specimens

The geometrical parameters are identical for the three specimens and are shown in Table 2.8. Each heat exchanger is composed of six vertical rows with a square frontal area, and a tube length of 0.36m. A 3-mm herringbone fin pitch is selected.

Table 2.8: Characteristics and geometrical properties of the three tested specimens

Tube material	copper	F_p (mm)	3
Fin material	aluminum	δf (mm)	0.2
Fin type	herringbone	P_T (mm)	45.00
Frontal area (m ²)	0.36*0.36	P_L (mm)	38.97
L_{tube} (m)	0.36	Θ_f (°)	~ 10
N_V	6	N_H	2

Fig. 2.22 shows the frontal and sides views of the uncoated specimen. The heat-exchanger circuitry could be shown in the side views (Fig. 2.22.b and Fig. 2.22.c).

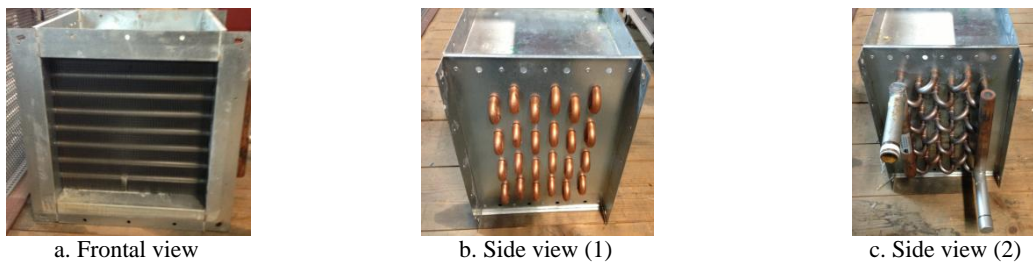


Fig. 2.22: Frontal and side views of the uncoated heat-exchanger specimen

2.5.2 Experimental apparatus and procedure

The diagram shown in Fig. 2.23 was used to measure the thermal hydraulic performance of the fin-and-tube heat exchanger. The tested fin-and-tube heat exchanger is noted HX02. The test bench is composed of a hot wet air generator and a water-cooling loop. The air circuit of the hot wet air generator includes mainly a blower (BW01), two electrical heaters (EH01 and EH02), and a steam injection system (HU01). As Fig. 2.23 suggests, airflow is driven by the air blower (BW01) through the first electrical heater (EH01, 50 kW), which heats the air to a desired temperature able to hold the desired humidity. The second electrical heater (EH02, 10 kW) controls the air temperature after the steam injection. Steam generated by a boiler could be injected into the system (HU01) in order to reach the desired air relative humidity. The needed steam quantity is provided by a water vaporization into a plate-heat exchanger (HX01) via a heat-exchange transfer between the hot oil entering from the boiler hot oil generator and the water entering from city water supply.

For the water-cooling loop, the water is used as a cold stream in the fin-and-tube heat exchanger. The water circuit includes mainly a water pump (Pump1) and a heat exchanger (HX03). The water entering the fin-and-tube heat exchanger is heated by the hot air stream. The water pump (Pump 1) supplies the hot water to the heat exchanger (HX03) where it is cooled. The coolant, which is a mixture of ethylene glycol and water, was supplied by a pump (Pump 2) to cool the water during experiments. The coolant had its temperature controlled by a chilled system.

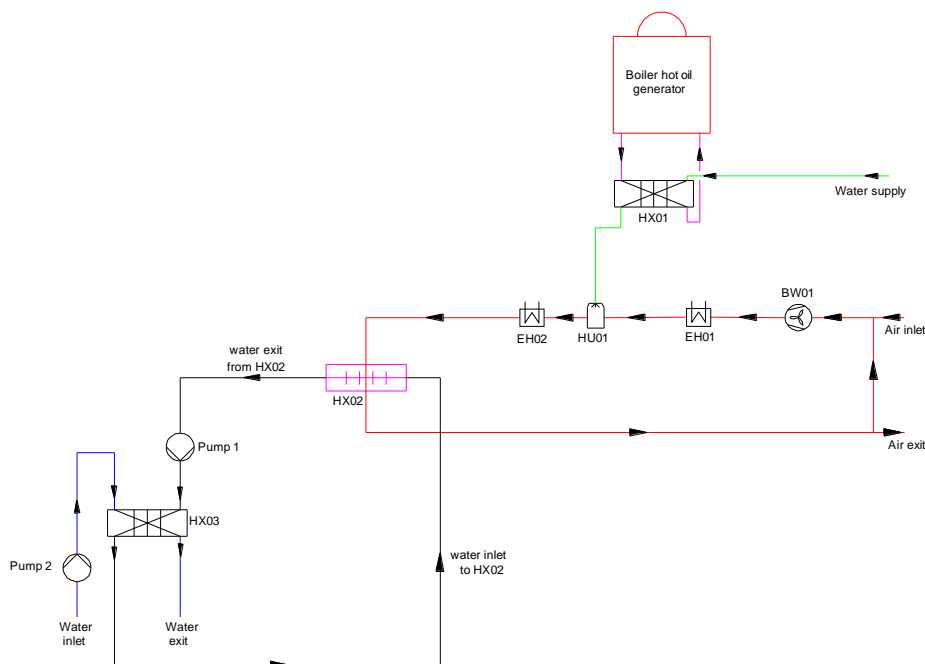


Fig. 2.23: Lay out for fin-and-tube heat-exchanger test bench

Fig. 2.24 shows a PID diagram (piping and instrumentation diagram) of the test bench. The test bench is instrumented in pressure sensors, temperature sensors, flow meters, and relative humidity sensors for evaluating thermal hydraulic performance of the fin-and-tube heat exchanger, and to establishing the energy balance between airside and waterside.

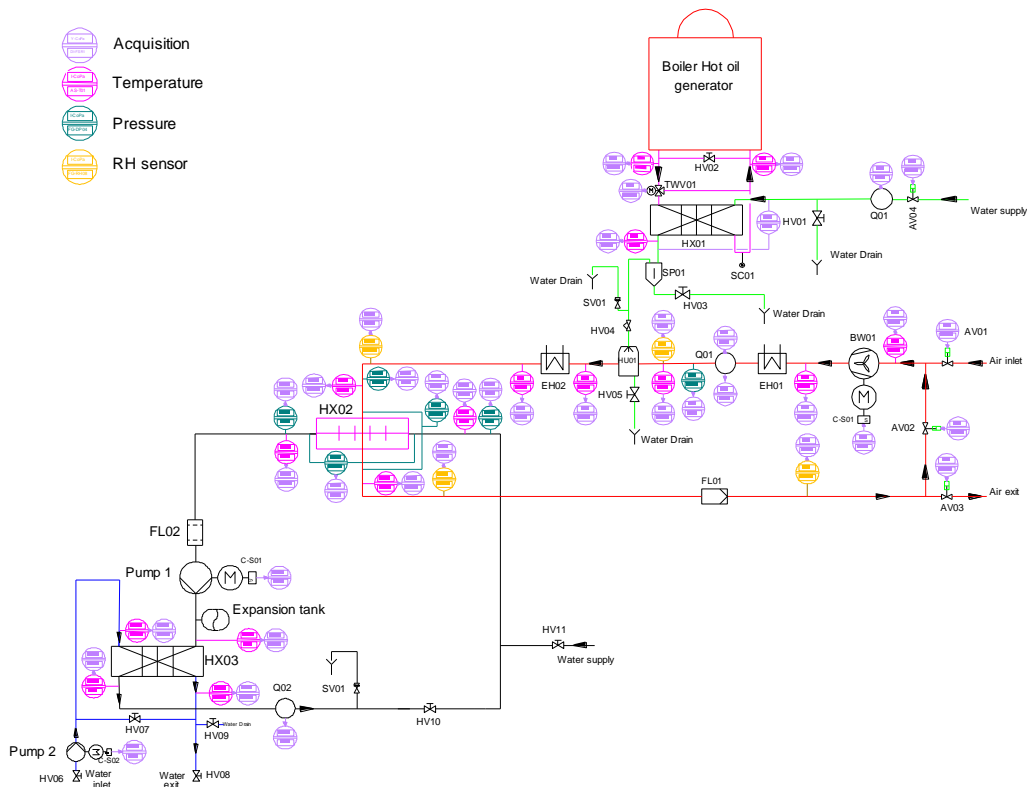


Fig. 2.24: PID diagram for fin-and-tube heat-exchanger test bench

Temperature sensors were positioned at the heat exchanger inlet and outlet to record the air and water inlet and outlet temperatures. Upstream and downstream water dew points of air were measured using hygrometers, and pressure drop across the heat exchanger was acquired with an electronic pressure transducer. An electromagnetic flow meter (Q02) was used to measure the water flow rate and a two-wing anemometer (Q01) was used to measure the airflow rate. In the oil circuit, temperature sensors were positioned at the inlet and outlet of the plate-heat exchanger (HX01) in order to control the oil temperature. The mass of steam injected is controlled using an automatic-valve (AV04). A temperature sensor is positioned to control the temperature of the steam exit from the plate-heat exchanger (HX01). A more detailed description of the test bench is presented in “Annex E”.

Fiberglass insulation of the fin-and-tube heat exchanger and air circuit has to be done in order to reduce thermal losses to the environment. Therefore, most of the data showed energy balance ($\|Q_a - Q_w\| / Q_{ave}$) within 5% and only these data were used for subsequent heat-transfer analysis and the average heat transfer (Q_{ave}) is taken into consideration.

Heat transfer and pressure drop for the three tested specimens were recorded over a range of operating conditions. For thermal-hydraulic measurements, the range of experimental conditions is provided in Table 2.9. As a result, inlet air temperature was varied between “60°C” and “140°C”, and upstream water dew point could be adjusted up to “60°C”. The airflow rate is varied from “500” to “4000” $m^3 \cdot hr^{-1}$ and the water mass flow rate is varied from “120” to “740” $g \cdot s^{-1}$. The water temperature at the fin-and-tube heat exchanger inlet is determined by the coolant capacity.

Table 2.9: Test conditions

Parameters	Variation range
Air inlet temperature (T_{air-in})	60°C - 140°C

Water dew point temperature (T_{dp})	Up to 60°C
Air volume flow rate (Q_{air})	500 - 4000 m ³ .hr ⁻¹
Airside Reynolds number (Re_{Dc})	1500 - 14000
Frontal air velocity ($V_{a,fr}$)	1 - 9 m.s ⁻¹
Effective air velocity ($V_{a,e}$)	1.5 - 15 m.s ⁻¹
Water mass flow rate (m_w)	120 - 740 g.s ⁻¹
Internal mass velocity (G)	150 - 1000 kg.m ⁻² .s ⁻¹

An experiment was initiated by circulating the airflow while bringing it to the desired temperature, velocity, and relative humidity. Water flow was then started to cool the heat exchanger. After a brief transient period at the beginning of each test (~5 minutes for dry test, and 10 ~ 15 minutes for wet test), it would reach steady state. Thermal hydraulic data would then be sampled out by a “CVI Lab-View” program for subsequent analysis. For wet tests, the experimental conditions were carefully set and monitored to ensure that water vapor condensation occurs inside the heat exchanger and then the temperature of part of the heat transfer surface was below the water dew point throughout the experiment.

2.6 Data reduction and interpretation

In fin-and-tube heat exchangers, it is usual to express the thermal-hydraulic performances with the Colburn j-factor and the friction factor of the heat exchanger, f. The Colburn j-factor for heat transfer is expressed by [PER 04]:

$$j = \frac{Nu_a}{Re_{D_h} Pr_a^{1/3}} = \frac{h_o}{c_{p,a} \cdot G_{c,a}} \cdot Pr_a^{2/3} \quad \text{Eq. 2.49}$$

Where the mass flux, $G_{c,a} = \frac{m_a}{A_c}$, corresponds to the minimum free flow area, and “ D_h ” is the hydraulic diameter defined by:

$$D_h = 4 \frac{A_c}{A_o} P_L \quad \text{Eq. 2.50}$$

In wet conditions, the sensible Colburn j-factor is expressed as a function of the sensible heat transfer coefficient at the airside [PER 04]:

$$j_{sensible} = \frac{Nu_a}{Re_{D_h} Pr_a^{1/3}} = \frac{h_{c,o}}{c_{p,a} \cdot G_{c,a}} \cdot Pr_a^{2/3} \quad \text{Eq. 2.51}$$

The heat-exchanger friction factor, f, could be expressed as [PER 04]:

$$f = \frac{2}{\rho_a} \cdot \frac{DP_a}{V_e^2} \cdot \frac{A_c}{A_o} \quad \text{Eq. 2.52}$$

The heat transfer and pressure drop correlations used on the waterside are in “Annex D”. Data reduction and interpretation follow the method detailed in Section 2.3.2. For evaluating thermal performance under dry conditions, the rate equations (Eq. 2.18 to Eq. 2.26) will be used. Under wet conditions, the rate equations (Eq. 2.27 to Eq. 2.42) will be used. These equations were programmed using “VBA excel” with all the measured data and the Colburn j and f factors were determined in an iterative manner.

Uncertainties in all measured data are listed in Table 2.10, and estimation of the relative uncertainties for all the calculated quantities followed the error propagation methodology as described below.

Table 2.10: Uncertainties in measured data

Parameter	Uncertainty	Measuring device
T _{air}	± 0.1°C	PT100 (4 wires)
T _{water}	± 0.1°C	PT100 (4 wires)
Q _{air}	± 0.30%	Anemometer
m _{water}	± 0.10%	Electromagnetic flow meter
RH	± 0.80%	Hygrometers
P _{water}	± 0.15%	Pressure sensors
ΔP _{water}	± 0.075%	Electronic pressure transducer
ΔP _{air}	± 0.075%	Electronic pressure transducer

Considering a given function that connects the calculated quantity, “X”, with several other measured parameters (a,b,c,...) as follows: [GLY 08]

$$X = f(a, b, c, \dots) \quad \text{Eq. 2.53}$$

The absolute uncertainty on the calculated value of X is given by:

$$\Delta X = \sqrt{\left(\frac{\partial f}{\partial a}\right)^2 \cdot (\Delta a)^2 + \left(\frac{\partial f}{\partial b}\right)^2 \cdot (\Delta b)^2 + \left(\frac{\partial f}{\partial c}\right)^2 \cdot (\Delta c)^2 + \dots} \quad \text{Eq. 2.54}$$

The relative uncertainty on the calculated value of “X” is equal to the absolute humidity over the calculated value of “X” as follows:

$$\frac{\Delta X}{X} = \frac{1}{X} \sqrt{\left(\frac{\partial f}{\partial a}\right)^2 \cdot (\Delta a)^2 + \left(\frac{\partial f}{\partial b}\right)^2 \cdot (\Delta b)^2 + \left(\frac{\partial f}{\partial c}\right)^2 \cdot (\Delta c)^2 + \dots} \quad \text{Eq. 2.55}$$

This gives a simple equation for estimating the uncertainty in a calculated quantity from the uncertainty in measured quantities from which it is calculated. This is what is meant by propagation of error.

Through a standard error propagation calculation, as described in Eq. 2.54, the average uncertainty on Colburn j factors was found to be about ± 5.8% under dry test conditions, and about ± 12.6% under wet test conditions. The higher j uncertainty in wet case is mostly from the uncertainty of upstream and downstream dew point measurements. The uncertainty in f factors is about ± 5.25% under both dry and wet test conditions, which comes mainly from the accuracy of pressure transducers and measurement of airflow rates.

2.7 Tests results and discussion

In this section, thermal hydraulic data (conventional Colburn j and f factors) of the tested heat exchangers are presented. A comparison will be drawn among the three tested specimens in order to illustrate the effect of surface coating and wet-ability on the heat-exchanger performances.

2.7.1 Dry-condition test data

Experiments were first conducted under dry test conditions to examine the impact of surface coating. The water dew point of circulating air was maintained low ($\sim 15^{\circ}\text{C}$) so that the surface temperature is always above the water dew point temperature. Therefore, no condensation initiated on the heat-exchanger surface. For each specimen, around 72-tested points have been done by varying the operating parameters in the corresponding range indicated in Table 2.9. Results show that the Colburn j and f factors vary mainly with the airside flow rate. None or little effect of the airside temperature on Colburn j and f factors was observed.

The experimental Colburn j and f factors are presented as a function of the airside Reynolds numbers in Fig. 2.25.a and Fig. 2.25.b respectively. Depending on the airflow rate, the airside Reynolds number will vary within the range [1500-14500], and the frontal airside velocity will vary within the range [1-9 $\text{m}\cdot\text{s}^{-1}$]. Fig. 2.25.a and Fig. 2.25.b show that the Colburn j and f factors decrease by increasing the airside Reynolds numbers. As a general trend, the data suggest that the treated specimens show slightly lower Colburn j and higher f factors than do the untreated heat exchanger. The values of Colburn j and f factors for the specimen with "Epoxy" treating are more scattered at a given Reynolds number compared to the two others specimens.

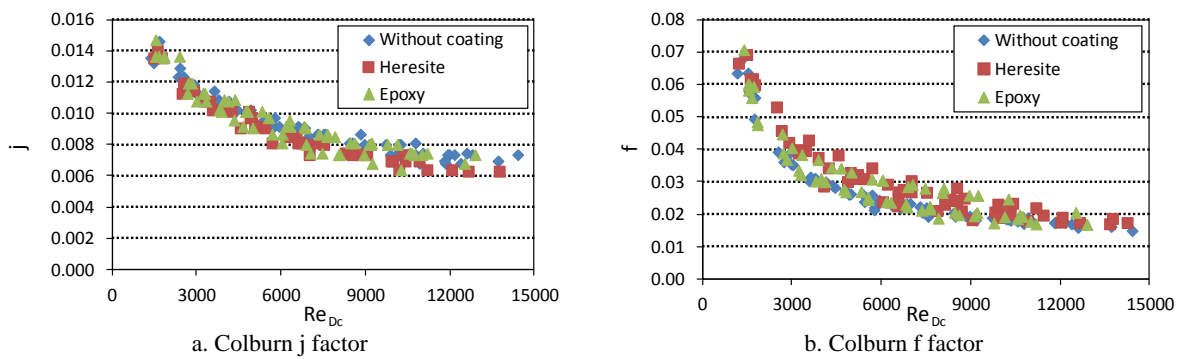


Fig. 2.25: Evolution of experimental: (a) Colburn j -factor, (b) f -factor as a function of the airside Reynolds number

In order to show clearly the effect of surface coating on the heat-exchanger performance, the experimental Colburn j and f factors are averaged over intervals of Reynolds numbers as shown in Fig. 2.26.a and Fig. 2.26.b respectively. Fig. 2.26.a shows that the three specimens display very similar behavior for the Colburn j factor at low Reynolds numbers. As the Reynolds number increases, a noticeable difference in the Colburn j factor between the three specimens appears. The specimen with 'Heresite' treating presents the lowest Colburn j factor, followed by the specimen with 'Epoxy' treating, while the untreated specimen presents the highest one.

Averaged f factors for the three-tested specimens are presented in Fig. 2.26.b. The specimen with 'Heresite' treating presents the highest f factor while the uncoated specimen presents the lowest one over the entire range of the Reynolds numbers. The specimen with "Epoxy" treating presents an f factor close to the uncoated one at low Reynolds numbers ($Re_{Dc} < 3000$), while it becomes closer to the 'Heresite' one at high Reynolds numbers.

The difference of Colburn j and f factors between the three-specimens is mainly due to the coating process. When analyzing the hydraulic performance data for partially wet tests, these differences will

be taken into account to ensure a clearer interpretation of the effect of water vapor condensation on surface coating.

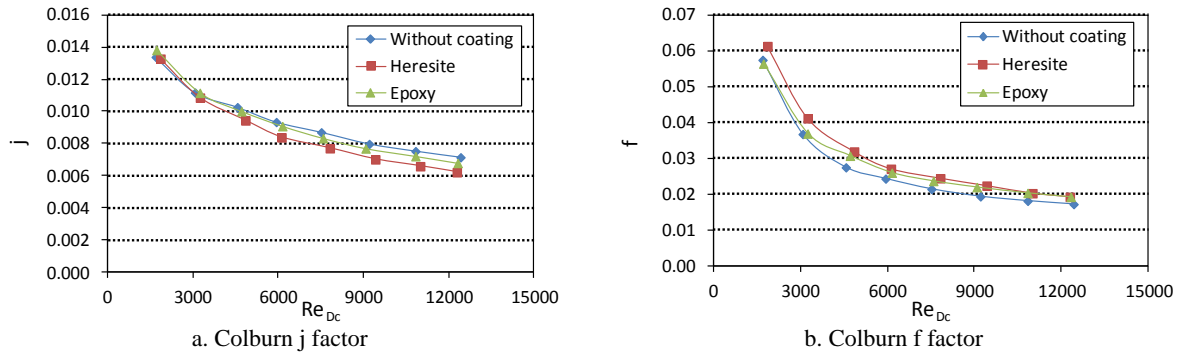


Fig. 2.26: Evolution of: (a) Colburn j-factor, (b) f-factor as a function of the airside Reynolds number

The relative variations of Colburn j and f factors for the ‘Heresite’ and ‘Epoxy’ specimens compared to the uncoated specimen as a function of the airside Reynolds number are shown in Fig. 2.27.a and Fig. 2.27.b respectively. Fig. 2.27.a shows that the relative decrease in the Colburn j factor varies between 3% and 13% for the specimen with ‘Heresite’ treating while it is less than 6% for the specimen with ‘Epoxy’ treating. The relative decrease in the f factor varies between 5 and 16% for the two specimens. The reason why the Colburn j factor for specimen with ‘Epoxy’ treating is higher than for the uncoated one at low Reynolds numbers ($Re_{Dc} < 3000$) is not clear. In general, it is due to experimental uncertainties at low air mass flow rate.

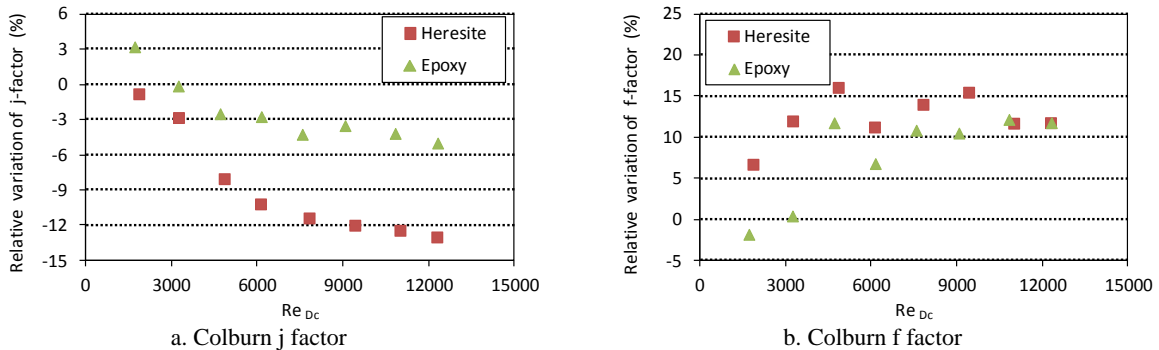


Fig. 2.27: Relative variations of: (a) Colburn j-factor, (b) f-factor as a function of the airside Reynolds number compared to the uncoated specimen

The evolution of the heat-exchanger area goodness (j/f) as a function of the airside Reynolds number is shown in Fig. 2.28.a for the three tested specimens. It is clear that the heat-exchanger area goodness for the specimen with ‘Heresite’ treating is the lower one over the entire range of the Reynolds numbers. The specimen with ‘Epoxy’ treating presents heat-exchanger area goodness close to the uncoated one at low Reynolds numbers ($Re_{Dc} < 3000$), while it becomes more close to the ‘Heresite’ one at high Reynolds numbers.

The relative variations of the heat-exchanger area goodness factor for the ‘Heresite’ and ‘Epoxy’ specimens compared to the uncoated specimen as a function of the airside Reynolds number are shown in Fig. 2.28.b. It varies between 6% and 25% for the specimen with ‘Heresite’ treating while it is less than 16% for the specimen with ‘Epoxy’ treating.

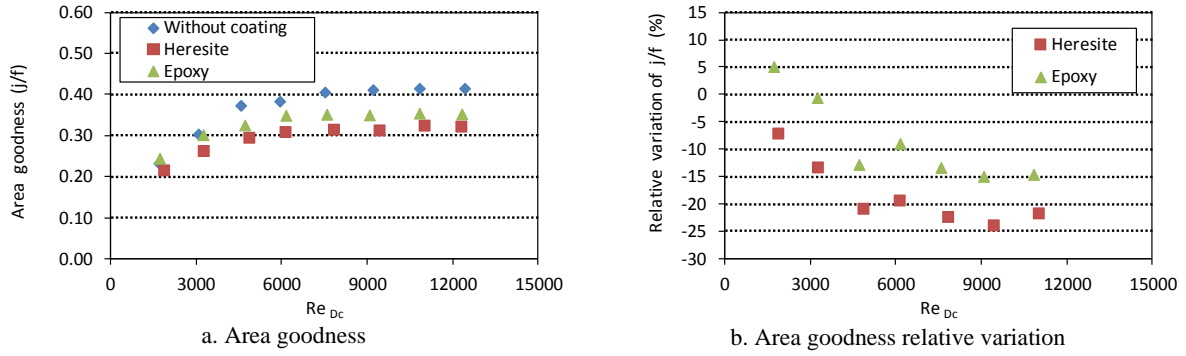


Fig. 2.28: Evolution of heat-exchanger area goodness (j/f) as a function of the airside Reynolds number

A comparison between experimental and correlated Colburn j and f factors is shown in Fig. 2.29 for the three tested specimens. Note that the correlated Colburn j and f factors are valid for a Reynolds number (Re_{Dc}) ranging between “300” and “10000” (see “Annex D” for correlations). Fig. 2.29 shows that a relative error within $\pm 40\%$ exists. The Colburn j factor is mainly underestimated, while the f factor is mainly overestimated.

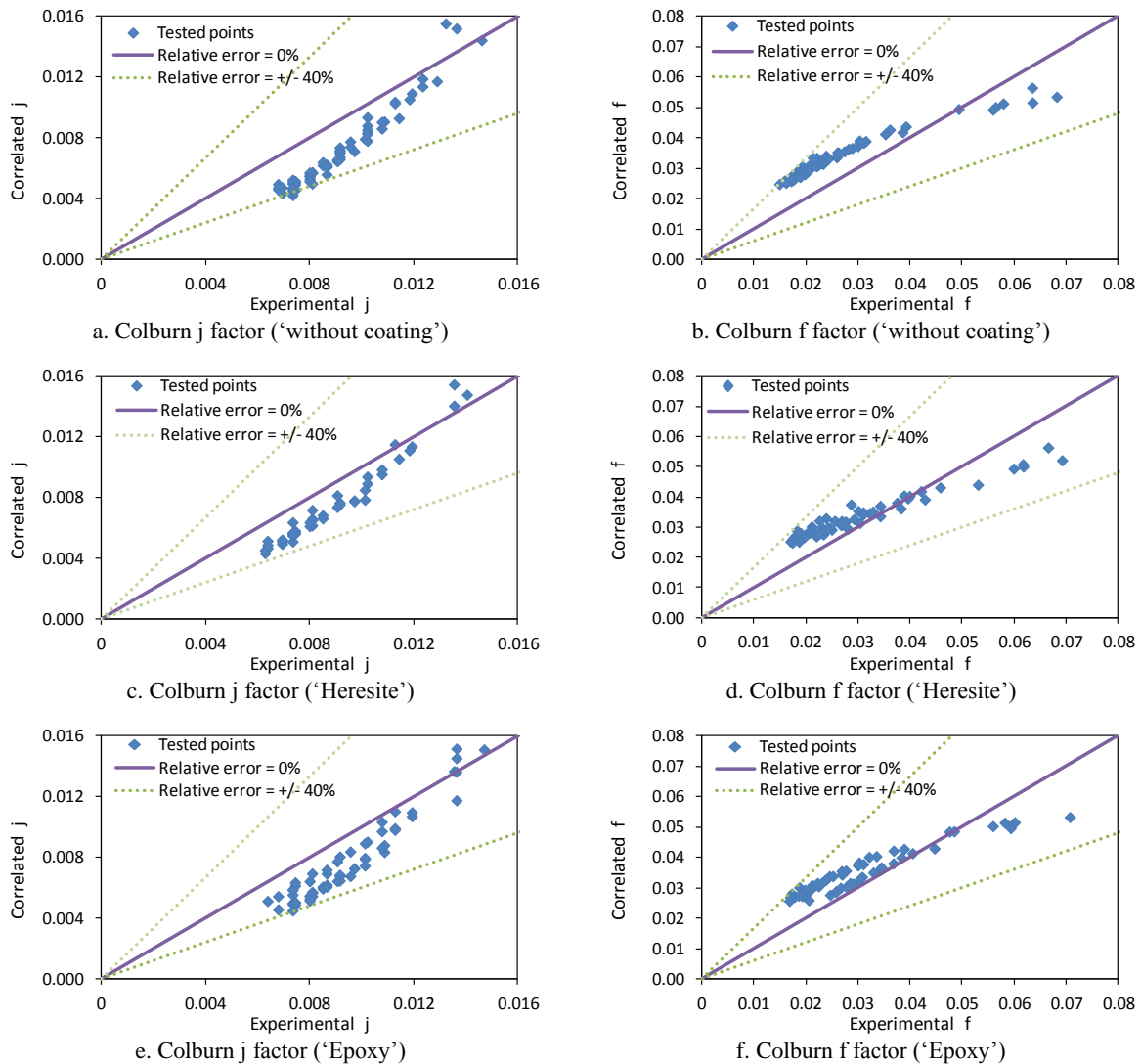


Fig. 2.29: Comparison between experimental and correlated Colburn j and f factors

The evolutions of the relative error between experimental and correlated Colburn j and f factors as a function of the airside Reynolds number are shown in Fig. 2.30.a and Fig. 2.30.b respectively for uncoated specimen. The relative errors are averaged over distant intervals of Reynolds numbers. Fig. 2.30 shows that the Colburn j factor (resp. f factor) is mainly underestimated (resp. overestimated) at high Reynolds numbers ($Re_{Dc} > 4000$).

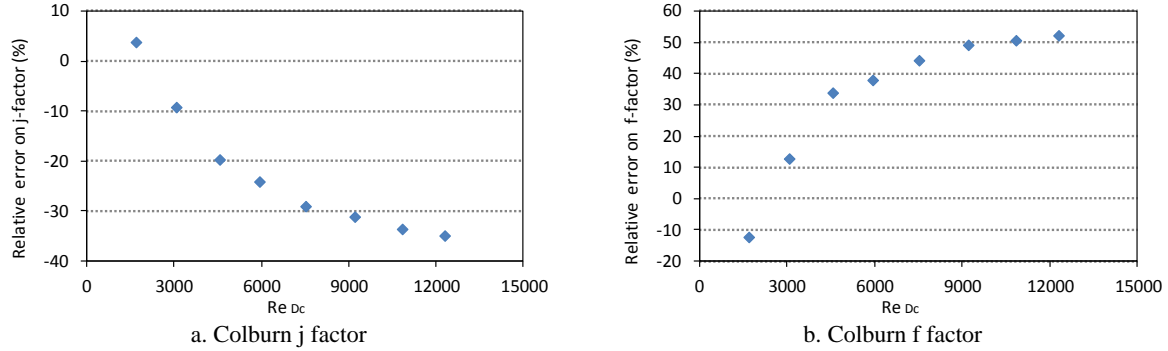


Fig. 2.30: Relative errors between experimental and correlated: (a) Colburn j -factor, (b) f -factor as a function of the airside Reynolds number for the uncoated specimen

In the general design method of fin-and-tube heat exchanger presented in § 2.3, the ranges of operating conditions used are listed in Table 2.11. The Reynolds number (Re_{Dc}) is varied between 800 and 2300. By referring to Fig. 2.30, relative errors are within 10% for the Colburn j factor and 15% for the f factor. Therefore, the airside correlations used in § 2.3 to calculate the Colburn j and f factors in dry mode are validated.

Table 2.11: Range of the operating conditions used in § 2.3

Parameters	Range
G	200 - 500 $\text{kg}\cdot\text{m}^{-2}\cdot\text{s}^{-1}$
$V_{a,s}$	0.8 - 2 $\text{m}\cdot\text{s}^{-1}$
$V_{a,e}$	1.4 - 3.8 $\text{m}\cdot\text{s}^{-1}$
Re_{Dc}	800 - 2300

For a given heat exchanger geometry, the Colburn j and f factors depend mainly on the airside Reynolds numbers. They could be correlated from the experimental data as follows.

For the “uncoated” specimen:

$$j_{\text{correlated new}} = 0.1493 Re_{Dc}^{-0.321} \quad \text{Eq. 2.56}$$

$$f_{\text{correlated new}} = 3.834 Re_{Dc}^{-0.580} \quad \text{Eq. 2.57}$$

For the specimen with “Heresite” treating:

$$j_{\text{correlated new}} = 0.2348 Re_{Dc}^{-0.381} \quad \text{Eq. 2.58}$$

$$f_{\text{correlated new}} = 4.6423 Re_{Dc}^{-0.585} \quad \text{Eq. 2.59}$$

For the specimen with “Epoxy” treating:

$$j_{\text{correlated new}} = 0.1853 Re_{Dc}^{-0.348} \quad \text{Eq. 2.60}$$

$$f_{\text{correlated new}} = 3.4236 Re_{Dc}^{-0.558} \quad \text{Eq. 2.61}$$

A comparison between the new correlated Colburn j and f factors and the experimental ones shows that the relative error is within $\pm 10\%$ for the Colburn j factor and $\pm 15\%$ for the f factor (Fig. 2.31).

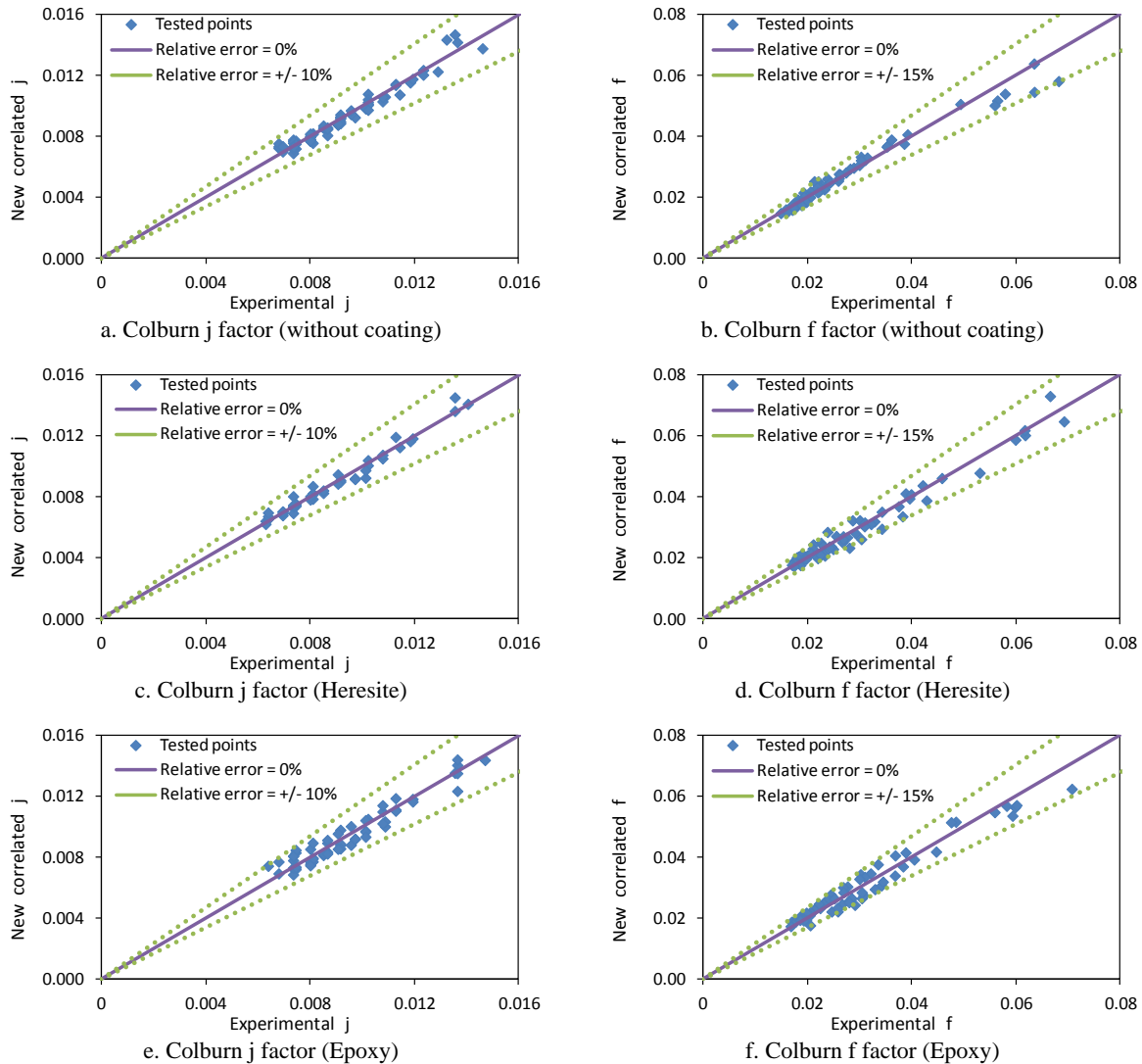


Fig. 2.31: Comparison between experimental and correlated Colburn j and f factors

The new correlated Colburn j and f factors listed in Eq. 2.56 to Eq. 2.61 are plotted as a function of the airside Reynolds number as shown Fig. 2.32. Trends of curves are similar so those presented Fig. 2.26.

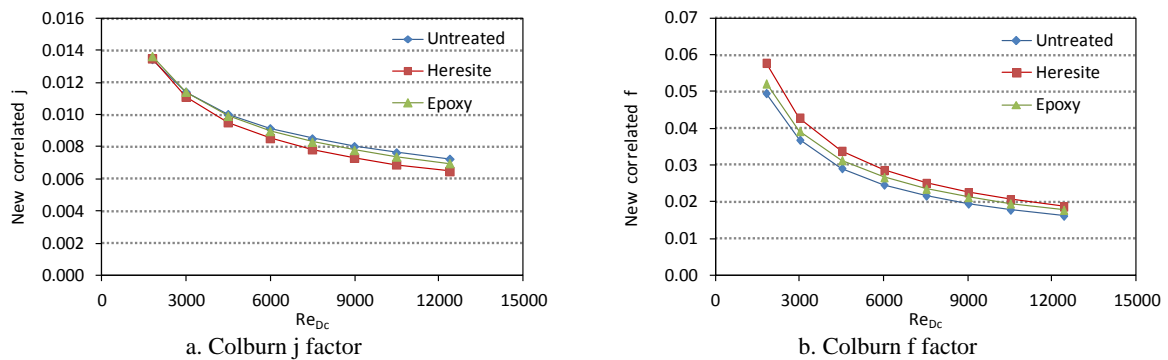


Fig. 2.32: Evaluation of the new correlated: (a) Colburn j -factor, (b) f -factor as a function of the airside Reynolds number for the three tested specimens

When analyzing the hydraulic performance data for partially wet test conditions, correlations shown in Eq. 2.56 to Eq. 2.61 will be used to calculate the Colburn j and f factors in dry region in order to ensure a clearer interpretation of the sensible Colburn j and wet f factors when dehumidification occurs.

2.7.2 Partially wet-condition test data

Experiments were conducted under partially wet-test conditions to examine the impact of surface coating. The water dew point of circulating air was maintaining relatively high ($\sim 60^\circ\text{C}$) so part of the heat-exchanger surface will be partially below the water dew point temperature. Therefore, a condensation initiated on heat-exchanger surface is detected. For each specimen, around 20-tested points are performed. These tests are carried out by varying the flow rate at both airside and waterside in the corresponding range indicated in Table 2.9. The inlet air temperature is maintained between 70°C and 90°C .

In the wet region, the sensible j -factor is calculated using Eq. 2.51, and the f factor is calculated using Eq. 2.52. In the dry region; depending on the surface treatment, validated Eq. 2.56 to Eq. 2.61 will be used to calculate the Colburn j and f factors.

Under wet conditions, the rate equations (Eq. 2.27 to Eq. 2.42) will be used. These equations were programmed using “VBA-excel” with all the measured data and the sensible Colburn j and wet f factors were determined iteratively.

During the experiments, the Reynolds number (Re_{Dc}) is kept above 4000 in order to maintain the desired water dew point ($\sim 60^\circ\text{C}$), because at low-air velocity, the quantity of water vapor injected is directly condensed into the air circuit thereby preventing water dew point rise.

The experimental Colburn j and f factors are presented as a function of the airside Reynolds number in Fig. 2.33.a and Fig. 2.33.b respectively. A comparison between Fig. 2.33 and Fig. 2.25 shows that the sensible Colburn j and the wet f factors are higher by around 20% compared to those obtained in dry case; this is due mainly to the enhanced surface roughness under water-vapor condensation mode.

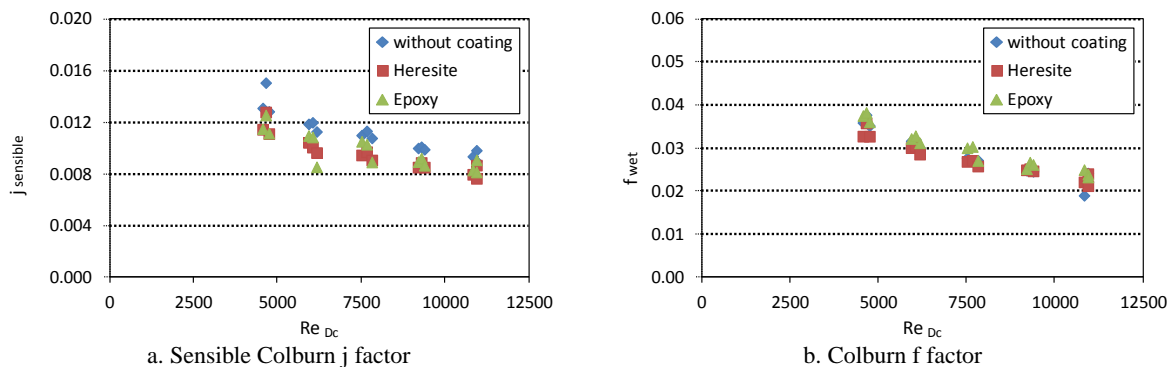


Fig. 2.33: Evolution of experimental : (a) Sensible Colburn j -factor, (b) Colburn f -factor as a function of the airside Reynolds number

In order to illustrate clearly the effect of surface wet-ability on the thermal hydraulic performances of the heat exchanger, the relative variations of the Colburn sensible j and f factors for the treated specimens compared to the untreated one is plotted as a function of the airside Reynolds number as

shown in Fig. 2.34. Note that the relative variations are averaged with respect to the airside Reynolds number.

Fig. 2.34.a shows that, by applying ‘Heresite’ surface treatment, heat-transfer performance of the heat exchanger is influenced. The relative decreases in the sensible Colburn j factor are within 14 to 15% over the entire range of the Reynolds numbers. These numbers are partially due to the coating impact on geometry, as the Colburn j factor of the heat exchanger with ‘Heresite’ treating was already 9 to 14% lower than the uncoated surface for the same range in the Reynolds numbers (refer to Fig. 2.27.a). A comparison between Fig. 2.34.a and Fig. 2.27.a shows that the degradation in the Colburn sensible j factor is observed mainly in the low Reynolds numbers range ($Re_{Dc} < 7500$). This small degradation is possibly due to the film-wise mode of condensation, which builds up an insulating liquid film and provides little portion of bare surface area for heat transfer. At high Reynolds numbers ($Re_{Dc} > 7500$), the air velocity increases the flow of the condensate toward the exit face of the heat exchanger, which reduces the thickness of the insulating liquid film and the relative decrease is almost the same obtained as for the dry case.

As also shown in Fig. 2.34.a, heat-transfer degradation was observed on the ‘Epoxy’ treated specimen. The relative decreases in the sensible Colburn j factor is around 15% (resp. 9%) at high (resp. low) airside Reynolds numbers. Note that in dry mode, the relative decreases is around 3% (resp. 6%) at high (resp. low) airside Reynolds numbers (refer to Fig. 2.27.a).

The relative variations of the wet f factor for the treated specimens compared to the untreated one are presented in Fig. 2.34.b. It can be seen that ‘Heresite’ treatment reduces pressure drop across the heat exchanger. The hydrophilic specimen displays slightly lower wet f factors than does the untreated one. This effect is quite visible at relatively low Reynolds numbers ($Re_{Dc} < 7500$). This is due mainly to the film wise mode of condensation. In addition, there is no noticeable difference for the wet f factors between the heat exchanger with ‘Epoxy’ treating and the untreated one, which avoids the criteria of bridging effect of the condensate retained on the fins and a selected fin pitch of 3 mm seems to be justified.

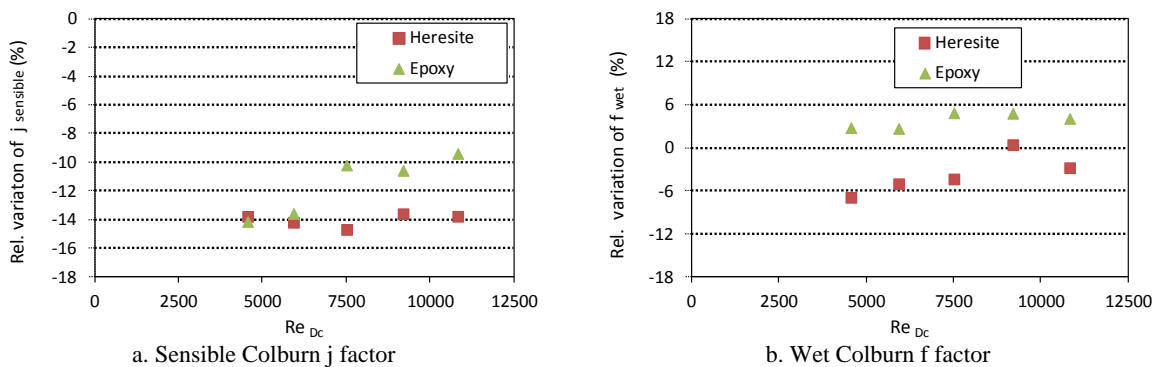


Fig. 2.34: Relative variations of: (a) Sensible Colburn j -factor, (b) f -factor compared to the uncoated specimen as a function of the airside Reynolds number

The evolution of the heat-exchanger area goodness (j/f) as a function of the airside Reynolds number is shown in Fig. 2.35.a for the three tested specimens. As a general trend, Fig. 2.35.a suggests that the uncoated specimen presents the highest heat-exchanger area goodness (j/f).

The relative variations of the heat-exchanger area goodness factor for the specimens with ‘Heresite’ and ‘Epoxy’ treating compared to the uncoated specimen as a function of the airside Reynolds number

are shown in Fig. 2.35.b. At relatively low Reynolds numbers ($Re_{Dc} < 7500$), the relative decreases for the specimen with ‘Heresite’ treating is lower than that of the specimen with ‘Epoxy’ treating, while the relative decreases are in the same range for both treated specimen at high Reynolds numbers. A comparison between Fig. 2.35.b and Fig. 2.28.b shows that the condensation mode promotes the specimen with ‘Heresite’ treating to the ‘Epoxy’ one.

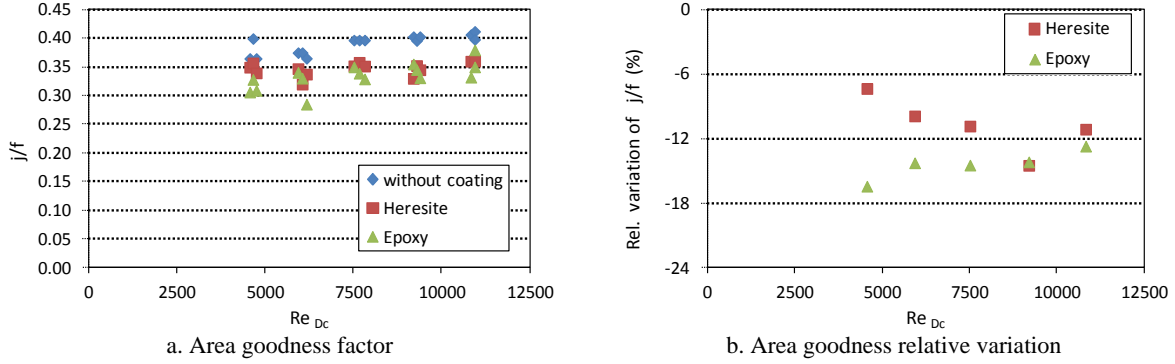


Fig. 2.35: Evolution of heat-exchanger area goodness (j/f) as a function of the airside Reynolds number

In conclusion, the specimen with ‘Heresite’ treating operates well in the wet condensation mode. Heat-transfer performance of the specimen with ‘Heresite’ treating is normally not strongly influenced by the condensation effect. However, pressure drop could be slightly reduced due to the enhancement of surface wet-ability. The specimen with ‘Epoxy’ treating is less efficient than the ‘Heresite’ one in the wet-condensation mode. No bridging effect was noticed even at low Reynolds numbers.

Similarly to the dry case, for a given heat-exchanger geometry, the sensible Colburn j and wet f factors depend mainly on the airside Reynolds numbers. They could be correlated from the experimental data in the Reynolds number range “ $4500 < Re_{Dc} < 11000$ ” as follows.

For the uncoated specimen:

$$j_{sensible\ correlated\ new} = 0.4677 Re_{Dc}^{-0.421} \quad \text{Eq. 2.62}$$

$$f_{wet\ correlated\ new} = 2.9723 Re_{Dc}^{-0.524} \quad \text{Eq. 2.63}$$

For the specimen with “Heresite” treating:

$$j_{sensible\ correlated\ new} = 0.3936 Re_{Dc}^{-0.419} \quad \text{Eq. 2.64}$$

$$f_{wet\ correlated\ new} = 1.5701 Re_{Dc}^{-0.456} \quad \text{Eq. 2.65}$$

For the specimen with “Epoxy” treating:

$$j_{sensible\ correlated\ new} = 0.2301 Re_{Dc}^{-0.355} \quad \text{Eq. 2.66}$$

$$f_{wet\ correlated\ new} = 2.5448 Re_{Dc}^{-0.502} \quad \text{Eq. 2.67}$$

Finally, it should be noted that, in the general design method of the fin-and-tube heat exchanger presented in § 2.3, correlations used for the sensible Colburn j and wet f factors are valid for a

Reynolds number (Re_{Dc}) ranging between “300” and “3500” (see “Annex D” for correlations) during dehumidification process. On the other hand, the new developed correlations from the experimental data (Eq. 2.62 to Eq. 2.67) are valid for a Reynolds number (Re_{Dc}) ranging between “4000” and “11000”. Therefore, a comparison of the relative errors between the correlated and the experimental correlations cannot be suitable in this case.

2.8 Conclusions

The recovery of low-temperature waste heat ($\sim 120^\circ\text{C}$) using an indirect-contact water-vapor condensation process via a fin-and-tube heat exchanger is a promising heat recovery technology provided the acid corrosion problems can be overcome in a cost-effective way.

Estimating the dew point of the acid gases is the starting point in understanding the corrosion problems in fin-and-tube heat exchangers whenever high-moisture content flue gases contain gaseous pollutants such as nitrogen oxides (NO_x), sulfur dioxide (SO_2) and sulfur trioxide (SO_3). While the precise dew point for sulfuric acid (H_2SO_4) formation depends on the SO_3 concentration, a rate of “2 ppm” SO_3 in flue gases could bring the acid dew point to a temperature in the same range as the inlet flue-gas temperature ($\sim 120^\circ\text{C}$). Thus, acid condensation is unavoidable and the safe zone almost does not exist when recovering heat at low-temperature level ($T \sim 120^\circ\text{C}$). Nitric acid (H_2NO_3) and sulfuric acid (H_2SO_3) condense at lower temperatures than sulfuric acid (H_2SO_4). Two distinct acid zones could be distinguished in the heat exchanger: higher temperature, with highly concentrated sulfurous acid and lower temperature with a dilute acid mixture, possibly containing sulfuric, hydrochloric, and nitric acids. Technologies that can minimize chemical attack while cooling exhaust gases below the condensation point could be achieved by using corrosion resistant materials.

The design of the fin-and-tube heat exchanger requires the combination of a very low driving temperature difference for heat extraction with a very low-pressure drop for the gas stream. The use of the net power produced by the ORC to optimize the operating and geometrical parameters of the fin-and-tube heat exchanger needs the assessment of the combined effect of heat transfer and pressure drop through the simultaneous interaction within the fin-and-tube heat exchanger. The geometry of an Organic Rankine Cycle (ORC) fin-and-tube heat exchanger has been derived, and optimized geometrical configurations have been found out. Results show that operation parameters (airside velocity, internal mass velocity), geometrical parameters (fin types, fin pitches, tube lengths, tube diameters, tube pitches) and fin-and-tube heat-exchanger circuitry could be optimized to ensure a compromise between net power produced by the ORC and heat exchanger compactness.

Condensation modes play a key role in the overall retention behavior and could affect the thermal-hydraulic performance of the heat exchanger. Water condensation on a heat exchanger can take the form of a drop-wise mode or a film-wise mode. Film-wise mode of condensation is more promising when the need arises for a surface on which the water can be removed without staying on the fin for long time.

In order to develop a better understanding of the impact of surface wet-abilities on thermal hydraulic performances of fin-and-tube heat exchangers, experimental data for thermal hydraulic performances for fin-and-tube heat exchangers with identical geometry and differing surface wet-ability are reported; conventional methods have been used to provide airside Colburn j and f factors. Two types of treated surface have been proposed: “Heresite” treating (hydrophilic aspect) and “Epoxy” treating (more hydrophobic aspect). These two coating technologies have effectively demonstrated their values

in protecting heat-transfer surfaces from corrosive attack, hereby appreciably increasing equipment service life.

Significant experimental findings show that under dry operation data, the treated specimens present degradation in thermal hydraulic performances compared to the uncoated specimen. The degradation is more noticeable for the specimen with “Heresite” treating rather than the ‘Epoxy’ one. This is mainly due to the coating manufacturing process.

Wet conditions data show that after applying hydrophilic surface treatment, heat transfer performance of the heat exchanger is normally not strongly influenced. Very slight heat-transfer degradation at low-airside Reynolds numbers was noticed due to the film-wise mode of condensation. However, pressure drop is more sensitive to the enhancement of surface wet-ability and can be reduced. The specimen with ‘Epoxy’ treating has less efficient behavior than the “Heresite” one, when moisture condensation occurs. No bridging effect was pointed out even at low Reynolds numbers.

Experimental studies were also conducted to develop new correlations from the experimental data for the Colburn j and f factors under dry and wet conditions for a wide range of Reynolds numbers for the three tested specimens: “uncoated”, “Heresite” treating, and “Epoxy” treating. Further experimental researches are needed to study the effect of the geometrical parameters of the heat exchanger (fin pitch, tube diameter...) on the developed correlations as well as on the surface wet-ability.

In summary, the Colburn j and f factors of wavy fins under dry and wet conditions for uncoated and coated heat exchangers have been elaborated; and an optimization method for heat-exchanger design has been developed in order to size ORC heat recovery fin-and-tube heat exchangers.

References

- [HUI 04] Huijbregts, W.M.M., Leferink, R., Latest advances in the understanding of acid dew point corrosion: corrosion and stress corrosion cracking in combustion gas condensates. *Anti-Corrosion Methods and Materials* 2004;51:173-183.
- [CHE 13] www.Chemengineering.wikispaces.com
- [CHEN 10] Chen, Q., Review of Industrial Condensing Boilers (Technology&Cost), Case Study: Thermal design of a condensing boiler in a large scale biomass district heating plant (40MW). Sheffield University Waste Incineration Centre (SUWIC), July 2010.
- [VER 74] Verhoff, F.H., Banchemo, J.T., Predicting Dew Points of Gases. *Chemical Engineering Progress* 1974;78:71-72.
- [PIE 77] Pierce, R.R., Estimating Acid Dewpoints in Stack Gases. *Chemical Engineering* 1977;84:125-128.
- [LEV 11] Levy, E., Bilirgen, H., DuPont, J., Recovery of water from boiler flue gas using condensing heat exchangers. Final technical report. Energy Research Center, Lehigh University, June 2011.
- [LU 87] Lu, P.C., Fu, T.T., Garg, S.C., Nowakowski, G., Boiler stack gas heat recovery. Technical note. Naval Civil Engineering Laboratory. California, September 1987.
- [SHA 78] Shah, R. K., Compact Heat Exchanger Surface Selection Methods. Proceedings of Sixth International Heat Transfer Conference, vol. 4, Hemisphere Publishing Corporation, Washington, DC, 1978, p. 193-199.
- [VAN 91] Van Den Bulck, E., Optimal Design of crossflow Heat Exchangers, *J. Heat Transfer* 1991;113:341-347.
- [BEJ 78] Bejan, A., General criteria for rating heat exchanger performance. *International Journal of Heat and Mass Transfer* 1978;21:655-658.
- [BEJ 79] Bejan, A., A study of entropy generation in fundamental convective heat transfer. *Journal of Heat Transfer* 1979;101:718-725.
- [KHA 06] Khan, W.A., Culham, J.R., Yovanovich, M.M., Optimal Design of Tube Banks in Cross-flow Using Entropy Generation Minimization Method. 44th Aerospace Sciences Meeting and Exhibit. 2006;9-12 January, Reno, Nevada.
- [ASH 08] Ashrae Systems and Equipment, Air-Cooling and Dehumidifying Coils. American Society of Heating, Refrigeration and Air-Conditioning Engineers. 2008, Chapter 22.
- [GRA 86] Gray, D.L., Webb, R.L., Heat transfer and friction correlation for plate finned tube heat exchangers having plain fins, Proc. 8th heat transfer conference, 1986, p. 2745-2750.
- [INC 96] Incropera, F.P., DeWitt, D.P., Fundamental of heat and mass transfer. 4th edition, John Willey & Sons, 1996.
- [PER 03] Perrotin, T., Clodic, D. Fin efficiency calculation in enhanced fin-and-tube heat exchangers in dry conditions. International Congress of Refrigeration, 2003, Washington.
- [PER 04] Perrotin, T., Air side investigation of high efficiency heat exchangers used in room air conditioners. Thesis 2004, Centre of Energy and Processes (CEP), Ecole des Mines de Paris, Paris, France.
- [THO 05] Thome, J.R., Engineering data book III. Laboratory of Heat and Mass Transfer. Swiss Federal Institute of Technology Lausanne (EPFL), 2005.
- [WOJ 05] Wojtan, L., Ursenbacher, T., Thome, J.R., Investigation of flow boiling in horizontal tubes: Part I-A new diabatic two-phase flow pattern map, *Int. J. Heat and Mass Transfer* 2005; 48:2955-2969.

- [THO 05] Thome, J.R., Engineering data book III. Condensation on external surfaces, Chapter 7. Laboratory of Heat and Mass Transfer. Swiss Federal Institute of Technology Lausanne (EPFL), 2005.
- [LIU 11] Liu, L., Effects of air-side surface wettability on the performance of dehumidifying heat exchangers. PhD thesis. University of Illinois at Urbana-Champaign, 2011.
- [THE 13] www.thermaltransfer.com
- [FRI 04] Epoxy and hydrophilic coatings used in aluminum finned heat exchangers. Technical Note. FRITHERM, 2004.
- [GLY 08] Glynn, E.F. Error analysis and propagation of errors. Stowers Institute for Medical Research, 2008, May 7.
- [BIG 01] Bigot, G., Etude et conception des systèmes Air/Air inversables utilisant des mélanges à glissement de température. Thesis 2001, Centre of Energy and Processes (CEP), Ecole des Mines de Paris, Paris, France.
- [GUN, 86] Gungor, E.K., Winterton, R.H.S., A general correlation for flow boiling in tubes and annuli, *International Journal of Heat and Mass Transfer* 1986;29:351-358.
- [DID, 02] O. Didi, M.B., Kattan, N., Thome, J.R., Prediction of two-phase pressure gradients of refrigerants in horizontal tubes. *International Journal of Refrigeration* 2002;25:935-947.
- [FRI 79] Friedel L., Improved friction pressure drop correlations for horizontal and vertical two-phase pipe flow. European Two-Phase Flow Group Meeting, Paper E2; 1979, June; Ispra, Italy.
- [POP 00] Popieil, C.O., Wojtkowiak, J., Friction factor in U-type undulated pipe, *J. Fluid Eng.*, 2000; 122:260–263.
- [PAD 09] Padilla, M., Revellin, R., Bonjour, J., Prediction and simulation of two-phase pressure drop in return bends, *International Journal of Refrigeration* 2009;32:1776-1783.
- [ROU 70] Rouhani, S.Z., Axelsson, E., Calculation of void volume fraction in the sub cooled and quality boiling regions. *Int. J. Heat Mass Transfer*, 1970;13:383–393.
- [WAN 97] Wang, C.C., Hsieh, Y.C., Lin, Y.T., Performance of plate finned tube heat exchangers under dehumidifying conditions, *ASME J. Heat transfer*, 1997;119:109-117.
- [WAN 98] Wang, C.C., Chang, C.T., Lin, Y.T., Heat and mass transfer for plate fin-and-tube heat exchangers with and without coating, *Int. J. Heat and Mass Transfer* 1998;41:3109-3120.
- [WAN 99] Wang, C.C., Du, Y.J. , Chang, Y.J., Tao, W.H., Air-side performance of herringbone fin-and-tube heat exchangers in wet conditions, *Canadian J. Chemical Engineering* 1999;77:1225-1230.
- [WAN 00a] Wang, C.C., Lin, Y.T., Lee, C.J., An airside correlation for plain fin-and tube heat exchangers in wet conditions, *International Journal of Heat and Mass Transfer* 2000; 43:1869-1872.
- [WAN 00b] Wang, C.C., Chi, K.Y., Chang, C.J., Heat transfer and friction characteristics of plain fin-and-tube heat exchangers, part II: Correlation, *International Journal of Heat and Mass Transfer* 2000;43:2693-2700.
- [WAN 02] Wang, C.C., Hwang, W.M., Lin Y.T., Empirical correlations for heat transfer and flow friction characteristics of herringbone wavy fin-and-tube heat exchangers, *International Journal of Refrigeration* 2002;25:673-680.

Chapter 3: Direct contact-condensation heat recovery

3.1 Introduction

One of the basic concepts that will be investigated for heat extraction from heat sources with high moisture and pollutant contents (SO_2 , NO_x ...) is a direct-contact water-vapor condensation involving a direct heat transfer between flue gases and cooling fluid (typically water) using a condensing unit. In a direct contact water-vapor condensation, the water is introduced into the hot flue-gas stream in a counter-flow directly using spray nozzles. The heated water stream exits through the heat-exchanger bottom and provides heat to the ORC system. By comparing to the indirect-contact water vapor condensation using a fin-and-tube heat exchanger, the absence of tubes reduces maintenance, increases system reliability, and decreases system cost. The elimination of the intervening wall increases the heat-transfer rate between the two fluids. The direct-contact heat exchanger is an ideal candidate for transferring latent heat from flue gases because spraying of fine water droplets can provide a large heat-transfer surface area for a relatively small temperature differences between the heating and cooling media. Direct contact of a water spray with flue gases also turns out to be a rather effective low-energy scrubber, which can reduce significantly flue-gas emissions.

This chapter deals with the process of direct-contact heat-transfer between flue gases and water flowing counter-currently in a condensing unit filled with packing materials. The design considerations of the condensing unit are based on hydraulics parameters (pressure drop and liquid hold-up) and on heat and mass transfer between flue gases and water inside the packing. The effects of hydraulic parameters on the condensing unit performances are explained. A two-fluid model using one-dimensional mass and energy conservation equations has been developed to predict the heat and mass transfer inside packing in order to determine the required packing height for a given operation parameters. Finally, a lab- scale direct-contact condenser with packing bed has been tested with counter-current flow stages. The objective of the experimental study is to examine the performance of various packing types with distinct surface geometry and wet-ability, in order to develop a better understanding of the impact of packing properties on the hydraulic parameters of the condensing unit and to compare their corresponding heat and mass transfer efficiencies.

3.2 Design of a condensing unit

3.2.1 Description of a Condensing unit

In a condensing unit, the water enters at the top of the column as a spray and flows downward through the column. Flue gases are drawn into the column using blower, and flows in a counter-flow direction to the water stream. If the blower is installed at the bottom of the column and it blows flue gases upward past the water stream, the column is called a forced draft column, whereas if the blower is at the top, it is an induced draft column [KLO 05]. The inside of the column is packed with a material providing a large surface area for both heat and mass transfer to take place from water droplets to flue gases, as shown in Fig. 3.1.

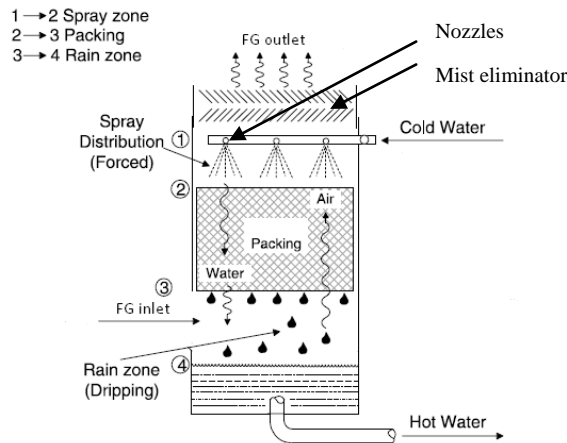


Fig. 3.1: Schematic of a counter-flow condensing unit

The packed material provides a large surface area for the liquid to wet and the area between gas and liquid phases is provided by liquid films and drops. In a counter-current-flow process, the cold water to be heated is sprayed into an upward flowing flue-gas stream using nozzles. Due to heat and mass transfer, the water temperature is increased while the flue-gas enthalpy is decreased because the flue gases are cooled and dehumidified by the water as it moves up. If either the liquid-injection rate or the gas-flow rate through the condensing unit is too high, a condition called flooding may occur. Flooding is a condition where the liquid is held in “pockets” inside the packing, and does not drain down through the packing. Flooding can be reduced by reducing the gas velocity through the column or by reducing the liquid-injection rate. In another flow arrangement used with condensing unit, co-current flow, both the exhaust gas and liquid phases enter at the top of the column and move downward over the packing material. This allows the condensing unit to operate at higher liquid and gas flow rates since flooding is not a problem [LOU 06]. The pressure drop is lower than with counter-current flow since both streams move in the same direction. However, a counter-current-flow arrangement results in the highest theoretically achievable efficiency because it has the closest temperature relationships between water and flue gases; the wet bulb temperature of entering flue gases approaches more closely the temperature of the leaving water than the wet bulb temperature of leaving flue gases approaches the temperature of entry water. The potential of realizing the highest possible mean temperature difference is thus arranged for optimum performance [ASH 08].

The nozzles are arranged in such a way that the water is uniformly distributed over the packing material. The rain zone is required to allow uniform flue-gas flow into the packing; however, from a thermal perspective, this is an inefficient portion of the condensing unit. It is only as large as necessary to allow even flue-gas flow. Davis [DAV 03] indicated that cooling achieved in one foot of packing can be more than cooling in ten feet of free-fall of water and, consequently, the transfer processes in the spray or rain zone may be ignored.

The mist eliminator is essential in the condensing unit for separating the entrained liquid droplets generated by the liquid distribution systems and avoid them going outside the condensing unit.

3.2.2 Packing types and corrugation geometry

The first developed packing type is the random packing, which consists of discrete pieces of packing of a specific geometrical shape, randomly packed in a column shell. During the evolution of random packing, a need for high-efficiency packing with an extremely low-pressure drop per theoretical stage arose. This led to the development of fill-and-structured packing [BIL 95].

The material for packing should be selected carefully based on thermal factor and wet-ability. Metal and plastic are commonly used materials. Fill packing (Fig. 3.2.a) are made of plastic and used generally in cooling tower applications. Polypropylene is standard use for plastic material and has limited temperature, less than 80°C. They have good corrosion resistance, high capacity, high efficiency, lower density, and low coefficient of elasticity. Disadvantages of plastic materials are low thermal stability and aging, poor wet-ability. Plastic packing can only be used up to moderate temperatures (< 80°C).



Fig. 3.2: Packing technology: a) Fill packing (polypropylene), b) "Montz" packing type "B1" (stainless steel),

Structured packing (Fig. 3.2.b) are generally made of metal and used frequently in distillation processes. Stainless steel and other alloy, beside carbon steel, are usually required because of their corrosion resistance. They have the highest capacity and efficiency, wider range geometries, good wet-ability and unbreakable compared with other materials. The high efficiency structured packing are composed mostly of corrugated (metal, stretched metal or wire gauze) sheets. The geometry of a corrugated sheet structured packing ("CSSP") is highly ordered and enables utilization of largest possible surface areas per unit volume. Thanks to its extremely large void fraction (porosity) and low liquid hold-up, "CSSP" has the potential for achieving high heat and mass transfer.

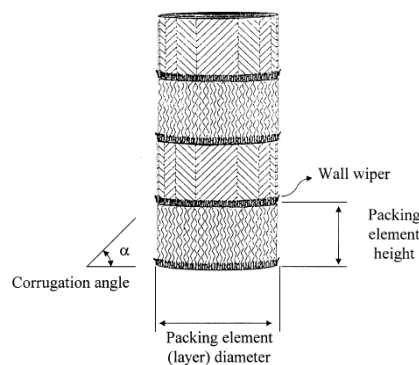


Fig. 3.3: Schematic illustration of a corrugated sheet structured packing [OLU 01]

As suggested in the sketch shown in Fig. 3.3, the packing will be installed as a column of certain height and section, consisting of a number of stacked elements (packing layers) with heights ranging generally from 0.15 to 0.3 m. The stacked elements are rotated to each other usually by 90° to produce a large-scale mixing effect for both gas and liquid at each transition from layer to layer. For "CSSP", each packing element layer is equipped with wall wipers to avoid excessive wall flow [OLU 01]. Each packing element segment consists of a number of corrugated sheets, each second with corrugations inclined in the opposite direction. Standard corrugation inclination angle is 45° and often an angle of 60° is offered. The specific surface area of the packing is defined as the surface area per unit volume. The most common specific surface area (a_p) is around 250 m²/m³, and some manufacturers offer surfaces from 100 to 750 m²/m³ as a standard. The flexibility in this respect depends on the design of the packing surface, which is the most distinctive proprietary characteristic of a packing. With the

exception of “Montz” packing type “B1” (refer to Fig. 3.2.b), all commercial corrugated sheets structured packing have a regular pattern of holes or other type of apertures in the surface. To some extent, this enables both phases to go to the other side of the sheet, which is however limited to the neighboring channel only. The flow channels are formed between tightly packed corrugation sheets with oppositely oriented channels enabling lateral flow parallel to sheet orientation only [OLU 99]. As mentioned above, the necessary (large-scale) mixing effect is achieved by rotating subsequent element: layer to each other by 90°, which is, however accompanied by a considerable pressure loss, due to the abrupt change in gas flow direction at each transition between packing layers. This component, as well as that due to gas-gas interaction at the interface created at the crossings of gas-flow channels, represents a major contribution to total pressure drop experienced by the gas at its zigzag way upward in a condensing unit [OLU 97]. However, the structured packing is considered an easy to understand and to implement gas-liquid contacting device. In general, the “CSSP” is a film-flow-type device and it works properly as long as the liquid moves as a continuous thin film held by surface tension. However, the surface and corrugation designs of proprietary packing differ considerably and this has a profound effect on packing performance.

For structured packing, a packing element layer comprises a large number of identical triangular flow channels created between corrugated plates with opposite orientation of corrugations. As illustrated in Fig. 3.4, which shows the basic zigzag flow-channel configuration and major corrugation dimensions, two sides of the triangular cross-section are occupied by walls. The third facing the neighboring sheet is open, creating an interface with the open side of crossing gas-flow channels from the opposite sheet. The length of individual channels depends on the element height, the corrugation angle, and the wall proximity. Channels ending at the wall are shorter and this implies that in a column with a diameter equal to or smaller than the packing element height, the gas flow makes relatively more bends than in the case of larger diameter column [OLU 97]. The gas flow can be considered as a continuous zigzag flow through a triangular channel of constant dimensions (Fig. 3.4). The total length of a typical zigzag flow channel is equal to the product of the number of packing elements (layers) in a column and the length of a straight gas-flow channel in a packing element. The latter is defined as the ratio of the packing element height, h_{pe} , and the sine of the corrugation inclination angle (α):

$$l_{G,pe} = \frac{h_{pe}}{\sin \alpha} \quad \text{Eq. 3.1}$$

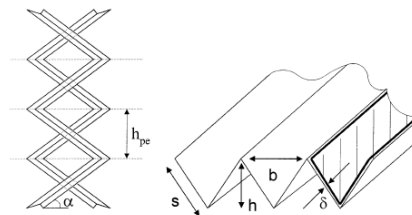


Fig. 3.4: Basic geometry and dimensions of triangular, gas-liquid flow channel [OLU 99]

The specific surface area of packing is defined by [VER 99]:

$$a_p = \frac{4s}{bh} = \frac{2\sqrt{b^2 + 4h^2}}{bh} \quad \text{Eq. 3.2}$$

The hydraulic (equivalent) diameter of a triangular gas-flow channel, specified by corrugation height, “h”, corrugation side length, “s”, and corrugation base width or pitch, “b”, with corrugation sides covered by a thin liquid film of constant thickness, “δ”, is [VER 99]:

$$d_{hG} = \frac{(bh - 2\delta s)^2}{bh} \left[\left(\frac{bh - 2\delta s}{2h} \right)^2 + \left(\frac{bh - 2\delta s}{b} \right)^2 \right]^{0.5} + \frac{bh - 2\delta s}{2h} \quad \text{Eq. 3.3}$$

The hydraulic diameter for gas in a dry triangular channel can be written as [OLU 01]:

$$d_{hG,dry} = \frac{2bh}{b + 2s} = \frac{2bh}{b + \sqrt{b^2 + 4h^2}} \quad \text{Eq. 3.4}$$

The V-shaped fraction of the cross-section of the triangular gas-flow channel occupied by the liquid film is defined as [OLU 01]:

$$\varphi = \frac{2s}{b + 2s} = \frac{\sqrt{b^2 + 4h^2}}{b + \sqrt{b^2 + 4h^2}} \quad \text{Eq. 3.5}$$

Where: s and b stand for the lengths of the corrugation side and flow channel (corrugation) base, respectively.

The corrugation height to base ratio of most conventional packing is around 0.5. Depending on the surface design, the thickness of sheet metal material ranges from 0.1 to 0.2 mm. Thanks to this, the porosity of sheet metal packing is extremely high, between 0.95 and 0.99.

3.2.3 Hydraulics of the condensing unit

The capacity of a condensing unit is determined by its effective cross-sectional area open to flue-gas flow. Normally, a column will be designed to operate at the highest economical pressure drop to ensure good liquid and gas distribution [COU 04]. Before the methods predicting the hydraulic capacity are discussed, a few concepts relating to the hydraulic capacity of structured packing need to be clarified.

Two key concepts are the pressure drop over the condensing unit and the liquid hold-up. The pressure drop over the condensing unit is self-explanatory, but the liquid hold-up needs to be defined. The liquid hold-up is defined as the amount of liquid that is retained (held back) in the packing material after the liquid feed to the column has been cut [KIS 92]. Both these factors are influenced by the superficial gas velocity and can be better understood by viewing Fig. 3.5 and Fig. 3.6.

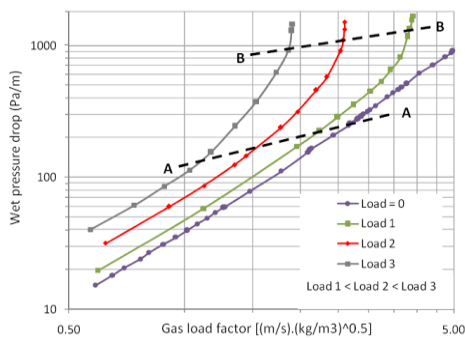


Fig. 3.5: Wet pressure drop as a function of gas load factor [LAM 10]

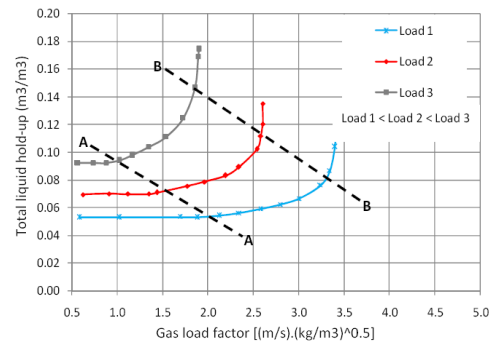


Fig. 3.6 : Liquid hold-up as a function of gas load factor [LAM 10]

The liquid hold-up has an effect on the pressure drop, the degree of wetting, the thickness of the liquid film and the gas-liquid mass and heat transfer. It should be noted that the total column hold-up is comprised of two contributing terms, namely the static hold-up and the dynamic hold-up [LAM 10]. The dynamic hold-up is defined as the liquid that freely drains from a packed column after the feed to the column has been cut off, and the static hold-up is defined as the remaining liquid in the packed column after the column has been allowed to drain for a prolonged time interval.

Values in Fig. 3.5 and Fig. 3.6 are used for explanatory purposes only and are generated from measured data. The typical pressure drop over a condensing unit as a function of gas-load factor is represented viewing Fig. 3.5 and Fig. 3.6, and represents a typical liquid hold-up profile for the same system and liquid loads. The gas-load factor (F_G) is a convenient way to describe the gas-flow rate in a condensing unit that is adjusted for the gas density [OLU 07].

$$F_G = u_{GS} \times \sqrt{\rho_a} \quad \text{Eq. 3.6}$$

In Eq. 3.6, “ u_{GS} ” is the superficial gas velocity given by:

$$u_{GS} = \frac{m_G}{\rho_a A} \quad \text{Eq. 3.7}$$

Where, in Eq. 3.7, “ m_g ” and “ ρ_a ” are the mass flow rate and density of flue gases; respectively, “ A ” is the cross-sectional area.

The liquid load is given by:

$$\text{Liquid load } (m^3 \cdot m^{-2} \cdot h^{-1}) = \frac{3600 \cdot m_w}{\rho_w \cdot A} \quad \text{Eq. 3.8}$$

In Eq. 3.8, “ m_w ” and “ ρ_w ” are the mass flow rate and density of water; respectively, “ A ” is the cross-sectional area.

From Fig. 3.5 and Fig. 3.6, three distinct regions can be identified and will be discussed accordingly.

✓ Pressure Drop Curve

Fig. 3.5 shows that the pressure drop curve at a specific liquid load is parallel to the pressure drop curve of the dry packing up to a certain gas-load factor (below line “A-A”). Beyond this point, the pressure drop increases rapidly with an increase in gas-load factor (between line “A-A” and “B-B”). Above line “B-B”, the pressure drop tends to infinity with a small increase in gas-load factor. Note that the dry pressure drop is the measured pressure drop in the absence of liquid flow while the wet pressure drop is the measured pressure drop when the packing material is wetted.

✓ Liquid hold-up Curve

Fig. 3.5 shows that the liquid hold-up, at a specific liquid load, is independent of the gas-load factor up to a certain point (line “A-A”). Up to this point, the liquid hold-up is only a function of liquid flow rate and liquid physical properties. Beyond this point, an increase in the gas-flow rate would lead to an increase in the liquid hold-up until line “B-B” is reached. Beyond this point, the liquid hold-up tends to infinity with an increase in gas-load factor. It should be noted that these regions coincide with the regions seen on the pressure drop curve. Based on the above discussions, the three regions of operability can be defined. These three regions are defined below [LAM 10].

- **The pre-loading region:** On both figures, this is the region before line “A-A” is reached. The pressure drop of the condensing unit is parallel to the dry column pressure drop and thus the liquid hold-up is independent of the gas-load factor and only dependent on the liquid load and liquid properties.
- **The loading region:** On both figures, this region is between lines “A-A” and “B-B”. The pressure drop and liquid hold-up in the condensing unit are functions of the gas flow (the wet pressure drop trend deviates from the dry pressure drop). The point where the pressure drop as well as the liquid hold-up starts to be influenced by the gas-load factor is known as the loading point (represented by line “A-A”). The loading point is defined as the point where the shear forces between the gas and liquid increase relative to the gravitational forces up to a point where the liquid droplets flowing the column become suspended. The point where the pressure drops as well as the liquid hold-up tend to infinity is known as the flooding point (represented by line “B-B”).
- **The flooding region:** At and beyond the flooding point, the gas-flow rate is large enough to prevent the liquid from flowing down the column. In addition, according to [BIL 99], the shear forces between the gas and liquid are larger than the gravitational force working in on the liquid and thus it is said that the liquid is entrained.

The hydraulic operating regime is closely related to the heat and mass transfer efficiency of packing. Normally there is a gradual increase in the efficiency with an increase in liquid and gas flow rates. There is a sharp increase in efficiency in the loading region, followed by a sharp decrease in the efficiency, as the flooding point is approached [KIS 92]. It is advised to design column to operate at 80% of their capacity at flooding [BIL 99]. Based on the above discussion, it is therefore extremely important to be able to predict the loading and flooding points.

3.2.4 Heat and mass transfer model inside the packing

Inside the packing, the water flows in counter-flow direction to the flue-gas flow. The water flow through the packing is physically one-dimensional as it is constrained to film-flow descending along the vertical. This requires that the heat and mass transfer in the packing be also a one-dimensional process. This simplification allows the water flow to be represented solely by two variables at each point, its temperature, and its mass flow rate.

A basic model of the condensing unit operation is proposed by combining the governing equations of heat and mass transfer between water and flue gas in the column. It is important to note that the model basically deal with heat and mass transfer analysis in the packing zone of the column, which is considered to be the main part of the column. The equations are derived according to the “Poppe” method of analysis for the cooling tower ([KLO 03], [KLO 05]) . The model is adapted to the condensation process. The governing equations that follow can be solved by the fourth order Runge - Kutta method [KLO 05].

Fig. 3.7 shows a control volume in the packing of a counter-flow condensing unit. Fig. 3.8 shows the flue-gas side control volume of the packing.

	$m_a(1+w_a-dw_a)$		$m_a(1+w_a-dw_a)$
m_w	h_a-dh_a	m_w	h_a-dh_a
h_w	w_a-dw_a	h_w	w_a-dw_a

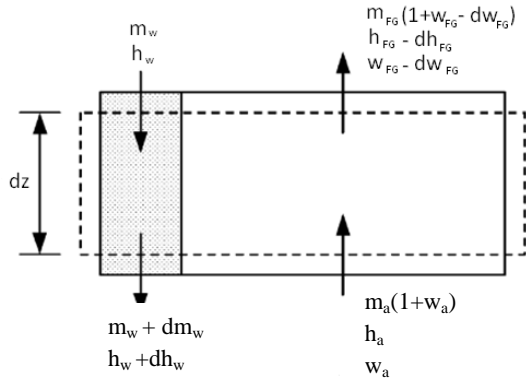


Fig. 3.7: Control volume of counter-flow packing [KLO 05]

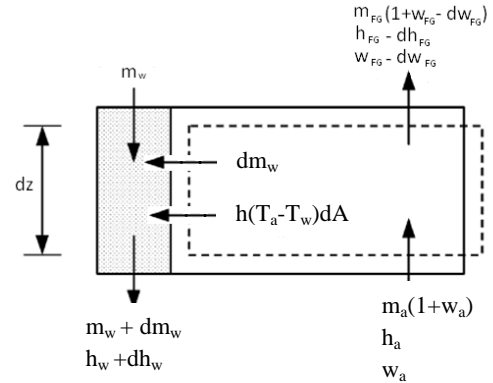


Fig. 3.8: Flue-gas side control volume of the packing [KLO 05]

A mass balance for the control volume in Fig. 3.7 yields to:

$$dm_w = m_a dw_a \quad \text{Eq. 3.9}$$

The energy balance for the control volume in Fig. 3.7 is as follows:

$$m_a dh_a - m_a (h_a - dh_a) = (m_w + dm_w)(h_w + dh_w) - m_w h_w \quad \text{Eq. 3.10}$$

$$m_a dh_a = m_w dh_w + dm_w (h_w + dh_w) \quad \text{Eq. 3.11}$$

$$m_a dh_a - m_w dh_w - h_w dm_w = 0 \quad \text{Eq. 3.12}$$

Substitute Eq. 3.9 into Eq. 3.10 and neglect “ $dm_w \cdot dh_w$ ” to find upon rearrangement:

$$dT_w = \frac{m_a}{m_w} \left(\frac{dh_a}{c_{pw}} - T_w dw \right) \quad \text{Eq. 3.13}$$

Consider the interface between the water and the flue gases in Fig. 3.8. An energy balance at the interface yields to:

$$dQ_{total} = dQ_{sensible} + dQ_{latent} \quad \text{Eq. 3.14}$$

Where: “ dQ_{latent} ” is the enthalpy transfer due to difference in gas concentrations between the saturated flue gases at the interface and the mean flue-gas stream and “ $dQ_{sensible}$ ” is the sensible heat transfer due to the difference in temperatures. The mass transfer at the interface is expressed by:

$$dm_w = k_m (w_a - w_{sw}) dA \quad \text{Eq. 3.15}$$

The corresponding enthalpy transfer for the mass transfer in Eq. 3.15 is:

$$dQ_{latent} = h_{fg} dm_w = h_{fg} k_m (w_a - w_{sw}) dA \quad \text{Eq. 3.16}$$

The convective heat transfer from Fig. 3.8 is given by:

$$dQ_{sensible} = h(T_a - T_w) dA \quad \text{Eq. 3.17}$$

The temperature differential in Eq. 3.17 can be replaced by an enthalpy differential. The enthalpy of saturated flue gases evaluated at the local bulk water temperature is given by:

$$h_{sw} = c_{pa}T_w + w_{sw}(h_{fg} + c_{pv}T_w) \quad \text{Eq. 3.18}$$

$$h_{sw} = T_w(c_{pa} + w_a c_{pv}) + w_{sw}h_{fg} + T_w c_{pv}(w_{sw} - w_a) \quad \text{Eq. 3.19}$$

The enthalpy of flue gases per unit mass of dry flue gases is expressed by:

$$h_a = c_{pa}T_a + w_a(h_{fg} + c_{pv}T_w) \quad \text{Eq. 3.20}$$

Subtract Eq. 3.20 from Eq. 3.19. The resultant equation can be simplified if the small differences in specific heats, which are evaluated at different temperatures, are ignored:

$$T_a - T_w = \frac{(h_a - h_{sw}) - (w_a - w_{sw})(h_{fg} + c_{pv}T_w)}{c_{pt}} \quad \text{Eq. 3.21}$$

Where “ c_{pt} ” is the total specific heat of flue gases per unit mass and defined as:

$$c_{pt} = c_{pa} + w_a c_{pv} \quad \text{Eq. 3.22}$$

Substitute Eq. 3.21 into Eq. 3.17. Substitute the resultant equation and Eq. 3.16 into Eq. 3.14 to find after rearrangement:

$$dQ_t = k_m \left[\frac{h}{c_{pt}k_m}(h_a - h_{sw}) + \left(1 - \frac{h}{c_{pt}k_m}\right)h_v(w_a - w_{sw}) \right] dA \quad \text{Eq. 3.23}$$

Where:

$$h_v = h_{fg} + c_{pv}T_w \quad \text{Eq. 3.24}$$

“ $\frac{h}{c_{pt}k_m}$ ” in Eq. 3.23 is known as the Lewis factor “ Le_f ” and is an indication of the relative rates of heat and mass transfer in a condensation process. The water condensation rate, however, is a function of the actual value of the Lewis factor.

The enthalpy transfer to the flue-gas stream from Eq. 3.23 is:

$$dh_a = \frac{1}{m_a} dQ_t = \frac{k_m dA}{m_a} \left[Le_f (h_a - h_{sw}) + (1 - Le_f) h_v (w_a - w_{sw}) \right] \quad \text{Eq. 3.25}$$

For a one-dimensional model of the packing, where the available area for heat and mass transfer is the same at any horizontal section through the packing, the transfer area for a section “ dz ” is usually expressed as:

$$dA = a_e A_{fr} dz \quad \text{Eq. 3.26}$$

Where “ a_e ” is the effective area density of the packing, i.e. the wetted area divided by the corresponding volume of the packing and “ A_{fr} ” is the corresponding frontal area.

Substitute Eq. 3.26 into Eq. 3.25 and find:

$$\frac{dh_a}{dz} = \frac{k_m a_e A_{fr}}{m_a} \left[Le_f (h_a - h_{sw}) + (1 - Le_f) h_v (w_a - w_{sw}) \right] \quad \text{Eq. 3.27}$$

Substitute Eq. 3.15 and Eq. 3.25 into Eq. 3.12, rearrange and find:

$$m_w dh_w = k_m dA \left[(h_a - h_{sw}) + (Le_f - 1) \left[(h_a - h_{sw} - (w_a - w_{sw}) h_v) \right] - (w_a - w_{sw}) c_{pw} T_w \right] \quad \text{Eq. 3.28}$$

Find upon rearrangement of Eq. 3.13:

$$\frac{dw}{dT_w} = \frac{1}{c_{pw} T_w} \frac{dh_a}{dT_w} - \frac{1}{T_w} \frac{m_w}{m_a} \quad \text{Eq. 3.29}$$

$$\frac{dw}{dT_w} = \frac{dh_a}{T_w dh_w} - \frac{1}{T_w} \frac{m_w}{m_a} \quad \text{Eq. 3.30}$$

Substitute Eq. 3.25 and Eq. 3.28 into Eq. 3.30 and find:

$$\frac{dw_a}{dT_w} = \frac{c_{pw} \frac{m_w}{m_a} (w_{sw} - w_a)}{(h_a - h_{sw}) + (Le_f - 1) \left[(h_a - h_{sw}) - (w_a - w_{sw}) h_v \right] - (w_a - w_{sw}) c_{pw} T_w} \quad \text{Eq. 3.31}$$

Substitute Eq. 3.31 into Eq. 3.30 and find:

$$\frac{dh_a}{dT_w} = \frac{m_w c_{pw}}{m_a} \left(1 + \frac{(w_a - w_{sw}) c_{pw} T_w}{(h_a - h_{sw}) + (Le_f - 1) \left[(h_a - h_{sw}) - (w_a - w_{sw}) h_v \right] - (w_a - w_{sw}) c_{pw} T_w} \right) \quad \text{Eq. 3.32}$$

From Eq. 3.9 and Eq. 3.15, find:

$$k_m dA = \frac{m_a dw_a}{w_a - w_{sw}} \quad \text{Eq. 3.33}$$

Divide both sides by “ m_w ” and introduce “ dT_w / dT_w ” to the right hand side of Eq. 3.33 and integrate to find:

$$\int \frac{k_m}{m_w} dA = \int \frac{m_a}{m_w} \frac{dw/dT_w}{w_a - w_s} dT_w \quad \text{Eq. 3.34}$$

From Eq. 3.34 find:

$$\frac{k_m}{m_w} A = \int \frac{m_a}{m_w} \frac{dw/dT_w}{w_a - w_s} dT_w \quad \text{Eq. 3.35}$$

Eq. 3.35 is defined as the “Merkel” number, i.e.

$$Me_p = \int \frac{m_a}{m_w} \frac{dw/dT_w}{w_a - w_s} dT_w \quad \text{Eq. 3.36}$$

Upon substitution of Eq. 3.31 into Eq. 3.36 and differentiation of the latter with respect to the water temperature, find:

$$\frac{Me_p}{dT_w} = \frac{c_{pw}}{(h_a - h_s) + (Le_f - 1)[(h_a - h_s) - (w_a - w_s)h_v] - (w_a - w_s)c_{pw}T_w} \quad \text{Eq. 3.37}$$

The ratio of the mass flow rates “ m_w/m_a ” changes as the flue gases move towards the top of the packing. The varying water mass flow rate can be determined from the known inlet water mass flow rate, “ $m_{w,in}$ ” as shown in Eq. 3.38.

$$m_{w,out} = m_{w,in} + m_a(w_{a,in} - w_{a,out}) \quad \text{Eq. 3.38}$$

The system of equations is represented by Eq. 3.31, Eq. 3.32, and Eq. 3.37. The fourth order “Runge–Kutta” method is used to solve it by dividing the packing into a number of intervals ($n = 100$ in this case) where the water temperature difference is equal across each interval, i.e.

$$\Delta T_w = (T_{w,out} - T_{w,in}) / n \quad \text{Eq. 3.39}$$

Refer to Kloppers [KLO 03] for detailed sample calculations to solve the governing equations according to the “Poppe” method.

3.2.5 Hydraulics and mass transfer predicting model for structured packing

In the operation of the condensing unit, the hydraulic and the heat and mass transfer processes occur simultaneously. For the authors, the liquid hold-up is the linking parameter. For the hydraulic analysis, the increase in the velocity of any phase increases the film thickness and the liquid hold-up of films and droplets, which leads to an increase in the pressure drop. For the heat and mass transfer analysis, the increase in hold-up produces an increase in interfacial area, and this gives higher heat and mass transfer rates.

The rate of heat and mass transfer in the condensing unit strongly depends on the effective interfacial area of the condensing unit. The effective surface area (a_e) for heat and mass transfer is different from the geometrical surface area (a_p) of the sheets because of the effects of hydraulic conditions and physical interaction of liquid on the sheets. A number of theoretical, semi-empirical, and empirical correlations for predicting the effective interfacial area in structured packing were reported in the literature. These models were developed for different packing and various process conditions using physical measurement methods such as electro resistivity and light transmission.

The pressure drop that occurs is due to the following factors: i) wall friction, ii) drag, and iii) abrupt changes in the flow path. The total area available to gas flow is reduced as the hold-up in the column causes the liquid films to become thicker.

A brief description of the model (“Delft” model) used for predicting hydraulics and mass transfer in the structured packing will be presented. This model links pressure-drop and mass transfer by using the liquid hold-up. The heat and mass transfer analogy [LI 06] is used to compute the heat transfer coefficients.

The effective gas and liquid velocities are defined respectively as ([BRA 92], [BRA 96]):

$$u_{Ge} = \frac{u_{Gs}}{(\varepsilon - h_L) \sin \alpha} \quad \text{Eq. 3.40}$$

$$u_{Le} = \frac{u_{Ls}}{\varepsilon h_L \sin \alpha} \quad \text{Eq. 3.41}$$

Where in Eq. 3.40 and Eq. 3.41, “ ε ” is the void fraction (porosity) of the packing, “ h_L ” is the liquid hold-up, “ u_{GS} ” is the superficial gas velocity defined by Eq. 3.7 and “ u_{LS} ” is the superficial liquid velocity defined by:

$$u_{LS} = \frac{m_w}{\rho_w A} \quad \text{Eq. 3.42}$$

In Eq. 3.42, “ m_w ” and “ ρ_w ” are the mass flow rate and density of water; respectively, and “ A ” is the cross-sectional area.

The “Delft” model was developed by Olujic [OLU 97]. It can be used to predict the pressure drop, liquid hold-up, heat and mass transfer and effective surface area in the condensing unit for “Montz” packing type “B1-45°”. Parameters investigated throughout the “Delft” model are shown in Table 3.1.

Table 3.1: Parameters investigated throughout the “Delft” model

Parameter	Units	Range
System pressure	Bar	0.33 - 4.14
Liquid density	Kg.m ⁻³	561 - 1000
Dynamic liquid viscosity	mPa.s	0.161 - 1
Surface tension	mN.m ⁻¹	8 - 72
Column diameter	m	0.192 - 1.4
Total surface area per unit volume	m ² .m ⁻³	244 - 394
Void fraction	m ³ .m ⁻³	0.96 - 0.98
Gas density	Kg.m ⁻³	0.84 - 13.14
Gas viscosity	mPa.s	0.0069 - 0.0185

3.2.5.1 Liquid hold-up

If the liquid is well distributed and there is no excessive entrainment, which is a reasonable assumption for the purpose of modeling packing hydraulics in the preloading region, then the liquid hold-up follows simply from the product of the nominal packing surface area, a_p , and the mean liquid film thickness, “ δ ”:

$$h_L = a_p \delta \quad \text{Eq. 3.43}$$

It is known from experimental observations that liquid hold-up is not affected significantly by gas flow in the preloading range [VER 99]. This implies that the liquid film thickness can be determined from correlations developed for liquid films in the absence of counter-current gas flow. The flow of thin liquid films over packing surfaces is assumed laminar, and the mean liquid film thickness can be estimated using the “Nusselt” formula for falling films adapted to the inclined wall situation as encountered in the present case ([OLU 99], [FER 09]):

$$\delta = \left(\frac{3\mu_L u_{Ls}}{\rho_L g a_p \sin \alpha} \right)^{1/3} \quad \text{Eq. 3.44}$$

Where: “ μ_L ” is the liquid viscosity, “ ρ_L ” is liquid density and “ g ” is gravitational acceleration. Liquid hold-up measurements have confirmed that Eq. 3.43 in conjunction with Eq. 3.44 reproduce the relation between operating hold-up and liquid load satisfactorily for the purposes of hydraulic calculations [OLU 97]. In general, influenced by gravity, the liquid will tend to flow at an angle steeper than the corrugation angle. Eq. 3.44 accounts for this, and for a flow along a “45°” inclined channel, it will give a film thickness approximately “12%” larger than that of a falling film.

3.2.5.2 Pressure drop

According to the “Delft” model, the static pressure gradient of a column assembled of corrugated sheet structured packing consists of three distinct contributions ([OLU 99], [LAR 02]):

$$\Delta P = \Delta P_{GL} + \Delta P_{GG} + \Delta P_{DC} = F_{load} (\zeta_{GL} + \zeta_{GG} + \zeta_{DC}) \frac{\rho_G u_{Ge}^2}{2} \quad \text{Eq. 3.45}$$

Where: subscripts “GL”, “GG” and “DC” refer respectively to pressure losses associated with the gas-liquid surface interaction, gas-gas interaction at the interface created between crossing gas flows, and direction changes at the transitions between packing elements and in the wall zone. In the right hand expression describing the overall pressure drop over the entire range of gas load, “ u_{Ge} ” is the effective gas velocity, which is always greater than the superficial velocity, “ ρ_G ” is the gas density, and “ F_{load} ” is a pressure-drop enhancement factor in the loading region. “ ζ_{GL} ”, “ ζ_{GG} ” and “ ζ_{DC} ” represent corresponding flow resistance coefficients. The first two, are considered independent of the cross sectional area, and the latter one is involved with the observed effect.

Although it is not justified theoretically to assume the pressure drop in the wall zone to be larger than that in the packing bulk, for practical reasons it was considered consisting of two resistances in series. The corresponding overall coefficient for direction change related losses is described as:

$$\zeta_{DC} = \frac{h_{pb}}{h_{pe}} (\zeta_{bulk} + \Psi \zeta_{wall}) \quad \text{Eq. 3.46}$$

Where; “ h_{pb} ” is packing height, “ h_{pe} ” is packing element height, and “ ζ_{bulk} ” and “ ζ_{wall} ” are the characteristic form drag coefficients for bulk- and wall zone, respectively. “ Ψ ” represents the ratio of the number of gas-flow channels ending at column walls and the number of gas-flow channels in the bottom cross section of a packing element or layer; i.e. the fraction of the total number of gas flow channels ending at column walls. The value of “ Ψ ” is given by:

$$\Psi = \frac{2h_{pe}}{\pi d_c^2 \tan \alpha} \left(d_c^2 - \frac{h_{pe}^2}{\tan^2 \alpha} \right)^{0.5} + \frac{2}{\pi} \arcsin \left(\frac{h_{pe}}{d_c \tan \alpha} \right) \quad \text{Eq. 3.47}$$

Where: “ d_c ” is the column diameter and “ α ” is the corrugation inclination angle.

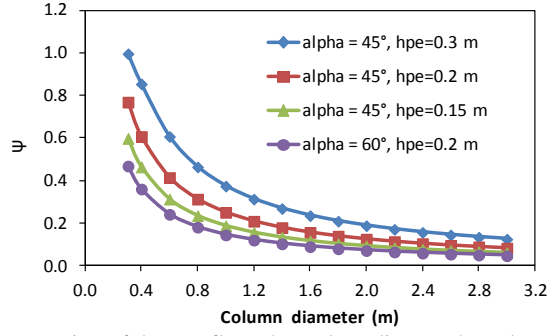


Fig. 3.9: Fraction of the gas-flow channels ending on the column walls as a function of corrugation angle and the packing element height

Fig. 3.9 shows the fraction of the gas-flow channels ending at column walls as a function of column diameter for two common corrugation inclination angles and three different packing element heights. In a column with a diameter of “1 m” containing a 45° packing with element height of 0.2 m, approximately 25% of all gas-flow channels will end on column walls. Obviously, the pressure-drop enhancement effect of the wall zone will be weakened with increasing corrugation angle and decreasing element height.

The bulk-zone direction change coefficient is expressed as a function of the corrugation angle as follows:

$$\zeta_{bulk} = 1.76(\cos \alpha)^{1.63} \quad \text{Eq. 3.48}$$

The wall-zone direction change is accounted for accordingly in the following empirical correlation:

$$\zeta_{wall} = \frac{4092u_{Ls}^{0.31} + 4715(\cos \alpha)^{0.445}}{\text{Re}_{Ge}} + 34.19u_{Ls}^{0.44}(\cos \alpha)^{0.779} \quad \text{Eq. 3.49}$$

Where: “ u_{Ls} ” is the liquid superficial velocity, “ Re_{Ge} ” is the Reynolds number based on the effective gas velocity (“ u_{Ge} ”):

$$\text{Re}_{Ge} = \frac{u_{Ge}\rho_G d_{hG}}{\mu_G} = \frac{u_{Gs}}{\sin \alpha (\varepsilon - h_L)} \frac{\rho_G d_{hG}}{\mu_G} \quad \text{Eq. 3.50}$$

Where: “ u_{Gs} ” is the superficial gas velocity, “ ρ_G ” is the gas density, “ μ_G ” is the gas dynamic viscosity, “ d_{hG} ” is the hydraulic diameter of gas-flow channel, “ ε ” is packing porosity, and “ h_L ” is liquid holdup.

In addition to the direction change imposed losses, the gas phase ascending through an irrigated column consisting of corrugated sheet structured packing also experiences frictional pressure loss. One source is gas/liquid friction at the surface of the descending liquid film and the other one, more pronounced, is the interaction of gas flows at the interfaces created between crossing gas-flow channels.

The overall gas/liquid interaction coefficient is given by:

$$\zeta_{GL} = \lambda \zeta_{GL} \frac{h_{pb}}{d_{hG} \sin \alpha} \quad \text{Eq. 3.51}$$

Where: “ λ ” represents the wetted perimeter of the triangular gas-flow channel, “ $\lambda=2s/(b+2s)$ ”, and “ ξ_{GL} ” is the friction factor given by:

$$\xi_{GL} = \left\{ -2 \log \left[\frac{(\delta / d_{hG})}{3.7} - \frac{5.02}{\text{Re}_{Grv}} \log \left(\frac{(\delta / d_{hG})}{3.7} + \frac{14.5}{\text{Re}_{Grv}} \right) \right] \right\}^{-2} \quad \text{Eq. 3.52}$$

Where: “ Re_{Grv} ” stands for a Reynolds number based on relative gas-phase velocity:

$$\text{Re}_{Grv} = \frac{\rho_{Ge} (u_{Ge} + u_{Le}) d_{hG}}{\mu_G} \quad \text{Eq. 3.53}$$

Where: “ u_{Le} ” is the mean film velocity and defined as:

$$u_{Le} = \frac{u_{Ls}}{a_p \delta} \quad \text{Eq. 3.54}$$

The gas/gas interaction is related to the third, open side of the gas flow channel and it proved to be a strong function of corrugation inclination angle, and it is expressed by:

$$\zeta_{GG} = (1 - \lambda) \xi_{GG} \frac{h_{pb}}{d_{hG} \sin \alpha} = 0.722(1 - \lambda)(\cos \alpha)^{3.14} \frac{h_{pb}}{d_{hG} \sin \alpha} \quad \text{Eq. 3.55}$$

As indicated in Eq. 3.45, the change in the pressure drop slope in the loading regime is represented by an enhancement factor, which is applied when the gas load reaches the critical loading point gas load. The loading point gas load is given by:

$$F_{G,lp} = u_{Ge,lp} (\varepsilon - h_L) \sin \alpha \sqrt{\rho_G} \quad \text{Eq. 3.56}$$

Where the effective loading point gas velocity is described as:

$$u_{Ge,lp} = \frac{(4294 u_{Ls} \cos \alpha) + 2.93}{(1453 u_{Ls} \cos \alpha) - \cos \alpha + 1.17} + \Omega \quad \text{Eq. 3.57}$$

Pressure drop enhancement in the loading region is given by:

$$F_{load} = 1453 u_{Ls} + \frac{1.17}{\cos \alpha} - \frac{4294 u_{Ls} + \frac{2.93}{\cos \alpha}}{u_{Ge} - \Omega} \quad \text{Eq. 3.58}$$

Here, “ Ω ” is a loading point constant, which takes into account a shift in loading point due to openings in the surface of the packing. This is difficult to determine exactly; for packing with holes, it is assumed that this value is equal to the fraction of the surface occupied by holes. Finally, the pressure drop at flooding is correlated by [GUA 97]:

$$\left(\frac{\Delta P}{\Delta z} \right)_{flood} = 1500 + 65000 u_{Ls} \quad \text{Eq. 3.59}$$

When Eq. 3.59 is applied, the values for $(\Delta P/\Delta Z)_{\text{flood}}$ range between 1000 and 3300 Pa/m.

3.2.5.3 Effective surface area

It is well understood that the heat and mass transfer rate within the condensing unit is directly related to the contact surface area between flue gases and water. In order to achieve a high rate of heat and mass transfer, it is important to produce good surface wetting and liquid contact with flue gases [WAN 06]. The wet-ability of the packing surface with liquid depends on the contact angle between the liquid film and the packing surface.

The following relation can be used to describe the effect of liquid load on the size of effective surface area for a metal sheet structured packing [WAN 06]:

$$a_e = a_p \frac{(1-\Omega)}{\left(1 + \frac{A}{u_{LS}^B}\right)} \quad \text{Eq. 3.60}$$

Where: “ Ω ” is the fraction of the surface area occupied by holes (0.1 for packing with a pattern of holes). “A” and “B” are the packing type and size-dependent constant (“A=0.000002143”, “B=1.5”, for Montz-pak “B1-250”) and “ u_{LS} ” is the superficial liquid velocity defined by Eq. 3.41.

3.2.5.4 Mass transfer coefficients

- **Gas-phase mass-transfer coefficient**

The “Delft” model assumes that over typical operating (F-factor) range, the overall gas-phase mass-transfer coefficient can be represented as an average of two individual, laminar, and turbulent flow contributions [OLU 99]:

$$k_G = \sqrt{k_{G,lam}^2 + k_{G,turb}^2} \quad \text{Eq. 3.61}$$

$$k_{G,lam} = \frac{Sh_{G,lam} \cdot D_G}{d_{hG}} \quad \text{Eq. 3.62}$$

$$k_{G,turb} = \frac{Sh_{G,turb} \cdot D_G}{d_{hG}} \quad \text{Eq. 3.63}$$

Where: “ D_G ” stands for the diffusion coefficient for gas phase ($\text{m}^2 \cdot \text{s}^{-1}$). The laminar and turbulent Sherwood numbers are respectively:

$$Sh_{G,lam} = 0.664 Sc_G^{1/3} \sqrt{\text{Re}_{Grv} \frac{d_{hG}}{l_{G,pe}}} \quad \text{Eq. 3.64}$$

$$Sh_{G,turb} = \frac{\text{Re}_{Grv} Sc_G \frac{\xi_{GL}\phi}{8}}{1 + 12.7 \sqrt{\frac{\xi_{GL}\phi}{8}} (Sc_G^{2/3} - 1)} \left[1 + \left(\frac{d_{hG}}{l_{G,pe}} \right)^{2/3} \right] \quad \text{Eq. 3.65}$$

Where the gas-phase “Schmidt” number is defined as:

$$Sc_{G,turb} = \frac{\mu_G}{\rho_G D_G} \quad \text{Eq. 3.66}$$

“ ξ_{GL} ” is given by Eq. 3.52 and “ $\frac{d_{hG}}{l_{G,pe}}$ ” as the ratio of hydraulic diameter and the length of gas flow channel within a packing element.

- **Liquid-phase mass-transfer coefficient**

The mass transfer resistance in liquid phase is considered as nearly negligible. The “Delft” model uses the same expression as proposed by Bravo et al. [BRA 92]. However, instead of the corrugation side, s , the characteristic length of the liquid flow path will be equal to the hydraulic diameter of the triangular flow channel defined by Eq. 3.67 [OLU 99]:

$$K_L = 2 \sqrt{\frac{D_L \mu_{Le}}{\pi 0.9 d_{hG}}} \quad \text{Eq. 3.67}$$

Where: “ D_L ” stands for the diffusion coefficient for liquid phase ($m^2 \cdot s^{-1}$).

3.2.5.5 Heat-transfer coefficients

As mentioned previously, the heat and mass transfer analogy is used to compute the heat-transfer coefficients for the liquid and gas. Therefore, the heat-transfer coefficients are computed as follows [LI 06].

- **Heat-transfer coefficient on the gas side**

$$\frac{Nu_G}{Pr_G^{1/3}} = \frac{Sh_G}{Sc_G^{1/3}} \quad \text{Eq. 3.68}$$

$$h_G = k_G (\rho_G C_{pG})^{1/3} \left(\frac{\lambda_G}{D_G} \right)^{2/3} \quad \text{Eq. 3.69}$$

- **Heat-transfer coefficient on the liquid side**

$$\frac{Nu_G}{Pr_G^{1/2}} = \frac{Sh_G}{Sc_G^{1/2}} \quad \text{Eq. 3.70}$$

$$h_L = k_L \left(\rho_L C_{pL} \frac{\lambda_L}{D_L} \right)^{1/2} \quad \text{Eq. 3.71}$$

Where “ λ ” denotes the thermal conductivity and “ D ” denotes the molecular diffusion coefficient.

- **Overall heat-transfer coefficient**

The overall heat transfer coefficient is given by:

$$h = \left(h_L^{-1} + h_G^{-1} \right)^{-1} \quad \text{Eq. 3.72}$$

The liquid hold-up in the Delft model is straightforward to predict as it is simply calculated from the packing geometric area and the liquid film thickness. The liquid film thickness is calculated from the

“Nusselt” formula for falling film with provision made for the inclination angle of the packing. All the parameters required in this model can be calculated from the characteristic lengths of the corrugated structured packing. The strong effect of corrugation angle on pressure drop is predicted fairly well with this model [FAI 00].

3.3 Model simulation and results

In this section, hydraulic, heat, and mass transfer analyses of the condensing unit are performed using structured packing with the parameters listed in Table 3.2.

Table 3.2: Parameters of structured packing used in the model simulation

Type	Montz B1-45°
a_p ($m^2 \cdot m^{-3}$)	244
ϵ (m^2/m^3)	0.980
b (m)	0.0225
h (m)	0.0120
s (m)	0.01645

The condensing unit parameters used in the simulation are shown Table 3.3. “DT” denotes the pinch value in the condensing unit between the entering flue-gas wet bulb temperature and the leaving water temperature. When not mention on figures, the liquid load is expressed in $m^3 \cdot m^{-2} \cdot hr^{-1}$. The water temperature at the condensing unit inlet is set to 45°C. A square cross-sectional area (A_{fr}) for the condensing unit is adopted in the model simulation.

Table 3.3: Condensing unit parameters

Gas Compositions	CO ₂ - 15.5% v, O ₂ - 6.8% v
T_{in} flue gas	120°C
T_{dp}	60°C
DT_{CU}	0.5 K

- **Effect of liquid load on pressure drop**

The effect of liquid load on the pressure drop is shown in Fig. 3.10. The change of slope in the plotted curves indicates the transition zone between the preloading and the loading regions. In the loading zone, the wet pressure drop depends on both the gas-load factor and the liquid loads. The wet pressure drop increases sharply by increasing the liquid load.

The repartition of the pressure drop is shown Fig. 3.11. The pressure drop due to gas-gas interaction is the dominant one, and accounts for around 55% of the total pressure drop. The pressure drops due to direction change account around 35% of the total pressure drop.

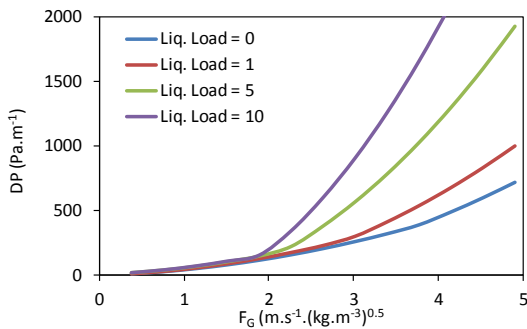


Fig. 3.10: Effect of liquid load on pressure drop (DT = 0.5 K, $A_{fr} = 0.6m \cdot 0.6m$)

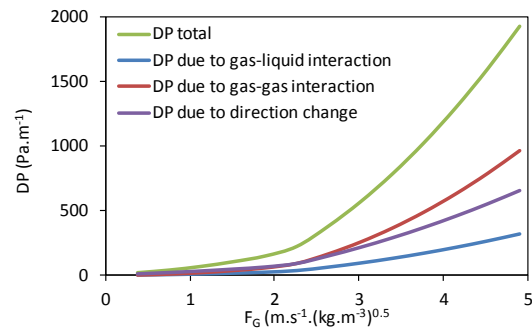


Fig. 3.11: Repartition of pressure drop (DT = 0.5 K, Liq. Load = $5 m^3 \cdot m^{-2} \cdot K^{-1}$, $A_{fr} = 0.6m \cdot 0.6m$)

- **Effect of liquid load on liquid hold-up**

The evolutions of the liquid hold-up as a function of the gas-load factor for various liquid loads are shown in Fig. 3.12. The transition between the preloading and the loading zones appears clearly in this figure.

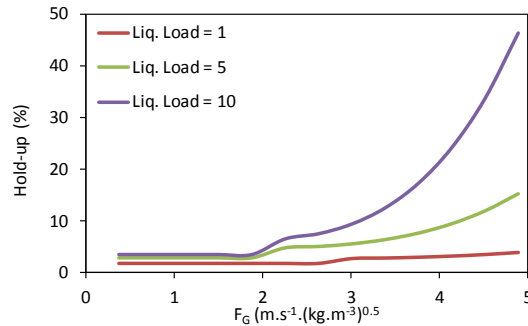


Fig. 3.12: Evolutions of the liquid hold-up as a function of the gas-load factor for different liquid loads ($DT = 0.5 \text{ K}$, $A_{fr} = 0.6\text{m} \times 0.6\text{m}$)

As shown in Fig. 3.12, the liquid hold-up is only a function of liquid flow rate in the preloading zone. In the loading zone, an increase in the gas flow rate would lead to an increase in the liquid hold-up. At high-liquid load, the liquid hold-up tends to infinity with an increase in the gas-load factor, and a flooding may occur. In this case, the gas flow rate is large enough to prevent the liquid from flowing down the condensing unit.

- **Effect of liquid load and pinch value on required packing height**

The effects of liquid load and pinch value (“DT”) on the required packing height for a wide range of gas-load factor are shown in Fig. 3.13.a and Fig. 3.13.b respectively. The required packing height decreases by decreasing the liquid load (Fig. 3.13.a) and by increasing the pinch value (Fig. 3.13.b).

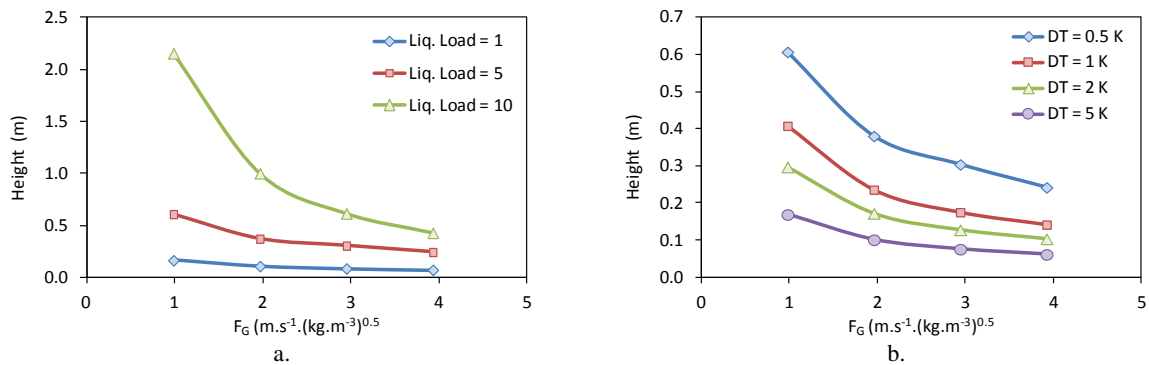


Fig. 3.13: Evolution of the required packing height as a function of the gas-load factor for various: a) liquid loads ($DT = 0.5 \text{ K}$, $A_{fr} = 0.6\text{m} \times 0.6\text{m}$), b) DT (Liq. Load = $5 \text{ m}^3 \cdot \text{m}^{-2} \cdot \text{K}^{-1}$, $A_{fr} = 0.6\text{m} \times 0.6\text{m}$)

- **General design considerations**

When designing a condensing unit, the selection of the cross-sectional area depends on the hydraulic parameters (pressure drop and liquid hold-up). The required packing height will be determined based on the heat and mass transfer calculations.

Table 3.4: Additional condensing unit parameters

m_{dg}	$1 \text{ kg} \cdot \text{s}^{-1}$
$T_{in \text{ water to CU}}$	50°C

m_w	$3.56 \text{ kg}\cdot\text{s}^{-1}$
Q_{CU}	$210 \text{ kJ}\cdot\text{kg}_{dg}^{-1}$

For the condensing unit, additional operating parameters to those indicated in Table 3.3 are shown in Table 3.4. These parameters correspond to the maximal net power in the ORC system using direct-contact condensation mode (refer to Chapter 1).

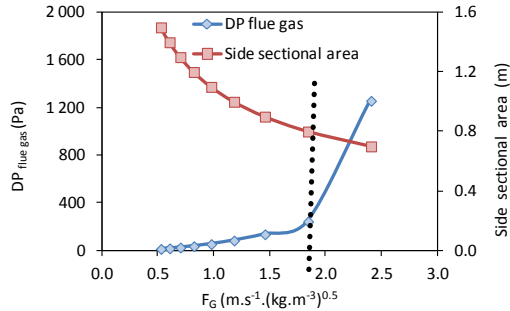


Fig. 3.14: Evolution of flue-gas pressure drop and side sectional area as a function of the gas-load factor

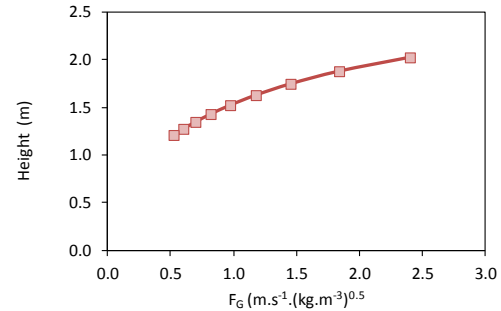


Fig. 3.15: Evolution of the required packing height as a function of the gas-load factor

Fig. 3.14 shows the evolutions of the flue-gas pressure drop and side sectional area as a function of the gas-load factor. The dashed line indicates the transition zone between the preloading and the loading zones. By increasing the gas-load factor, an increase in the pressure drop occurs accompanied by a decrease in the side sectional area (Fig. 3.14). The selection of the corresponding sectional area depends on the allowable pressure losses throughout the condensing unit. Nevertheless, it is advised to operate in the loading region to ensure appropriate liquid and gas distribution.

Fig. 3.15 shows the evolution of the required packing height as a function of the gas-load factor. The required packing height increases with the gas-load factor increase.

Fig. 3.16.a and Fig. 3.16.b show, respectively, the evolutions of the temperature and heat transfer capacity along the packing height. In order to operate in loading region, the side sectional area is set to 0.8 m. The bottom part of the condensing unit operates essentially as a flue-gas cooling section promoting saturation of the supplied hot flue gases. Both flue-gas humidification and subsequent dehumidification take place. Fig. 3.16.b shows that the humidification will occur in the bottom section, i.e. within a short packing segment ($< 0.5 \text{ m}$) where flue gases gain latent heat and lose sensible heat. In this section, the flue-gas temperature drops by around 40°C (Fig. 3.16.a). Above this section, a flue-gas dehumidification occurs (Fig. 3.16.b).

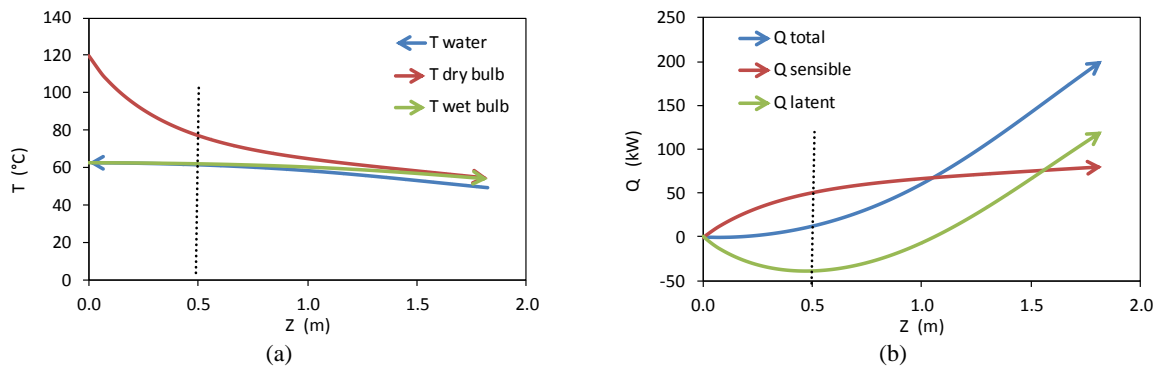


Fig. 3.16: Evolutions of : a) Temperature, b) Heat-transfer capacity, vs. required packing height (side sectional area = 0.8 m)

Fig. 3.17 illustrates the condensation process of flue gases using the background of a psychrometric chart. Wet bulb and dew point lines are marked by dashed lines. The humidification and dehumidification processes of flue gases are shown clearly in this figure.

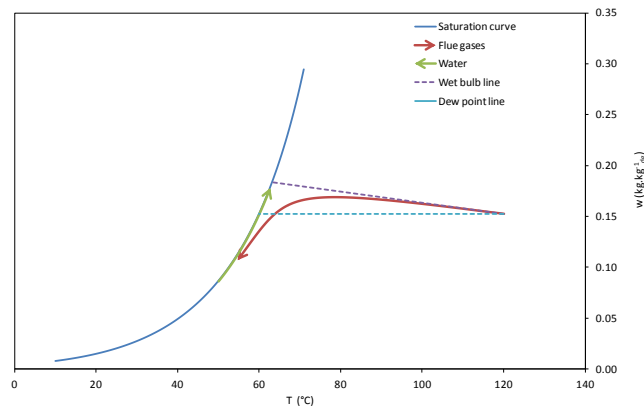


Fig. 3.17: Direct-contact condensation process using a psychrometric chart (side sectional area = 0.8 m)

3.4 Experimental methods

The objective of the experimental study is to examine the performance of various packing types with distinct surface geometry and wet-ability, in order to deepen understanding of the impact of packing properties on the condensing unit hydraulic parameters and to compare their corresponding heat and mass-transfer efficiencies. Another objective is to validate the predicted hydraulic as well as the heat and mass transfer models.

3.4.1 Description of the lab-scale condensing unit

The layout of the lab-scale condensing unit is shown Fig. 3.18. A square cross sectional area of “0.6m * 0.6m” is selected. A solid cone-shaped spray nozzle with square impact area is chosen. The nozzle is positioned in such a way that the water is uniformly distributed over the packing material. The mist eliminator is installed horizontally on the top of the liquid distribution system. The gas stream, with the entrained droplets generated by nozzles, flows upward through the mist eliminator. The gas can pass through the eliminator freely; liquid droplets are held by the eliminator and coalesce with other droplets, and drain down once heavy enough. A mist eliminator with solid vane type is selected. It is characterized by a relatively low-water loss ratio and low-pressure drop [YU 10]. More details about the characteristics of the lab-scale condensing unit, dimensions, as well as the selection of the nozzle and the mist eliminator can be found in “Annex E”.

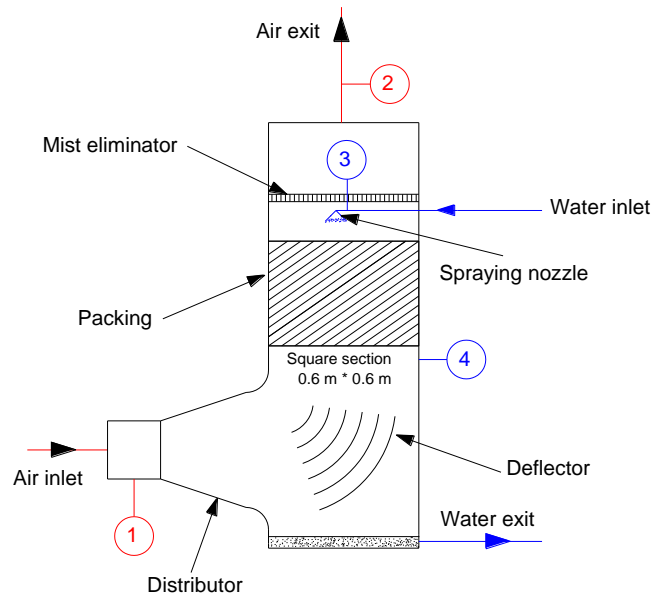


Fig. 3.18: Layout of the lab-scale condensing unit
(all dimensions are in mm)

Fig. 3.19 shows the various types of tested packing. Four types of metallic structured packing (“B1-45°”, “B1-60°”, “B1-M” and “B1-MN”), and one type of polypropylene packing with wavy corrugation shape (“PP”) will be tested. All the types of structured packing are imported from “Montz” company [MON 13], and the “PP” packing is imported from “GEA” company [GEA 13].

“Type B1” is made from stainless steel (“SS-316L”); it has proven its reliability in many technical applications. The excellent characteristics are ensured by the regular arrangement and the special surface structure. Two corrugation angles are available: “B1-45°” (Fig. 3.19.a) and “B1-60°” (Fig. 3.19.b). Compared to “B1-45°”, “B1-60°” is proposed to reduce the pressure drop at the flue-gas side.

“B1-M” (Fig. 3.19.c) and “B1-MN” (Fig. 3.19.d) are capacity-enhanced structured packing. These two types present identical geometry with the difference that “B1-MN” is perforated. Based on manufacture data, “B1-M” and “B1-MN” combine all advantages of the metal sheet packing “B1-45°”, with new geometrical features. They offer many features: at the lower and upper ends of each packing element, the orientation of the corrugation gradually approaches the vertical axis. The advantages of this geometrical modification are the following: the flue-gas flow smoothly changes direction at the interface between two packing elements. At the interface, gas flow is nearly parallel to the vertical axis of the column. The gas velocity is therefore reduced by about 25% compared to the velocity inside the packing element. Both factors reduce the pressure drop and the shear forces, which are especially critical at the interface due to the presence of thicker and less stable liquid films. As a result, premature flooding at the interface is no longer of concern. In the internal part of the packing element, the geometrical features of “Type M” or “Type MN” and “Type B1” are identical. Hence, heat and mass transfer efficiency is similar, but with a significant reduction in pressure drop.

The polypropylene packing “PP” with wavy geometry (Fig. 3.19.e) is characterized by a good leach resistance and wash resistant. The “sanipacking” prevents growth of “Legionella pneumophila” and other bacteria. It has a lasting effect against “Legionella pneumophila” and a large number of gram-positive and gram-negative bacteria on the surface of the fill. It works by disrupting the metabolic process of unwanted microorganisms at the cell wall level, thus interrupting their ability to function, grow, and reproduce.

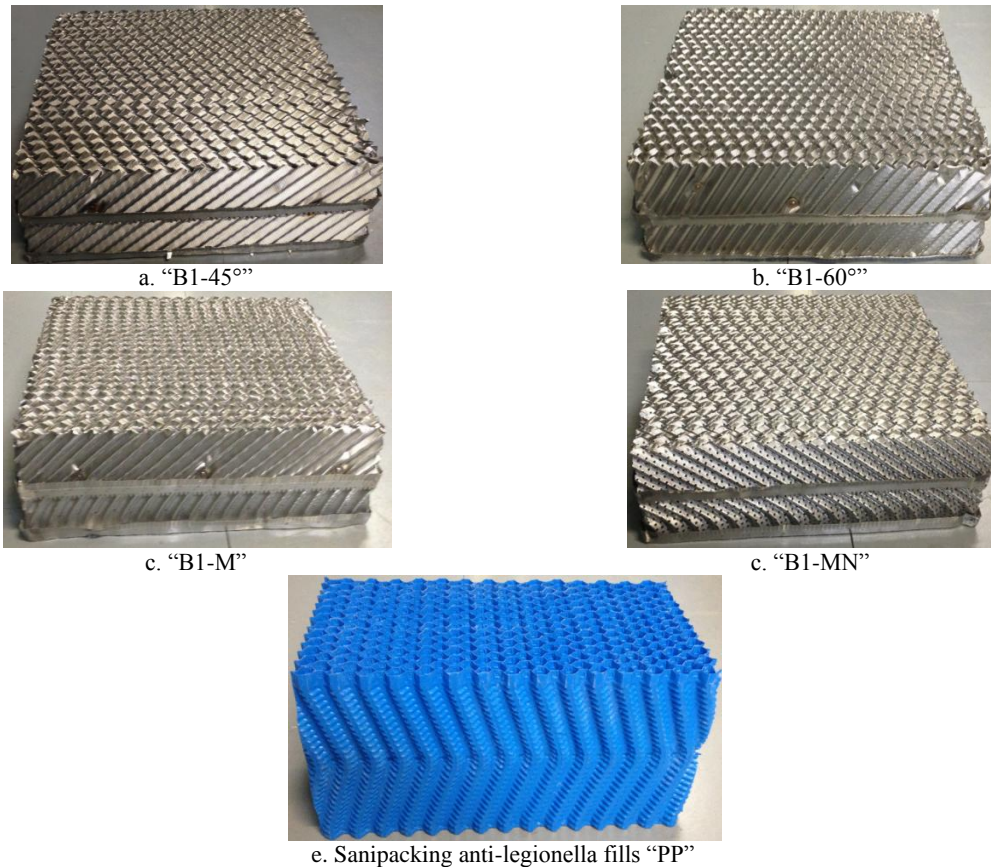


Fig. 3.19: Tested packing types

The five tested types of packing are characterized by the same cross sectional area ($0.6\text{m} \times 0.6\text{m}$) and the same specific surface area ($a_p = 250 \text{ m}^2 \cdot \text{m}^{-3}$). The packing element height, “ h_{pe} ”, is 0.2 m for stainless steel packing and 0.3 m for polypropylene packing. Each type of stainless steel packing is equipped with two wall wipers.

3.4.2 Experimental apparatus and procedure

The diagram shown in Fig. 2.23 was used to characterize the direct-contact process between air and water. It is mainly composed of a wet air generator and a water loop. The tested condensing unit is noted “CU”. The air circuit is the same as used to test the fin-and-tube heat exchanger specimens (refer to Chapter 2). It includes mainly a blower (BW01), two electrical heaters (EH01 and EH02), and a steam injection system (HU01). As Fig. 2.23 suggests, airflow is driven by the air blower (BW01) through the first electrical heater (EH01, 50 kW), which heats the air to a desired temperature able to hold the desired humidity. The second electrical heater (EH02, 10 kW) rules the air temperature disruption after steam injection. Steam generated by a boiler could be injected into the system (HU01) in order to acquire the desired relative air humidity. The needed steam quantity is provided by water vaporization into a plate-heat exchanger (HX01) through a heat-exchange transfer between the hot oil entering from the boiler hot oil generator and the water entering from outside.

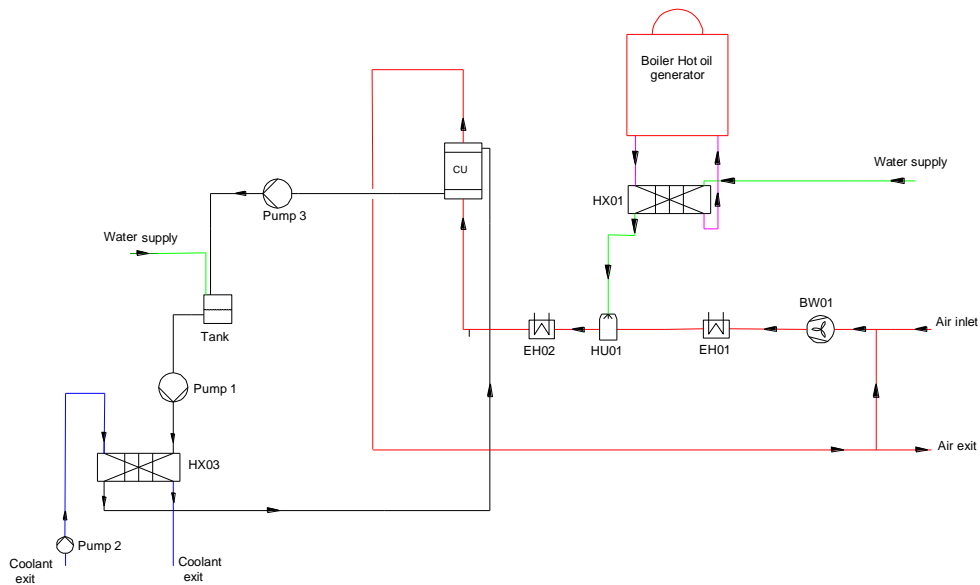


Fig. 3.20: Layout of the condensing unit test bench

The hot water circuit includes two pumps (“Pump 1” and “Pump 3”), a water tank, and a plate-heat exchanger (HX03). A direct heat transfer occurs between the sprayed water and the hot air in the condensing unit. The hot water, recovered at the bottom of the condensing unit, is then pumped by “Pump 3” to enter the tank where it is pumped by “Pump 1” to the heat exchanger (HX03) and it is cooled. The coolant, a mixture of ethylene glycol and water, was supplied by a pump (Pump 2) to cool the water during the experiments. The coolant had its temperature controlled by a chilled system.

Shown in Fig. 2.24 is a P&ID diagram (piping and instrumentation diagram) of the test bench. The test bench is instrumented in pressure, temperature, flow meters, and relative humidity sensors to evaluate the thermal hydraulic performance of the condensing unit, and to establish the energy balance between airside and waterside.

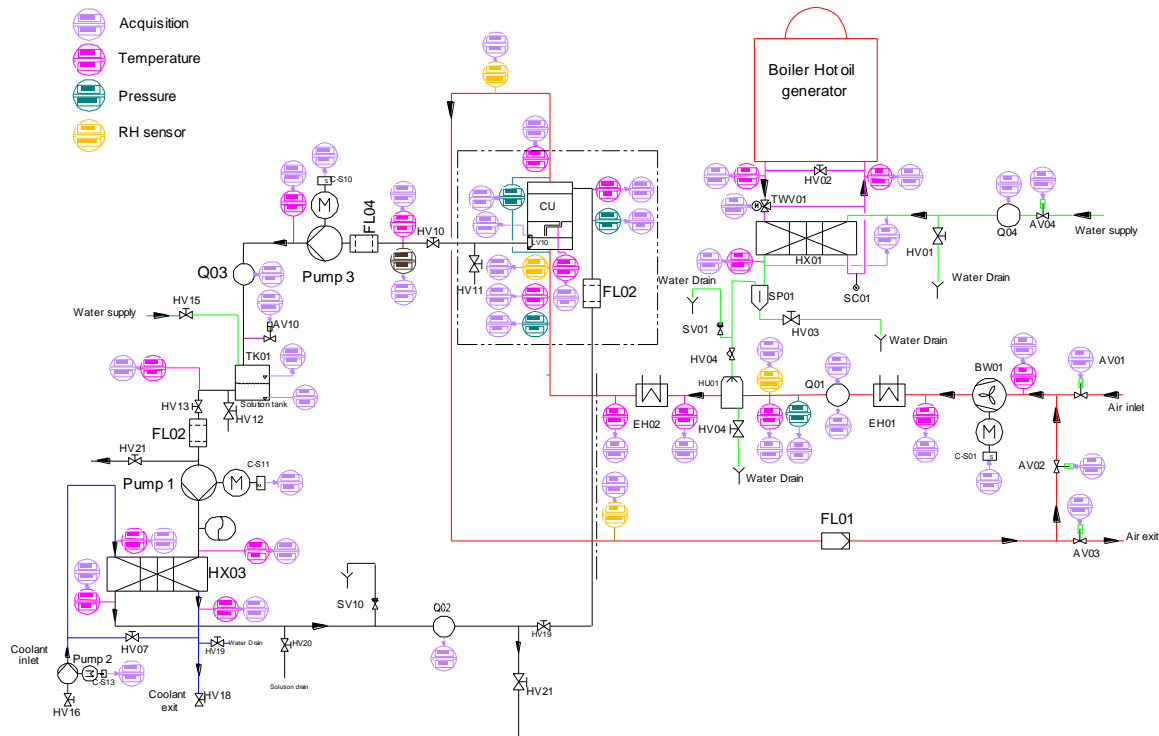


Fig. 3.21: P&ID diagram of the condensing unit test bench

Temperature sensors were positioned at the condensing unit inlet and outlet to record the air and water “in” and “out” temperatures. Inlet water temperature is measured at the inlet water pipe of condensing unit (states “3” in Fig. 3.18), and outlet water temperature is measured right at the bottom of the packing materials (states 4 in Fig. 3.18). Air inlet and outlet temperatures are measured at the inlet and outlet air ducts respectively (states “1” and “2” in Fig. 3.18). Air inlet conditions, right at the entrance at the packing material, are derived analytically from the air conditions at state “1” by considering no change occurring in the absolute humidity in the rain zone. Upstream and downstream water dew points of the air were measured using hygrometers, and pressure drop across the condensing unit was acquired via an electronic pressure transducer. An electromagnetic flow meter (Q02) was used to measure the water flow rate and an anemometer (Q01) was used to measure the airflow rate. In the oil circuit, temperature sensors were positioned at the inlet and outlet of the plate-heat exchanger (HX01) in order to control the oil temperature. The mass of steam injected is controlled using an automatic-valve (AV04). A temperature sensor is positioned to control the temperature of the steam exiting from the plate-heat exchanger (HX01).

Fiberglass insulation for the condensing unit and air circuit has to be done in order to reduce thermal losses with outside environment.

Heat and mass transfer and pressure drop for each tested packing were recorded over a range of operating conditions. For thermal-hydraulic measurements, the ranges of experimental conditions are provided in Table 3.5. As a result, inlet air temperature is limited to “70°C” (temperature limit for the polypropylene packing). The airflow rate is varied from “500” to “4000” $\text{m}^3 \cdot \text{hr}^{-1}$ and the water mass flow rate is varied from “100” to “700” $\text{g} \cdot \text{s}^{-1}$. The water temperature at the condensing unit inlet is varied between “40°C” and “50°C”.

Table 3.5: Tests operating conditions

Parameters	Range conditions
------------	------------------

Air temperature	65°C - 70°C
Water dew point temperature	Up to 60°C
Air volume flow rate	500 - 4000 m ³ .hr ⁻¹
Gas load factor (F)	0.5 - 3 m.s ⁻¹ .(kg.m ⁻³) ^{0.5}
Water mass flow rate	100 - 700 g.s ⁻¹
Liquid load	1 - 7 m ³ .m ² .s ⁻¹
T _{in water to CU}	40 - 50°C

An experiment was initiated by circulating the airflow while bringing it to the desired temperature, velocity, and relative humidity. Then water flow starts to be heated in the condensing unit. After a transient period at the beginning of each test (~10 minutes), it would arrive at steady state. Once an experiment reached the steady state, reading of all conditions remained almost constant within their experimental uncertainty throughout the rest of the experiment. All measured data would then be sampled out by a “CVI Lab-View” program for subsequent analysis.

3.4.3 Data reduction and interpretation

The heat-transfer capacity will be calculated via the energy balance at both water and humid air. The energy balance for water is given by:

$$Q_w = m_w \cdot c_{pw} \cdot (T_{water,out} - T_{water,in}) \quad \text{Eq. 3.73}$$

The energy balance for humid air is given by:

$$Q_{air} = m_{dg} \cdot (h_{air,in} - h_{air,out}) = m_{dg} \cdot [c_{p,dg} \cdot (T_{air,in} - T_{air,out}) + 2501 \cdot (h_{air,in} - h_{air,out})] \quad \text{Eq. 3.74}$$

In order to compare the heat and mass transfer performances with various types of packing, an overall heat-transfer coefficient “U” could be defined via Eq. 3.75 as follows:

$$U = \frac{Q}{a_p \cdot z \cdot A \cdot (\Delta TLM)} \quad \text{Eq. 3.75}$$

All the relevant quantities in Eq. 3.75 are calculated from Eq. 3.73 and Eq. 3.74.

Since the effective area for heat/mass transfer between humid air and water depends on the packing types, the calculated overall heat-transfer coefficient will be based on the nominal area of the packing (a_p) as shown in Eq. 3.75.

Estimation of the relative uncertainties for all calculated quantities follows the error propagation methodology as already shown in Chapter 2. Through a standard error propagation calculation, the average uncertainty on U factor was found to be about $\pm 8.03\%$.

3.5 Tests results and discussion

In this section, thermal and hydraulic parameters of the tested packing are presented. A comparison will be drawn among the five tested specimens in order to illustrate the effect of surface type and surface wet-ability on the direct-contact process performances.

3.5.1 Experimental pressure drop at the airside

During pressure drop measurements, some problems were encountered caused by the pressure sensor clogging due to the entrained water particles within the airflow. Only dry pressure drop for “PP”, “B1-45°”, and “B1-60°” and wet pressure drop for “PP”, and “B1-45°” are recorded. Air at ambient conditions is passed through the condensing unit.

A comparison of dry pressure drop between three packing types (“PP”, “B1-45°” and “B1-60°”) is shown in Fig. 3.22. This figure shows that “PP” and “B1-60°” present almost the same dry pressure drop. “B1-45°” presents higher dry pressure drop and can account for around four times that obtained with “B1-60°” at high-gas-load factor.

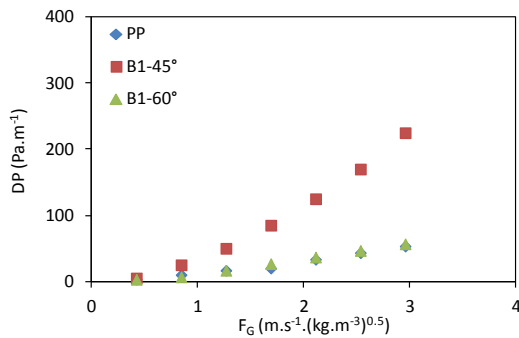


Fig. 3.22: Comparison of dry pressure drop between “PP”, “B1-45°” and “B1-60°”

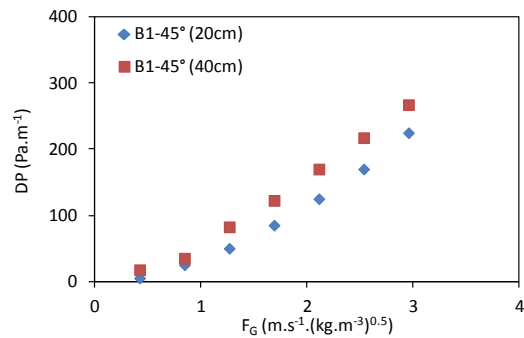


Fig. 3.23: Effect of the number of packing elements on dry pressure drop

Fig. 3.23 shows the effect of the number of packing elements on dry pressure drop. Using two packing elements will increase the dry pressure drop per meter by around 30%. This could be explained by the fact that the use of two packing elements involves an additional pressure drop due to gas-gas interaction at the interface created between crossing gas flows, and due to the direction changes at the transitions between packing elements.

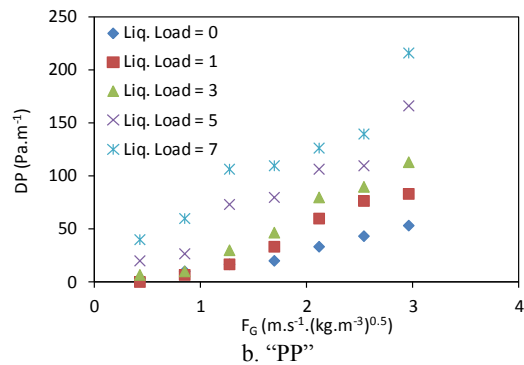
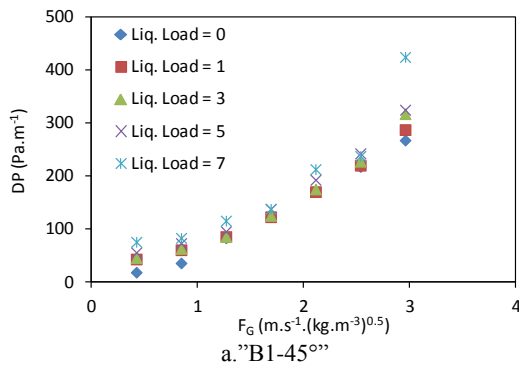


Fig. 3.24: Experimental wet pressure drop for: a) “B1-45°”, b) “PP”

Fig. 3.24.a and Fig. 3.24.b show the evolutions of the experimental pressure drop for various liquid loads as a function of the gas-load factor for “B1-45°” and “PP”. The wet pressure drop increases by increasing both the gas-load factor and the liquid load. The wet pressure drop is more dependent on liquid load for “PP” than for “B1-45°”. This is mainly due to surface wet-ability. Water on polypropylene is poorly wetting and presents higher probability to form liquid bridges causing runoff formation, which block the flue-gas flow.

A comparison between the correlated pressure drop and the experimental one is shown in Fig. 3.25 for “B1-45°”. The experimental pressure drop is measured using two packing elements in order to take into consideration the effect of direction change at the transitions between packing elements. Fig. 3.25 shows that the pressure drop is mainly underestimated over the entire range of liquid loads and gas-load factors, within a relative error of 30%.

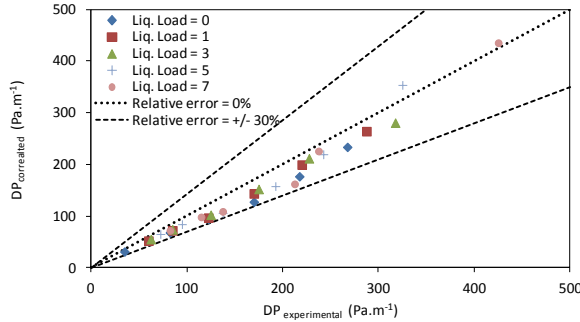


Fig. 3.25: Comparison between correlated and experimental pressure drop (“B1-45°”)

3.5.2 Comparison of the overall heat-transfer coefficient

Hereinafter, in the comparison of heat and mass transfer efficiency with various types of packing, the overall heat transfer coefficient “U” defined in Eq. 3.75 will be used. This factor is based on the nominal area of the packing (a_p).

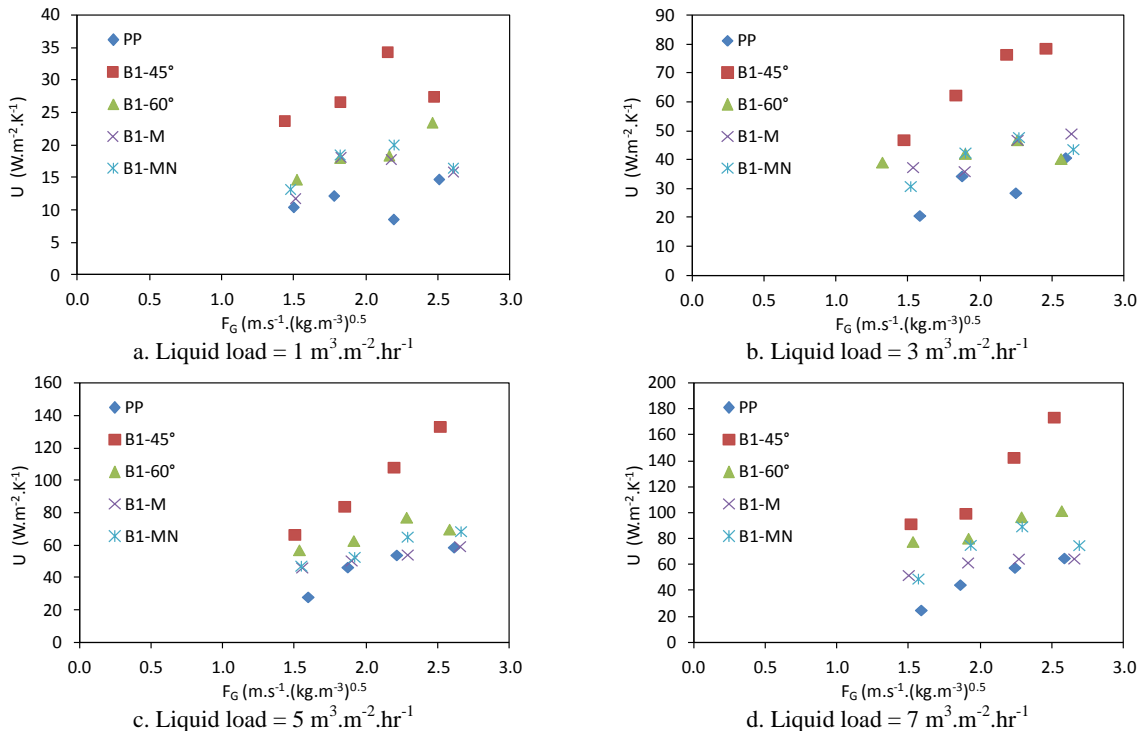


Fig. 3.26: Comparison of U-factors for the tested packing under various liquid loads

A comparison of “U-factor” between the various types of packing (“PP”, “B1-45°”, “B1-60°”, “B1-M”, and “B1-MN”) is shown in Fig. 3.22. Various liquid loads in the range “1” to “7” $\text{m}^3.\text{m}^{-2}.\text{hr}^{-1}$ are employed. As a general trend, the “U-factor” increases by increasing the gas-load factor and by increasing the liquid load. “B1-45°” presents the highest “U-factor”, while the “PP” presents the lowest one. “B1-60°”, “B1-M” and “B1-MN” present generally lower “U-factors” compared to “B1-

45°”, which is inconsistent with the manufacturer data. At high-gas-load factor, and for a liquid load higher than $3 \text{ m}^3 \cdot \text{m}^{-2} \cdot \text{hr}^{-1}$, the “U-factor” for “B1-45°” is around “1.5” to “2” times that obtained for “B1-60°” (or “B1-M”, “B1-MN”).

3.5.3 Comparison between the predicted and correlated heat-exchange capacity

A comparison between the predicted and the correlated water temperature at the condensing unit exit is shown in Fig. 3.27.a, Fig. 3.27.b, and Fig. 3.27.c at water temperatures at the condensing unit inlet of “40°C”, “45°C”, and “50°C” respectively. The structured packing “B1-45°” is used for this purpose, since the “Delft” model used in this study is developed for this type of packing. The mass transfer coefficient is calculated analytically using the heat and mass transfer analogy defined in Eq. 3.68 and Eq. 3.70. This assumption could be validated since a little water vapor condensation occurs. The effective surface area is calculated using Eq. 3.72. Values in brackets in Fig. 3.27 indicate liquid-load values. For a given water temperature at the condensing unit inlet, it is observed that the water temperature at the condensing unit exit increases by increasing both the gas-load factor and the liquid loads. As a general trend, predicted and measured exit water temperatures present very good agreement. The water temperature at the condensing unit exit is predicted within less one Kelvin, and it is generally overestimated.

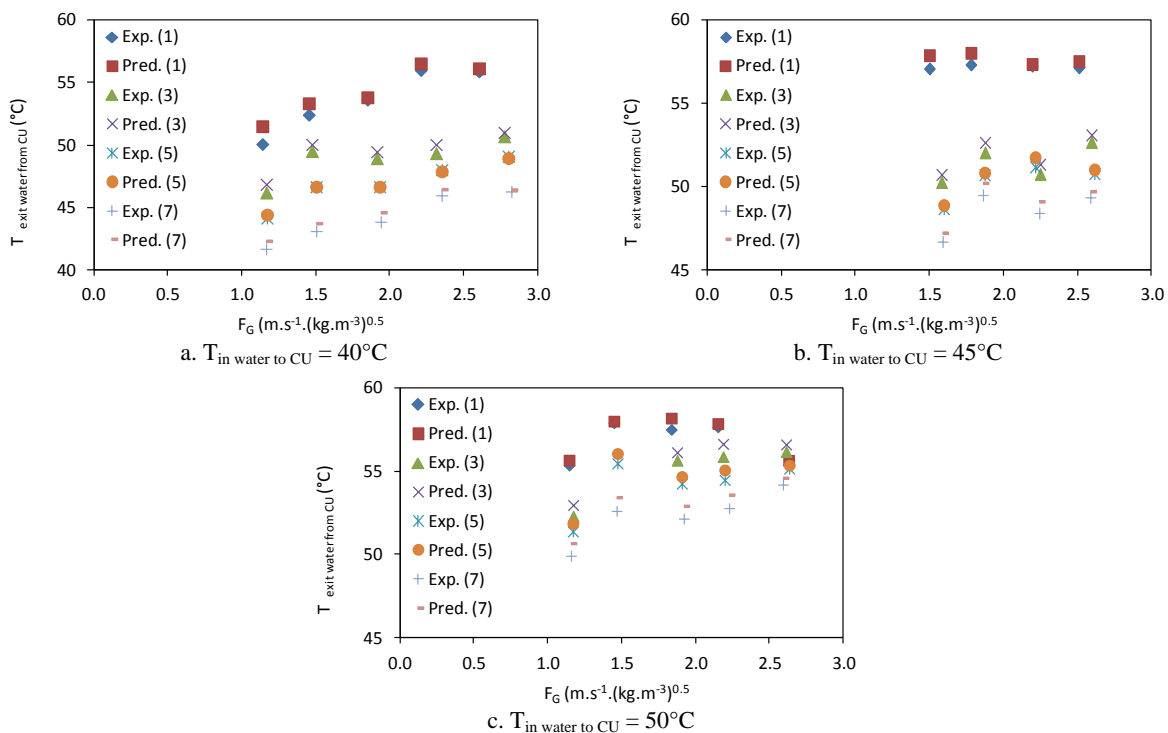


Fig. 3.27: Comparison between the predicted and the correlated exit water temperatures (“B1-45°”)

In order to validate the heat and mass transfer model, a comparison between the experimental and the correlated heat exchanger capacities is shown in Fig. 3.28. The water temperature at the condensing unit inlet is varied between “40°C” and “50°C”. The heat-transfer capacity is mainly overestimated within a relative error of 15%.

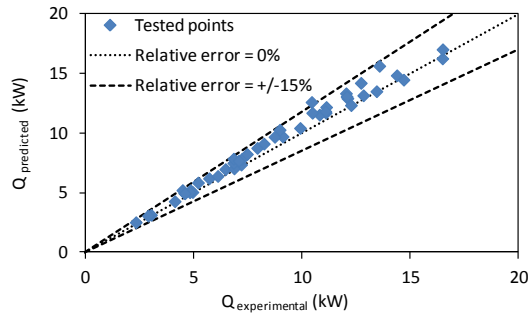


Fig. 3.28: Comparison between correlated and experimental heat-exchange capacity (“B1-45°”)

Further experimental tests are needed in order to validate the heat and mass transfer coefficients as well as the validity of heat and mass transfer analogy (Lewis factor) under a relatively high water vapor condensation rate.

3.6 Conclusions

The recovery of industrial low-temperature heat sources with high-moisture content using a direct-contact heat exchanger has received attention because heat is transferred between the two-fluids (typically gas and water) on structured surfaces. The two fluids move in counter-flow direction in vertical column comprising a packing fill, and the liquid is dispersed in small particles. Liquid droplets are ideal for transferring latent heat from flue gases because spraying water droplets can provide a large heat-transfer surface area in the presence of relatively small temperature differences between the heating and cooling media.

The direct heat exchange between flue gases and water occurs via packing materials. The design considerations of the condensing unit are based on hydraulic parameters (pressure drop and liquid hold-up) and on heat and mass transfer between flue gases and water through the packing. The knowledge of the hydraulic characteristics is essential for the condensing unit design. Three operating regions can be defined: the pre-loading region where the pressure drop in the condensing unit is parallel to the dry column pressure drop, and thus the liquid hold-up is independent of the gas-load factor and only dependent on the liquid load and liquid properties; the loading region where the pressure drop and liquid hold-up in the condensing unit are functions of the gas flow (the pressure drop trend deviates from the dry column pressure drop); and the flooding region where the gas flow rate is large enough to prevent the liquid from flowing down the column. A 1-D mathematical model for heat and mass transfer is presented in order to determine the required column height for a given operating parameters. In designing a condensing unit, the cross-sectional area will be selected based on hydraulic parameters and depending on the maximal allowable pressure drop at the flue-gas side.

Experimental study is performed in order to validate the predicted hydraulic as well as the heat and mass transfer models inside packing. A laboratory scale condensing unit is built with a square cross sectional area of “0.6 m x 0.6 m”. Different types of packing are tested with various surface geometries and wet-ability in order to compare their corresponding heat and mass transfer efficiencies and to develop deeper understanding of the impact of packing properties on the condensing unit hydraulic parameters. Within this aim, four types of stainless-steel-structured packing “Montz” technology (“B1-45°”, “B1-60°”, “B1-M”, and “B1-MN”) and one type of polypropylene packing “PP” are tested. From the pressure drop data that have been able to be measured, “B1-45°” presents a dry pressure drop almost four times higher than those obtained with “B1-60°” and “PP”. Pressure-drop

model validation for “B1-45°” shows that the correlated pressure drop is underestimated by around 30% compared to the experimental one over the entire tested range of liquid loads and gas-load factors. A comparison of “U-factor” between the various tested packing shows that “B1-45°” presents the highest “U-factor”, while the “PP” presents the lowest “U-factor”. “B1-60°”, “B1-M” and “B1-MN” show noticeable heat transfer degradations compared to “B1-45°”. Heat-transfer model validation for “B1-45°” shows that the correlated heat-exchange capacity is overestimated by around 15% compared to the experimental one. Finally, further experimental tests are needed in order to validate the heat and mass transfer coefficients as well as the validity of heat and mass transfer analogy (Lewis factor) under a relatively high water vapor condensation rate.

References

- [KLO 05] Kloppers, J.C., Kroger, D.G., A critical investigation into the heat and mass transfer analysis of counter-flow wet cooling towers. *Int. J. Heat and Mass Transfer*, 2005;48:765-777.
- [LOU 06] Loudon, D., The effect of Prewetting on the pressure drop, liquid hold-up and gas liquid mass transfer in Trickle Column Reactor, University of Pretoriavo, 2006.
- [ASH 08] Ashrae Systems and Equipment, Air-Cooling and Dehumidifying Coils. American Society of Heating, Refrigeration and Air-Conditioning Engineers. 2008, Chapter 22.
- [DAV 03] Davis, D., Personal Correspondence, Cooling Tower Institute, 2003.
- [BIL 95] Billet, R., Schultes, M., Fluid Dynamics and Mass Transfer in the Total Capacity Range of Packed Columns up to the Flood Point. *Chem. Eng. Tech*, 1995;18:371-379.
- [OLU 01] Olujic, Z., Jansen, H., Kaibel, B., Rietfort, T., Zich, E., Stretching the capacity of structured Packings. *Ind. Eng. Chem. Res.*, 2001;40:6172-6180.
- [OLU 99] Olujic, Z., Kamerbeek, A.B., De Graauw, J., A corrugation geometry based model for efficiency of structured distillation packing. *Chemical Engineering and Processing*, 1999; 38:683-695.
- [OLU 97] Olujic, Z., Development of a complete simulation model for predicting the hydraulic and separation performance of distillation columns equipped with structured packings. *Chem. Biochem. Eng. Q.*, 1997;11:31-46.
- [OLU 99] Olujic, Z., Effect of column diameter on pressure drop of a corrugated sheet structured packing, Institution of Chemical Engineers, *Trans IChemE*, 1999, vol. 77, part A.
- [VER 99] Verschoof, H.J., Olujic, Z., A general correlation for predicting the loading point of corrugated sheet structured packings, *Ind. Eng. Chem. Res.*, 1999;38:3663-3669.
- [COU 04] Coulson, J.M., Richardson, J.F., *Chemical Engineering*, 2004, Vol. 6. Fourth edition.
- [KIS 92] Kister, H.Z., *Distillation Design*, 1992, McGraw-Hill, New York.
- [LAM 10] Lamprecht, S. M., Establishing a facility to measure packed column hydrodynamics, Thesis, 2010, Department of Process Engineering at the University of Stellenbosch.
- [OLU 07] Olujic, Z., Behrens, M., Experimental Characterization and Modeling of the Performance of a Large Specific Area High Capacity Structured Packing. *Ind. Eng. Chem. Res.*, 2007;46:883-893.
- [BIL 99] Billet, R., Schultes, M., Prediction of Mass Transfer Columns with dumped and Arranged Packings: Updated Summary of the Calculation Method of Billet and Schultes, *Trans. IChemE*, 1999;77:498-504.
- [KLO 03] Kloppers, J.C., A critical evaluation and refinement of the performance prediction of wet-cooling towers, Ph.D. Thesis, University of Stellenbosch, Stellenbosch, South Africa, 2003.
- [KLO 05] Kloppers, J.C., Kroger, D.G., A critical investigation into the heat and mass transfer analysis of counter-flow wet cooling towers, , *Int. J. Heat and Mass Transfer*, 2005;48: 765-777.
- [LI 06] Li, Y., Klausner, J.F., Mei, R., Knight, J., Direct contact condensation in packed columns , *Int. J. Heat and Mass Transfer*, 2006;49:4751-4761.
- [BRA 92] Bravo, J.L., Rocha, J.A., Fair, J.R., A comprehensive model for the performance of columns containing structured packing, *ICHEME Symp. Ser.*, 1992;128:489-507.
- [BRA 96] Bravo, J.L., Rocha, J.A., Fair, J.R., Distillation columns containing structured packing: a comprehensive model for their performance, Mass transfer model, *Ind. Eng. Chem. Res.*, 1996;35:1660-1667.

- [FER 09] Fernandes, J., Lisboa, P.F., Simoes, P.C., Mota, J.P.B., Saadjian, E., Application of CFD in the study of supercritical fluid extraction with structured packing: wet pressure drop calculation, *J. of Supercritical Fluids*, 2009;50:61-68.
- [LAR 02] Larachi, F., Petre, C.F., Iliuta, I., Grandjean, B., Tailoring the pressure drop of structured packings through CFD simulations, *Chemical Engineering and Processing*, 2002;42:535-541.
- [GUA 97] Gualito, J.J., Cerino, F.J., Cardenas, J.C., Rocha, J.A., Design method for distillation columns filled with metallic, ceramic, or plastic structured packings, *Ind. Eng. Chem. Res.*, 1997;36:1747-1757.
- [WAN 06] Wang, G.Q., Yuan, X.G., Yu, K.T., A method for calculating effective interfacial area of structured packed distillation columns under elevated pressure, *Chemical Engineering and Processing*, 2006;45:691-697.
- [FAI 00] Fair, J.R., Seibert, A.F., Behrens, M., Saraber, P.P., Olujić, Z., Structured Packing Performance - Experimental Evaluation of Two Predictive Models, *Ind. Eng. Chem. Res.*, 2000;39:1788-1796.
- [YU 10] Yu, Y., Clodic, D., Conception initiale et simulation des EUs/CUs, 2010. Ecole des Mines de Paris, Center for Energy and Processes (CEP), Palaiseau, France.
- [MON 13] www.montz.de
- [GEA 13] www.gea-2h.com

Chapter 4: Innovative thermodynamic cycles for low-temperature wet heat sources

4.1 Introduction

Flue gases of industrial processes may present high-moisture content with various concentrations of pollutants such as nitric oxide (NO_x), sulfuric oxide (SO_x), and hydrochloric acid (HCl). Cooling flue gases below the water dew point temperature can achieve significant increases in energy efficiency via recovering the latent heat of evaporation. Classical heat recovery technologies using ORC include direct and indirect-contact water vapor condensation. In indirect-contact water-vapor condensation, heat is removed from flue gases by passing them generally through tubular heat exchangers. A challenge with this condensation mode is that the water vapor in flue gases will condense and reacts with sulfuric, sulfurous, nitric, and possibly hydrochloric oxides, resulting in corrosive depositions on the heat-exchanger surface. This will reduce heat-transfer rates, lifetime and lead to increased pressure drops and reduced efficiency. In this case, the heat-exchanger design requires using advanced materials to withstand exposure to corrosion problems (cf. Chapter 2) or frequently replacing heat-exchanger components, making probably the process economically unfeasible. In direct-contact water-vapor condensation, heat is transferred between the two fluids (typically flue gases and water) on packing fills leading to efficient heat and mass transfers (cf. Chapter 3). However, a decrease in the net power is expected compared to the indirect-contact condensation owing to the thermodynamic limitation of the circulating water temperature and to the additional temperature difference “ ΔT ” due to heat transfer loop between the circulating water and the working fluid.

Another challenge arises in the ORC systems when recovering low-temperature heat sources is the low-turbine expansion ratio since the evaporation temperature must be kept below the entering water dew point temperature in order to recover the latent heat.

Therefore, there is a compelling need to develop novel technologies to overcome the presented actual challenges. Thermodynamic cycles based on direct-contact water-vapor condensation using desiccant dehumidification technology could be an effective way to accomplish this purpose. In fact, while in contact with flue gases, desiccant can increase the entering wet bulb temperature by reducing the equilibrium surface water vapor pressure and therefore increasing the power produced as well as the turbine expansion ratio.

This chapter discusses the water sorption characteristics of desiccant materials and explains the implication of those characteristics in low-temperature heat-recovery systems. After a short review of the existing heat recovery technologies, the desiccant operation mode and its effect on the equilibrium wet bulb temperature are shown. Innovative thermodynamic cycles based on the liquid desiccant technology are presented, adapted, and improved in order to overcome the challenges faced in the classical heat recovery technologies.

4.2 Review of the existing heat recovery technologies

In this section, a review of the existing heat recovery modes (direct and indirect-contact water-vapor condensation) to recover low-temperature heat sources with high-moisture content using ORC is presented. In the following, “ICC” denotes “ORC with indirect-contact water-vapor condensation” and “DCC” denotes “ORC with direct-contact water-vapor condensation using pure water as heat-transfer medium”.

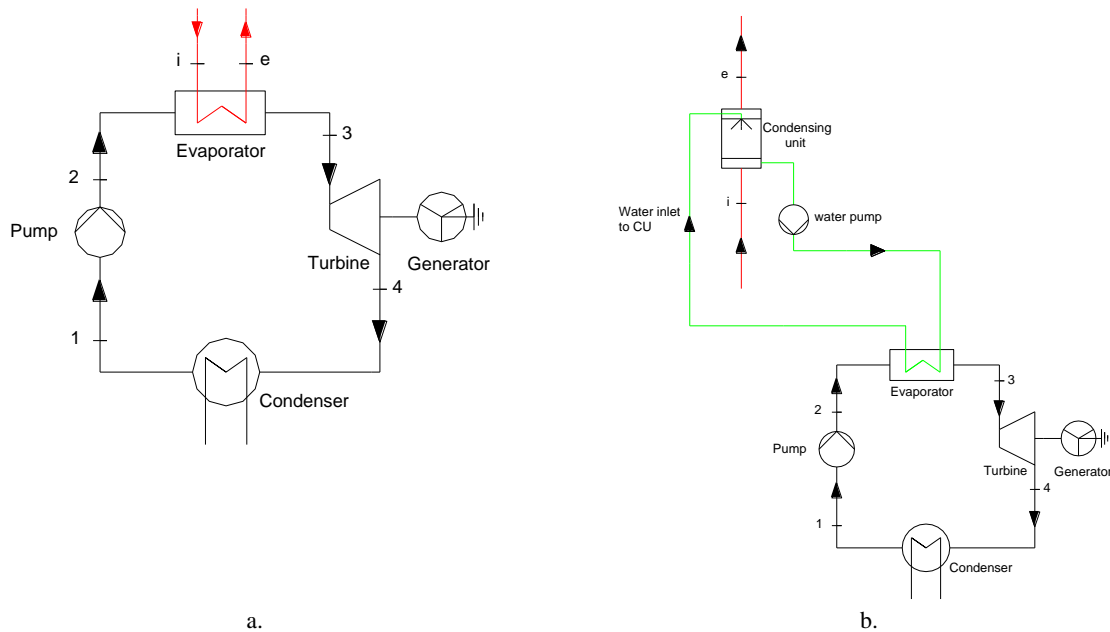


Fig. 4.1: Existing heat recovery technologies using: (a) “ICC” and (b) “DCC”

The layout diagrams of both “ICC” and “DCC” are shown in Fig. 4.1.a and Fig. 4.1.b respectively. In “ICC” mode, flue gases heat directly the working fluid in the evaporator, while in “DCC” mode, the heat is transferred to the evaporator using a heat-transfer medium (typically water). For calculations, the ORC operating parameters are given in Table 1.5. The condensation temperature is set to 25°C. R-245fa is selected as working fluid.

Table 4.1: Input data for the ORC analysis

Parameters	Value
Flue gas compositions (molar basis)	CO ₂ - 15.5% v , O ₂ - 6.8% v
T _{in} flue gases	120°C
Working fluid	R-245fa
Pinch Evaporator (ΔT_{evap})	3 K
SH _{evap}	0 K
Minimum pinch in CU ($\Delta T_{\text{min CU}}$)	0.5 K
T _{out} flue gases from CU - T _{in} water to CU	2 K
SC _{cond}	2 K
η_t	80%
η_p	85%

Fig. 4.2 shows the evolutions of the net power for various water dew point temperatures under a wide range of evaporation temperatures for the “ICC”. Fig. 4.2 points out that the maximal net power occurs at an evaporation temperature below the water dew point temperature; therefore, a large quantity of water vapor condensation will occur, thereby recovering a great portion of latent heat.

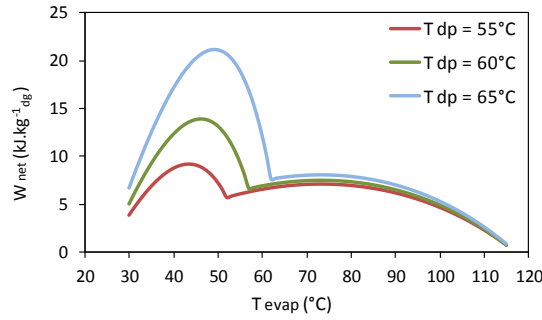


Fig. 4.2: Evolution of net power as a function of the evaporation temperature for the “ICC” (R-245fa)

For the “DCC”, Fig. 4.3.a shows a parametric optimization of the water temperature at the evaporator inlet with respect to the net power. The evaporation temperature of the working fluid is calculated in order to optimize the net power. Fig. 4.3.a shows that the net power increases by increasing the water temperature at the evaporator inlet. This latter is limited by the entering wet bulb temperature with a minimum of 0.5 K below it (minimum pinch in the condensing unit).

Fig. 4.3.b shows the evolution of the net power as a function of the evaporation temperature for a water temperature at the evaporator inlet equal to the entering wet bulb temperature minus 0.5 K. The net power curves present local optima at evaporation temperatures found below the corresponding water dew point temperatures.

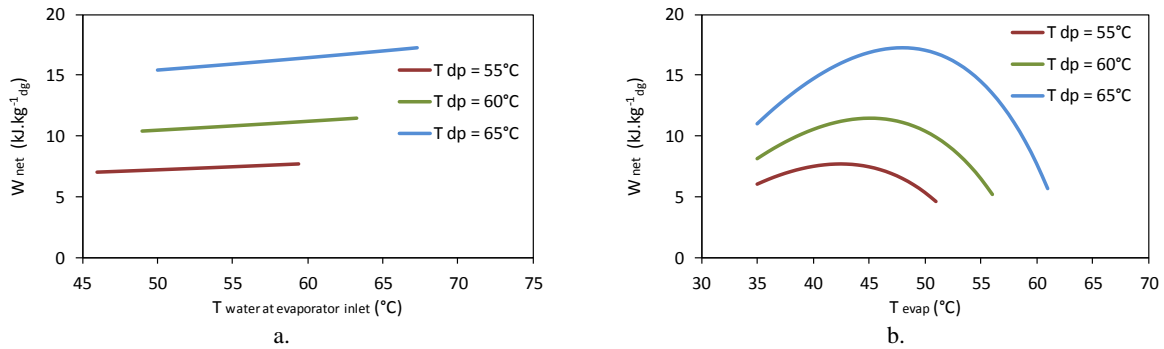


Fig. 4.3: Evolution of net power for the “DCC” as a function of: a) water temperature at the evaporator inlet and b) evaporation temperature (R-245fa)

Based on Fig. 4.2 and Fig. 4.3, a comparison of the net power and the turbine expansion ratio between “ICC” and “DCC” is shown in Table 4.2. Depending on the water dew point temperature, the use of the “DCC” mode reduces the net power by 17 to 19% compared to the “ICC” mode. In addition, Table 4.2 shows that the two heat recovery modes present a relatively low turbine expansion ratio due to the low operating evaporation temperatures.

Table 4.2: Comparison of the net power and turbine expansion ratio between “ICC” and “DCC” (R-245fa)

Heat recovery modes	$T_{dp} = 55^{\circ}\text{C}$	$T_{dp} = 60^{\circ}\text{C}$	$T_{dp} = 65^{\circ}\text{C}$
	$W_{net} (\text{kJ.kg}^{-1}.\text{dg})$		
“ICC”	9.22 (100%)	13.90 (100%)	21.13 (100%)
“DCC”	7.69 (83.4%)	11.50 (82.7%)	17.16 (81.2%)
	Turbine expansion ratio (Γ)		
“ICC”	1.89	2.06	2.27
“DCC”	1.83	1.99	2.18

To overcome those challenges, innovative opportunities should be considered by developing new heat recovery technologies for replacing existing ones enabling heat recovery from heat sources with high-moisture contents and therefore increasing effective options for heat recovery. Thermodynamic cycles based on desiccant heat-recovery technology could be an effective solution to replace the classical existing heat-recovery technologies. The use of a desiccant to strip water vapor from a flue-gas stream appears to be a novel application based on the lack of literature found. Current applications for stripping water vapor from gases are natural gas drying, building dehumidification, and cooling [DAA 12]. Desiccant dehumidification is currently not used in heat recovery applications.

4.3 Desiccant: operation and selection

4.3.1 Desiccant operation

Desiccants can dry gases particularly when the latent load is large in comparison to the sensible load and the energy cost to regenerate the desiccant is relatively low. Desiccants function by transferring moisture because of a difference between the water vapor pressure at their surface and that of the surrounding flue gases. When the vapor pressure at the desiccant surface is lower than that of flue gases, the desiccant will attract moisture. When the vapor pressure at the desiccant surface is higher than that of flue gases, the desiccant will release moisture [ASH 01a].

Fig. 4.4 shows the relationship between desiccant moisture content and its surface vapor pressure. The desiccant moisture content refers to the quantity of water presented in the desiccant solution. As the moisture content of the desiccant rises, so does the water vapor pressure at its surface. At some point, the vapor pressure at the desiccant surface is the same as that of flue gases and the two fluids are in equilibrium. Then, moisture cannot move in either direction until some external force changes the vapor pressure at the desiccant or at the flue gases.

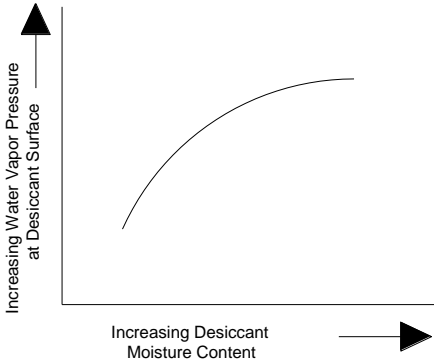


Fig. 4.4: Desiccant water vapor pressure as a function of moisture content [ASH 01a]

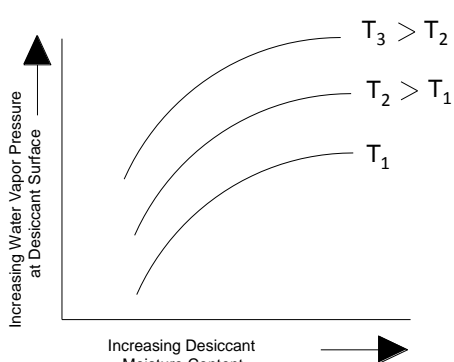


Fig. 4.5: Desiccant water vapor pressure as a function of desiccant moisture content and temperature [ASH 01a]

Fig. 4.5 shows the effect of temperature on the vapor pressure at the desiccant surface. Both higher temperature and increased moisture content increase the vapor pressure at the desiccant surface [ASH 00].

4.3.2 Liquid sorption

The principle of liquid sorption is the incorporation of a substance in one state (flue gases) into another substance of a different state (liquid) [DAA 12]. In this case, flue gases are in direct contact with a liquid desiccant into a liquid absorption dehumidifier (typically a condensing unit). Different

types of desiccant materials could be used such as lithium bromide (LiBr), lithium chloride (LiCl), or glycol solutions.

In the liquid absorption dehumidifier, flue gases brought in contact with a liquid desiccant solution. The liquid has a vapor pressure lower than water at the same temperature, and flue gases passing over the solution approaches this reduced pressure; so it is dehumidified. The vapor pressure of a liquid absorption solution is directly proportional to its temperature and inversely proportional to its concentration [ASH 01a]. Fig. 4.6 illustrates the effect of increasing desiccant concentration on the water vapor pressure at its surface for different mass fractions. As the mass of the desiccant material in the mixture increases, the vapor pressure of the mixture decreases. This pressure difference allows the desiccant solution to absorb moisture from flue gases whenever the vapor pressure of flue gases is higher than that of the solution. From a slightly different perspective, the vapor pressure of a given concentration of absorbent solution approximates the vapor pressure values of a fixed relative humidity line on a psychrometric chart. Higher solution concentrations give lower equilibrium relative humidity, which allow the absorbent to dry flue gases to lower levels [ASH 01a].

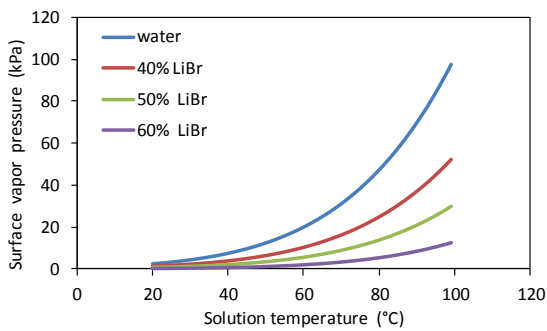


Fig. 4.6: Surface vapor pressure of aqueous lithium-bromide solutions (%mass LiBr)

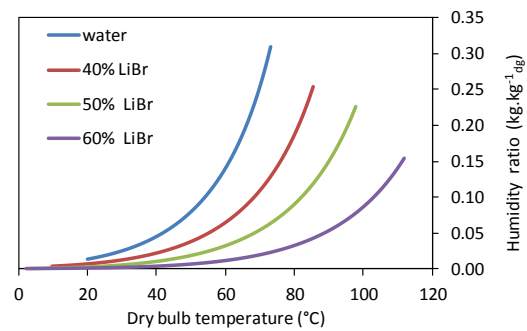


Fig. 4.7: Aqueous lithium-bromide equilibrium using the shape of a psychrometric chart (%mass LiBr)

Fig. 4.7 shows the relationship between the humidity ratio of flue gases in equilibrium with a liquid desiccant (water-lithium bromide) as a function of its concentration and temperature for different mass fractions. The graph has the same general shape as a psychrometric chart, with the relative humidity lines replaced by desiccant concentration lines. With high contact efficiency, flue gases could leave the liquid absorption dehumidifier at a temperature and humidity ratio very close to the entering temperature and equilibrium humidity ratio of the desiccant [ASH 01a]. During dehumidification, moisture is absorbed from the flue-gas stream and dilutes the desiccant solution. The diluted solution must be re-concentrated in order to elevate its water vapor pressure and equilibrium humidity ratio.

In standard practice, the behavior of a liquid desiccant is controlled by adjusting its concentration. As a practical matter, however, the absorption process is limited by the exposed surface area of the desiccant and by the contact time allowed for the reaction. More surface area and more contact time allow the desiccant to approach its theoretical capacity.

4.3.3 Desiccant selection

Several liquid desiccants are commercially available: tri-ethylene glycol, bi-ethylene glycol, ethylene glycol, and brine such as calcium chloride (CaCl_2), lithium chloride (LiCl), lithium bromide (LiBr), and calcium bromide (CaBr_2), which are used singly, or in a combination. The usefulness of a particular liquid desiccant depends upon the application. However, tri-ethylene glycol, bi-ethylene glycol and ethylene glycol have low-vapor pressure that causes high-evaporation rate into flue gases

being dehumidified, which makes the regeneration process more complicated. The brine desiccants are good candidate materials since they have good desiccant characteristics. A disadvantage of lithium chloride and calcium chloride brines is that they are highly corrosive. The present study will be based on the aqueous lithium-bromide solution.

4.4 Properties of aqueous lithium-bromide solution

4.4.1 Composition

The composition of water-lithium bromide solutions can be expressed either in mass fraction (ξ) or mole fraction (x). For aqueous lithium bromide-water solutions, the mass fraction “eksi” (ξ) is defined as the ratio of mass of anhydrous lithium bromide to the total mass of solution [CON 04], i.e.

$$eksi = \xi = \frac{m_L}{m_L + m_W} \quad \text{Eq. 4.1}$$

Where: “ m_L ” and “ m_W ” are the mass of anhydrous lithium bromide and water in solution, respectively. The composition can also be expressed in terms of mole fraction of lithium bromide as:

$$x = \frac{n_L}{n_L + n_W} \quad \text{Eq. 4.2}$$

Where: “ n_L ” and “ n_W ” are the number of moles of anhydrous lithium bromide and water in solution, respectively. The number of moles of lithium bromide and water can easily be obtained from their respective masses in solution and molecular weights, thus:

$$n_L = \frac{m_L}{M_L} \quad \text{Eq. 4.3}$$

$$n_W = \frac{m_W}{M_W} \quad \text{Eq. 4.4}$$

Where: “ M_L ” (86.8 kg.kmol⁻¹) and “ M_W ” (18.0 kg.kmol⁻¹) are the molecular weights of anhydrous lithium bromide and water respectively.

4.4.2 Vapor pressure

In general, the total pressure of a solution is equal to the sum of vapor pressures of the solute and the solvent. However, in the case of aqueous lithium bromide solution, the vapor pressure of pure lithium bromide can be ignored because its value is much lower than that of the water. When lithium bromide is dissolved in water, the boiling point of the solution at a given pressure is raised. However, if the temperature of the solution remains constant, the dissolved lithium bromide reduces the solution vapor pressure.

The vapor pressure of aqueous lithium-bromide solution could be calculated using the following relationship given as follows [KAI 01]:

$$\log P = k_o + k_1 / (T_{dp} + 273.15) + K_2 / (T_{dp} + 273.15)^2 \quad \text{Eq. 4.5}$$

Where:

$$k_0 = 7.05, k_1 = -1603.54, k_2 = -104095.5$$

The water dew point temperature for air in contact with aqueous lithium-bromide solution is correlated by [KAI 01]:

$$T_{dp} = \sum_{i=0}^2 \sum_{j=0}^3 A_{ij} (\xi - 40)^j T^i \quad \text{Eq. 4.6}$$

$$(20 \leq T \leq 210 \text{ }^\circ\text{C}, 40 \leq \xi \leq 65 \text{ wt. \%})$$

In Eq. 4.6, coefficients are given Table 4.3.

Table 4.3: Coefficients for water dew point calculation of the aqueous lithium bromide solutions [KAI 01]

j	A _{0j}	A _{1j}	A _{2j}
0	-9.133128E0	9.43969E-1	-7.324352E-5
1	-4.759724E-1	-2.882015E-3	-1.556533E-5
2	-5.638171E-2	-1.345453E-4	1.992657E-6
3	1.108418E-3	5.852133E-7	-3.924205E-8

Note that the correlation presented in Eq. 4.6 is valid for clean air. For flue gases, the water dew point depends on the flue-gas composition and it should be calculated by trial and error procedure using the value of the humidity ratio. The humidity ratio is given by [ASH 01b]:

$$w = \frac{M_{wv}}{M_{dg}} \cdot \frac{P_w}{P_t - P_w} \quad \text{Eq. 4.7}$$

Where: “M_{wv}” and “M_{dg}” are the molar masses of the water vapor and dry gases respectively, “P_w” is the partial pressure of water vapor, and “P_t” is the total pressure.

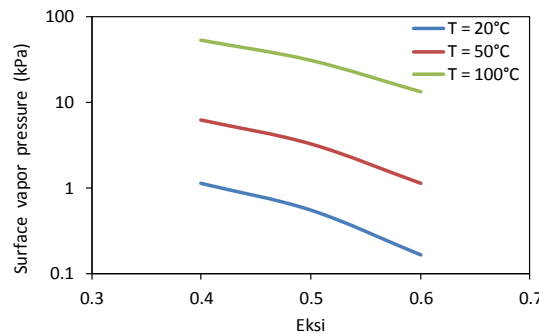


Fig. 4.8: Surface vapor pressure as a function of “eksi”

Fig. 4.8 shows the evolution of the surface vapor pressure as a function of the mass fraction of lithium-bromide in the aqueous solution. The Y-Axis is plotted in “Log scale”. Higher concentration and lower temperatures result in lower water vapor pressures.

4.4.3 Heat capacity and enthalpy of water – lithium bromide solutions

Since strong water-lithium bromide solution deviates from ideal solution behavior, it is observed that when water and anhydrous lithium bromide at same temperature are mixed adiabatically, the temperature of the solution increases considerably [KAI 01]. This indicates that the mixing is an

exothermic process with a negative heat of mixing. Hence, the mass enthalpy of the solution is given by:

$$h = \xi h_L + (1 - \xi) h_w + \Delta h_{mix} \quad \text{Eq. 4.8}$$

Where: “ h_L ” and “ h_w ” are the mass enthalpies of pure lithium bromide and water, respectively at the same temperature.

Feuerecker *et al.* [FEU 93] developed a correlation for the enthalpy taking into account the heat of dilution. The lithium bromide - water enthalpy is given by:

$$h = \sum_{n=0}^4 a_n \xi^n + T \sum_{n=0}^3 b_n \xi^n + T^2 \sum_{n=0}^2 c_n \xi^n + T^3 d_o \quad \text{Eq. 4.9}$$

The solution heat capacity is given by [FEU 93]:

$$c_p = \sum_{n=0}^3 b_n \xi^n + 2T \sum_{n=0}^2 c_n \xi^n + 3T^2 d_o \quad \text{Eq. 4.10}$$

With: h : enthalpy (kJ.kg^{-1}), T : temperature (K)

($40 \leq \xi \leq 75 \text{ wt. \%}$, $273 \leq T \leq 463 \text{ K}$)

Coefficients used in “Eq. 4.9” and “Eq. 4.10” are listed in Table 4.4.

Table 4.4: Coefficients for enthalpy and heat capacity calculations of the aqueous lithium-bromide solutions

i	a_i	b_i	c_i	d_i
0	-954.8	-3.293E-1	7.4285E-3	-2.269E-6
1	47.7739	4.076E-2	-1.5144E-4	-
2	-1.59235	-1.36E-5	1.3555E-6	-
3	2.09422E-2	-7.1366E-6	-	-
4	-7.688E-5	-	-	-

Fig. 4.9 shows a chart giving the enthalpy-temperature-mass fraction data for water-lithium bromide solutions. For a given temperature, the raise in enthalpy at high “eksi” values (> 0.55) is due to the heat of dilution.

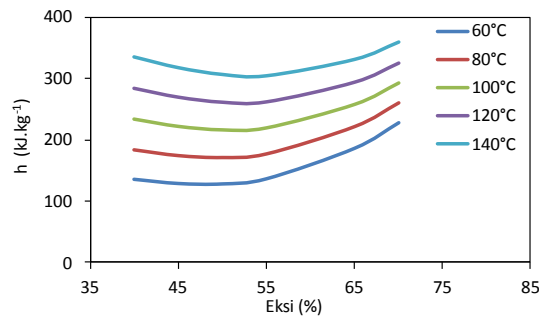


Fig. 4.9: Enthalpy-Temperature-Concentration diagram for aqueous lithium-bromide solution

4.4.4 Equilibrium chart (“Dühring” Plot)

The properties of an aqueous lithium-bromide solution, including vapor pressure, temperature, and the mass fraction at equilibrium, may be illustrated on an equilibrium chart based on the “Dühring” plot, as shown in Fig. 4.10 [KIS 08]. The ordinate of the equilibrium chart is the saturated vapor pressure of water in log-scale (kPa absolute) and the corresponding saturation temperature plotted on an inclined axis. The abscissa of the chart is the the solution temperatures. Mass fraction or concentration lines are inclined lines and are not parallel to each other. At the bottom of the concentration lines, there is a crystallization line or saturation line [KIS 08]. If the temperature of a solution of constant mass fraction of lithium bromide drops below this line – or if the mass fraction of lithium-bromide of a solution of constant temperature is higher than the saturated condition – the part of lithium bromide exceeding the saturated condition tends to form solid crystals.

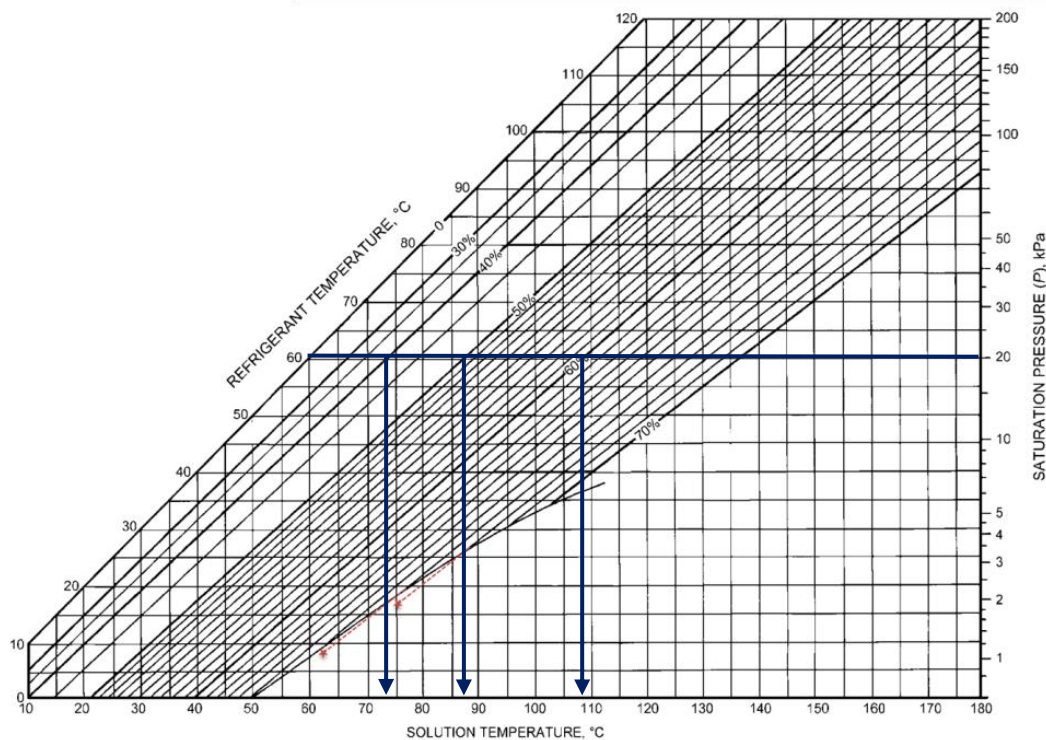


Fig. 4.10: Equilibrium chart for aqueous lithium bromide solution (“Dühring” Chart) [KIS 08]

The effect of desiccant material on the evolution of the water dew point temperature (and consequently on the entering wet bulb temperature) could be shown clearly by considering the blue lines plotted in Fig. 4.10. Considering a water vapor saturation pressure of 20 kPa, the equilibrium temperature is around 60°C using a pure water solution. For aqueous lithium-bromide solution, the corresponding equilibrium temperature at 20 kPa is lifted up to around 75°C, 88°C, and 109°C for a mass fraction of 40%, 50% and 60% respectively.

4.5 Direct-contact condensation using aqueous lithium-bromide solution

In direct contact condensation heat-recovery process (Fig. 1.36), the liquid desiccant is distributed onto an extended heat and mass transfer surface that consists in a packing material [DIE 04]. The packing provides a large surface for flue gases to contact the liquid desiccant where flue gases are cooled and dehumidified. The liquid desiccant removes sensible and latent heat from process flue gases via the liquid desiccant material. In the basic configuration, concentrated and cooled liquid desiccant flows downward through a condensing unit. Flue gases pass up through the condensing unit,

transferring both moisture and heat to the counter-flowing liquid desiccant. The liquid desiccant leaves the bottom of the condensing unit diluted by the water absorbed from flue gases. The heated liquid desiccant stream recovered at the bottom of the condensing unit is then sent to an evaporator to transfer heat to the working fluid of the power generation unit. Once the heat is extracted from the desiccant solution, a desiccant control system is required to reestablish the concentration of the desiccant solution by adding a desiccant material (lithium-bromide).

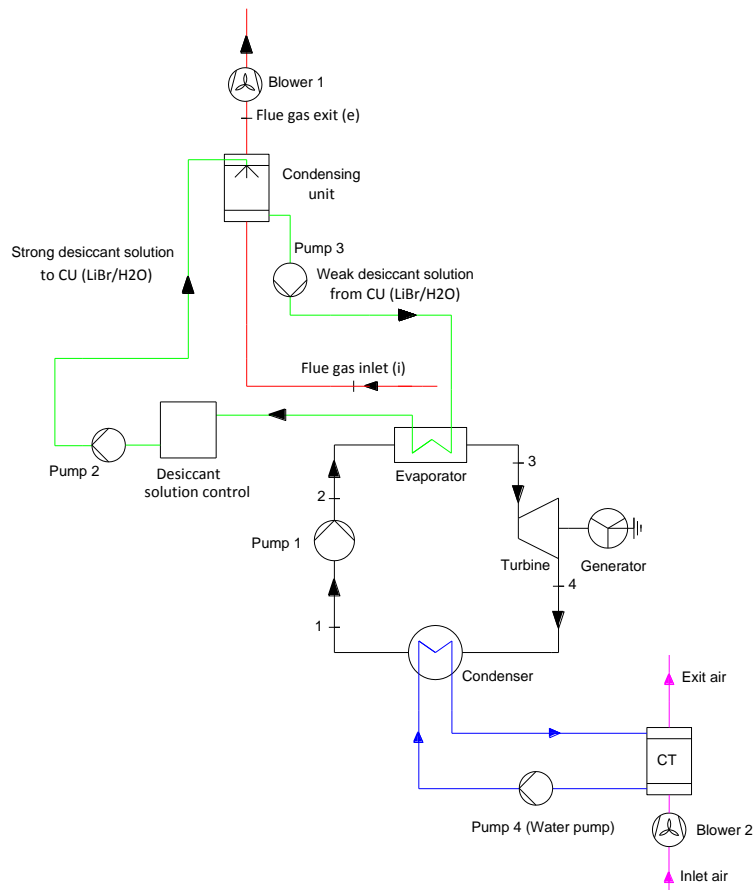


Fig. 4.11: ORC with direct contact condensation using aqueous lithium-bromide solution

Following calculations will be done by taking into account the auxiliary consumptions. Additional ORC parameters to those indicated in Table 1.5 are listed in Table 4.5. R-245fa properties are calculated using REFPROP 9.0 [LEM 10] developed by NIST. A computer program employing “Excel/VBA” was developed to simulate the thermodynamic performances of the presented cycle.

Table 4.5: Additional ORC input data

Parameters	Value
T_{dp}	60°
Pinch condenser (ΔT_{cond})	2 K
$T_{in/out}$ water to/from condenser	25/30°C
$CT_{approach} = T_{out}$ cold water from CT - T_{in} air wet bulb to CT	5 K
$DT_{CT} = T_{in}$ water to CT - T_{out} air from CT	3 K
T_{air} drv/wet bulb inlet to CT	25/20°C

Since the circulating desiccant solution can only reach a temperature equivalent to adiabatic saturation temperature of flue gases, the heat is to be transferred to the working fluid at a temperature lower than

the entering wet bulb temperature. For a given “eksi”, Table 4.6 shows the corresponding values of the water dew point and wet bulb temperatures. The entering wet bulb temperature can reach almost 111°C for “eksi” equal to 0.6.

Table 4.6: Corresponding water dew point and wet bulb temperatures depending on “eksi”

Eksi	T_{dp} (°C)	T_{wb} (°C)
0	60.0	63.8
0.4	74.8	77.3
0.5	88.7	90.9
0.6	110.1	110.9

The net power and the auxiliary consumptions are given by:

$$W_{net} = W_{turbine} - W_{pump\ ORC} - W_{auxiliary\ consumptions} \quad \text{Eq. 4.11}$$

$$W_{auxiliary\ consumptions} = W_{blower\ 1} + W_{blower\ 2} + W_{pump\ 2} + W_{pump\ 3} \quad \text{Eq. 4.12}$$

Equipment efficiencies and estimated pressure drops are listed in Table 4.7.

Table 4.7: Equipment efficiencies and estimated pressure drop

Parameters	Values
$\eta_{blower\ CU} / \eta_{blower\ CT}$	80 %
$\eta_{cold\ water\ pump} / \eta_{liquid\ desiccant\ pump}$	85 %
$DP_{blower\ 1} / DP_{blower\ 2}$	150 Pa
$DP_{pump\ 2} / DP_{pump\ 3} / DP_{pump\ 4}$	50 kPa

Fig. 4.12.a (resp. Fig. 4.12.b) shows the evolution of the turbine power (resp. net power) as a function of the solution temperature at the evaporator inlet for various “eksi”. For a given solution temperature at the evaporator inlet, the evaporation pressure is calculated in order to optimize the net power. The improvement provided by the desiccant solution compared to a pure water solution (“eksi” = 0) appears clearly on the values of the turbine power (Fig. 4.12.a) and the net power (Fig. 4.12.b). As “eksi” increases, both turbine and net powers increase. For a given “eksi”, the turbine and net powers increase by increasing the solution temperature at the evaporator inlet. The maximal turbine and net powers are reached for a solution temperature at the evaporator inlet equal to the corresponding entering wet bulb temperature with a minimum of 0.5 K below it (minimum pinch in the condensing unit).

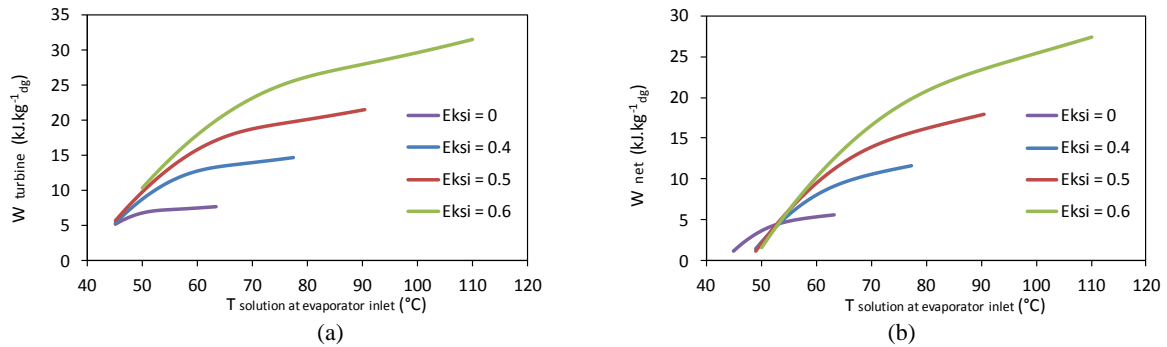


Fig. 4.12: Evolutions of: a) turbine power, b) net power, as a function of the solution temperature at the evaporator inlet for various “eksi”

Values of maximal turbine and net powers are listed in Table 4.8 for various “eksi”. The turbine power (resp. net power) increase from $7.74 \text{ kJ.kg}^{-1}_{\text{dg}}$ ($5.59 \text{ kJ.kg}^{-1}_{\text{dg}}$) for “eksi = 0” to $31.53 \text{ kJ.kg}^{-1}_{\text{dg}}$ ($27.69 \text{ kJ.kg}^{-1}_{\text{dg}}$) for “eksi = 0.6”.

Table 4.8: Effect of “eksi” on maximal turbine and net powers

Eksi	$W_{\text{turbine}} (\text{kJ.kg}^{-1}_{\text{dg}})$	$W_{\text{net}} (\text{kJ.kg}^{-1}_{\text{dg}})$
0	7.74	5.59
0.4	14.73	11.89
0.5	21.54	18.27
0.6	31.53	27.69

The relative improvement made by using a desiccant solution on the maximal turbine and net powers compared to a pure water solution (“eksi” = 0) is shown in Table 4.9. By varying “eksi” from 0.4 to 0.6, the relative improvement of the turbine power (resp. net power) varies from 90.3% (resp. 112.7%) to 307.3% (resp. 395.3%).

Table 4.9: Relative improvement of the maximal turbine and net powers for various “eksi”

Eksi	$(\Delta W_{\text{turbine}}/W_{\text{turbine}})^* (\%)$	$(\Delta W_{\text{net}}/W_{\text{net}})^* (\%)$
0.4	90.3	112.7
0.5	178.3	226.8
0.6	307.3	395.3

*: calculated relative to a pure water solution (“eksi”=0)

The effect of “eksi” on the evaporator capacity and on the mass of water vapor condensate is shown in Fig. 4.13.a and Fig. 4.13.b respectively. The evaporator capacity and the mass of water vapor condensate decrease by increasing the solution temperature at the evaporator inlet up to a certain limit where they remain almost constant. By increasing “eksi”, both evaporator capacity and the mass of water vapor condensate increase.

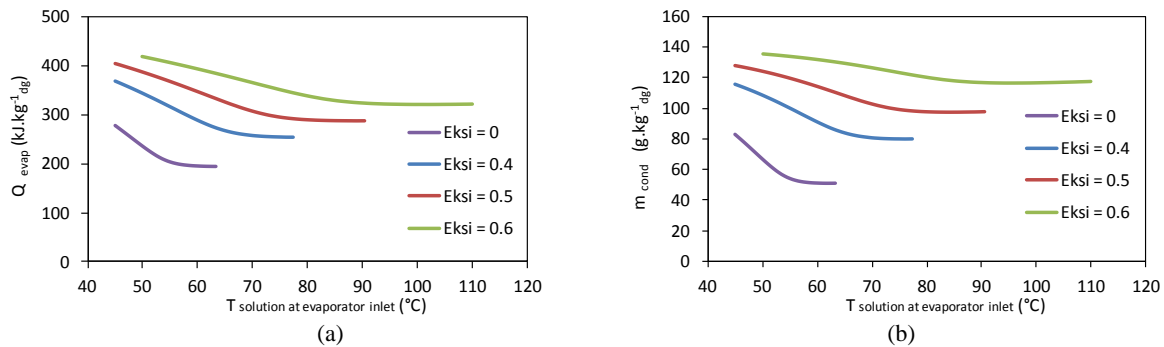


Fig. 4.13: Evolutions of: a) evaporator capacity, b) mass of water vapor condensate, as a function of the solution temperature at the evaporator inlet for various “eksi”

As stated previously, the liquid desiccant leaves the bottom of the condensing unit diluted by the water absorbed from flue gases. Thus, the desiccant mass fraction in the solution must be reestablished to its initial concentration by adding desiccant material. Fig. 4.14 shows the required mass of desiccant material in tons per day for a $1 \text{ kg}_{\text{dg}}.\text{s}^{-1}$ as a function of the solution temperature at the evaporator inlet for various “eksi”. The required mass of desiccant material to be added diminishes by decreasing the value of “eksi” and by increasing the solution temperature at the evaporator inlet.

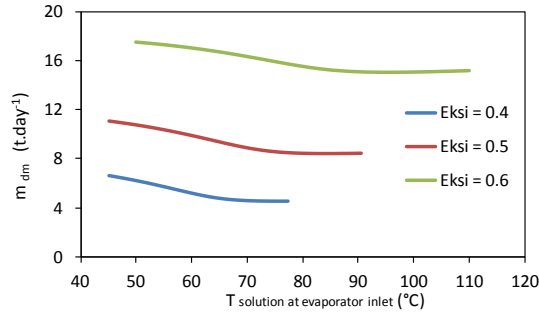


Fig. 4.14: Required mass of desiccant material to be added as a function of the solution temperature at the evaporator inlet for various eksi ($1 \text{ kg}_{\text{dg}} \cdot \text{s}^{-1}$)

By referring to Fig. 4.12.b and Fig. 4.14, in order to maximize the net power and to minimize the required mass of desiccant material to be added, the solution temperature at the evaporator inlet must be kept as high as possible. Therefore, for each value of “eksi”, the solution temperature at the evaporator inlet will be equal to the corresponding entering wet bulb temperature with a minimum of 0.5 K below it (minimum pinch in the condensing unit).

After setting the solution temperature at the evaporator inlet, the effect of the evaporation temperature will be studied. The evolution of the evaporation temperature as a function of the turbine and net powers for various “eksi” is shown in Fig. 4.15. A local optimum exists for each “eksi”. As the latter increases, the local optimum moves away.

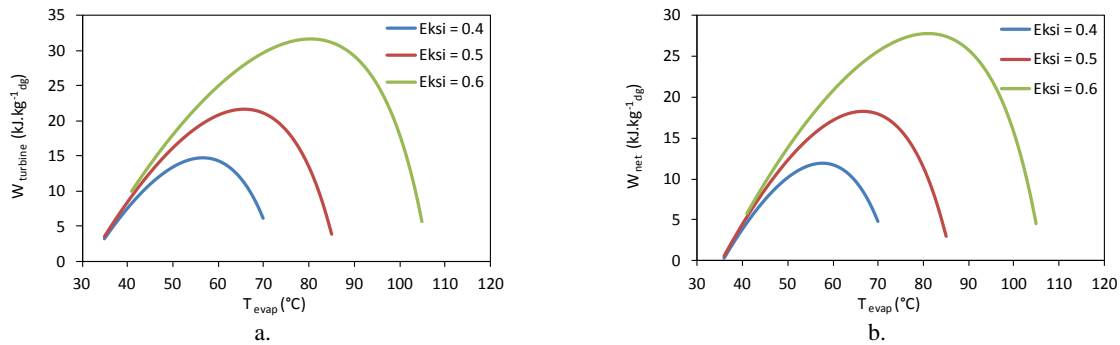


Fig. 4.15: Evolution of the turbine and net powers as a function of the evaporation temperature for various “eksi”

The effect of evaporation temperature on both the required mass of desiccant material to be added and the mass of water vapor condensation is shown in Fig. 4.16.a and Fig. 4.16.b respectively for a “ $1 \text{ kg}_{\text{dg}} \cdot \text{s}^{-1}$ ”. As the evaporation temperature increases, the required mass of desiccant material to be added decreases (Fig. 4.16.a) since less condensation occurs in the condensing unit (Fig. 4.16.b).

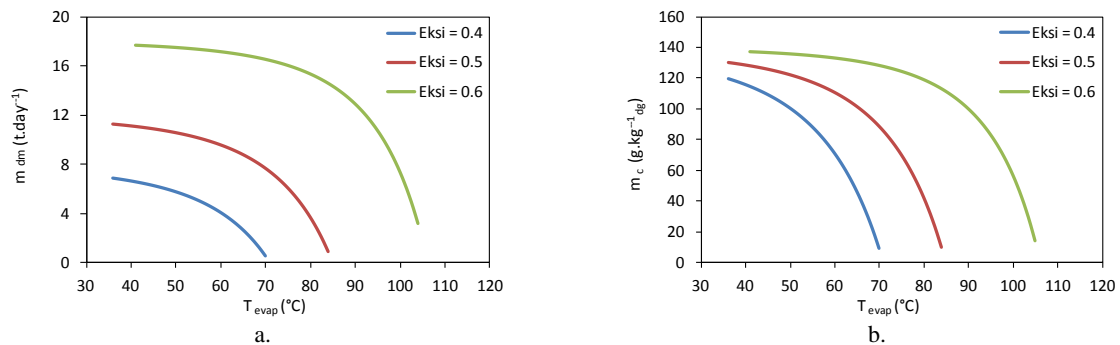


Fig. 4.16: Effect of evaporation temperature on: a) required mass of desiccant material, and b)

mass of water vapor condensation for various “eksi” ($1 \text{ kg}_{\text{d.e.}}\cdot\text{s}^{-1}$)

By combining Fig. 4.15.b and Fig. 4.16.a, ratios between the gains in the net power achieved by using a desiccant solution (compared to “ICC” and “DCC” cycles) to the mass of the added desiccant material could be defined as follows:

$$\text{Ratio}_{\text{ICC}} (\text{kWh}\cdot\text{t}_{\text{dm}}^{-1}) = \frac{\Delta W_{\text{net}}}{3600\cdot m_{\text{dm}}} = \frac{(W_{\text{net}} - W_{\text{net ICC}})}{3600\cdot m_{\text{dm}}} \quad \text{Eq. 4.13}$$

$$\text{Ratio}_{\text{DCC}} (\text{kWh}\cdot\text{t}_{\text{dm}}^{-1}) = \frac{\Delta W_{\text{net}}}{3600\cdot m_{\text{dm}}} = \frac{(W_{\text{net}} - W_{\text{net DCC}})}{3600\cdot m_{\text{dm}}} \quad \text{Eq. 4.14}$$

Where: “dm” denotes desiccant material; “ m_{dm} ” is the mass of added desiccant material expressed in tons. In Eq. 4.13 and Eq. 4.14, the gain in the net power is calculated compared to “ICC” (Eq. 4.13) and “DCC” (Eq. 4.14) respectively.

Fig. 4.17.a and Fig. 4.17.b show the evolutions of ratios defined in Eq. 4.13 and Eq. 4.14 as a function of the evaporation temperature. As shown in Fig. 4.17, these ratios are relatively small and cannot exceed $35 \text{ kWh}\cdot\text{t}_{\text{dm}}^{-1}$ (Ratio_{ICC}) and $40 \text{ kWh}\cdot\text{t}_{\text{dm}}^{-1}$ (Ratio_{DCC}).

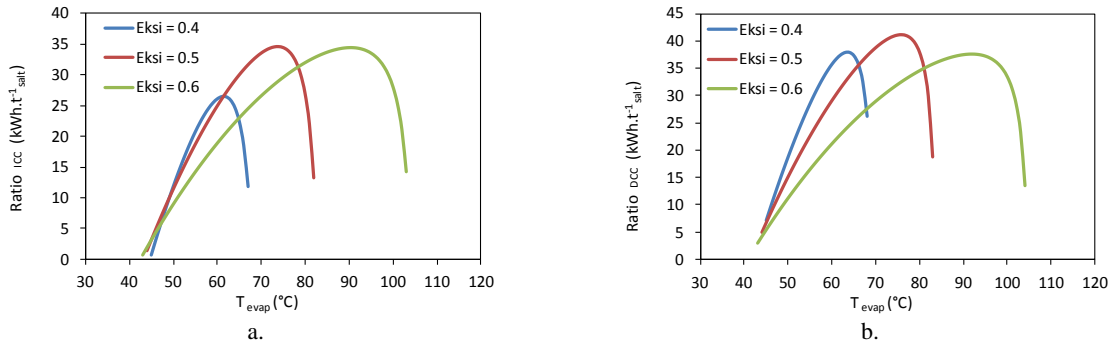


Fig. 4.17: Evolutions of: (a) Ratio_{ICC} (Eq. 4.13) and (b) Ratio_{DCC} (Eq. 4.14), as a function of the evaporation temperature

In conclusion, while the net power improvement looks attractive by using an aqueous lithium-bromide solution rather than a pure water solution, the ratio between a kWh produced and the needed mass of desiccant material to be added is very small making the present process economically unfeasible. In fact, by considering a ratio of $40 \text{ kWh}\cdot\text{t}^{-1}$, the cost of the sold power gain will be around $3.2 \text{ €} / 40 \text{ kWh}$ (assuming a price of 0.08 € for a 1 kWh sold), while one ton of anhydrous lithium bromide costs around 800 € . Therefore, regeneration process must be provided in order to evaporate the water absorbed from flue gases. Next sections describe the possible regeneration methods and their feasibility.

4.6 Regeneration process using solar energy

As stated previously, the moisture transfer from flue gases to the liquid desiccant in the condensing unit causes desiccant dilution resulting in a reduction in its ability to absorb more water. Therefore, the desiccant must be brought to its original concentration. The regeneration process requires heat that can be obtained from a low-temperature source, for which solar energy is suitable. Fig. 4.18 shows the regeneration cycle based on solar energy. Once the heat is extracted from the desiccant solution, water evaporation through solar energy could reestablish the desiccant solution to its original concentration.

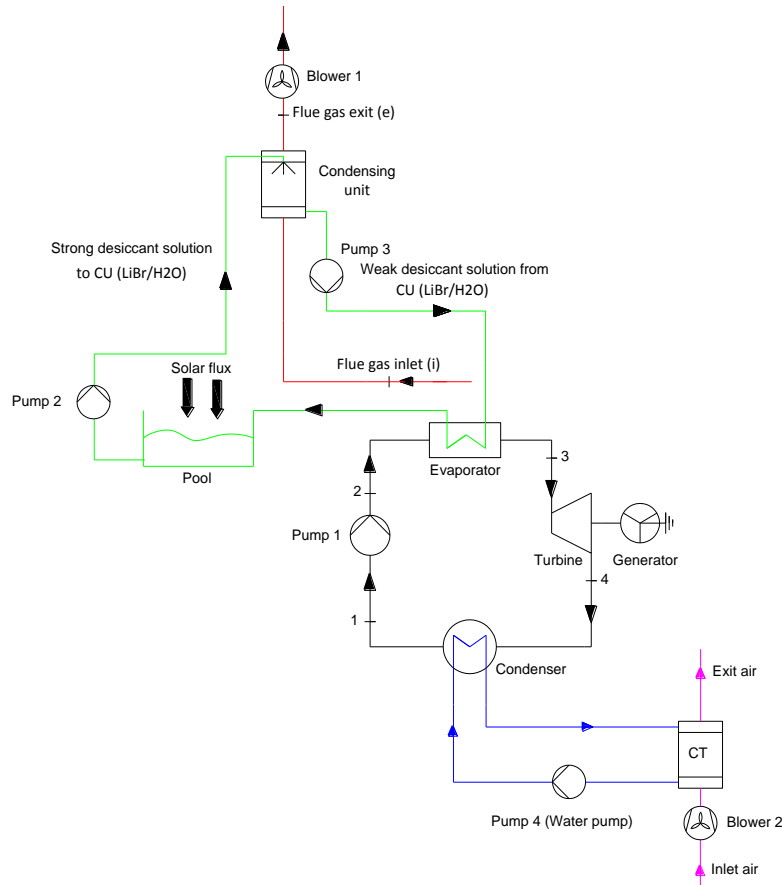


Fig. 4.18: Regeneration cycle using solar energy

The required heat capacity to evaporate the total mass of the water condensate during an entire day can be calculated by:

$$Q_{evap} = 24 \cdot 3600 \cdot (L_{v_{water}} + H_d) \cdot m_{cond} \quad \text{Eq. 4.15}$$

hours.day⁻¹ seconds.hour⁻¹

Where in Eq. 4.15, “ Q_{evap} ” is expressed in kJ.day⁻¹, “ $L_{v_{water}}$ ” is the latent heat of water vaporization expressed in kJ.kg⁻¹, “ H_d ” is the heat of dilution in kJ.kg⁻¹, and “ m_{cond} ” is the mass of water vapor condensate expressed in kg.s⁻¹. Table 4.10 shows the heat of dilution of lithium bromide for various “eksi”.

Table 4.10: Heat of dilution of lithium bromide for various “eksi” [5]

“eksi”	H_d (kJ.kg ⁻¹)
0.4	40
0.5	140
0.6	375

The available solar heat capacity during an entire day can be expressed by:

$$Q_{solar} = 3600/1000 \cdot \varphi \cdot N \quad \text{Eq. 4.16}$$

In Eq. 4.16, “ Q_{solar} ” is expressed in kJ.day⁻¹.m⁻², “ φ ” is the solar flux expressed in W.m⁻², and “ N ” is the number of sunshine hours per day. By assuming a mean solar flux of 1000 W.m⁻², and eight-hour sunshine per day, the value of available solar heat capacity is:

$$Q_{\text{solar}} = 3600/1000.1000.8 = 28800 \text{ kJ.day}^{-1}.\text{m}^{-2}$$

The total surface area needed to evaporate the mass of water vapor condensation is:

$$S_{\text{pool}} = Q_{\text{evap}} / Q_{\text{solar}} \quad \text{Eq. 4.17}$$

Assuming a square pool section area, the poolside is calculated by:

$$\text{Pool side} = \sqrt{S_{\text{pool}}} = \sqrt{Q_{\text{evap}}/Q_{\text{solar}}} \quad \text{Eq. 4.18}$$

Fig. 4.19 shows the evolution of the poolside as a function of the water evaporation rate for various “eksi”. By varying the water evaporation rate from 1 to 10 m³.day⁻¹, the corresponding variation of the pool side ranges from around 10 m to 30 m.

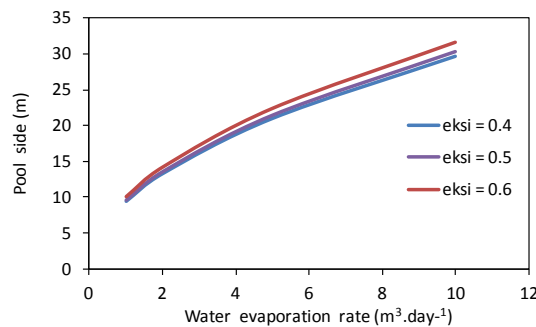


Fig. 4.19: Evolution of the pool side as a function of the water evaporation rate for various “eksi”

For calculations, the ORC process parameters are the same as those indicated in Table 1.5, Table 4.5, and Table 4.7. The evolutions of the water evaporation rate and the poolside as a function of the solution temperature at the evaporator inlet are shown respectively in Fig. 4.20.a and Fig. 4.20.b for a 1 kg_{dg}.s⁻¹. Calculations are done by neglecting the system thermal losses. For a given water temperature at the evaporator inlet, the evaporation pressure is calculated in order to optimize the net power. As shown in Fig. 4.20, the water evaporation rate and, consequently, the poolside decrease by increasing the water temperature at the evaporator inlet up to a certain limit where they remain almost constant.

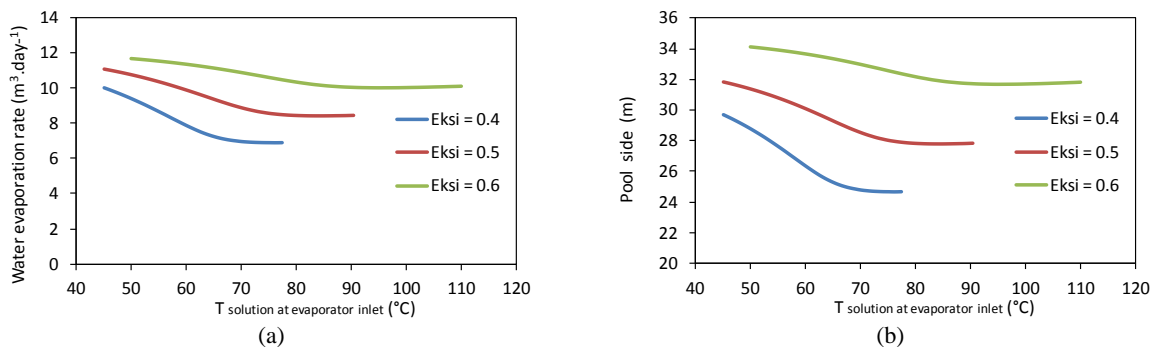


Fig. 4.20: Evolution of: (a) water evaporation rate, (b) pool side as a function of the water temperature at the evaporator inlet for various “eksi” (1 kg_{dg}.s⁻¹)

Therefore, in order to minimize the required pool dimensions, the solution temperature at the evaporator inlet must be kept as high as possible, which lead also to a maximal net and turbine powers (refer to Fig. 4.12). Therefore, the solution temperature at the evaporator inlet will be set equal to the corresponding entering wet bulb temperature with a minimum of 0.5 K below it (minimum pinch in the condensing unit).

In order to study the effect of the evaporation temperature, Fig. 4.21 shows the evolution of the water evaporation rate as a function of the evaporation temperature for a $1 \text{ kg}_{\text{dg}} \cdot \text{s}^{-1}$. In particular, Fig. 4.21 shows a decrease in the evaporation rate while the evaporation temperature increases.

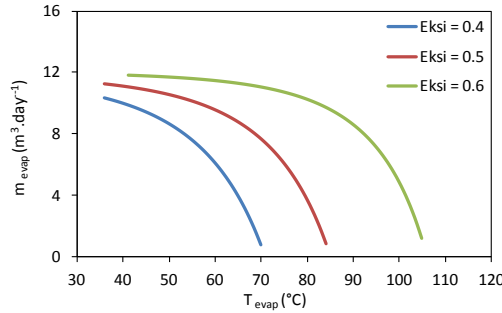


Fig. 4.21: Evolution of the water evaporation rate as a function of the evaporation temperature for a $1 \text{ kg}_{\text{dg}} \cdot \text{s}^{-1}$

By combining Fig. 4.15.b and Fig. 4.21, ratios between the gains in the net power achieved by using a desiccant solution (compared to “ICC” and “DCC”) to the mass of water evaporated could be defined as follows:

$$Ratio_{ICC} (\text{kWh} \cdot \text{m}_e^{-3}) = \frac{\Delta W_{net}}{3600 \cdot m_e} = \frac{(W_{net} - W_{net \text{ ICC}})}{3600 \cdot m_e} \quad \text{Eq. 4.19}$$

$$Ratio_{DCC} (\text{kWh} \cdot \text{m}_e^{-3}) = \frac{\Delta W_{net}}{3600 \cdot m_e} = \frac{(W_{net} - W_{net \text{ DCC}})}{3600 \cdot m_e} \quad \text{Eq. 4.20}$$

Where: “ m_e ” denotes the mass of water evaporated.

In Eq. 4.19 and Eq. 4.20, gains in the net power are calculated compared to “ICC” (Eq. 4.19) and “DCC” (Eq. 4.20) respectively.

Fig. 4.22.a and Fig. 4.22.b show the evolution of the ratios defined in Eq. 4.19 and Eq. 4.20 as a function of the evaporation temperature. These ratios increase by increasing the value of “eksi”. Ratios presented in Fig. 4.22 are relatively small and cannot exceed “ $50 \text{ kWh} \cdot \text{m}_e^{-3}$ ” for “Ratio_{ICC}” and “ $58 \text{ kWh} \cdot \text{m}_e^{-3}$ ” for “Ratio_{DCC}”.

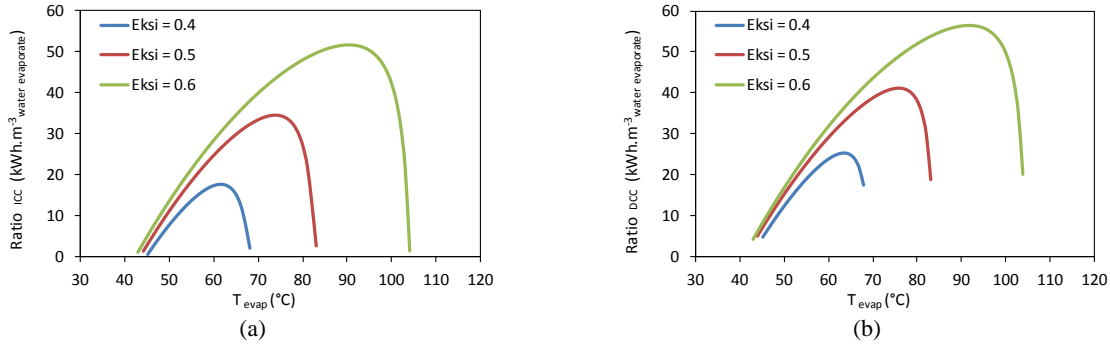


Fig. 4.22: Evolutions of: (a) Ratio_{ICC} (Eq. 4.19) and (b) Ratio_{DCC} (Eq. 4.20), for a wide range of evaporation temperatures for various “eksi”

Fig. 4.23.a and Fig. 4.23.b show the evolutions of the turbine and net powers as a function of the water evaporation rate for a 1 kg_{dg}·s⁻¹. The solution temperature at the evaporator inlet is set equal to the corresponding entering wet bulb temperature with a minimum of 0.5 K below it. In particular, Fig. 4.23.a and Fig. 4.23.b illustrate the minimum evaporation rate at which the use of aqueous lithium-bromide solution improves the turbine and net powers compared to “ICC” and “DCC” cycles.

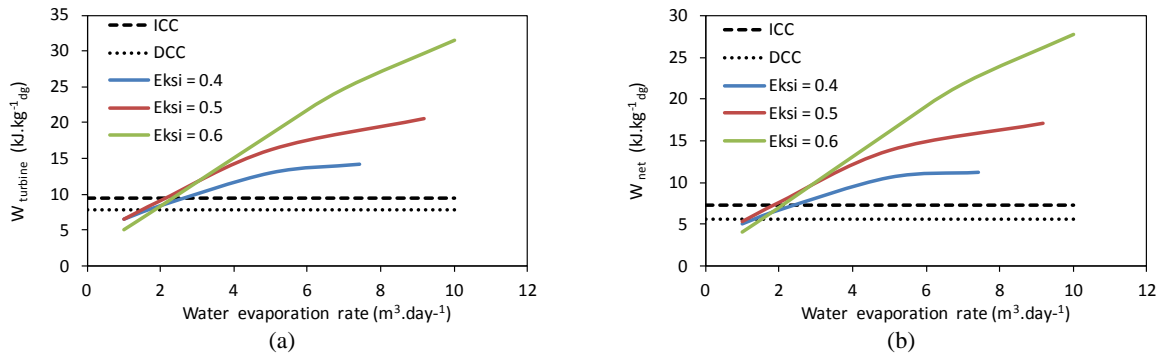


Fig. 4.23: Evolutions of: (a) turbine power, and (b) net power, as a function of the water evaporation rate for a 1 kg_{dg}·s⁻¹

The relative variations of the turbine and net powers as a function of the water evaporation rate for various “eksi” compared to “ICC” are shown in Fig. 4.24. Compared to “ICC” cycle, the use of aqueous lithium bromide solution improves the net power starting from a water evaporation rate of “1.8”, “2”, and “2.2” m³·day⁻¹ (per 1 kg_{dg}·s⁻¹) for “eksi” values of “0.4”, “0.5” and “0.6” respectively.

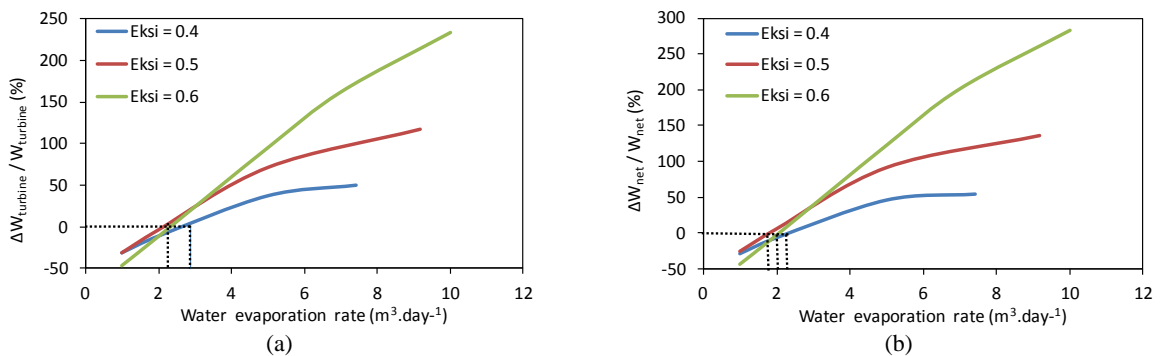


Fig. 4.24: Relative variations of: (a) turbine power, and (b) net power, as a function of the water evaporation rate for various “eksi” compared to “ICC” (1 kg_{dg}·s⁻¹)

Finally, it should be noted that the presented regeneration cycle can operate only during the sunshine hours and it is strongly dependant on weather statement.

4.7 Conventional Regeneration Cycle (CRC) using an evaporating unit

Another regeneration technology option is to evaporate the quantity of water absorbed from flue gases into a separate regenerator. This could be done by using an evaporating unit (EU). As shown in Fig. 4.25, diluted solution at the evaporator exit is pumped to the evaporating unit (EU). Outside ambient air contacts the heated solution in the evaporating unit; water evaporates from the desiccant solution into the air since the water partial pressure in the air stream is lower than the water partial pressure in the desiccant solution, and the solution is re-concentrated. Desiccant solution is continuously re-circulated between the condensing unit and the evaporating unit to complete the cycle.

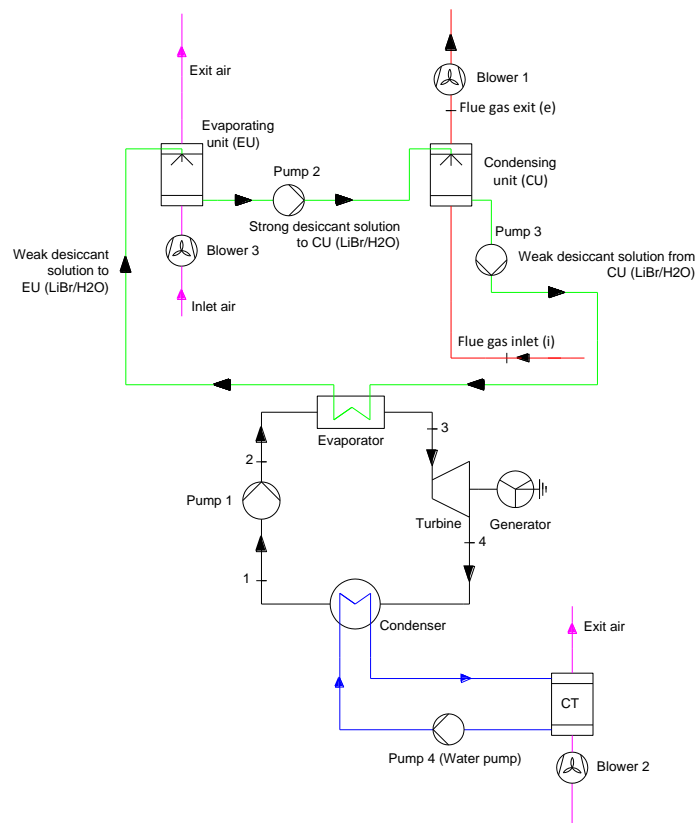


Fig. 4.25: Conventional Regeneration Cycle (CRC) using an evaporating unit

For calculations, the ORC process parameters are the same as those indicated in Table 1.5, Table 4.5 and Table 4.7. Additional parameters for the evaporating unit are shown in Table 4.11.

Table 4.11: Evaporating Unit process parameters

Parameters	Values
$DT_{EU} = T_{in\ solution\ to\ EU} - T_{out\ air\ from\ EU}$	3 K
$T_{air\ dry/wet\ bulb\ inlet\ to\ EU}$	25/20 °C
$\eta_{blower\ 3}$	80 %
$DP_{blower\ 3}$	150 Pa

Similarly to the cooling tower operation, the water temperature at the evaporating unit exit will be limited by the entering air wet bulb temperature. However, in the case of using a liquid desiccant, the outside ambient air enters the evaporating unit at supersaturated state, and thus the entering water dew point temperature exceeds the entering wet bulb temperature as observed

Fig. 4.26. Therefore, the exit water temperature from the evaporating unit will be limited by the entering water dew point temperature.

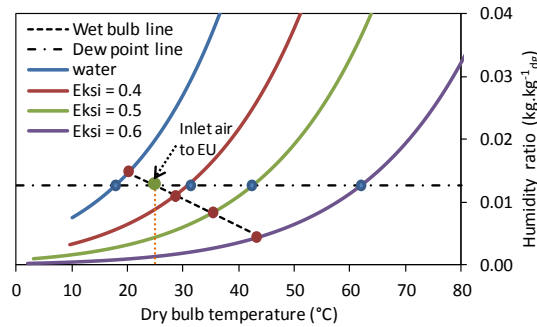


Fig. 4.26: Aqueous lithium-bromide equilibrium in the evaporating unit (EU)

The system plotted in Fig. 4.25 presents an operating point if the quantity of water absorbed from flue gases in the condensing unit is totally evaporated in the evaporating unit. In other term, an operating point exists if the following heat capacity equation is valid:

$$Q_{evaporator} + Q_{EU} = Q_{CU} \quad \text{Eq. 4.21}$$

The evolution of the heat capacities of the condensing unit, evaporating unit, and evaporator as a function of the evaporation temperature are shown in Fig. 4.27 for “eksi = 0.4”. The solution temperature at the evaporator inlet is set to be equal to the corresponding entering wet bulb temperature with a minimum of 0.5 K below it (minimum pinch in the condensing unit). Fig. 4.27 shows that the heat capacity of the evaporating unit exceeds that of the condensing unit up to an evaporation temperature of 62°C. Note that the heat capacity of the condensing unit is constant since the entering solution temperature to it is fixed. Eq. 4.21 reveals the presence of an operating point located at an evaporation temperature around 72°C. At this point, a very small heat capacity is exchanged in the evaporator.

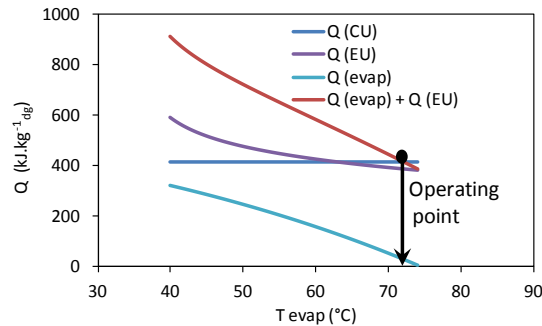


Fig. 4.27: Evolutions of heat capacities as a function of the evaporation temperature (eksi = 0.4)

At the operating point, Fig. 4.28.a and Fig. 4.28.b show that the corresponding values of the turbine and net powers are well below those obtained by using “ICC” and “DCC”. Therefore, the actual regeneration system seems to be unsatisfying.

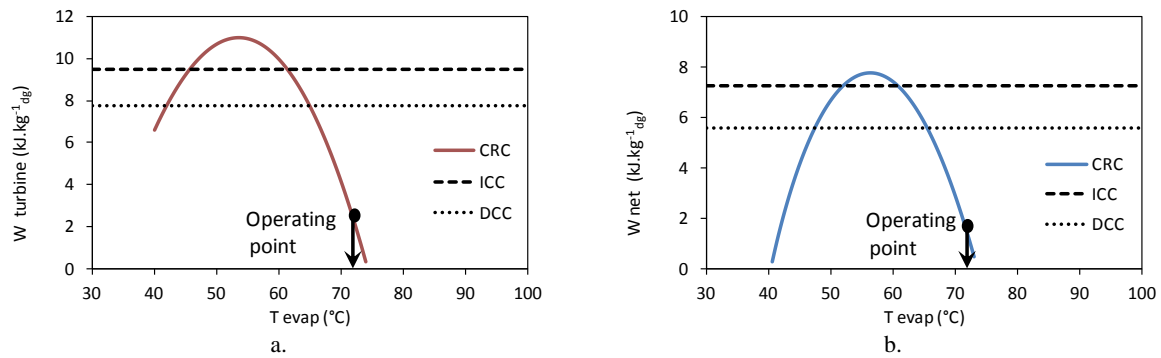


Fig. 4.28: Evolutions of: a) turbine power, and b) net power, as a function of the evaporation temperature (eksi = 0.4)

Fig. 4.29.a (resp. Fig. 4.29.b) shows the aqueous lithium-bromide equilibrium in the condensing unit (resp. evaporating unit) at the operating point. In the condensing unit, flue gases are to be cooled from 120°C to around 30°C while in the evaporating unit, the entering ambient air temperature is bringing from 25°C to around 70°C.

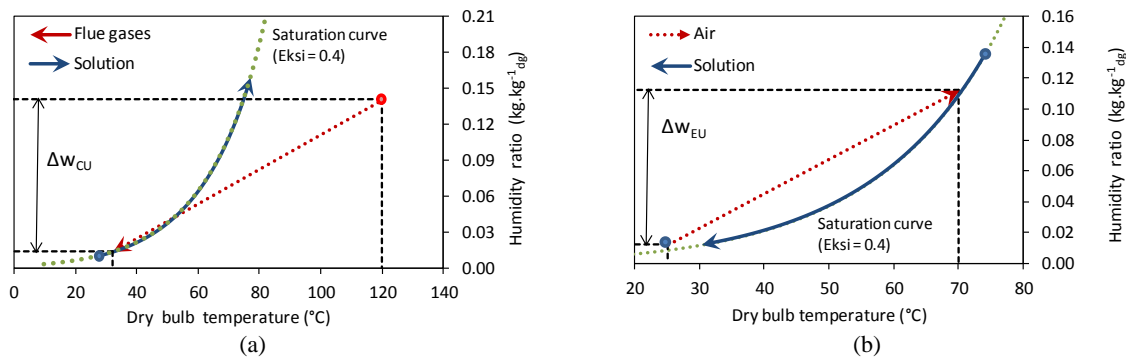


Fig. 4.29: Aqueous lithium-bromide equilibrium in: (a) CU, and (b) EU, at the operating point

In conclusion, using an evaporating unit in order to evaporate the quantity of water absorbed from flue gases could not be an effective solution using the actual conventional regeneration cycle (“CRC”). Related improvement of the actual cycle should be considered, as it will be shown in the following section.

4.8 Improved Regeneration Cycle (IRC)

By lowering the amount of the dehumidification rate in the condensing unit, the regeneration capacity needed to evaporate the quantity of water absorbed from flue gases decreases. Therefore, an equilibrium operating point could be found at lower evaporation temperature and the performance of the conventional regeneration cycle could be increased. One possible solution is to heat the desiccant solution entering the condensing unit since higher solution temperature results in higher water vapor pressures and therefore reduced dehumidification rate.

By referring to Fig. 4.29.b, the air exits the evaporating unit at a relatively high temperature (~70°C) and therefore it could be used to heat the desiccant solution entering the condensing unit. Fig. 4.30 shows an improved regeneration cycle where the design includes a counter-flow heat exchanger (HEX1) between air and desiccant solution exiting the evaporating unit. In this case, a large portion of the heat transferred from the desiccant solution to the air in the evaporating unit will be recovered in “HEX1”.

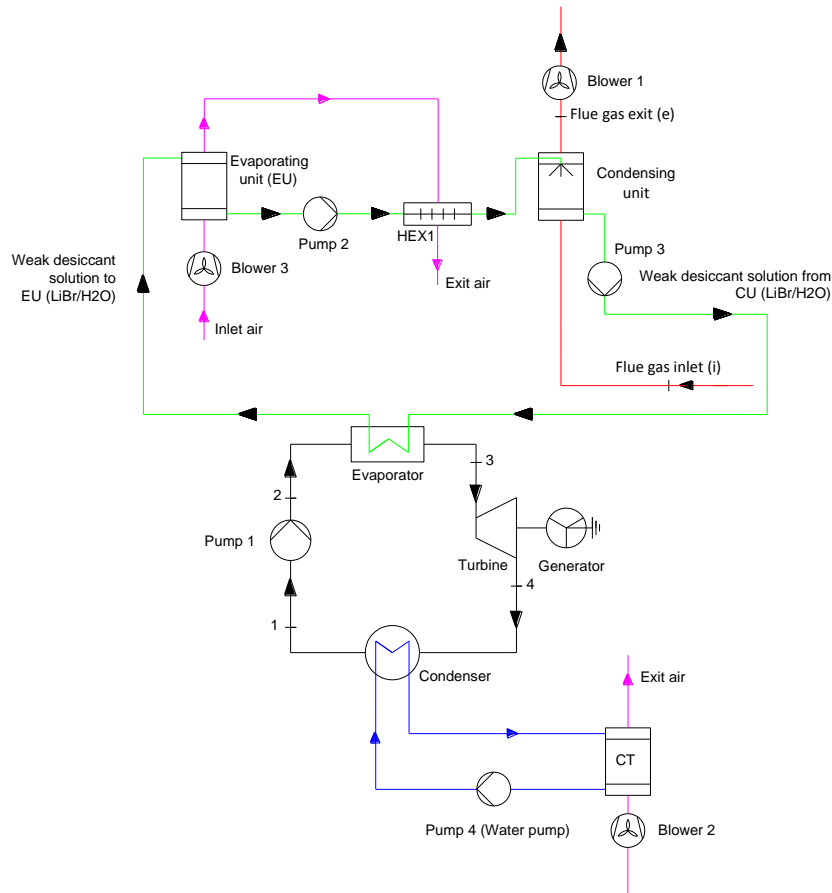


Fig. 4.30: Improved regeneration cycle (“IRC”)

For the cycle evaluation, the ORC process parameters are the same as those indicated in Table 1.5, Table 4.5, Table 4.7 and Table 4.11. Additional pressure drop of 150 Pa on the airside is estimated in “HEX1”.

4.8.1 Operating point

The desiccant solution is heated in the condensing unit and in HEX1, and cooled in the evaporator and in the evaporative unit. Therefore, the system presented in Fig. 4.30 presents an operating point if the following heat transfer equation is valid:

$$\underbrace{Q_{\text{evaporator}} + Q_{\text{EU}}}_{Q_1} = \underbrace{Q_{\text{CU}} + Q_{\text{HEX1}}}_{Q_2} \quad \text{Eq. 4.22}$$

Evolutions of quantities Q_1 and Q_2 presented in Eq. 4.22 as a function of the evaporation temperature are shown in Fig. 4.31 for “eksi” equal to 0.4. The solution temperature at the evaporator inlet is set to be equal to the corresponding entering wet bulb temperature with a minimum of 0.5 K below it (minimum pinch in the condensing unit). An operating point is identified at the crossing between the two curves and the corresponding evaporation temperature is around 64°C.

The distribution of the heat-exchanger capacities (CU, EU, HEX1 and evaporator) as a function of the evaporation temperature shows that “HEX1” capacity is the only one to present an increase with the evaporation temperature increase. At the operating point, the same heat exchange occurs in the

condensing unit and the evaporating unit on one hand, and in the evaporator and “HEX1” on the other hand.

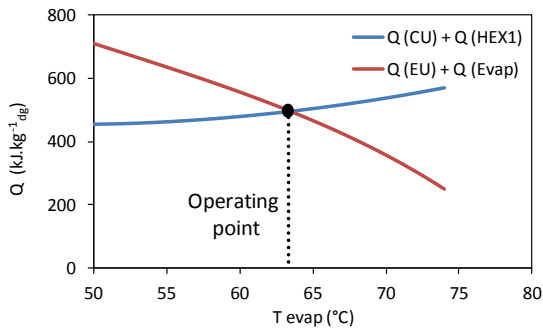


Fig. 4.31: Operating point determination for the “IRC” (“eksi” = 0.4)

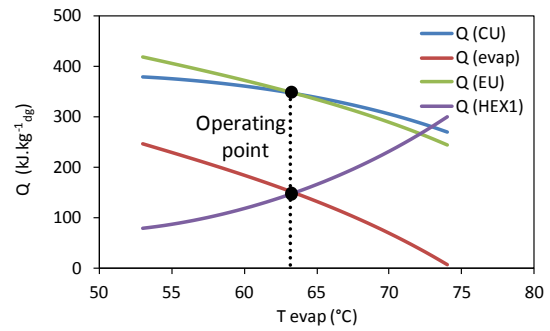


Fig. 4.32: Evolutions of heat capacities as a function of the evaporation temperature (“eksi” = 0.4)

The evolutions of the turbine and net powers as a function of the evaporation temperature are shown in Fig. 4.33.a and Fig. 4.33.b respectively. These figures show that the “IRC” presents a slight improvement in the turbine and net powers at the operating point compared to the “ICC” cycle.

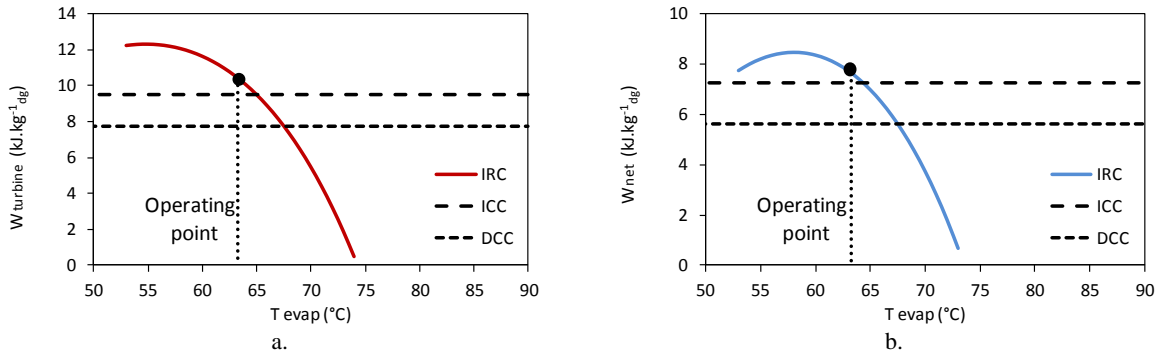


Fig. 4.33: Evolution of: a) turbine power, and b) net power, as a function of the evaporation temperature (“eksi” = 0.4)

The evolutions of the turbine and net powers as a function of “eksi” at the operating point are shown in Fig. 4.34.a and Fig. 4.34.b respectively. These figures show that the optimal “eksi” value is around 0.43. Beyond this value, a decrease in the turbine and net powers is expected.

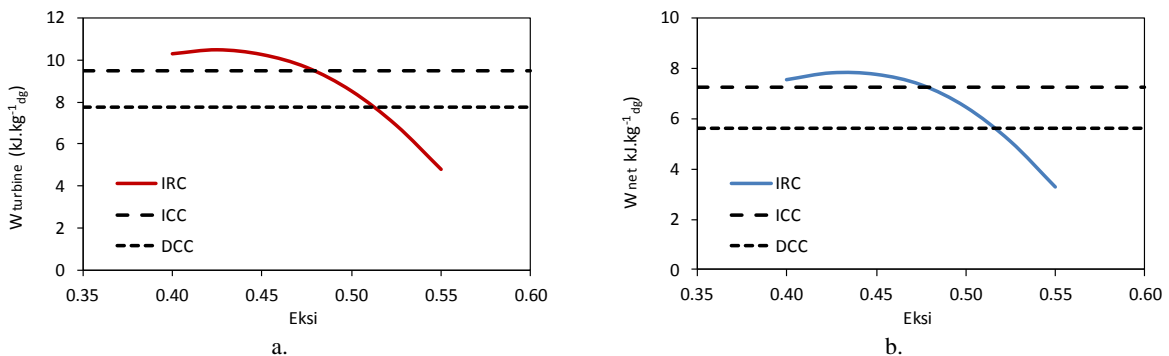


Fig. 4.34: Evolutions of: a) turbine power, and b) net power, as a function of “eksi”

Fig. 4.35.a (resp. Fig. 4.35.b) shows the aqueous lithium-bromide equilibrium in the condensing unit (resp. evaporating unit) at the optimal operating value of “eksi” (eksi = 0.43). In the condensing unit, flue gases are to be cooled from 120°C to around 48°C while heating the desiccant solution from around 46°C to 77°C. In the evaporating unit, the desiccant solution is to be cooled from around 63°C

to 31°C. Thus, “HEX1” gives the heat necessary to raise the desiccant solution temperature by around 17°C.

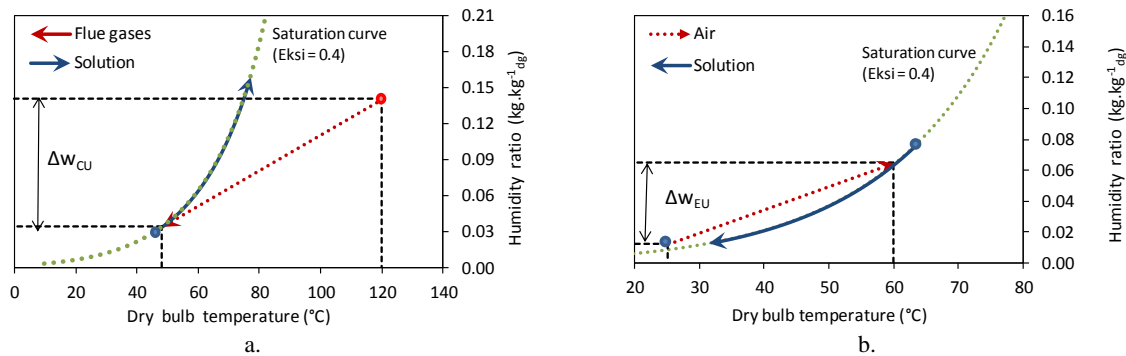


Fig. 4.35: Aqueous lithium-bromide equilibrium in: (a) CU, and (b) EU, at the optimal operating value of “eksi” (eksi = 0.43)

4.8.2 Effect of water dew point temperature

In this section, the “IRC” is evaluated and compared to “ICC” and “DCC” at three water dew point temperatures: 55, 60, and 65°C respectively as shown in Table 4.12. Calculations are done using the operating conditions listed in Table 1.5, Table 4.5, Table 4.7, and Table 4.11. For “ICC” and “DCC”, the evaporation pressure is optimized with respect to the net power.

Depending on the water dew point temperature, the net power varies from 5.2 to 11.9 kJ.kg⁻¹.dg for the “IRC”, compared to a variation between 4.3 to 12.1 kJ.kg⁻¹.dg (resp. 3.2 to 9.4 kJ.kg⁻¹.dg) for the “ICC” (resp. “DCC”). The turbine expansion ratio varies between 2.84 to 3.28 for “IRC”, while it varies between 1.66 and 1.95 (resp. 1.62 and 1.89) for “ICC” (resp. “DCC”).

Table 4.12: Effect of water dew point temperature on heat recovery processes (“IRC”, “ICC”, and “DCC”)

T _{dp} (°C)	P _{cond} (MPa)	P _{evap} (MPa)	W _{turbine} (kJ.kg ⁻¹ .dg)	W _{net} (kJ.kg ⁻¹ .dg)	τ
“ICC”					
55	0.1896	0.3152	5.9	4.3	1.66
60	0.1901	0.3411	9.5	7.2	1.79
65	0.1900	0.3714	15.2	12.1	1.95
“DCC”					
55	0.1900	0.3069	4.8	3.2	1.62
60	0.1902	0.3313	7.7	5.6	1.74
65	0.1901	0.3599	12.3	9.4	1.89
“IRC”					
55	0.1893	0.5374	7.3	5.2	2.84
60	0.1892	0.5787	10.4	7.8	3.06
65	0.1891	0.6206	15.2	11.9	3.28

The relative improvement provided by the “IRC” compared to the “ICC” and “DCC” are shown in Table 4.15. As the water dew point increases, the relative improvement of the turbine and net powers decrease. For a water dew point temperature of 55°C, the “IRC” improves the net power by 20.6% (resp. 61.5%) compared to “ICC” (resp. “DCC”). At high water dew point temperature (T_{dp} = 65°C), the “IRC” reduces slightly the net power compared to the “ICC”. Finally, the “IRC” could improve the turbine expansion ratio up to 75%.

Table 4.13: Relative improvement provided by “IRC” compared to “ICC” and “DCC”

T _{dp} (°C)	(ΔW _{turbine} /W _{turbine}) (%)	(ΔW _{net} /W _{net}) (%)	(Δτ/τ) (%)
----------------------	--	--	------------

“ICC”			
55	22.8	20.6	70.7
60	10.4	8.0	70.5
65	0.0	-1.9	68.0
“DCC”			
55	51.1	61.5	75.8
60	35.0	40.4	75.6
65	23.3	26.1	73.4

4.8.3 Effect of condensation temperature

In this section, the “IRC” is evaluated and compared to “ICC” and “DCC” at three ambient air conditions (T_{db}/T_{wb}): 13/18°C, 20/25°C, and 23/28°C corresponding to condensation temperatures of 24.9, 31.9, and 34.9°C respectively as shown in Table 4.14.

Table 4.14: Effect of condensation temperature on heat recovery processes

Air conditions (T_{db}/T_{wb})	T_{in}/T_{out} water condenser	T_{cond} (°C)	P_{cond} (MPa)	P_{evap} (MPa)	$W_{turbine}$ (kJ.kg ⁻¹ _{dg})	W_{net} (kJ.kg ⁻¹ _{dg})	τ
“ICC”							
13/18	18/23	24.9	0.1474	0.3180	14.12	11.11	2.16
20/25	25/30	31.9	0.1900	0.3411	9.49	7.26	1.80
23/28	28/33	34.9	0.2111	0.3520	7.72	5.79	1.67
“DCC”							
13/18	18/23	24.9	0.1474	0.3081	11.67	8.84	2.09
20/25	25/30	31.9	0.1901	0.3313	7.74	5.59	1.74
23/28	28/33	34.9	0.2112	0.3423	6.24	4.35	1.62
“IRC”							
13/18	18/23	24.9	0.1468	0.5642	14.56	11.38	3.84
20/25	25/30	31.9	0.1892	0.5638	10.47	7.84	2.98
23/28	28/33	34.9	0.2100	0.5801	8.85	6.45	2.76

Calculations are done using the operating conditions listed in Table 1.5, Table 4.5, Table 4.7, and Table 4.11. For “ICC” and “DCC”, the evaporation pressure is optimized with respect to the net power. Depending on the condensation temperatures, the net power varies from 6.45 to 11.38 kJ.kg⁻¹_{dg} for “IRC”, compared to a variation between 5.79 to 11.11 kJ.kg⁻¹_{dg} (resp. 4.35 to 8.84 kJ.kg⁻¹_{dg}) for “ICC” (resp. “DCC”). Concerning the turbine expansion ratio, it varies between 2.76 to 3.84 for “IRC”, while it varies between 1.67 and 2.16 (resp. 1.62 and 2.09) for “ICC” (resp. “DCC”).

The relative improvement provided by the “IRC” compared to the “ICC” and “DCC” are shown in Table 4.15. As the condensation temperature increases, the relative improvement of the turbine and net powers decrease. Compared to “ICC” (resp. “DCC”), the “IRC” improves the net power by 2.4% (resp. 28.7%) at low-condensation temperature (24.9°C) and by 11.4% (resp. 48.4%) at high-condensation temperature (34.9°C). Finally, the “IRC” improves greatly the turbine expansion ratio compared to “ICC” and “DCC”. This improvement could reach 84%.

Table 4.15: Relative improvement provided by “IRC” compared to “ICC” and “DCC”

Air conditions (T_{db}/T_{wb})	T_{in}/T_{out} water to/from condenser	T_{cond} (°C)	$(\Delta W_{turbine}/W_{turbine})$ (%)	$(\Delta W_{net}/W_{net})$ (%)	$(\Delta \tau/\tau)$ (%)
“ICC”					
13/18	18/23	24.9	3.1	2.4	78.2
20/25	25/30	31.9	10.4	8.0	66.0
23/28	28/33	34.9	14.6	11.4	65.6
“DCC”					
13/18	18/23	24.9	24.7	28.7	83.9
20/25	25/30	31.9	35.0	40.4	71.0
23/28	28/33	34.9	41.9	48.4	70.4

4.9 Model validation using “ASPEN” software

This section presents a validated modeling methodology implemented in “ASPEN” for the improved regeneration cycle (“IRC”) using aqueous lithium-bromide solution. “ASPEN” is a process modeling software for steady-state process modeling [BER 04]. The user interface is based on a library of ready-made, user-editable “Fortran-based” component models. By connecting these components with material, heat, and work streams and providing values of predefined inputs, complex processes could be modeled.

In order to develop an “ASPEN” model for “IRC” cycle using aqueous lithium-bromide solution, the properties of lithium bromide-water mixture should be carefully represented. The “ELECNRTL” model is used. This model takes into consideration the activity-coefficient property for the lithium bromide-water mixture, since the operating conditions and fluids being modeled with this method are designed for electrolytes.

The condensing and evaporation units are modeled by using the “Radfrac” columns. Condenser and evaporator are modeled using heater blocks. Flue gas, aqueous lithium bromide-water solution, working fluid (“R-245fa”), and outside airflows are marked respectively by red, blue, black, and magenta color lines.

Fig. 4.36 presents the “IRC” flow-sheet model implemented in “ASPEN”. The power obtained at the turbine outlet is 10.5 kW. Using the same ORC input data as for the flow sheet model presented in Fig. 4.36, this value is to be compared to the value 10.4 kW obtained in Table 4.12. With this very slight difference in turbine power, the calculations of the VBA model are validated.

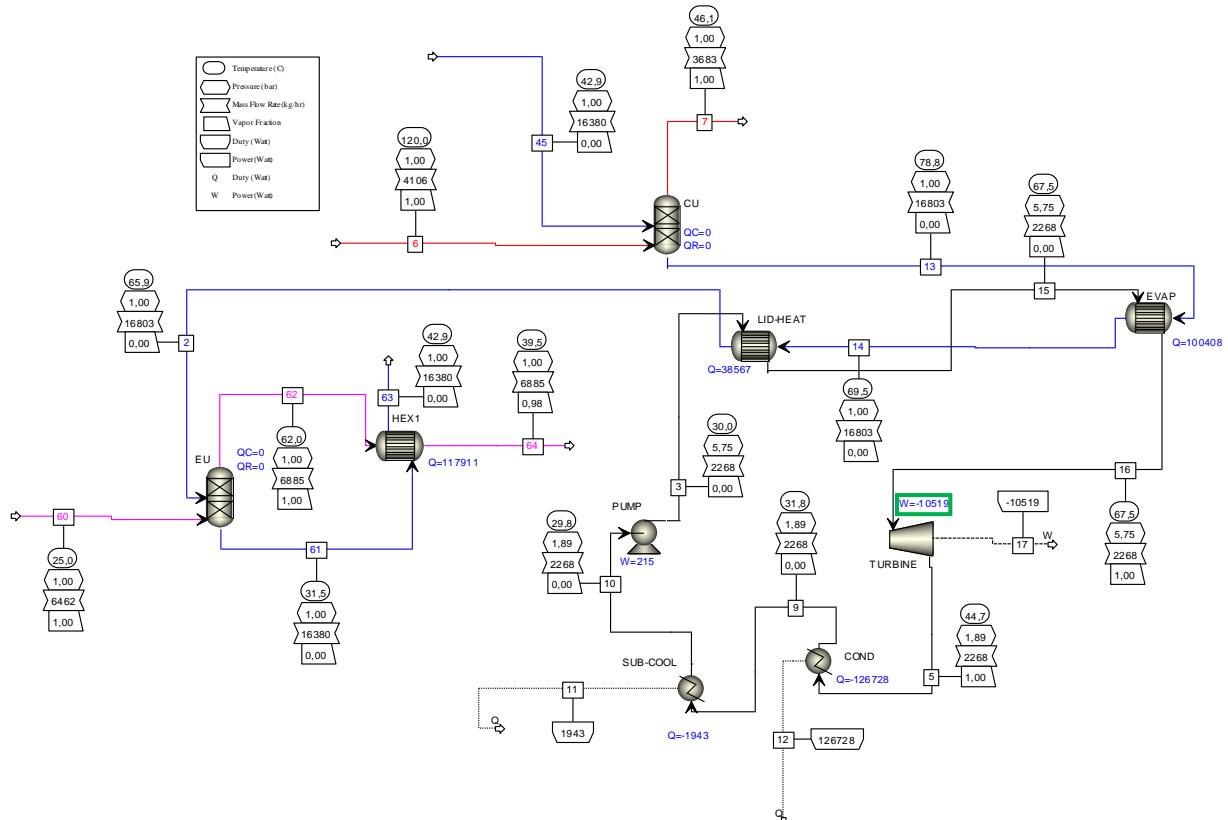


Fig. 4.36: “ASPEN” flow-sheet model for “IRC”

4.10 Conclusions

Low-temperature flue gases with high-moisture contents are abundant in large quantity. Cooling flue gases below the condensation point could achieve significant increases in energy efficiency. Classical heat recovery technologies face many challenges while recovering latent heat below the water dew point temperature. In the indirect-contact water-vapor condensation (“ICC”), corrosive substances could deposit on the heat-exchanger surface, thus reducing heat-transfer rates, lifetime, leading to increased pressure drops, and reduced efficiency. In the direct-contact water-vapor condensation (“DCC”), a net power loss is expected owing to the thermodynamic limitation of the circulating water temperature and to the additional temperature difference “ ΔT ” due to heat-transfer loop between the circulating water and the working fluid. In addition, the two heat recovery processes admit low-turbine expansion ratio since the evaporation temperature must be kept below the entering water dew point temperature when recovering latent heat.

Development opportunities include developing new heat recovery technologies. Emerging and novel technologies may hold promise for replacing existing technologies, enabling heat recovery from “wet” heat sources and increasing options for low-temperature heat recovery. Innovative thermodynamic cycles based on desiccant dehumidification using direct contact water-vapor condensation process are presented. Desiccant materials could act on the surface water vapor pressure and thus changing the entering equilibrium wet bulb temperature when in contact with flue gases. Desiccants transfer moisture because of a difference between water vapor pressure at their surface and that of the surrounding flue gases. When the vapor pressure at the desiccant surface is lower than that of flue gases, the desiccant attracts moisture. When the vapor pressure at the desiccant surface is higher than that of flue gases, the desiccant will release moisture.

Net power improvement seems to be very attractive by using the desiccant dehumidification technology compared to the classical heat recovery technologies (“ICC” and “DCC”). Nevertheless, in normal operation mode, the desiccant solution is diluted by the water absorbed from flue gases and the solution must be regenerated to its initial concentration by adding continuously a desiccant material in order to ensure a continuous operation cycle. However, this method is not practical since the ratio between a kWh produced and the mass of added desiccant material is very small making the process economically unfeasible. Therefore, regeneration methods should be provided.

One possible regeneration option is to use the solar energy in order to evaporate the quantity of water absorbed from flue gases. However, the needed evaporation rate is large enough and a quantity above “ $2.2 \text{ m}^3 \cdot \text{day}^{-1}$ ” (at $T_{\text{dp}} = 60^\circ\text{C}$) is required for each “ $1 \text{ kg}_{\text{dg}} \cdot \text{s}^{-1}$ ” in order to achieve an improvement in the net power in comparison to “ICC”. In addition, the cycle can operate only during the sunshine hours and it is strongly dependant on weather statement.

Another regeneration option consists to evaporate the quantity of water absorbed from flue gases into a separate regenerator. This could be done by using an evaporative unit (EU) operating with outside ambient air. An equilibrium point between the condensation rate in the condensing unit and the evaporation rate in the evaporating unit could be identified at relatively high-evaporation temperature; thus, the resulting net power is very low. Therefore, in order to increase the net power, an improved regeneration cycle “IRC” is proposed, where a counter-flow heat exchanger between the air and the desiccant solution exiting the evaporating unit is integrated into the conventional regeneration cycle. In this case, a large portion of the heat transferred from the desiccant solution to the air in the evaporating unit will be recovered in this heat exchanger, and the system could present an operating point at lower evaporation temperatures, resulting into higher net power.

The presented “IRC” constitutes a promising novel thermodynamic cycle in recovering low-temperature heat sources with high-moisture content. It can overcome the challenges faced in the classical heat recovery technologies (“ICC” and “DCC”). Results show that by varying the water dew point temperature between 55 and 65°C , and the ambient air temperature between 18 and 28°C , the “IRC” improves the net power up to 20.6% (resp. 61.5%) and the turbine expansion ratio up to 78.2% (resp. 83.3%) compared to “ICC” (resp. “DCC”).

For further work, it is interesting to study a hybrid heat-recovery technology by combining the presented “IRC” with the solar energy. This could be another possible promising option in recovering low-temperature heat sources with high moisture content.

References

- [DAA 12] Daal, L., Kamphuis, H., Stam, A., Konings, T., Huibers, M., Rijen, S., Ruijter, J., Evaluation of different water vapor capture technologies and energy modeling results for membrane technology; DNV-KEMA the Netherlands, Department PGR-PCW, 2012.
- [ASH 01a] Ashrae Fundamentals, Sorbents and desiccants. American Society of Heating, Refrigeration and Air-Conditioning Engineers. 2001, Chapter 22.
- [ASH 00] Ashrae Systems and Equipment, Desiccant dehumidification and pressure drying equipment. American Society of Heating, Refrigeration and Air-Conditioning Engineers. 2000, Chapter 22.
- [CON 04] Aqueous solutions of lithium and calcium chlorides: Property formulations for use in air conditioning equipment design. M. CONDE ENGINEERING, 2004.
- [KAI 01] Kaita, Y., Thermodynamic properties of lithium bromide-water solutions at high temperatures. International Journal of Refrigeration 2001;24:374-390.
- [ASH 01b] Ashrae Fundamentals, Psychometrics. American Society of Heating, Refrigeration and Air-Conditioning Engineers. 2001, Chapter 6.
- [FEU 93] Feuerecker, G., Scharfe, J., Greitter, I., Frank, C., Alfeld, G., Measurement of thermo physical properties of LiBr-solutions at high temperatures and concentrations. International Absorption Heat Pump Conference, ASME, 1993;31:493-99.
- [KIS 08] Kisari, P., Wang, K., Abdelaziz, O., Vineyard, E.A. Crystallization Temperature of Aqueous Lithium Bromide Solutions at Low Evaporation Temperature. Whole Building and Community Integration, Energy & Transportation Science Division, Oak Ridge National Laboratory. 2008
- [DIE 04] Dieckmann, J., Roth, K., Brodrick, J., Liquid desiccant air conditioners. Ashrae journal, 2004.
- [LEM 10] Lemmon E.W., Huber M.L., McLinden M.O., Reference Fluid Thermodynamic and Transport Properties. NIST Standard Reference Database 23, Version 9.0, 2010.
- [BER 04] Bernards M., Overney R., ASPEN Plus 12.1 Instructional tutorials. University of Washington. Department of Chemical Engineering, 2004.

General conclusions

Recovered and regenerated waste heat is an emission-free substitute for costly purchased fuels or electricity. Most unrecovered waste heat (more than 50%) is at low temperatures ($< 120\text{-}150^\circ\text{C}$). While low-temperature waste heat presents lower thermal and economic value than high-temperature heat, it is ubiquitous and available in large quantities and it should not be neglected in pursuing researches and development opportunities for waste heat recovery and regeneration.

Low-temperature waste-heat recovery technologies face technical and economic barriers especially when recovering polluted exhaust streams (SO_x , NO_x ,...) with-high moisture content. In order to promote low-temperature waste heat recovery, efforts are undertaken in the present thesis to extend the feasibility of conventional heat recovery technologies, as well as to promote new technologies that can be applied to waste heat sources (not typically exploited for waste heat recovery) by way of electricity production using the well-proven Organic Rankine Cycle (ORC).

Conventional heat recovery technologies include indirect and direct-contact water-vapor condensation recovery depending on which the heat is transferred between the hot stream (flue gases) and the cold stream (working fluid), using or not an intervening wall respectively. Thermodynamic optimization is performed for both heat recovery modes and the effects of water-vapor condensation on cycle performance are pointed out. For ORC using an indirect contact water-vapor condensation, depending on the evaporation temperature, two operating regions can be identified in the evaporator: “sensible heat region” where mostly sensible heat is recovered, and “latent heat region” where a large portion of latent heat is recovered. An optimum for the net power can be identified in each region. Water dew point affects very much the net power ratio between the two optima. The indirect contact condensation is the most favorable heat recovery scheme concerning the net power, provided the acid corrosion problems can be overcome in a cost-effective way.

The ORC with direct-contact heat exchanger has received attention because there are no heat-transfer surfaces exposed to corrosion. It may be considered to consist of two-stages: the humidification stage and the dehumidification stage. The entering wet-bulb temperature determines the operating temperature level throughout the system and limits the circulating water temperature. The maximal net power in the direct-contact system is reached for a final water temperature nearby the entering wet bulb temperature of flue gases. However, a net power loss is expected compared to the indirect-contact heat exchanger owing to the thermodynamic limitation of the circulating water temperature and to the additional temperature difference “ ΔT ” due to heat transfer loop between the circulating water and the working fluid.

The ORC with hybrid heat-recovery process consists in recovering the sensible (resp. latent) heat in an indirect-(resp. direct) contact heat exchanger. It leads to a potential increase in the net power compared to the direct-contact condensation process, while avoiding surface corrosion problems due to water-vapor condensation faced in the indirect-contact condensation process.

The integration of a two-stage ORC in an attempt to recover heat from both optima (sensible and latent optima) is promising when the net power values at both optima are in the same range. Depending on the water dew point temperature, the two-stage ORC could lead to a potential increase in the net power, up to 60% compared to a simple stage ORC.

The auxiliary consumptions play a crucial role when recovering low-temperature heat sources since the overall efficiency is as low as 5%. They could affect the cycle operating parameters as well as the working fluid selection. “R-1234yf” is identified as a promising working fluid over the entire range of water dew point temperatures. Wet fluids (“ammonia”, “R-152a”...) become promising at high-water dew point temperatures if high auxiliary consumptions take place. Using blends as working fluid instead of a pure working fluid could be an effective solution to minimize the auxiliary consumptions by creating temperature glides in the heat exchangers. A particular importance for the R-1234yf/R-245fa blend is to be set when recovering heat at this temperature level (< 120-150°C).

Estimating the dew point of acid gases is the starting point in understanding the corrosion problems in the indirect-contact heat exchanger whenever high-moisture content flue gases contain gaseous pollutants such as nitrogen oxides (NO_x), sulfur dioxide (SO₂), and sulfur trioxide (SO₃). The acid dew point is handled by the “SO₃” content and a rate of “2 ppm SO₃” could bring the acid dew point to a temperature in the same range of the inlet flue-gas temperature (~120°C). Thus, acid condensation is unavoidable and the safe zone almost does not exist when recovering heat at low-temperature level.

A general method adapted at low-temperature level has been elaborated to design an optimized indirect-contact heat exchanger (fin-and-tube heat exchanger). The geometry of the fin-and-tube heat exchanger has been derived, and optimized geometrical configurations have been found out by ensuring a compromise between the net power produced by the ORC and the fin-and-tube heat-exchanger compactness.

Technologies that can minimize chemical attack while cooling exhaust gases below the acid and water dew points could be achieved by using corrosion resistant materials. Two types of treated surface have been proposed: “Heresite” treating (hydrophilic aspect) and “Epoxy” treating (more hydrophobic aspect). Experimental investigations have allowed the study of the impact of surface wet-abilities on thermal hydraulic performances of fin-and-tube heat exchangers. Under dry operation data, the treated specimens present degradation in thermal hydraulic performances compared to the uncoated specimen. The degradation is more noticeable for the specimen with “Heresite” treating rather than with the “Epoxy” one. Wet-condition data show that for “Heresite” treating, heat-transfer performance of the heat exchanger is normally not strongly influenced. Very slight heat-transfer degradation at low airside Reynolds numbers due to the film-wise mode of condensation was noticed. However, pressure drop is more sensitive to the enhancement of surface wet-ability and can be reduced. The specimen with “Epoxy” treating has less efficient behavior than the “Heresite” in dehumidification mode.

In the condensing unit, the direct-heat exchange between flue gases and water occurs via packing materials. The design considerations of the condensing unit are based on hydraulic parameters (pressure drop and liquid hold-up) and on heat and mass transfer between flue gases and water through the packing. The knowledge of the hydraulic characteristics is essential for the design of the condensing unit. Three operating regions can be identified: the pre-loading region, the loading region and the flooding region. A 1-D mathematical model for heat and mass transfer is presented in order to determine the required packing height for given operating parameters. In designing a condensing unit, the cross-sectional area will be selected depending on the hydraulic parameters and on the maximal allowable pressure drop at the flue-gas side.

Experimental studies were conducted in order to validate the developed model and to examine the performance of various packing types with distinct surface geometry and wet-ability on the condensing unit behavior. Four types of stainless steel structured packing imported from “Montz”

("B1-45", "B1-60", "B1-M", and "B1-MN") and one type of polypropylene packing "PP" are tested. From the pressure drop data that have been able to be measured, "B1-45" presents a dry pressure drop almost four times higher than those obtained with "B1-60" and "PP". Pressure-drop model validation for "B1-45" shows that the correlated pressure drop is underestimated by around 30% compared to the experimental one over the entire range of liquid loads and gas-load factors. A comparison of "U-factor" between the various tested packing shows that "B1-45" presents the highest "U-factor", while the "PP" presents the lowest one. "B1-60", "B1-M" and "B1-MN" present a noticeable heat and mass transfer degradation compared to "B1-45". Heat-transfer model validation for "B1-45" shows that the correlated heat-exchange capacity is overestimated by around 15% compared to the experimental one.

Innovative opportunities are considered by developing new heat recovery technologies for replacing existing ones enabling heat recovery from heat sources with high-moisture contents and therefore increasing effective options for heat recovery. Novel thermodynamic cycles based on desiccant heat-recovery technology could be an effective solution to overcome the challenges faced in the conventional heat-recovery technologies. Desiccant materials could act on the surface water vapor pressure and thus changing the entering equilibrium wet bulb temperature when in contact with flue gases.

Net power improvement seems to be very attractive by using the desiccant dehumidification technology compared to the conventional heat recovery technologies. Nevertheless, in normal operation mode, the desiccant solution is diluted by the water absorbed from flue gases and the solution must be reestablished to its initial concentration by adding continuously a desiccant material in order to ensure a continuous operation mode. However, this method is not practical since the ratio between a "kWh" produced and the mass of added desiccant material is very small making the process economically unfeasible. Therefore, regeneration methods should be provided in order to evaporate the quantity of water absorbed from flue gases.

Regeneration processes could be provided using either solar energy or an evaporative unit. When using solar energy, the needed evaporation rate is relatively large enough and a quantity above "2.2 m³.day⁻¹" (square pool section area around 15 m * 15 m) at a water dew point of 60°C is required for each "1kg_{dg}.s⁻¹" in order to achieve an improvement in the net power in comparison with the conventional heat recovery technologies. In addition, the cycle can operate only during the sunshine hours and it is strongly dependent on weather statement.

By using an evaporative unit operating with outside ambient air, the water is evaporated from the desiccant solution into the air since the water partial pressure in the air stream is lower than the water partial pressure in the desiccant solution. In this case, an equilibrium point between the condensation rate in the condensing unit and the evaporation rate in the evaporating unit could be identified at relatively high-evaporation temperature, and the resulting net power is very low. Therefore, in order to increase the net power, an improved regeneration cycle "IRC" is proposed, where a counter-flow heat exchanger between the air and the desiccant solution exiting the evaporating unit is integrated into the conventional regeneration cycle. The presented "IRC" constitutes a promising novel thermodynamic cycle in recovering industrial low-temperature heat sources with high-moisture content. It can overcome challenges faced in the classical heat recovery technologies, by preventing corrosion problems, increasing both net power and turbine expansion ratio. The proposed "IRC" shows a good behavior over a wide range of water dew point temperatures (55 to 65°C) and outside ambient air conditions (18 to 28°C).

Future works

Following the investigations described in this thesis, there are several lines of research arising that should be pursued as follows:

- Efforts must be undertaken to study the economic feasibility of the indirect-contact water-vapor condensation recovery technology. Cost benefit analyses should be conducted to provide estimates of the costs and benefits by cooling flue gases to temperature below the water dew point and to estimate how much flue-gas moisture it would be possible to recover economically.
- Long-term laboratory corrosion tests designed to simulate the corrosive condensate solutions could be conducted to identify innovative materials that would provide adequate service life along with desired heat transfer and structural properties. The tests could cover the two main corrosion locations in the heat exchanger: higher temperature, with highly concentrated sulfuric acid and lower temperature with a dilute acid mixture, possibly containing sulfurous, hydrochloric, and nitric acids.
- In addition to pollutant contents (SO_x , NO_x , ...), industrial flue gases may contain dust causing particulates fouling. Clogged heat exchanger can cause capacity loss and high-head pressure. Periodically cleaning heat-exchanger methods should be provided and experimental studies could be conducted to optimize the operating flue-gas velocity as well as the fin-pitch choice in order to avoid fouling and clogging problems.
- Experimental validation of the innovative desiccant dehumidification technology could be conducted in order to prove the concept performance and its economical benefits.

Annex A: Evaluation of the chemical exergy

The exergy of a system (relative to the assumed reference environment) depends on system temperature, pressure, and composition; the first two contribute to thermo-mechanical exergy, and the effect of composition to chemical exergy. The mass exergy can be expressed as:

$$Ex = (h - T_o \cdot s)_i + \sum y_i \cdot (\mu_i - \mu_{io})_{T_o, P_o} \quad (i = \text{CO}_2, \text{O}_2, \text{N}_2, \text{H}_2\text{O}) \quad \text{Eq. A.1}$$

Where subscript “o” refers to the specified reference state, “h” and “s” are respectively the mass enthalpy and entropy, “ μ ” is the chemical potential, and “y” is the mass fraction. The chemical exergy is defined as the work obtainable due to difference in the chemical potentials between the environmental state and the dead state. The chemical exergy, $\psi = \sum y_i \cdot (\mu_i - \mu_{io})_{T_o, P_o}$, depends on the mass fraction of every species in the system, y_i , their chemical potential at the reference temperature and pressure, $\mu_i(T_o, P_o, x_i)$ and the chemical potential of each species in the reference environment, $\mu_i(T_o, P_o, x_{io})$. The molar fractions of the different components at the dead reference state are shown in Table A.1. The chemical potential at a given state is calculated using REFPROP 9.0.

Table A.1: Molar fractions of the different components at the dead reference state (20°C, 1 bar)

Components	molar fraction, x_i
N ₂ / O ₂ / H ₂ O/ CO ₂	0.7651/0.2062/0.0190/0.0003

When the cooling reaches the initial water dew point at which water vapor condensation begins, the partial pressure of water vapor decreases continuously. Therefore, the total pressure of flue gases decreases, while the partial pressure of the dry-gas components (CO₂, O₂, N₂) remains constant. Thus, for the dry components (CO₂, O₂, N₂), the chemical exergy will be constant when the flue-gas cooling occurs and the variation of the chemical exergy is nil. The chemical exergy is due mainly to water vapor condensation.

Fig. A shows the evolutions of the thermo-mechanical and the chemical exergy differences calculated for a 1-K gas cooling as a function of the heat-source temperature for various water dew point temperatures. By comparing Fig.A.1.a and Fig.A.1.b, it can be concluded that the chemical exergy is less than 1% of the thermo-mechanical exergy and can be neglected.

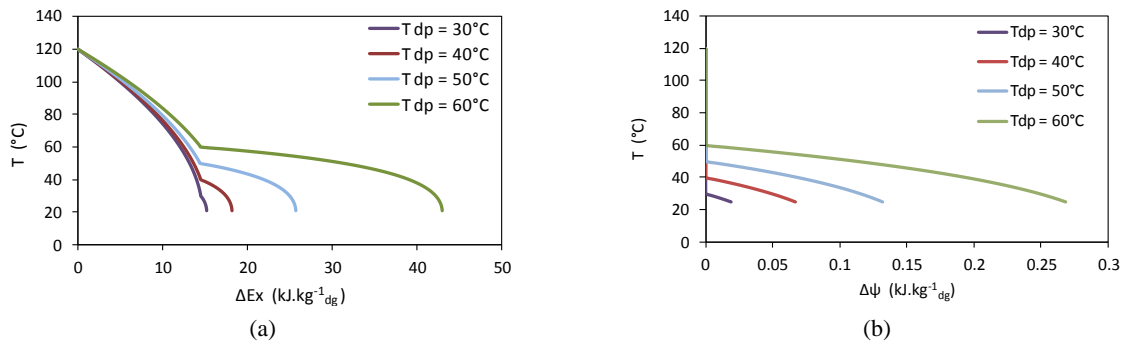


Fig. A.1: Evolution of: (a) thermo-mechanical, (b) chemical exergy differences as a function of the heat source temperature for various water dew point temperatures

Annex B: Cooling tower parameters

In order to ensure a cold source for the condenser, a wet cooling tower could be used. Fig. B.1 shows a schematic diagram of a cooling water system. The main components of a cooling tower are the following: packed columns heat exchanger, air blower and cooling water pump.

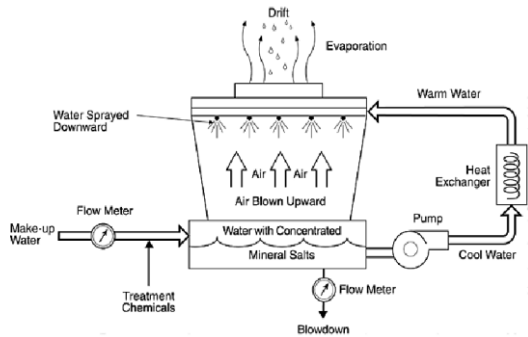


Fig. B.1: Schematic diagram of a cooling water system

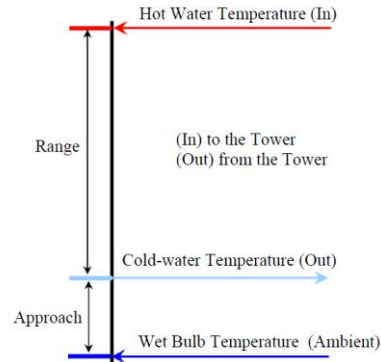


Fig. B.2: Cooling tower range and approach

➤ Factor of influence for Cooling Tower performance

Several factors influence the cooling tower performances and must be considered in the selection of a cooling tower, such as the cooling capacity, range, approach, wet bulb temperature.

- CT Range: this is the difference between the cooling tower water inlet and outlet water (Eq. B.1 & Fig. B.2):

$$\text{CT Range} = T_{\text{cold water inlet}} - T_{\text{cold water outlet}} \quad \text{Eq. B.1}$$

- CT Approach: this is the difference between the outlet cold-water temperature and the entering wet bulb temperature. The lower the approach, the better the cooling tower performance (Eq. B.2 & Fig. B.2):

$$\text{CT Approach} = T_{\text{cold water outlet}} - T_{\text{entering wet bulb}} \quad \text{Eq. B.2}$$

- CT Effectiveness: this is the ratio between the range and the ideal range, i.e. the difference between cooling water inlet temperature and ambient wet bulb temperature (Eq. B.3), or in other words it is: $\text{Range}/(\text{Range} + \text{Approach})$. The higher this ratio, the higher is the cooling tower effectiveness.

$$\text{CT eff.} = 100 * (T_{\text{cold water inlet}} - T_{\text{cold water outlet}}) / (T_{\text{cold water inlet}} - T_{\text{entering wet bulb}}) \quad \text{Eq. B.3}$$

- Wet bulb temperature: it is an important factor in performance of evaporative water cooling equipment. The wet bulb temperature of the air entering the cooling tower determines the exiting water temperature.

Annex C: Optimization procedures

This annexes shows the algorithms used during the optimization of the thermodynamic cycles. The optimization procedures are done using the Golden Section (GS) search technique (Fig. C.1). The objective function is $f(x)$ and the search domain is $[x_l, x_h]$.

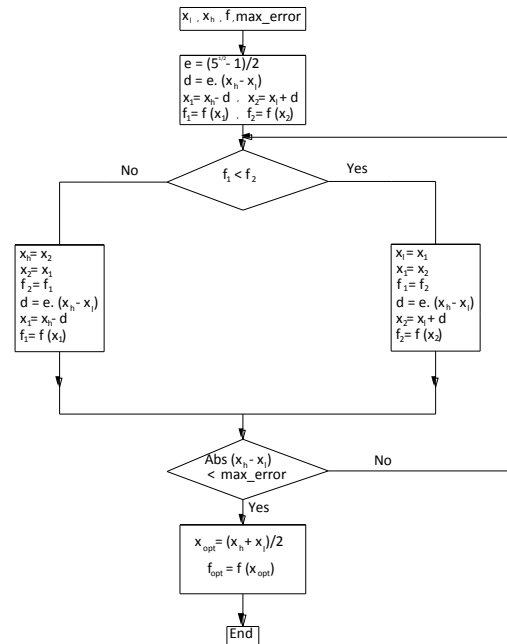


Fig. C.1: Golden section (GS) search technique

Fig. C.2a and C.2b show the optimization algorithms for simple ORC with, respectively, direct and indirect-contact water vapor condensation. The evaporation pressure and evaporator superheat are optimized in order to maximize the net power using the golden section (GS) method.



Fig. C.2: Optimization algorithms for simple ORC with : (a) indirect-contact condensation (direct evaporator), (b) both direct and indirect (indirect evaporator)-contact condensation

Fig. C.3 shows the optimization algorithm for ORC with hybrid heat-recovery mode. The evaporation pressure and evaporator superheat are optimized in order to maximize the net power. The exit water temperature from “HEX1” is calculated to ensure the corresponding pinch in the condensing unit.

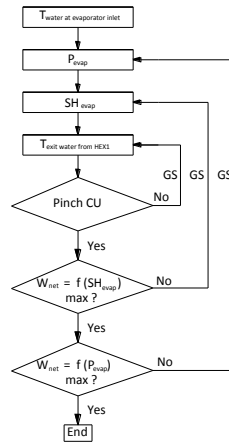


Fig. C.3: Optimization algorithm for ORC with hybrid heat-recovery mode

Fig. C.4a and C.4b show the optimization algorithms for, respectively, typical and enhanced two-stage ORCs. For the typical two-stage ORC, the evaporation pressures and the evaporator superheats are optimized with respect to the net power by following the order indicated in the algorithm diagram (Fig. C.4a). The same optimization procedure is valid for the enhanced two-stage ORC except that there is no superheat at the exit of Evaporator 1.

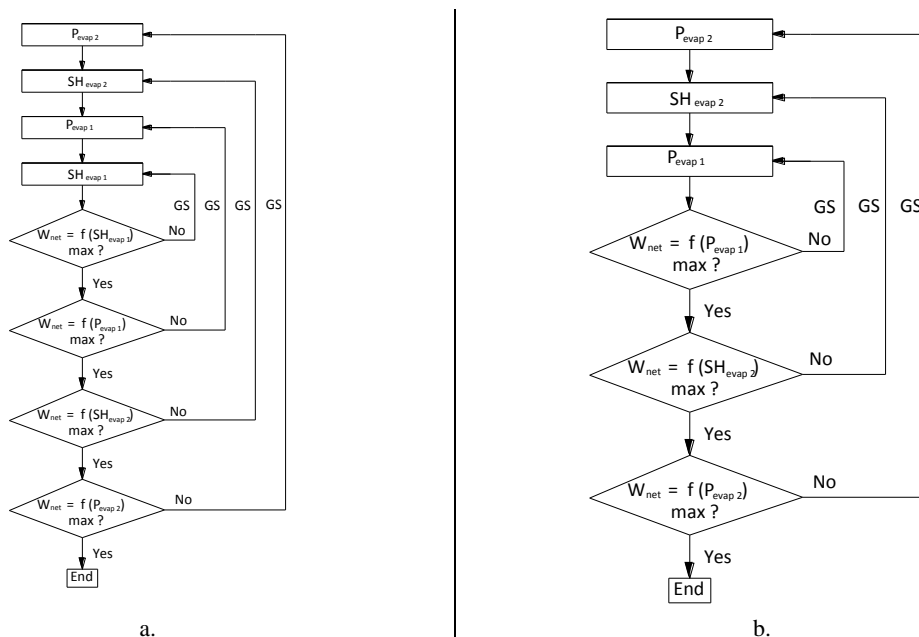


Fig. C.4: Optimization algorithms for: (a) typical two-stage ORC , (b) enhanced two-stage ORC

When taking into account the auxiliary consumptions, Fig.C.5, Fig.C.6, Fig.C.7, and Fig.C.8 show respectively, the optimization algorithms for simple ORC with direct and indirect contact condensation, simple ORC with direct contact condensation, simple ORC with hybrid heat-recovery process, and enhanced two-stage ORC. In this case, the evaporation pressure, the boiler superheat, and the condensation pressure will be optimized with respect to the net power by following the order indicated in the algorithm diagrams. When using a binary blend as working fluid, the optimization

procedure becomes more complicated. In this case, Y_{C1} represents the molar fraction of Component 1 (C_1) of the blend. Due to the temperature glides in the evaporator and in the condenser, the pinch point in both heat exchangers must be calculated carefully by dividing the corresponding composite curves into many intervals and by proceeding by trial and error procedure.

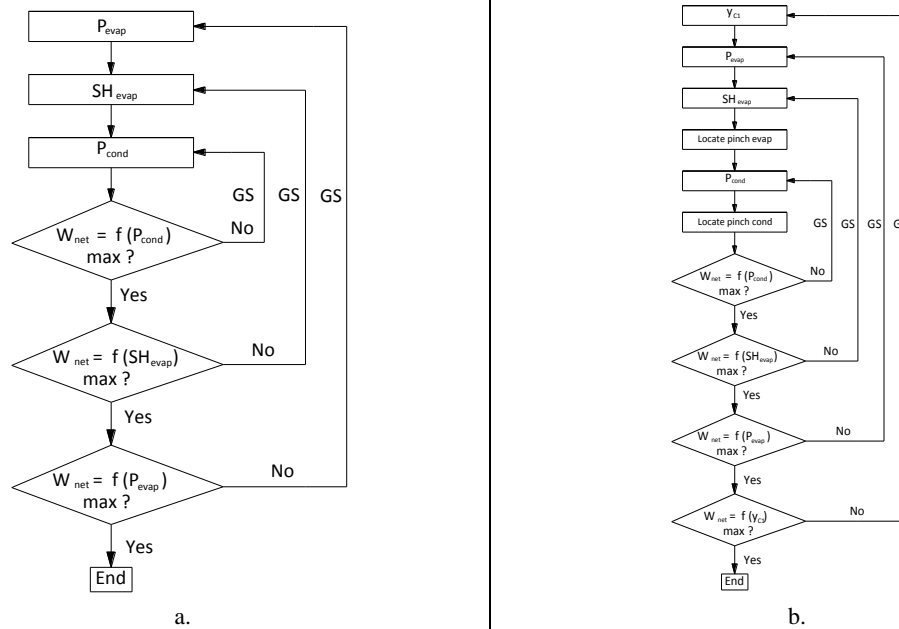


Fig. C.5: Optimization algorithms for simple ORC with indirect-contact condensation when auxiliary consumptions are taken into account: (a) pure working fluid, (b) binary-blend working fluid

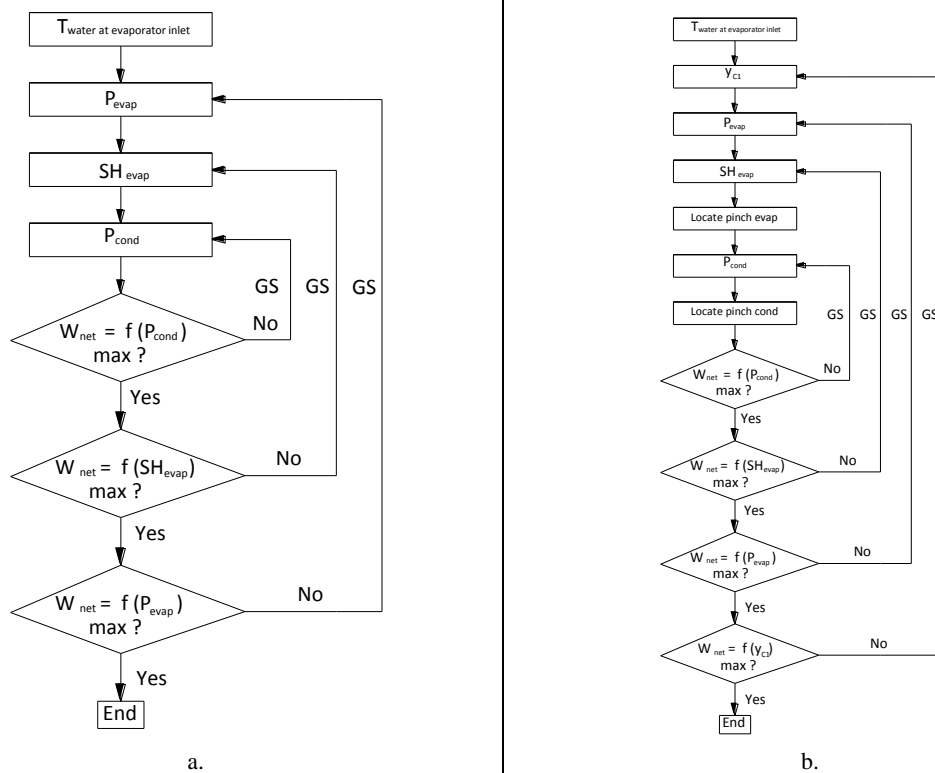


Fig. C.6: Optimization algorithms for simple ORC with direct-contact condensation when auxiliary consumptions are taken into account (a) pure working fluid, (b) binary-blend working fluid

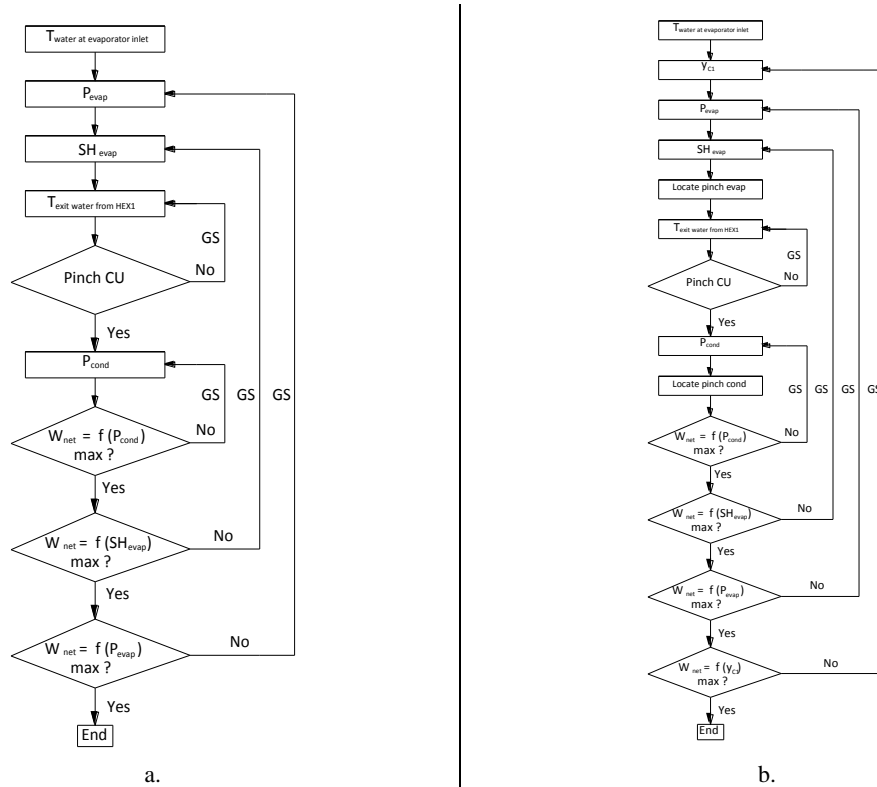


Fig. C.7: Optimization algorithms for simple ORC with hybrid heat recovery mode when auxiliary consumptions are taken into account: (a) pure working fluid, (b) binary-blend working fluid

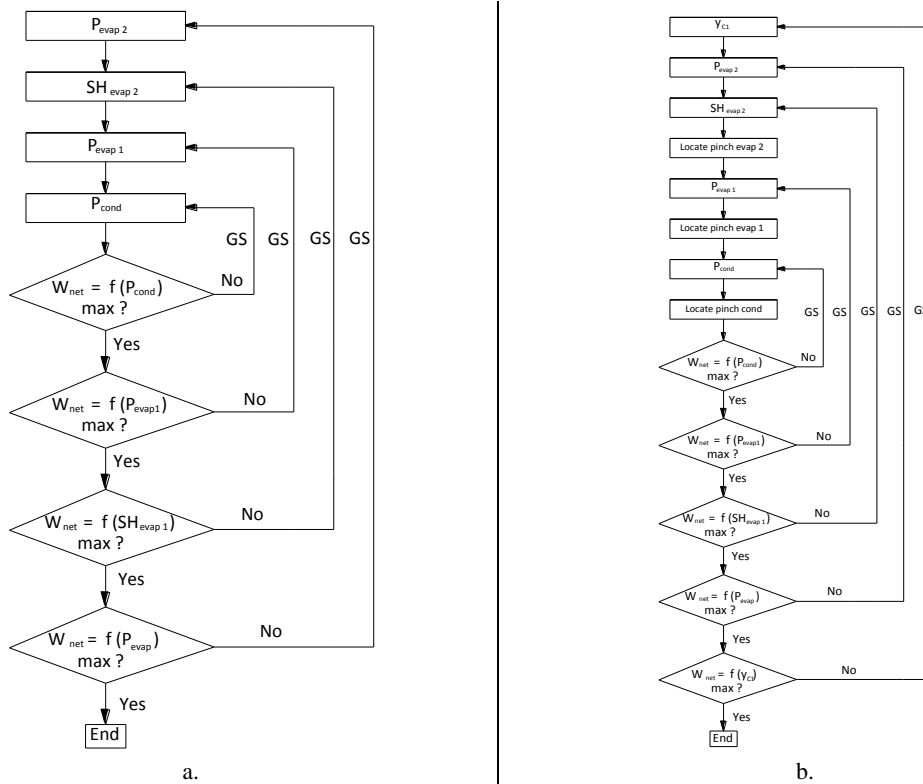


Fig. C.8: Optimization algorithms for enhanced two-stage ORC when auxiliary consumptions are taken into account: (a) pure working fluid, (b) binary-blend working fluid.

When auxiliary consumptions are taken into account, Fig.C.9 shows the optimization algorithm for trans-critical ORC. “DT” denotes the temperature difference between the inlet heat-source temperature

and the working-fluid temperature at the evaporator outlet. In this case, in addition to the evaporation and condensation pressures, “DT” will also be optimized with respect to the net power.

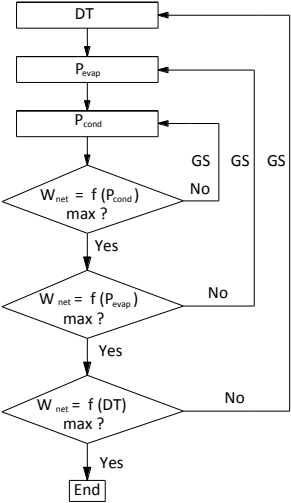


Fig. C.9: Optimization algorithm for trans-critical ORC when auxiliary consumptions are taken into account

Annex D: Heat-transfer and pressure drop correlations used in fin-and-tube heat exchanger

This annex details the heat transfer and pressure drop correlations used in the design of the fin-and-tube heat exchanger. The references shown in this annex are referred to Chapter 2.

a. Heat-transfer correlation at working fluid side

The single-phase heat-transfer coefficient in liquid and vapor phases is calculated using “Dittus-Boelter” correlation [BIG 01].

$$\text{Nu}_k = 0.023 \cdot \text{Re}_k^{0.8} \cdot \text{Pr}_k^a \quad \text{Eq. D.1}$$

$$h_k = \text{Nu}_k \cdot \frac{\lambda_k}{D_h} \quad \text{Eq. D.2}$$

Where: “a = 0.4” for liquid phase and “a = 0.3” for vapor phase.

For two-phase evaporation flow, the correlation listed in Table D.1 is used.

Table D.1: Two-phase evaporation heat-transfer correlation [GUN, 86]

Correlation	Fluids	Range of parameters / Comments
$h_{tp} = S \cdot h_{pmb} + E \cdot h_L$		
$E = 1 + 24000 \cdot \text{Bo}^{1.16} + 1.37 \cdot \left(\frac{1}{X_H} \right)^{0.86} \cdot \text{Fr}_L^{(0.1-2\text{Fr}_L)}$	Water R-11 R-12	-For saturated flow boiling -Parameters: G(kg.m ⁻² .s ⁻¹): 12.4 - 8179.3
$S = \left[1 + 0.00000115 \cdot E^2 \cdot \text{Re}_L^{1.17} \right]^{-1} (\text{Fr}_L)^{1/2}$	R-22 R-113	q _w (w.cm ⁻²): 0.035 - 262 Re: 568.9 - 8.75*10 ⁵
$X_H = \left(\frac{\mu_l}{\mu_v} \right)^{0.1} \cdot \left(\frac{1-x}{x} \right)^{0.9} \cdot \left(\frac{\rho_v}{\rho_l} \right)^{0.5}$	R-114 Ethylene glycol	Pr: 0.0023 - 0.895 D (mm): 2.95 - 32.0 x: 0 - 0.95
$h_{pool} = 55 p_r^{0.12-0.21 \log_{10} \varepsilon} \left[-\log(p_r) \right]^{-0.55} M^{-0.5} q^{0.67}$		

b. Pressure drop in tubes

The total two-phase pressure drop in a tube is the sum of the gravity pressure drop (dP/dz)_{gravity}, the acceleration pressure drop (dP/dz)_{acceleration}, and the frictional pressure drop (dP/dz)_{frictional} [DID 02].

$$\left(\frac{dP}{dz} \right)_{total} = \left(\frac{dP}{dz} \right)_{frictional} + \left(\frac{dP}{dz} \right)_{acceleration} + \left(\frac{dP}{dz} \right)_{gravity} \quad \text{Eq. D.3}$$

The gravity pressure drop is given by:

$$\left(\frac{dP}{dz} \right)_{gravity} = \rho_{tp} \cdot g \cdot \sin\theta \quad \text{Eq. D.4}$$

Where: “θ” is the inclination angle from the horizontal and “ρ_{tp}” is the density given by:

$$\rho_{tp} = \varepsilon \cdot \rho_{vap} + (1 - \varepsilon) \cdot \rho_{liq} \quad \text{Eq. D.5}$$

For a horizontal tube, there is no change in static head so the gravity pressure drop is nil. The acceleration pressure drop for two-phase flow reflects the change in kinetic energy of the flow and it is given by:

$$\Delta P_{\text{acceleration}} = G^2 \cdot \left\{ \left[\frac{x^2}{\rho_v \cdot \epsilon} + \frac{(1-x)^2}{\rho_l \cdot (1-\epsilon)} \right]_{\text{out}} - \left[\frac{x^2}{\rho_v \cdot \epsilon} + \frac{(1-x)^2}{\rho_l \cdot (1-\epsilon)} \right]_{\text{in}} \right\} \quad \text{Eq. D.6}$$

For an evaporating flow, the kinetic energy of the outgoing flow is larger than that of the incoming flow since the vapor-phase density is less than that of the liquid. Hence, the momentum pressure drop results in lower pressure at the exit than that at the inlet.

For the calculation of the single-phase frictional pressure drop, the ‘‘Blasius’’ equation will be used as follows [DID 02]:

$$\left(\frac{dP}{dz} \right)_{k_0} = f_k \frac{2 \cdot G}{d_i \cdot \rho_k} \quad \text{Eq. D.7}$$

$$f_k = 0.046 \cdot \text{Re}_{k_0}^{-0.2} \quad \text{Eq. D.8}$$

The frictional pressure drop in two-phase flows is typically predicted using the correlation listed in Table D.2.

Table D.2: Two-phase friction pressure drop correlation [FRI 79]		Range
Correlation		
$\left(\frac{dP}{dz} \right)_{\text{frictional}} = \left(\frac{dP}{dz} \right)_{l_0} \cdot \Phi_{\text{fr}}^2$		
$\Phi_{\text{fr}}^2 = E + \frac{3.24 \cdot F \cdot H}{\text{Fr}_H^{0.045} \cdot \text{We}_L^{0.035}}$	$E = (1-x)^2 + x^2 \frac{\rho_L \cdot f_v}{\rho_v \cdot f_L}$	$\mu_l / \mu_v < 1000$ $0 \leq x \leq 1$ Flow regime: Adiabatic annular two phase flow
$F = x^{0.78} \cdot (1-x)^{0.224}$	$H = \left(\frac{\rho_L}{\rho_v} \right)^{0.91} \left(\frac{\mu_v}{\mu_L} \right)^{0.19} \left(1 - \frac{\mu_v}{\mu_L} \right)^{0.7}$	

c. Frictional pressure drop in elbow

The pressure drops in the return bends may be important and must be taken into account. Fig. D.1 shows a sketch of a 180° return bend connecting two parallel straight tubes.

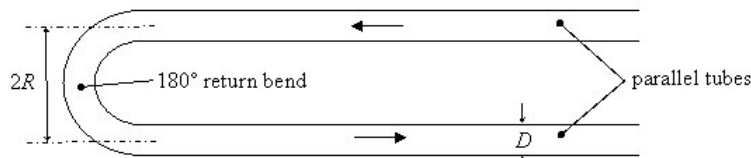


Fig. D.1: Schematic of a 180° return bend

In single-phase flow, the frictional pressure drop is calculated by:

$$\left(\frac{dP}{dz} \right)_{k_0} = f_D \frac{2 \cdot G}{D_i \cdot \rho_k} \quad \text{Eq. D.9}$$

The following correlation is proposed for Darcy friction factor, f_D for bend as follows [POP 00]:

$$\ln\left(\frac{f_D \text{Re}}{64}\right) = 0.021796 + 0.0413356(\ln D_n)^2 \quad \text{Eq. D.10}$$

$$D_n = \frac{2rV}{\nu} \sqrt{\frac{r}{R}} = \text{Re} \sqrt{\frac{r}{R}} \quad \text{Eq. D.11}$$

Where: “ D_n ” is the Dean number, “Re” is the Reynolds number, “V” is the mean velocity along the tube, “ ν ” is the coefficient of kinematic viscosity, and “ $2r$ ” is the tube diameter that is bent into an arc of radius “R”.

In two-phase flow, the correlation of Padilla *et al.* [PAD 09] is used. The frictional pressure drop is considered the sum of the frictional pressure gradient that would be obtained in straight tubes and the singular pressure gradient. As a result, the total measured pressure gradient in return bends is given by the following relation:

$$\left(-\frac{dP}{dz}\right)_{rb} = \left(-\frac{dP}{dz}\right)_{st} + \left(-\frac{dP}{dz}\right)_{\text{sing}} \quad \text{Eq. D.12}$$

Where: $(-dp/dz)_{st}$ is the frictional pressure gradient that would be reached in straight tubes. The second term $(-dp/dz)_{\text{sing}}$ is the singular pressure gradient and is given by the following relation:

$$\left(-\frac{dP}{dz}\right)_{\text{sing}} = a \left[\frac{\rho_v J_v^2}{R} \right] \left[\frac{J_l^2}{R} \right]^b \quad \text{Eq. D.13}$$

Where: $a = 0.047 \text{ s}^{2/3}/\text{m}^{1/3}$; $b = 1/3$; R is the curvature radius; J_v and J_l are the superficial velocities of the vapor and liquid written as:

$$J_v = \frac{G \cdot x}{\rho_v} \quad \text{Eq. D.14}$$

$$J_l = \frac{G \cdot (1-x)}{\rho_L} \quad \text{Eq. D.15}$$

d. Void fraction

The void fraction (ε) is the key physical value for determining numerous other important parameters, such as the two-phase density and the two-phase viscosity, and is of fundamental importance in models for predicting flow pattern transitions, and acceleration pressure drop. The void fraction is defined as:

$$\varepsilon = A_G / (A_G + A_L) \quad \text{Eq. D.16}$$

Where: “ A_G ” is the area of the cross-section of the channel occupied by the vapor phase and “ A_L ” is that of the liquid phase.

The void fraction is correlated using the “Drift Flux Method” as follows:

$$\varepsilon = \frac{x}{\rho_G} \left\{ C_o \left(\frac{x}{\rho_G} + \frac{1-x}{\rho_L} \right) + \frac{U_{GU}}{G} \right\}^{-1} \quad \text{Eq. D.17}$$

In Eq. D.17, “ U_{GU} ” is the drift velocity.

For horizontal tubes, “ C_o ” and “ U_{GU} ” are correlated as follows [ROU 70]:

$$C_o = 1 + c_o(1-x) \quad \text{Eq. D.18}$$

Where: “ c_o ” = 0.12 and the term (1-x) have been added to the other expression to give:

$$\bar{U}_{GU} = 1.18(1-x) \left[\frac{g\sigma(\rho_L - \rho_G)}{\rho_L^2} \right]^{1/4} \quad \text{Eq. D.19}$$

$$\varepsilon = \frac{x}{\rho_G} \left\{ [1 + 0.12(1-x)] \left(\frac{x}{\rho_G} + \frac{1-x}{\rho_L} \right) + \frac{1.18}{G} \left[\frac{g\sigma(\rho_L - \rho_G)}{\rho_L^2} \right]^{1/4} (1-x) \right\}^{-1} \quad \text{Eq. D.20}$$

e. Heat transfer and pressure drop correlations at flue-gas side

The correlations used for the Colburn j and f factors at the flue-gas side are shown in Table D.3.

Table D.3: References of the correlations used at the flue-gas side

	Heat transfer		Pressure drop	
	Dry	Wet	Dry	Wet
Plain fins	[GRA 86]	[WAN 00a]	[WAN 00b]	[WAN 00a]
Wavy fins	[WAN 02]	[WAN 99]	[WAN 02]	[WAN 99]

Annex E: Test-bench description

a. Sensors specifications

Temperatures are measured using ‘PT100’ sensors with four wire connections (Fig. E.1c). The temperature sensor ‘PT100’ measures a resistance. Resistance thermometers work on the principle that the resistance of a metal varies with temperature. The ‘PT 100’ sensor is a temperature transducer based on the resistance change of platinum with temperature. Values are transmitted to a data acquisition system via a 4-conductors measurement.

The pressure sensors used are of type ‘Keller’ (Fig. E.1a) measuring the absolute pressure. The ‘Keller’ series are equipped with an electronic signal processing based microcontroller to provide the best possible accuracy. The accuracy is 0.03% at ambient temperature, and varies from 0.1% (10°C to 40°C) to 0.15% (-10°C to 80°C). The output signal of the pressure sensors is two-wire 4 - 20 mA, with a non-separated input voltage supply.

The differential pressure is measured using a differential pressure sensor (Fig. E.1b) that measures the difference between two pressures, one connected to each sensor side. A ‘Rosemount 2051’ pressure transmitter type combining 0.075% reference accuracy is used. The output signal is two-wire 4 - 20 mA, with a separated input voltage supply.

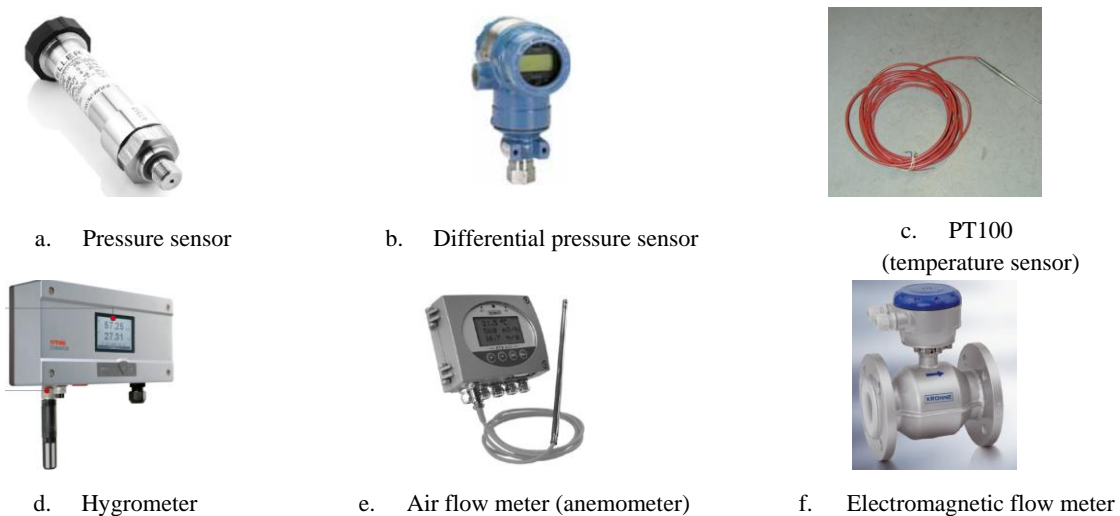


Fig. E.1: Sensors specifications

‘Rotronic’ type hygrometers (Fig. E.1d) are used with a humidity range between 0 and 100% and a fluid temperature range between -100°C and 200°C. The accuracy is $\pm 0.8\%$ at $23\pm 5^\circ\text{C}$. The output signal is two-wire 4 - 20 mA, with a separated input voltage supply.

The flow meter used at the airside (Fig. E.1e) is a two-wing anemometer (‘Kimo’ manufacturer). The measuring range is to 0-30 m/s and the accuracy is $\pm 0.3\%$. The output signal is two-wire 4 - 20 mA, with a separated input voltage supply.

To measure the water mass flow rate in the water circuit, an ‘Optiflux 4100’ electromagnetic flow meter (Fig. E.1g) is used (‘Krohne’ manufacturer). The output signal is two-wire 4 - 20 mA, with a separated input voltage supply.

b. Test-bench mounting and operation

The test bench is composed of two main circuits:

- The air circuit including the air preparation unit used to heat and to humidify the air
- The water circuit

b.1 Preparation unit for heating and humidifying air

This unit includes mainly a blower with variable speed to ensure a wide range of frontal velocity on the heat exchangers, air heaters to heat ambient air to a desired temperature to be able to hold the desired humidity and a steam injection system.

The blower is as shown in Fig. E.2. The air blower was sized based on the air volume flow rate and airside pressure-drop estimation. It is a variable speed centrifugal reaction “VARS 500“ (“AIRAP” manufacturer) and provides a maximal volume flow rate around $4000 \text{ m}^3 \cdot \text{hr}^{-1}$ at 50 Hz. The maximal allowable temperature at the blower inlet is 80°C .

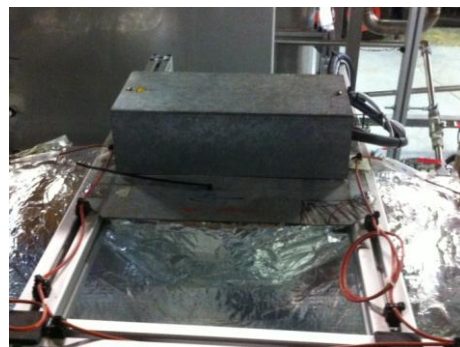


Fig. E.2: Variable speed blower

The electrical air heaters are shown in Fig. E.3. EH01 (50 kW) has a square section shape containing 15 heating elements. EH02 (10 kW) has a circular shape. For safety reasons, the electrical heaters are self-fitted by a security thermostat to cut the electric input at a given temperature limit (220°C). The role of EH01 is to heat the ambient air to a desired temperature to be able to hold the desired humidity. EH02 rules the air temperature disruption after water injection.



(a) EH01 (50 kW)



(b) EH02 (10 kW)

Fig. E.3: Electrical air heaters

The moist air unit is a steam injection system. Fig. E.4 shows the steam injection system, the safety valve, and the hand valve. The latter is used to control the quantity of steam injected. The needed steam quantity is provided by cold water vaporization into a plate-heat exchanger (HX01) through a heat-exchange transfer between the hot oil entering from the boiler hot oil generator and the cold water

entering from outside. The plate-heat exchanger (with the corresponding inlet and outlet fluids) is shown in Fig. E.5.

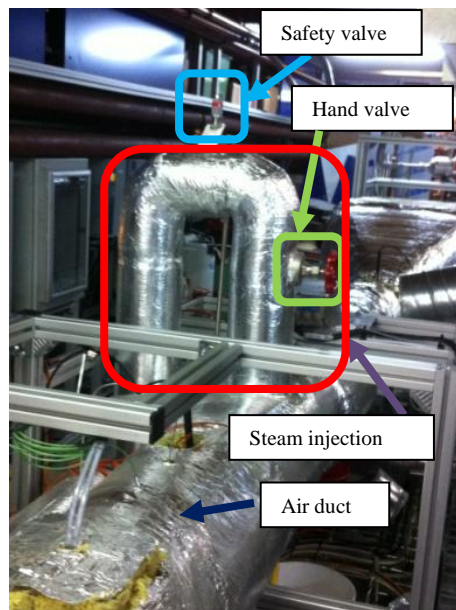


Fig. E.4: Steam injection system

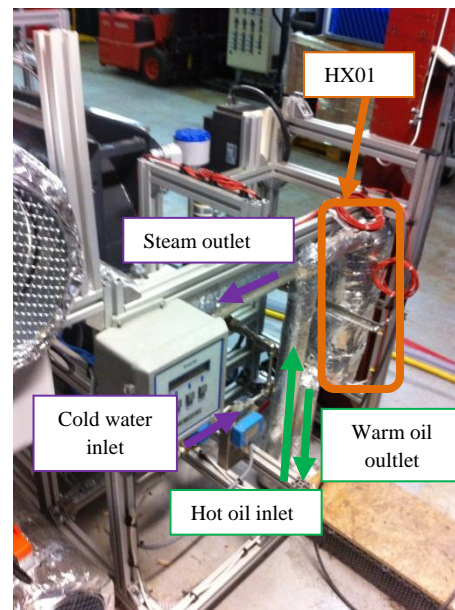


Fig. E.5: Plate-heat exchanger (HX01) with the corresponding inlet to and outlet fluids

An electro valve (“parker series”, 7321B) is used to control the quantity of water entering the PHX. A “Coriolis” flow meter is installed to measure the corresponding flow rate. Fig. E.6 shows the electro vane and the “Coriolis” flow meter.

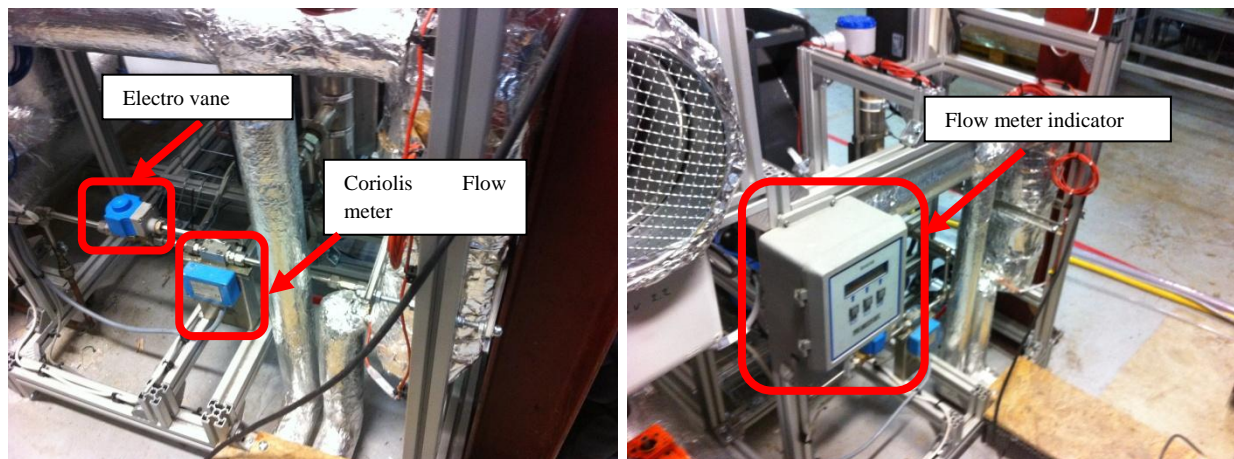


Fig. E.6: Electro vane and flow meter mounted at the “HX01” water inlet

A level sensor is used to control the water level inside the plate-heat exchanger (Fig. E.7). The level sensor measures position and water level (at liquid state) inside the plate heat exchanger by direct method. It is controlled by two operating levels: low level and high level. If the quantity of water in the plate-heat exchanger is lower than the low level, an automatic valve will open and then the cold water enters the heat exchanger. If the quantity of water is higher than the high level, then the automatic valve will cut the entering water to the plate-heat exchanger.



Fig. E.7: Level sensor



Fig. E.8: Water steam separator

To ensure the injection of pure steam and to avoid condensate water to enter into the air circuit, a liquid / vapor separator is installed at the same vertical line of the entering steam into the air circuit (Fig. E.8). The condensed water at the separator outlet is drained to the outside.

The inlet, exit, and recirculation air ducts are shown in Fig. E.9. Air recirculation is of importance to reach given water dew point temperature ($> 50^{\circ}\text{C}$). Each air duct is equipped with a motorized air damper in order to control the air opening.

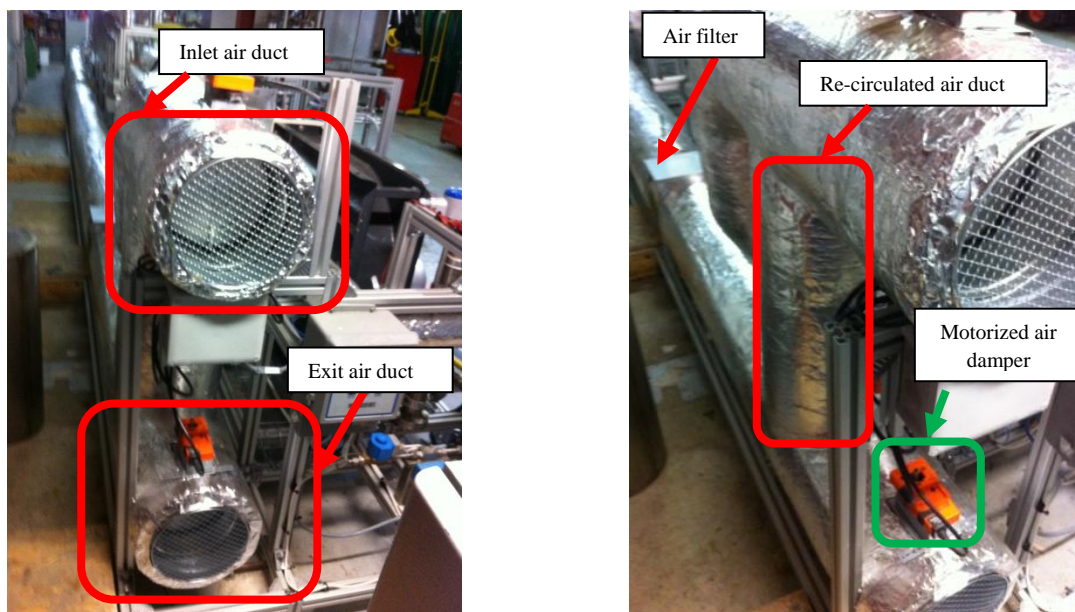


Fig. E.9: Inlet, exit, and re-circulated air ducts

b.2 Water circuit for fin-and-tube heat exchanger

The water circulation pipes as well as the main components of the water and coolant circuits are shown respectively in Fig.E.10 and Fig.E.11. The water at the exit of the fin-and-tube heat exchanger is pumped by Pump 1 to the plate-heat exchanger (HX03) where it is cooled by the coolant that is pumped; in turn by Pump 2.

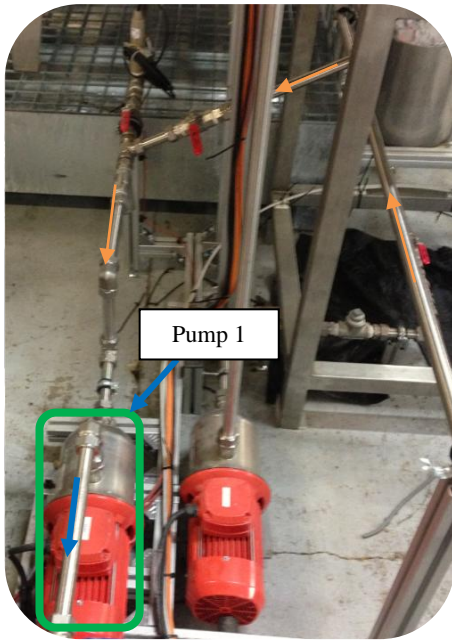


Fig. E.10: Water circulation pipes

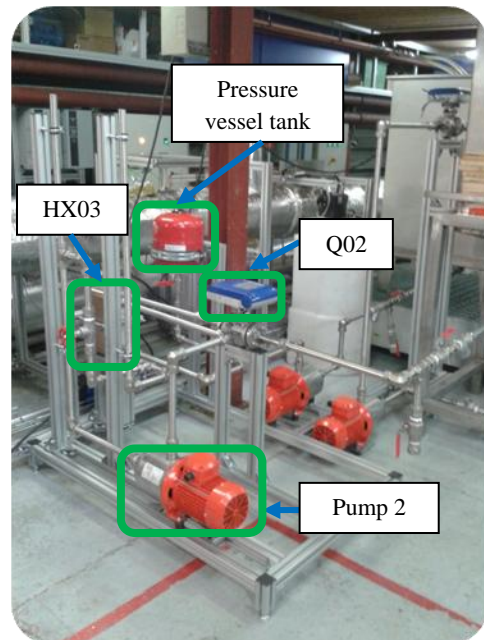


Fig. E.11: Main components of the water and coolant circuits

The mounted fin-and-tube heat exchanger (HX02) to be tested is shown in Fig. E.12 with its inlet and the outlet air ducts.

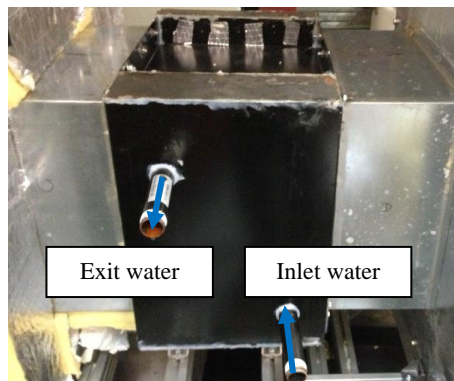


Fig. E.12: Mounted fin-and-tube heat exchanger

b.3 Lab-scale condensing unit

Fig. E.13 shows the layout diagram of the lab-scale condensing unit. In order to establish a uniform airflow at the deflector exit, CFD (Computational Fluid Dynamics) calculations show that a total length around 0.5 m (rain zone) is required. The packing material can be as high as 1.5 m.

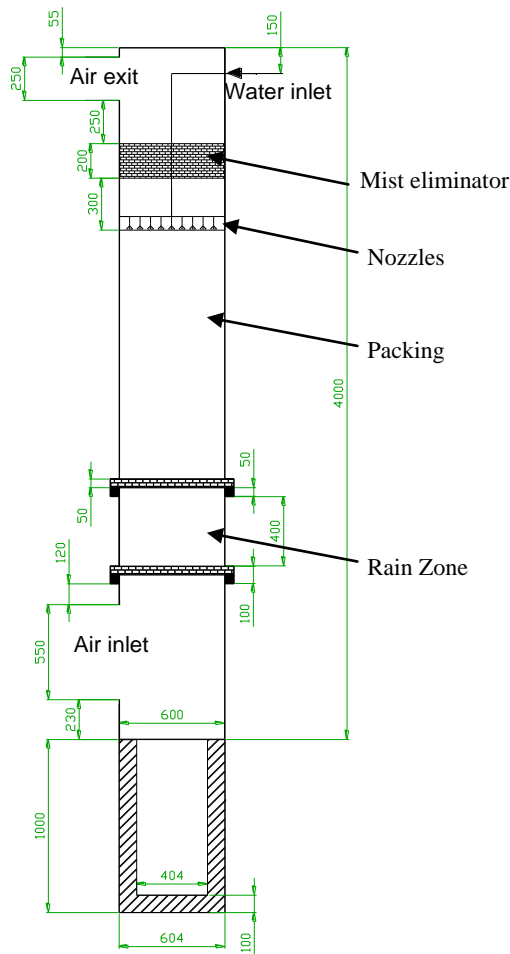


Fig. E.13: Layout of the lab-scale condensing unit
(all dimensions are in mm)

The condensing unit includes two parts (Fig.E.14a and Fig. E.14b). Each part is equipped with sight glasses to visualize water pulverization and water flow distribution. Fig.E.14a shows the “PP” packing mounted inside the condensing unit, the placement of the air diffuser, the air deflector, the airflow (black arrow) and the water flow (red arrow) directions.

As shown in Fig. E.14b, the nozzle is attached at the end of a stainless-steel tube with a double adapter ring. The tube, which holds the nozzle, was fixed at two places in order to prevent it moving during operation. The optimal spray distance should be kept between the nozzle and the top of the packing. An extension tube is provided to hold the nozzle when testing different packing heights in order to keep the optimal spray distance. The demister shown in Fig.E.14b is used to prevent backflow liquid into the air circuit.

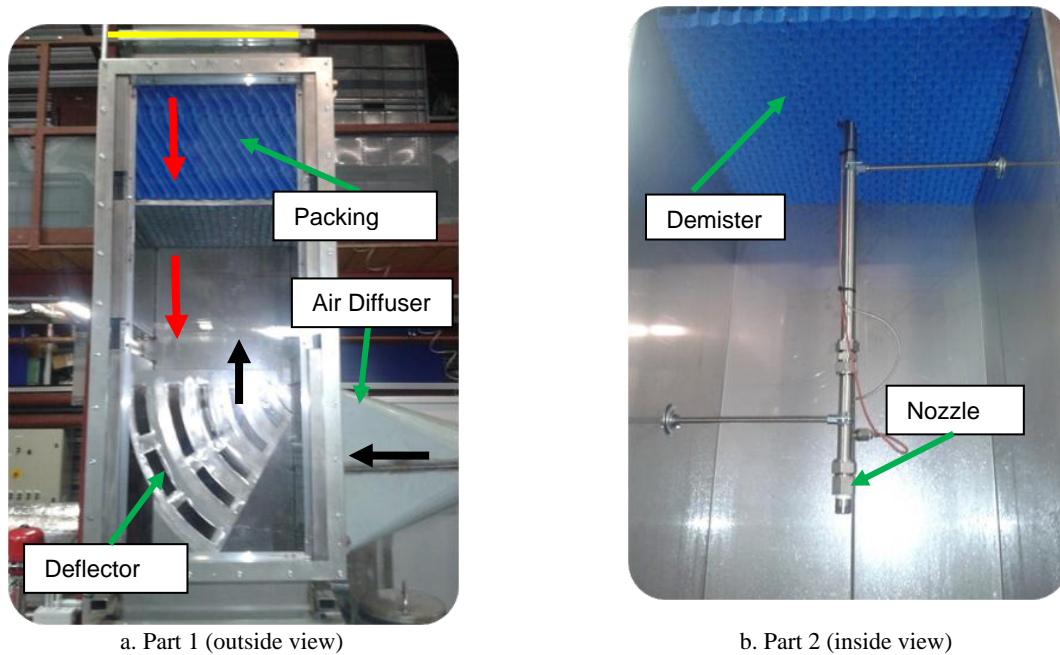


Fig. E.14: Condensing unit components

The water outlet temperature is measured right at the packing outlet using a collector tube. The tube, positioned horizontally, is welded to the wall at the bottom of the packing, and cut along its length (Fig. E.15). A small slope with the horizontal was arranged for the tube in order to allow the water flow through the tube.

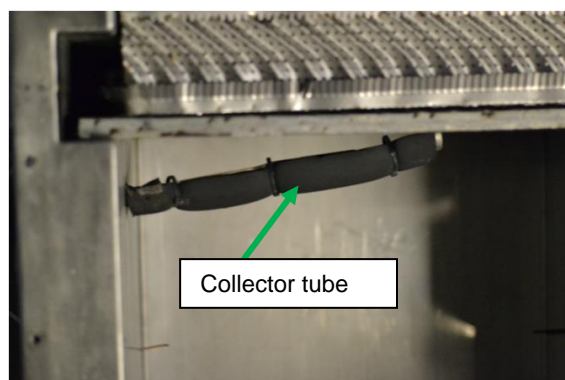


Fig. E.15: Collector tube inside the condensing unit

Fig. E.16 shows the main components of the water and coolant circuits (Pump 1, Pump 2, Pump 3, TK01, HX03). Fig. E.17 shows the water and coolant flow circulation. The coolant (blue arrows) is pumped by “Pump 2” (arrow 2) through “HX03” to cool down the hot water and then it exits to the outside (arrow 3). In the water circuit (red arrows), the water is pulverized into the condensing unit (arrow 1), recovered at the condensing unit exit into a small tank and then pumped by “Pump1” (arrow 2) to enter the “Tank 1” (1m³, arrow 3). At the exit of “Tank 1” (arrow 4), the water is pumped to “HX03” (arrow 5) by “Pump 1” where it is cooled (arrow 6) before being sprayed again to continue the cycle operation.

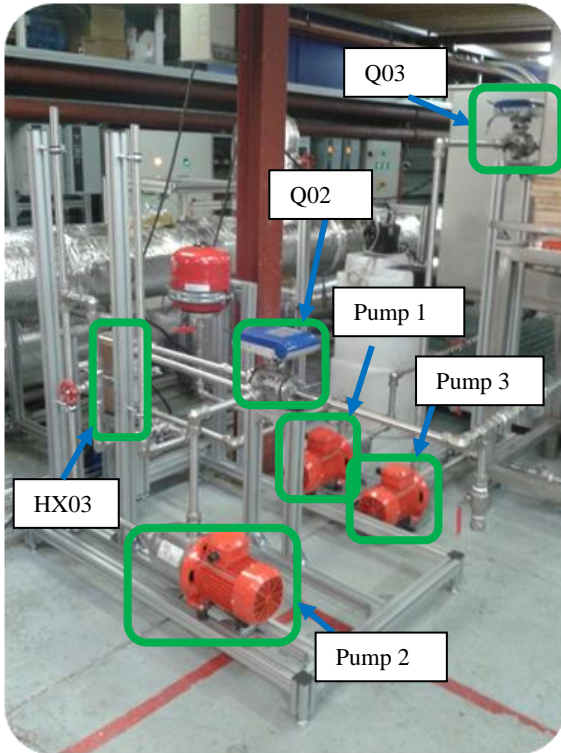


Fig. E.16: Main components of the water and coolant circuits

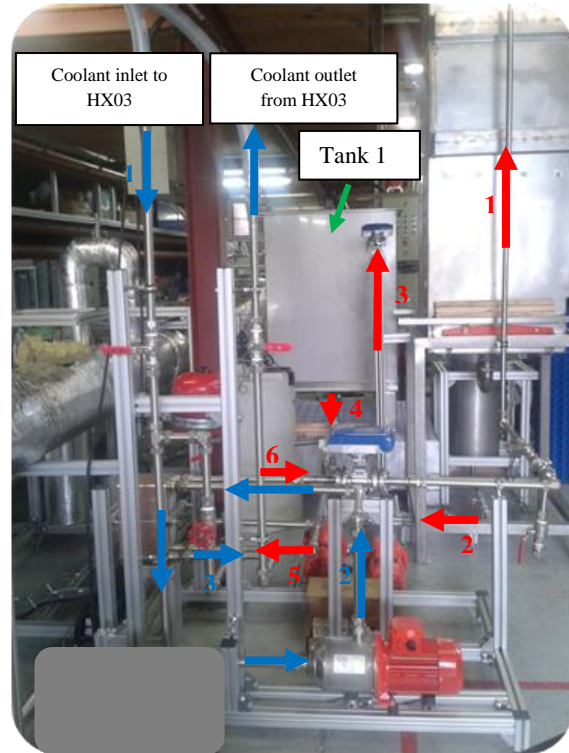


Fig. E.17: Coolant circuit (blue arrows) and water circuit (red arrows)

The galvanized steel air ducts (tubes and elbows, “Ø 250 mm”) are assembled to connect the condensing unit to the ventilation air system (blower) (Fig. E.18).



Fig. E.18: Air ducts

➤ Nozzles

The uniformity of liquid spray distribution used in the condensing unit is important to maximize the efficiency of mass and heat exchange between the liquid and flue gases. A poor choice of nozzles can

have a significant impact on the heat exchange and mass transfer efficiencies. The key factors affecting spraying distribution are nozzles technology, spray distance, and coverage area.

Each nozzle is characterized by a spray angle. The spray distance can be calculated from the coverage area using a triangular relationship. Fig. E.19 shows the spray angle, the spray distance, and the coverage area.

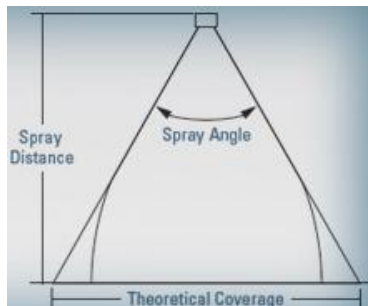


Fig. E.19: Nozzle coverage area



Fig. E.20: Square impact area

When using a square cross-sectional area, the spray nozzles will be then selected with a square impact area (Fig. E.20). A solid cone-shaped spray pattern type with square impact area is selected. The spray angle varies from 40° to 102° at 7psi (0.5bar). It performs a uniform spray across their entire spray area and is ideal for installations requiring complete coverage of rectangular areas or spray zones. Removable caps and vanes for easy inspection and cleaning are available on many models.

HH-SQ



One-piece body
1/8" to 3/4" NPT or BSPT (M)

Fig. E.21: Solid cone-shaped spray pattern with square impact area (spray.com)

One nozzle is found to be sufficient for a square section 0.6 x 0.6 m². The HH-SQ (50 SQ) type has been used (Fig. E.21). The nozzle parameters are shown in Table E.1.

Table E.1: Nozzle parameters

Type	HH- SQ(50 SQ)
Number	1
Inlet connection	3/4"
Pressure drop (bar)	≈ 1.4
Spray angle (°)	≈ 75

➤ Mist eliminators

The mist eliminator is installed horizontally on the top of the liquid distribution system (nozzles). The gas stream, with entrained droplets generated by nozzles, flows upward through the eliminator. The gas can pass through the eliminator freely; liquid droplets are held by the eliminator and coalesce with other droplets, and drain down once heavy enough. Two types of mist capture principles should be distinguished as illustrated in Fig. E.22: vane and wire mesh.

- For the vane eliminator, the gas flow changes directions by passing through (a1) wherever momentums of droplets keep then moving in straight way (a2), striking the vanes. Captured droplets merge until they are large and heavy enough to trick down (a3).
- For the mesh eliminator, the liquid droplets are retained on the wire surface (b1), become larger, spread to the lower surface of the eliminator (b3), and fall down/through.

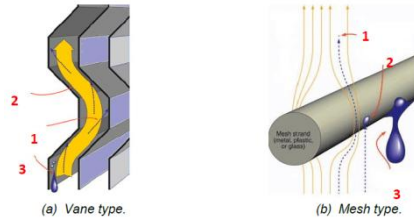


Fig. E.22: Capture principle of vane and mesh eliminators

Compared to mesh type, the vane type mist-eliminators are characterized by a lower pressure drop but by a higher water loss ratio. The water loss ratio is defined as the fraction of pulverized water crossing the mist eliminators. When recovering industrial waste heat, the rate training of water droplets is not a primary constraint, and the flue-gas pressure drop remains the target. Thus, the solid vane technology is more promising and has been used in our study.

Acknowledgements: Application of the results and framework to the cement production industry

The present thesis has been done under the framework of a “European” project launched by the “European Union” with the acronym “LOVE” (LOW temperature heat Valorization through Electricity production) with the overall aim to develop and test innovative technological solutions toward efficient and economically viable electricity production through valorization of low-temperature waste heat in process industries.

The cement industry, on which the “LOVE” project focuses as an emblematic test case, represents one of the most energy-intensive industrial sectors, since it accounts for 8% of the industrial energy use and 25% of the energy and process CO₂ emissions worldwide. The cement industry has the infrastructure to enable the deployment of the new technologies developed within the “LOVE” project, notably in “Europe”, thus ensuring their “European” wide applicability. Two world leading cement producers have joined this project: “HOLCIM and CEMEX”. They have the infrastructure to enable the deployment of newly developed technologies not only in “Europe” but worldwide.

In the cement production process, flue gases are released into the atmosphere at the raw mill exit and after cleaning, at 120°C or below. Low-temperature gases are also released at the cement mill exit. Therefore, the intent is to install two pilot-demonstration power units in two cement plants located in “Northern Germany” thus allowing for the deployment of technological solutions in an important region not only due to its production levels but also due to its commitment toward more energy-efficient and environmentally friendly process solutions.

By the conclusion of the “LOVE” project, two transportable demonstration power units will have been built and operated at two cement plants with an electrical power output of “100 kW” using presently wasted low-temperature heat through an Organic Rankine Cycle (ORC). The two heat sources are the following:

- Source “A”: “Raw mill” exit at “HOLCIM Höver” plant.
- Source “B”: “Cement mill” exit at “CEMEX Kollenback” plant

The characteristics of the heat sources are shown in Table 1. Source “A” is characterized by an inlet dry bulb temperature of 112°C, and a water dew point temperature of 61.7°C. Source “B” is characterized by an inlet temperature of 110°C and a water dew point temperature of 60°C.

Table 1: Heat sources characterization

Parameters	Units	Source A	Source B
T _{inlet flue gases}	°C	112	110
T _{water dew point}	°C	61.7	60
T _{wet bulb}	°C	64.7	62.7
SO ₂ content	ppm	~ 100	-
% CO ₂	% v	16.37	-
% H ₂ O	% v	21.28	-
% O ₂	% v	5.82	-
% N ₂	% v	56.52	-

A direct-contact condensation process will be used to recover heat from Source “A” due to the presence of pollutant contents (SO₂, CO₂...). However, using only a direct-contact heat exchanger will lead to a large equipment size due to the required high working fluid and hot water mass flow rates (refer to Chapter 1); in addition, a low turbine expansion ratio is expected. In order to reduce the

equipment size and to increase the turbine expansion ratio, a hybrid heat-recovery process has been mounted and the design circulating water temperature is set to 95°C. For Source “B” (clean heat source), an indirect-contact water-vapor condensation system will be investigated for heat recovery.

Fig. 1 shows the hybrid heat-recovery integration at “HOLCIM Höver” plant. Fig. 2 shows the fin-and-tube heat-exchanger integration at “CEMEX Kollenback” plant.

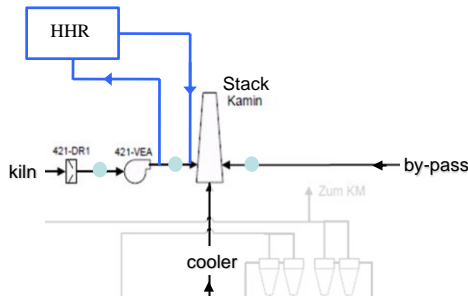


Fig. 1: Hybrid heat recovery integration at “HOLCIM Höver” plant (Source “A”)

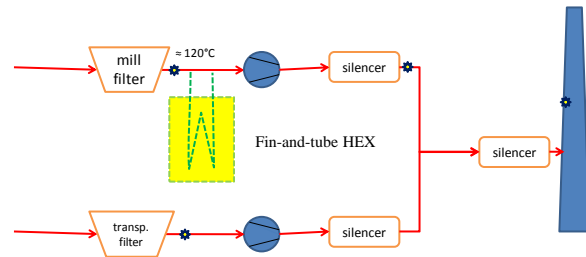


Fig. 2: Fin-and-tube heat exchanger integration at “CEMEX Kollenback” plant (Source “B”)

As expected, the ORC system will be tested during three months at each plant. The condenser, turbine, and pump will be shared between the two plants. The used working fluid is “R-245fa”. The design evaporation pressure is set to 0.5 MPa. The outside air conditions at the design point are estimated to be 25/20°C ($T_{dry\ bulb}/T_{wet\ bulb}$). The turbine, delivered by “Cryostar” (partner in “LOVE” project), presents an efficiency around 80% at the design conditions. In order to produce a “100 kW” at the turbine outlet, the required flue-gas volume flow rate for Source “A” is calculated to be 56,300 N.m³/hr, while for Source “B”, only 32,000 N.m³/hr are available on site and the generated turbine power will be around “55 kW”.

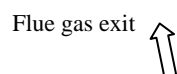
- **Hybrid heat recovery mode mounted at Source “A”**

The operating parameters of the fin-and tube heat exchanger and the condensing unit mounted at Source “A” are shown in Table 2. The mass of working fluid in ORC system (R-245fa) is equal to “7.25 kg.s⁻¹”.

Table 2: Operating parameters of the fin-and tube heat exchanger and the condensing unit (Source “A”)

Parameters	Units	Fin-and-tube heat exchanger	Condensing unit
$V_{dry\ flue\ gases\ at\ normal\ conditions}$	Nm ³ /hr _{dg}	56278	56278
$T_{inlet\ FG}$	°C	112.0	64.0
$T_{inlet\ dp}$	°C	61.7	61.7
$T_{inlet\ wet\ bulb}$	°C	64.7	61.8
$T_{inlet\ water}$	°C	61.3	57.5
$T_{outlet\ water}$	°C	95.0	61.3
$m_{hot\ water}$	Kg.s ⁻¹	9.67	9.67
Q	kW _{th}	1368.24	155.08

The hybrid heat-recovery system mounted at Source “A” is shown in Fig. 3. Flue gases enter the fin-and-tube heat exchanger and then flow into the condensing unit.



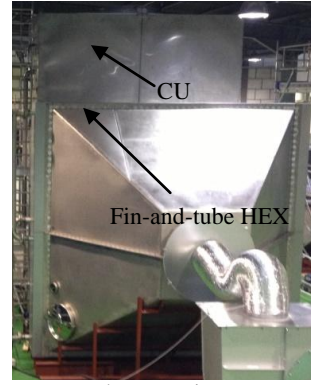
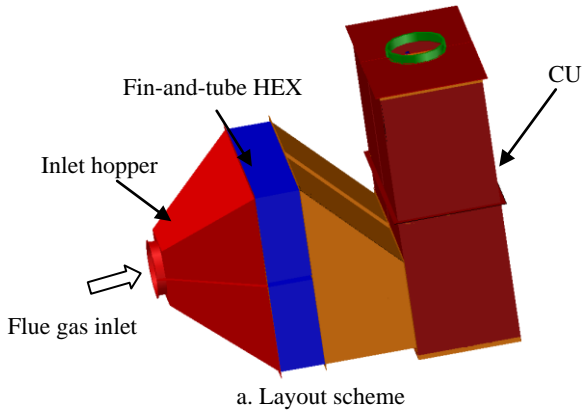


Fig. 3: Hybrid heat recovery system mounted at the Raw mill exit at “HOLCIM Höver” site

Frontal views for the fin-and-tube heat exchanger mounted at Source “A” are shown in Fig. 4. For feasibility and costs reasons, copper tubes/ aluminum fins are selected.

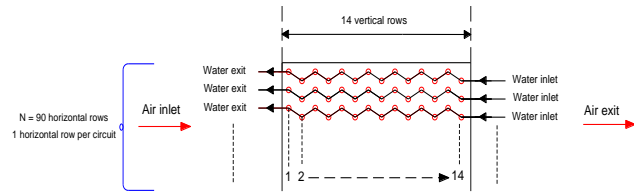


Fig. 4: Fin-and-tube heat exchanger mounted at Source “A”

Based on the design method shown in Chapter 2, the geometrical and operating parameters of the fin-and-tube heat exchanger mounted at Source “A” are shown in Table 3. The fin-and-tube heat exchanger will be composed of “90” horizontal rows and “14” vertical rows.

Table 3: Geometrical and operating parameters for the fin-and-tube heat exchanger mounted at Source “A”

Tube/Fin materials	Copper/aluminum	G ($\text{kg}\cdot\text{m}^{-2}\cdot\text{s}^{-1}$)	714
HEX depth (mm)	0.545	$V_{a,s}$ ($\text{m}\cdot\text{s}^{-1}$)	1.83
HEX length (mm)	4.05	$V_{a,e}$ ($\text{m}\cdot\text{s}^{-1}$)	3.03
HEX height (mm)	4.05	Estimated $DP_{\text{flue gases}}$ (Pa)	~ 150
N_{tubes}	1260	Estimated DP_{water} (kPa)	~ 28

Based on the design method shown in Chapter 3, the geometrical and operating parameters of the condensing unit mounted at Source “A” are shown in Table 4. For feasibility and cost reasons, polypropylene wavy packing “PP” is selected.

Table 4: Operating parameters of the Condensing Unit mounted at Source “A”

A_{fr}	$\text{m}^2\cdot\text{m}$	4*2.25
F_{factor}	$\text{m}\cdot\text{s}^{-1}\cdot(\text{kg}\cdot\text{m}^{-3})^{0.5}$	2.70
$F_{\text{@ loading point}}$	$\text{m}\cdot\text{s}^{-1}\cdot(\text{kg}\cdot\text{m}^{-3})^{0.5}$	2.41
u_{gs}	$\text{m}\cdot\text{s}^{-1}$	2.98
Liquid load	$\text{m}^3\cdot\text{m}^{-2}\cdot\text{h}^{-1}$	3.96
Packing height	m	0.6
Condensing Unit height	m	~ 6
Estimated $DP_{\text{flue gases}}$	Pa	~100

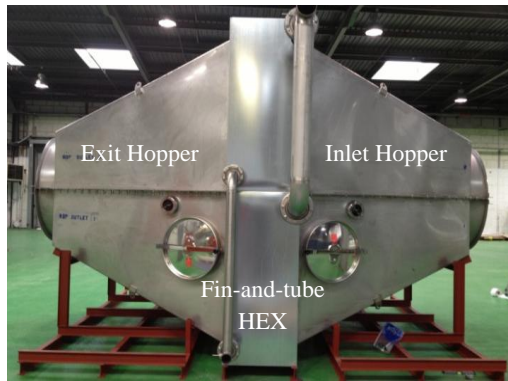
- **Indirect-contact heat recovery mode mounted at Source “B”**

As stated previously, Source “B” is a clean heat source; therefore, an indirect-contact water-vapor condensation system will be investigated for heat recovery. The operating parameters of the fin-and tube heat exchanger mounted at Source “B” are shown in Table 5.

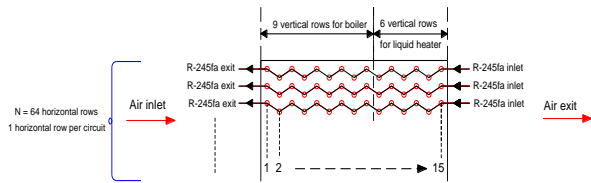
Table 5: Operating parameters of the fin-and-tube heat exchanger mounted at Source “B”

Parameters	Units	Source B
$V_{\text{dry flue gases at normal conditions}}$	$\text{Nm}^3/\text{hr}_{\text{dry FG}}$	32,000
$T_{\text{inlet flue gases}}$	$^{\circ}\text{C}$	110.0
$T_{\text{dp inlet}}$	$^{\circ}\text{C}$	60.0
$T_{\text{evap @ saturated vapor}}$	$^{\circ}\text{C}$	62.7
Boiler superheat	K	0.0
Pinch evaporator	K	3.0
$m_{\text{R-245fa}}$	kg/s	3.89
Q_{evap}	kWth	826.45

Side views for the fin-and-tube heat exchanger mounted at Source “B” are shown in Fig. 5. For feasibility and cost reasons, copper tubes/ aluminum fins are selected.



a. Side view



b. Layout (side view)

Fig. 5: Fin-and-tube heat exchanger mounted at Source “B”

The parameters of the fin-and tube heat exchanger mounted at Source “B” are shown in Table 6. The fin-and-tube heat exchanger will be composed of 64 horizontal rows and 15 vertical rows.

Table 6: Geometrical and operating parameters of the fin-and-tube heat exchanger mounted at Source “B”

Tube/Fin materials	Copper/aluminum	$G (\text{kg}\cdot\text{m}^{-2}\cdot\text{s}^{-1})$	404
HEX depth (mm)	0.585	$V_{\text{a,s}} (\text{m}\cdot\text{s}^{-1})$	1.87
HEX length (mm)	2.88	$V_{\text{a,e}} (\text{m}\cdot\text{s}^{-1})$	3.10
HEX height (mm)	2.88	Estimated $DP_{\text{flue gases}} (\text{Pa})$	~ 150
N_{tubes}	960	Estimated $DP_{\text{R-245fa}} (\text{kPa})$	~ 45

Etude et conception d'un système thermodynamique producteur du travail mécanique à partir d'une source chaude à 120°C

RESUME :

Les fumées à basse température (<120-150 °C) sortant des procédés industriels pourraient être récupérées pour la production d'électricité et constituent un moyen efficace de réduction de la consommation d'énergie primaire et des émissions de dioxyde de carbone. Cependant, des barrières techniques tels que la faible efficacité de conversion, la nécessité d'une grande zone de transfert de chaleur, et la présence de substances chimiques corrosives liées à une forte teneur en humidité lors du fonctionnement en environnement sévère entravent leur application plus large. Cette thèse porte particulièrement sur les secteurs industriels les plus énergivores rencontrant actuellement des difficultés à récupérer l'énergie des sources de chaleur à basse température dans des environnements hostiles. Des cycles thermodynamiques existants basés sur le Cycle de Rankine Organique (ORC) sont adaptés et optimisés pour ce niveau de température. Deux méthodes de récupération de chaleur classiques sont étudiées plus particulièrement : les déshumidifications à contact direct et indirect. Des méthodes de conception optimisées pour les échangeurs de chaleur sont élaborées et validées expérimentalement. Pour la déshumidification à contact indirect, des matériaux à revêtement anticorrosifs sont proposés et testés. Pour la déshumidification à contact direct, les effets du type et de la géométrie des garnissages sur les performances hydrauliques sont étudiés. Des cycles thermodynamiques innovants basés sur la technologie de déshydratation liquide sont proposés. Un cycle de régénération amélioré (IRC) est développé. Comparé aux technologies de récupération de chaleur classiques, l'IRC proposé améliore à la fois la puissance nette et le taux de détente de la turbine en prévenant par ailleurs les problèmes de corrosion.

Mots clés : Valorisation de la chaleur à basse température, Cycle de Rankine Organique (ORC), Déshumidification par contact indirect, Déshumidification par contact direct, Déshumidification par absorption.

Study and design of a thermodynamic system generating mechanical work from a hot source at 120°C

ABSTRACT:

Low-temperature waste-gas heat sources (< 120-150°C) exiting several industrial processes could be recovered for electricity production and constitute an effective mean to reduce primary energy consumption and carbon dioxide emissions. However, technical barriers such as low conversion efficiency, large needed heat transfer area, and the presence of chemically corrosive substances associated with high moisture content when operating in harsh environment impede their wider application. This thesis focuses on particularly energy-hungry industrial sectors characterized by presently unsolved challenges in terms of environmentally hostile low-temperature heat sources. Existing thermodynamic cycles based on Organic Rankine Cycle (ORC) are adapted and optimized for this temperature level. Two conventional heat recovery methods are studied more particularly: indirect and direct contact dehumidification. Optimized design methods for heat exchangers are elaborated and experimentally validated. For the indirect contact dehumidification, advanced anti-corrosion coated materials are proposed and laboratory tested. For the direct contact dehumidification, the effects of packing material and geometry on the corresponding hydraulic performances are underlined. Innovative thermodynamic cycles based on the liquid desiccant technology are investigated. An improved regeneration cycle (IRC) is developed. Compared to the conventional heat recovery technologies, the proposed "IRC" improves both net power and turbine expansion ratio besides preventing faced corrosions problems.

Keywords : Low-temperature heat valorization, Organic Rankine Cycle (ORC), Indirect contact dehumidification, Direct contact dehumidification, Desiccant dehumidification.